Technische Universität München

Phenomenology of dark matter searches: simplified models and novel model-independent approaches

Dissertation

by

Sebastian Wild

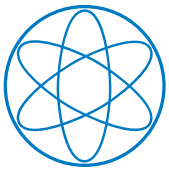

Physik Department T30d

Technische Universität München

Phenomenology of dark matter searches: simplified models and novel model-independent approaches

Sebastian Wild

Vollständiger Abdruck der von der Fakultät für Physik der Technischen Universität München zur Erlangung des akademischen Grades eines

Doktors der Naturwissenschaften

genehmigten Dissertation.

Vorsitzender:	Prof. Dr. Stefan Schönert
Prüfer der Dissertation:	1. Prof. Dr. Alejandro Ibarra
	2. Prof. Dr. Andreas Weiler
	3. Prof. Nicolao Fornengo, Univ. di Torino/Italien (nur schriftliche Beurteilung)

Diese Dissertation wurde am 05.07.2016 bei der Technischen Universität München eingereicht und durch die Fakultät für Physik am 05.09.2016 angenommen.

Abstract

Despite the overwhelming gravitational evidence for the presence of dark matter in our Universe, we still lack an understanding of its particle physics nature. In this work, we investigate the phenomenology of weakly interacting massive particles (WIMPs), a well-motivated class of dark matter candidates which can be probed by direct detection, indirect detection and collider experiments. We first study the complementarity between these search strategies by considering three different t-channel simplified models, in which the Standard Model of particle physics is extended in a minimal way in order to accommodate a viable dark matter candidate. In particular, we take into account various higher-order corrections both to the annihilation as well as to the scattering process of dark matter, and we find that these can be crucial for assessing the detectability of WIMPs within these scenarios. Subsequently, we discuss a variety of model-independent approaches for interpreting data from direct and indirect detection experiments. To this end, we first investigate the impact of generic higher-order corrections on the flux of neutrinos produced by dark matter annihilations in the Sun. Afterwards, we confront the DAMA modulation signal to null search experiments in the context of the non-relativistic effective theory for dark matter-nucleon interactions, which constitutes an (almost) model-independent approach regarding the particle physics of dark matter. Lastly, by developing a novel method for combining data from direct detection experiments and neutrino telescopes which is model-independent with respect to the astrophysics of dark matter, we derive for the first time an halo-independent upper limit on the scattering cross section of dark matter with nucleons.

Zusammenfassung

Trotz der überzeugenden Beweise für die Existenz von Dunkler Materie in unserem Universum sind deren teilchenphysikalischen Eigenschaften noch immer nicht bekannt. In dieser Arbeit beschäftigen wir uns daher mit der Phänomenologie von schwach wechselwirkenden massiven Teilchen (WIMPs), einer Klasse an Dunkle-Materie-Kandidaten die in Experimenten zur direkten und indirekten Detektion sowie in Teilchenbeschleunigern untersucht werden können. Wir betrachten zunächst die Komplementarität dieser Detektionsstrategien anhand dreier vereinfachter t-channel Modelle, in welchen das Standardmodell der Teilchenphysik auf minimale Weise erweitert wird, so dass das Phänomen der Dunklen Materie erklärt werden kann. Hierbei berücksichtigen wir insbesondere Korrekturen höherer Ordnung sowohl im Annihilations- als auch im Streuprozess der Dunklen Materie, welche essenziell zur Beobachtbarkeit der betrachteten Szenarien beitragen. Anschließend diskutieren wir eine Reihe modellunabhängiger Methoden der Interpretation von Experimenten zur direkten und indirekten Detektion. Hierfür untersuchen wir zunächst die Auswirkungen von Korrekturen höherer Ordnung auf den Neutrinofluss welcher von Annihilationen der Dunklen Materie im Inneren der Sonne erzeugt wird. Im Anschluß daran konfrontieren wir das DAMA Modulationssignal mit den Ergebnissen anderer Experimente im Kontext der nicht-relativistischen effektiven Theorie der Streuung von Dunkler Materie an Nukleonen, ein nahezu modellunabhängiger Ansatz bezüglich der teilchenphysikalischen Eigenschaften der Dunklen Materie. Zu guter Letzt entwickeln wir eine neue Methode zum Vergleich der Daten von Experimenten zur direkten Detektion und Neutrinoteleskopen, welche modellunabhängig bezüglich der astrophysikalischen Eigenschaften der Dunklen Materie ist. Inbesondere verwenden wir diesen Ansatz für die erstmalige Berechnung einer oberen Grenze an den Streuquerschnitt von Dunkler Materie mit Nukleonen, welche nicht von der Geschwindigkeitsverteilung der Dunkle-Materie-Teilchen abhängt.

Contents

Introduction

Early in the 20th century, a few astronomers such as Kelvin [1], Öpik [2], Kapteyn [3] and Oort [4] realized that a significant fraction of the matter content of our Galaxy could be in the form of non-luminous *dark matter*[1]. However, to these pioneers of the field the very existence and hence of course also any detailed properties of this population of invisible matter remained unclear. More than 100 years later, we find ourselves in a very different situation: a large variety of convincing evidence for the existence of dark matter has emerged, based on independent observations across several orders of magnitude in length scale; we will briefly recapitulate the most important pieces of evidence in Sec. 1.1 and 1.2. However, all of these observations are solely based on the gravitational nature of dark matter, and hence we have still no understanding of the even most basic particle physics properties of dark matter, such as its mass or spin. One of the few facts we actually know about the dark matter particle is that it can not be part of the *Standard Model of particle physics*, which otherwise has proven to be an extremely successful description of particle physics below the TeV scale. In view of that situation, determining the fundamental properties of dark matter and embedding them into an appropriate extension of the Standard Model is among the most pressing open issues in modern (astro)particle physics, and will be the motivating theme throughout this thesis.

Specifically, we will investigate the phenomenology of *weakly interacting massive particles* (WIMPs), a particularly well-motivated and popular class of candidates for the particle nature of dark matter. As we will explain in more detail in Sec. 1.3, WIMPs are hypothetical particles with a mass the GeV-to-TeV range, interacting with Standard Model particles with a strength comparable to the weak interaction. Intriguingly, models containing a WIMP as the dark matter candidate can naturally accommodate for the amount of dark matter as observed in today's Universe, a fact that is commonly seen as one of the strongest motivation for the idea of WIMPs. Interestingly, there are several ways of testing this paradigm with current and near-future experiments, most notably by means of direct, indirect and collider searches, which will be introduced in Sec. 2. In fact, several experiments have already conducted searches for non-gravitational interactions of dark matter, unfortunately with no unambiguous success so far. However, there are good reasons to expect a wealth of new data within the next decade, hopefully shedding light on whether WIMPs are indeed realized in nature.

It is important to stress that WIMPs constitute a whole *class* of dark matter candidates, with a considerable freedom in the construction of a specific particle physics model containing a WIMP. This leads to the problem that in most cases there is no unique way of translating the results from direct, indirect and collider searches into measurements or constraints on e.g. the dark matter mass or its interaction strength with Standard Model particles. Given the large variety of possible underlying models with different degree of complexity, a natural and minimalistic way for interpreting the data is given by *simplified models*. In such a framework, one extends the Standard Model of particle physics in a minimal way such that the new theory can accommodate for the presence of dark matter,

[1] We refer to [5] for a comprehensive review on the history of the subject.

thereby ignoring other potentially existing new degrees of freedom which are not relevant for the dark matter phenomenology. Typically, a simplified model involves a new particle acting as the WIMP, and in some cases one also introduces a mediator responsible for the interactions of the dark matter particle with the Standard Model degrees of freedom. The virtue of such an approach involving only a few new parameters is that one can map the experimental results from various searches onto the low-dimensional parameter space of the theory, allowing for interesting complementarity studies between the different search strategies. Most importantly, in many cases a simplified model can be either confirmed or fully excluded with future experiments, and thus constitutes a highly predictive framework. We will follow precisely this approach in part II of this thesis, where we investigate the impact of direct, indirect and collider searches on three different *t-channel simplified models*, namely Dirac dark matter in Sec. 3, real scalar dark matter in Sec. 4 and Majorana dark matter in Sec. 5.

However, as the name already suggests, it is also conceivable that the most minimal constructions of simplified models do not capture all relevant aspects of the dark matter phenomenology. In fact, there are well-known examples for more complex UV-complete theories, in which several new states contribute to the scattering and annihilation processes of dark matter. Furthermore, if dark matter interacts e.g. with a very light mediator, a pseudoscalar or only with photons via one-loop processes, the signatures expected in direct and indirect searches could be drastically different from the expectations of "vanilla" simplified models. Lastly, when translating experimental results into constraints on a simplified model, as it is done in part II of this work, one often makes specific assumptions on the astrophysical properties of the galactic dark matter population, which might or might not be fulfilled. Hence, in addition to possible complications from the particle physics side, it is also important to investigate the impact of non-standard astrophysical properties of dark matter on the interpretation of experimental data.

We take all of these considerations as motivation for part III of this thesis, in which we try to extract as much *model-independent* information as possible from the results of direct and indirect detection experiments. Concretely, in Sec. 6 we investigate the impact of (model-independent) higher-order corrections to the dark matter annihilation process in the Sun, which are particularly important if dark matter annihilates into light fermion-antifermion pairs. Subsequently, in Sec. 7 we confront the dark matter interpretation of the modulation signal observed by the DAMA collaboration to null results from other direct and indirect detection experiments, without adopting a specific particle physics model, but by instead working in the non-relativistic effective theory for dark matter-nucleon interactions. Lastly, in Sec. 8 we develop a novel method for analyzing data from direct detection experiments and neutrino telescopes which does not rely on specific assumptions regarding the velocity distribution of dark matter, leading for the first time to *halo-independent* upper limits on the scattering cross section of dark matter with nucleons.

In summary, this thesis consists of three parts: in part I, including Sec. 1 and 2, we give a general introduction to the astro- and particle physics of dark matter, covering the gravitational evidence, an introduction to the concept of WIMPs, as well as the basics of direct, indirect and collider searches. In part II, given by Sec. 3, 4 and 5, we then investigate the constraints on three different t-channel simplified models arising from the different search strategies. Afterwards we turn to part III in which we discuss model-independent ways of interpreting the experimental data. Concretely, in Sec. 6 we investigate higher-order corrections to the dark matter annihilation process in the Sun, before interpreting the DAMA modulation signal in the context of the non-relativistic effective theory for dark

matter-nucleon interactions in Sec. 7. Furthermore, in Sec. 8 we develop a halo-independent approach for analyzing data from direct and indirect dark matter searches. Finally, in part IV we present our conclusions.

This thesis is largely based on the following publications:

[6] **High-energy neutrino signals from the Sun in dark matter scenarios with internal bremsstrahlung**,
A. Ibarra, M. Totzauer, S. Wild, JCAP **1312** (2013) 043.

[7] **Higher order dark matter annihilations in the Sun and implications for IceCube**,
A. Ibarra, M. Totzauer, S. Wild, JCAP **1404** (2014) 012.

[8] **Sharp Gamma-ray Spectral Features from Scalar Dark Matter Annihilations**,
A. Ibarra, T. Toma, M. Totzauer, S. Wild, Phys. Rev. D 90 (2014) 043526.

[9] **Dirac dark matter with a charged mediator: a comprehensive one-loop analysis of the direct detection phenomenology**,
A. Ibarra, S. Wild, JCAP **1505** (2015) 047.

[10] **A novel approach to derive halo-independent limits on dark matter properties**,
F. Ferrer, A. Ibarra, S. Wild, JCAP **1509** (2015) 052.

[11] **Signatures from Scalar Dark Matter with a Vector-like Quark Mediator**,
F. Giacchino, A. Ibarra, L. Lopez Honorez, M. H. G. Tytgat, S. Wild, JCAP **1602** (2016) 002.

[12] **DAMA confronts null searches in the effective theory of dark matter-nucleon interactions**,
R. Catena, A. Ibarra, S. Wild, JCAP **1605** (2016) 039.

In particular, we remark that several figures contained in this work have been previously published in one of the articles listed above.

Part I

ASTRO- AND PARTICLE PHYSICS OF DARK MATTER

1. Dark matter: observational evidence and basic properties

The focus of this thesis is on exploring and constraining the particle physics properties of dark matter. The underlying motivation for these investigations is the convincing evidence for the existence of dark matter in the past and present-day Universe. Hence, in Sec. 1.1 we give a brief introduction to the most important observations leading to the notion of dark matter. We then discuss in Sec. 1.2 the basic properties of the population of dark matter in the Milky Way, which play a pivotal role in the interpretation of direct and indirect detection experiments. Finally, in Sec. 1.3 we discuss the necessary requirements for any viable particle physics candidate for dark matter, before introducing WIMPs as the class of candidates discussed in the rest of this work.

1.1. Gravitational evidence for dark matter

Starting more than 100 years ago, a large variety of evidence for the presence of a significant amount of dark matter in the Universe has emerged from several independent observations. In this section, we present a brief overview of the most important pieces of evidence, referring to [13–15] for much more detailed reviews.

1.1.1. Astrophysical observations of individual galaxies and galaxy clusters

One of the most elementary arguments for the existence of dark matter is given by observations of galactic rotation curves. Pioneered by Vera Rubin and collaborators in the 1960s and 1970s [17, 18], spectroscopic observations of various galaxies revealed that the rotation curves $v(r)$ corresponding to the trajectories of objects within a single galaxy are flat, i.e. independent of the distance r to the galactic center, for values of r far beyond the visible part of the corresponding galaxy. On the other hand, defining $M(r)$ to be the total gravitating mass within a sphere of radius r and assuming spherical symmetry, Newton's law of gravity predicts the scaling $v(r) \propto \sqrt{M(r)/r}$, and hence naively $v(r)$ should decrease as $1/\sqrt{r}$ outside the visible region of the galaxy, in strong contrast to the observations by Rubin et. al. This suggests a significant amount of non-luminous matter on galactic scales, giving rise to $M(r) \propto r$ at large r, and hence explaining the observed flat rotation curves. The situation is illustrated in Fig. 1.1, which shows a more recent measurement of the rotation curve of the galaxy NGC 6503 [16], compared to the expected contributions from interstellar gas, the (visible) galactic disk, and the inferred contribution from a dark matter halo.

Even earlier, in 1933 Fritz Zwicky presented a compelling argument for the existence of dark matter in clusters of galaxies [19]. By applying the virial theorem to the Coma Cluster, he was able to infer the total gravitating mass M from observations of the cluster radius R_C and the velocity dispersion σ_v of the galaxies via $M = R_C \sigma_v^2 / G$ [20]. When comparing this to the absolute luminosity L of the Coma Cluster, he concluded that the mass-to-light ratio M/L is roughly 500 times larger than the solar value $M_\odot/L_\odot$ [21]. While

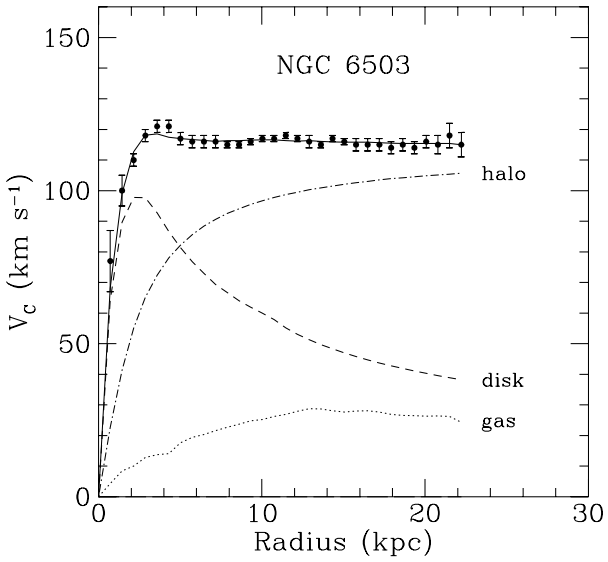

Figure 1.1.: Rotation curve measurement of the galaxy NGC 6503, together with the contributions attributed to the galactic disk, the interstellar gas, as well as the halo of dark matter. Figure has been taken from [14], while originally it has been published in [16].

this ratio is expected to have some dependence on the properties of the stars, the magnitude of the discrepancy led him to the conclusion that there is a substantial amount of "Dunkle Materie" (dark matter) present in the cluster. More than 40 years later, X-ray observations revealed that the Coma Cluster contains a halo of hot gas, constituting about five times the mass which is visible in form of stars [15]. Even though this invalidates the quantitative estimation of the amount of dark matter obtained by Zwicky, the qualitative conclusion about the existence of dark matter in galaxy clusters remains unchanged, and in fact is supported by modern observational methods applied to several other clusters [22].

A rather modern and striking piece of evidence for dark matter arises from the double galaxy cluster 1E 0657-558, which is better known as the "Bullet Cluster", a system consisting of two separate galaxy clusters that passed through each other $\simeq 100\,\mathrm{Myr}$ ago [23]. The spatial distribution of the hot gas in each cluster, which is known to dominate the visible mass of the system, can be inferred from X-ray observations, as shown in Fig. 1.2. On the other hand, the distribution of gravitating mass within the Bullet Cluster can be determined from weak gravitational lensing: the bending of light by strong gravitational fields, an effect predicted by General Relativity, leads to systematic distortions of the images of objects which are in the background of the cluster system (see e.g. [24] for more details). This can be used to map the gravitational potential of the Bullet Cluster, with the result also shown in Fig. 1.2. Evidently, there is a significant offset between the visible and gravitating mass of the system, which is commonly interpreted as the deacceleration of the hot gas due to electromagnetic interactions, while the dark matter components were not (or at least much less) affected by the collision process. It is also important to notice that while the flat rotation curves in principle can also be explained by a modification of the law of gravity such as the MOND framework [25, 26], the Bullet Cluster observation necessarily implies the presence of a non-luminous form of matter which interacts at most weakly with baryons [27].

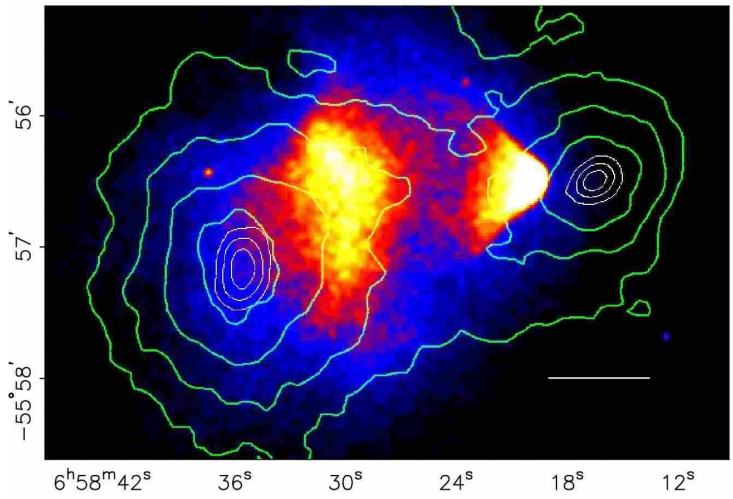

Figure 1.2.: Image of the Bullet Cluster system, with the X-ray observations shown via the color coding, while the contours of constant gravitational potential inferred from weak gravitational lensing are indicated by the green solid curves. Figure taken from [23].

Lastly, also strong gravitational lensing leading to the appearance of arcs or even multiple images of a background object can be employed for inferring the mass profile of certain galaxy clusters. Comparing again to the visible amount of matter in the form of stars or hot gas, evidence for the existence of a dominant dark matter component has been found e.g. in the galaxy cluster Abell 1689 [28].

1.1.2. Role of dark matter in cosmology

So far, we have discussed the evidence for the presence of dark matter in astrophysical objects such as galaxies and galaxy clusters. Interestingly, it turns out that dark matter is also an essential ingredient in the Standard Model of Cosmology, also known as the *Λ-CDM model* (with CDM denoting *cold dark matter*, as explained below), which successfully describes the evolution of the Universe as a whole, starting from the Big Bang up to present times. In the following, we recapitulate only briefly the features of the Λ-CDM framework which are most important for our purposes; see e.g. [29, 30] for comprehensive reviews on the subject.

In the Standard Model of Cosmology, the expansion of the Universe is described by means of a scale factor $a(t)$. In the minimal six-parameter Λ-CDM model, i.e. in particular assuming a flat Universe, the rate of expansion given by the Hubble parameter $H(a) \equiv \dot{a}/a$ can be calculated from [30]

$$H(a) = H_0 \sqrt{\Omega_{\mathrm{m}} a^{-3} + \Omega_{\mathrm{rad}} a^{-4} + \Omega_\Lambda}\,, \tag{1.1}$$

where H_0 is the present-day Hubble constant. Furthermore, we defined $\Omega_X \equiv \rho_X/\rho_c$, where $\rho_c = 3H_0^2/8\pi G$ is the critical density of the Universe, while ρ_X is the energy density of the contribution X to the total energy budget of the Universe. More specifically, ρ_{m} is the matter density, ρ_{rad} describes the energy density in form of radiation, while ρ_Λ includes the contribution arising from a cosmological constant in the Einstein equations, also denoted as *dark energy*. Notice also that Eq. (1.1) in particular implies the relation $1 = \Omega_{\mathrm{m}} + \Omega_{\mathrm{rad}} + \Omega_\Lambda$.

The (rescaled) matter density Ω_m can be decomposed as the sum of a dark matter component Ω_DM and a contribution from ordinary baryonic matter Ω_b. In the rest of this section, we present the most relevant methods to experimentally determine Ω_DM and Ω_b. Most importantly, we will arrive at the conclusion that cosmological data clearly implies a significant contribution of dark matter to the total matter density, in agreement with the astrophysical evidences presented in the previous section.

Temperature and polarization fluctuations in the CMB

Probably the most important technique to probe cosmological models, and in particular to determine the density parameters Ω_X introduced above, is the observation of the *Cosmic Microwave Background* (CMB). Early in the Universe, photons were tightly coupled to the primordial plasma by frequent interactions with free electrons and protons. Approximately 380,000 years after the Big Bang, the Universe cooled down sufficiently in order to allow for the formation of stable neutral atoms, making it essentially transparent to photons. The photons, being in thermal equilibrium up to that point, then decoupled from the subsequent evolution of the Universe, and since then have only been subject to the redshift induced by the growing scale factor $a(t)$. They can be observed today as a nearly perfect black body spectrum with $T \simeq 2.73\,\mathrm{K}$. However, acoustic oscillations in the primordial plasma induced by the interactions of matter and radiation led to small density fluctuations, which nowadays can be observed as temperature and polarization fluctuations in the CMB [31]. Importantly, baryons and dark matter had a different impact on the oscillations in the plasma, as the former are subject both to gravitational as well as to electromagnetic interactions, while the (uncharged) dark matter component only feels the gravitational force[1]. Consequently, the power spectra of the temperature and polarization fluctuations of the CMB depend sensitively on both Ω_DM and Ω_b. These fluctuations have been measured with an impressive accuracy, most recently by the Planck satellite, leading to the values [32]

$$\Omega_\mathrm{DM} h^2 = 0.1198 \pm 0.0015 \quad \text{and} \quad \Omega_\mathrm{b} h^2 = 0.02225 \pm 0.00016\,, \tag{1.2}$$

where $h = 0.6727 \pm 0.0066$ is the present-day Hubble constant H_0 expressed in units of 100 $\mathrm{km\,s^{-1}\,Mpc^{-1}}$, as determined also by Planck [32]. These results are not only a convincing evidence for the existence of dark matter on cosmological time and length scales, but also determine the total amount of dark matter with high accuracy. In particular, Eq. (1.2) implies that 84.3 % of the matter content in the Universe is in form of non-baryonic dark matter, which in fact is in good agreement with the (much less precise) estimates of the dark matter content in galaxy clusters, c.f. Sec. 1.1.1.

Big Bang Nucleosynthesis

The baryon density Ω_b can also be determined by employing the framework of Big Bang Nucleosynthesis (BBN), which describes the production of the light nuclei ^{2}H, ^{3}He, ^{4}He and ^{7}Li in the early Universe (see e.g. [33] for a recent review). For $T \gg 1\,\mathrm{MeV}$, processes mediated by the weak interaction kept neutrons and protons in chemical equilibrium, while for $T \lesssim 1\,\mathrm{MeV} \simeq m_n - m_p$, the abundance of neutrons became exponentially suppressed. Some of the "frozen-out" neutrons have decayed into protons, while others survived long enough to form stable nuclei. Clearly, the abundance of light nuclei produced in this way depends explicitly on the initial baryon density. Matching the observed abundances of

[1] The potential presence of weak interactions between dark matter and baryons is irrelevant for this point.

Deuterium, Helium and Lithium in today's Universe to the prediction by BBN requires $\Omega_b h^2 = 0.021 - 0.025$ [34], in perfect agreement with the value given in Eq. (1.2). Combining this with the total matter density inferred from the CMB observations, BBN not only confirms the existence of dark matter, but is also one more evidence for its non-baryonic nature.

Large scale structure formation

On very large scales, the Universe exhibits a pronounced structure in the form of filaments of galaxy clusters with large voids in between, as observed e.g. by the Sloan Digital Sky Survey [35]. Within the Λ-CDM model, these structures are interpreted as the result of the growth of the initial small density fluctuations in the primordial plasma, as they are imprinted in the CMB [36, 37]. The formation of structures can be modeled with the help of N-body simulations, which describe the dynamical evolution of the matter content in the expanding Universe. Interestingly, including a substantial amount of dark matter in such simulations is crucial for reproducing the observed large scale structure: dark matter allows for the efficient growth of the initial structures via gravitational instabilities, while baryons alone would not clump effectively enough due to the radiation pressure counteracting the formation of overdense regions. In particular, it is the presence of dark matter that leads to an hierarchical *bottom-up* picture of structure formation, where first small structures such as dark matter (sub-)halos are formed, which then merge into larger objects such as galaxies and galaxy clusters, in good agreement with observations.

To be more precise, this mechanism requires dark matter to be *cold*, i.e. non-relativistic at the time most relevant for structure formation, as hot dark matter would have washed out the initial regions of enhanced matter density. As we will discuss in Sec. 1.3, this leads to important restrictions on the viability of several particle physics realizations for dark matter.

Finally, let us remark that while the large scale structure of the Universe is well compatible with the paradigm of cold dark matter, on scales relevant for individual galaxies, N-body simulations based on the Λ-CDM model are in conflict with e.g. the number of observed satellite galaxies orbiting the Milky Way [38]. However, it is not yet established whether this is actually a problem of the model, which could point e.g. to warm dark matter or to strong self-interactions of dark matter, or whether it is an artefact of the simulations which do not fully take into account the baryonic effects in the formation of individual galaxies [39, 40].

1.2. Dark matter in the Milky Way

Based on the strong evidence for the existence of a significant amount of dark matter in the Universe, we also expect dark matter to be present in our Galaxy, the Milky Way. This is the basis for the idea of direct and indirect dark matter searches, which will be introduced in detail in Sec. 2, and hence it is crucial to have a good understanding of the properties of the galactic dark matter population in order to correctly interpret the results of the corresponding experiments.

First, let us discuss the spatial distribution of the dark matter density $\rho(\vec{r})$ within the Milky Way. For other galaxies, it is feasible to infer the dark matter profile directly from observations of rotation curves; in particular, a flat rotation curve outside the visible part of a galaxy suggests the scaling $\rho(\vec{r}) \propto 1/r^2$ for large $r \equiv |\vec{r}|$. However, determining the rotation curve of the Milky Way itself is notoriously difficult due to the fact that all observations are

necessarily done from within the crowded Galactic plane. Despite this complication, a recent compilation of data relevant for the Milky Way rotation curve [41] shows a clear preference for the existence of dark matter in our Galaxy, consistent with the asymptotic behavior $\propto 1/r^2$ observed in several other galaxies [42, 43]. However, pinning down the dark matter distribution of the Milky Way at $r \lesssim 5\,\mathrm{kpc}$ by means of rotation curve measurements is still out of reach [42]. Hence, in order to estimate the behavior of $\rho(\vec{r})$ in the innermost region of the Milky Way, one typically employs N-body simulations for the formation of galaxies, see e.g. [44, 45]. A commonly used parametrization for the dark matter distribution extracted from such simulations is the spherically symmetric Navarro-Frenk-White (NFW) profile [46], which in its generalized form is given by

$$\rho_{\mathrm{NFW}}(r) \propto \frac{1}{\left(\frac{r}{r_s}\right)^{\gamma}\left(1+\frac{r}{r_s}\right)^{3-\gamma}}\,, \tag{1.3}$$

with $r_s \simeq 20\,\mathrm{kpc}$ being the scale radius, while viable values for the inner slope of the dark matter profile are given by $\gamma \simeq 1.0 - 1.4$ [47–49]. Alternatively, a good fit to several simulations is also obtained with the Einasto profile [50, 51], which is defined through

$$\rho_{\mathrm{Ein}}(r) \propto \exp\left\{-\frac{2}{\alpha}\left[\left(\frac{r}{r_s}\right)^{\alpha}-1\right]\right\}\,, \tag{1.4}$$

with $\alpha \simeq 0.17$ and $r_s \simeq 20\,\mathrm{kpc}$. We furthermore remark that both the NFW and the Einasto profile, which feature a dark matter cusp for $r \to 0$, are known to be in conflict with rotation curve measurements of several other galaxies that are better fitted by a cored dark matter distribution, a situation known as the core-vs-cusp problem [52]. Similar to the missing satellite problem mentioned briefly in the previous section, this tension might originate from the non-consideration of baryonic effects in the formation of galaxies [53], but could also be explained by strong self-interactions of dark matter [54].

Furthermore, for direct and indirect dark matter searches it is important to have reliable estimates for the normalization of the dark matter profile $\rho(\vec{r})$; in particular, the event rate in direct detection experiments is proportional to the local dark matter density $\rho_0 \equiv \rho(r_\odot)$, where $r_\odot \simeq 8.5\,\mathrm{kpc}$ is the distance of the Solar System to the Galactic Center [55]. The local dark matter density can be inferred either from rotation curve measurements (assuming a spherically symmetric halo), or from velocity measurements of nearby stars, which can be used as tracers for the local gravitational potential, and hence allow to estimate the local value of the dark matter density. Typical values obtained by these methods are $\rho_0 \simeq 0.3 - 0.4\,\mathrm{GeV/cm^3}$, see e.g. [43, 56, 57].

In addition to the halo profile $\rho(\vec{r})$, also the velocity distribution of dark matter particles at the position of the Solar System, $f_{\mathrm{3D}}^{(\mathrm{Gal})}(\vec{v})$, enters the interpretation of direct detection experiments; the impact on the corresponding phenomenology will be discussed in detail in Sec. 2.1. In contrast to the spatial distribution of dark matter which can at least partially be inferred from rotation curve measurements, there is no experimental data which could be employed for directly determining the local velocity distribution. Hence, one typically relies on simplifying theoretical assumptions, with the most popular one being the *Standard Halo Model* (SHM) [58], in which $f_{\mathrm{3D}}^{(\mathrm{Gal})}(\vec{v})$ takes the form of a Maxwell-Boltzmann distribution with an additional cut-off,

$$f_{\mathrm{3D}}^{(\mathrm{Gal})}(\vec{v}) = \frac{1}{\sqrt{2\pi}\sigma}\exp\left(-\frac{|\vec{v}|^2}{2\sigma^2}\right)\,\theta\left(v_{\mathrm{esc}}-|\vec{v}|\right)\,. \tag{1.5}$$

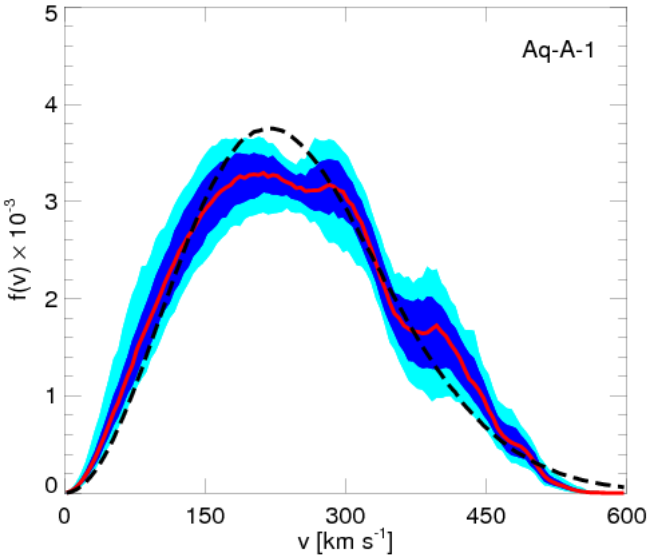

Figure 1.3.: Velocity distribution of dark matter extracted from the Aquarius simulation, together with the best-fit Maxwell-Boltzmann distribution. Figure taken from [66].

Here, σ is the velocity dispersion, which in the SHM is related to the local circular speed v_0 via $\sigma = \sqrt{3/2}\, v_0$. The local circular speed can be estimated by analyzing the velocities of tracer objects in the Milky Way, with recent works favoring values between $v_0 \simeq 218$ km/s [59] and $v_0 \simeq 244$ km/s [60–63]. Moreover, in Eq. (1.5) $v_{\rm esc}$ denotes the Galactic escape velocity, corresponding to the largest possible velocity of a dark matter particle being bound to the gravitational potential of the Milky Way. Based on observations of high-velocity stars, the recent RAVE survey finds $v_{\rm esc} = 533^{+54}_{-41}$ km/s [64]. We also remark that formally the Maxwell-Boltzmann distribution is only valid for an isothermal halo profile $\rho(\vec{r}) \propto 1/r^2$, while for other spatial distributions such as the NFW or Einasto profile, one can in principle determine the corresponding functional form of $f_{\rm 3D}^{\rm (Gal)}(\vec{v})$ by means of the Eddington formula [65].

Besides inferring the dark matter velocity distribution from simplifying arguments such as the ones leading to the SHM, it can also be estimated from N-body simulations, similar to the halo profile $\rho(\vec{r})$ as discussed at the beginning of this section. Interestingly, various simulations indicate substantial deviations of $f_{\rm 3D}^{\rm (Gal)}(\vec{v})$ from the simple Maxwell-Boltzmann picture, often related to recent merging processes between infalling dark matter subhalos and the galactic disk, leading to a non-equilibrated part of the dark matter population which is not included in the Maxwell-Boltzmann distribution [67]. Such processes can lead e.g. to individual streams of dark matter, or to a dark disk containing low-velocity dark matter particles aligned with the baryonic disk. One example for the output of a N-body simulation is shown in Fig. 1.3, together with the best-fit Maxwell-Boltzmann distribution. While the result of an individual simulation of course does not have to be related to the actual local velocity distribution, the simulations indicate that direct detection rates (and in fact also the capture process of dark matter in the Sun, c.f. Sec. 2.2) can potentially be significantly affected by the non-maxwellian structure of $f_{\rm 3D}^{\rm (Gal)}(\vec{v})$, which consequently constitutes an

important systematic uncertainty when interpreting the corresponding experimental data[2]. Motivated by this situation, we will present in Sec. 8 a novel method which allows to infer particle physics properties of dark matter from direct and indirect detection experiments in a *halo-independent* way, i.e. without specifying the form of $f_{\rm 3D}^{\rm (Gal)}(\vec{v})$.

1.3. Particle dark matter: constraints and candidates

Up to date, all sources of evidence for the existence of dark matter are based on its gravitational interaction alone, and hence do not reveal detailed information about its *particle nature*. In view of that situation, determining fundamental properties of the dark matter particle such as its mass, spin and interaction strength with Standard Model particles is one of the most important open questions in elementary particle physics. In this section, we first list the basic characteristics every dark matter candidate has to fulfill, before focusing on WIMPs as a specific class of candidates, introducing in particular the concept of thermal freeze-out of dark matter particles.

Properties of the dark matter particle: evidence for physics beyond the Standard Model of particle physics

The evidences presented in Sec. 1.1 lead to a list of necessary requirements for any particle physics candidate for dark matter. First, the dark matter particle needs to be stable or to have a lifetime significantly larger than the age of the Universe. As we will see in part II of this thesis, this is often related to a discrete global symmetry forbidding the decay of the lightest particle which is charged non-trivially under this symmetry. Secondly, the very fact that it is dark forbids a significant electric charge of the dark matter particle; for example, from observations of magnetic fields in galaxy clusters one can derive the upper bound $|q_{\rm DM}| \lesssim 10^{-14}\,|e|(m_{\rm DM}/{\rm GeV})$ [70]. Next, the evidence for dark matter arising from the CMB as well as the determination of the baryonic density Ω_b via BBN requires the dark matter particle to be non-baryonic. This excludes in particular baryonic matter in form of *MACHOs* (Massive astrophysical compact halo objects) [71] as the dominant form of dark matter[3]. Furthermore, there are several constraints on the type of interactions of the dark matter particle: from the displacement of the hot gas and the center of the gravitational potential observed in the Bullet Cluster one can set an upper limit on the self-interaction cross section of dark matter, $\sigma_{\text{DM-DM}}/m_{\rm DM} \lesssim 1\,{\rm cm}^2/{\rm g} \simeq 1.8\,{\rm barn/GeV}$ [73, 74], which is however significantly larger than typical weak-scale interactions expected for a large variety of candidates (see below). On the other hand, the interaction of dark matter with Standard Model particles by now is strongly constrained for a large set of dark matter masses, most notably by direct and indirect searches, which can even exclude some models with interaction strengths smaller than the Standard Model weak force. This will be discussed in much more detail in Sec. 2, and in several other parts of this thesis.

The most simple and elegant solution for the dark matter puzzle would of course be an explanation within the Standard Model of particle physics, which in fact is an extremely successful description of the interactions of elementary particles up to the TeV scale. However, among all particles contained in the Standard Model, i.e. all charged leptons, neutrinos,

[2] See however [68, 69] for recent works claiming that the Maxwell-Boltzmann distribution might actually be a good approximation to the actual velocity distribution.

[3] These candidates have also been excluded by microlensing observations [72].

quarks and composite hadrons, gauge bosons as well as the recently discovered Higgs particle, only the three neutrinos meet all requirements for a viable dark matter candidate mentioned above. Indeed, Standard Model neutrinos have been considered as a promising dark matter candidate in the past [75, 76]; however, there is one more known characteristic of the dark matter particle which is not part of the list in the previous paragraph: successful structure formation requires dark matter to be cold, i.e. non-relativistic at the time when structures in the Universe start to form, as discussed in Sec. 1.1.2. Experimentally, the masses of the Standard Model neutrinos are constrained to values below $\simeq 2.2\,\mathrm{eV}$ [77], and hence their relativistic nature during structure formation implies that neutrinos would constitute hot dark matter.

Taking together all of these arguments, the existence of dark matter hence strongly points towards physics beyond the Standard Model. Interestingly, also completely independent arguments suggest an extension of the Standard Model of particle physics, most notably the non-zero neutrino masses, the observed baryon asymmetry in the Universe, as well as the unexplained origin of the apparently unnatural huge separation between the weak and the Planck scale, commonly known as the hierarchy problem. Indeed, there are several proposed theories which try to address one or several of these shortcomings of the Standard Model, and at the same time provide a viable dark matter candidate. Popular examples include supersymmetric theories featuring the neutralino or the gravitino as the possible dark matter particle (see e.g. the review in [78]), Kaluza-Klein theories based on extra space-time dimensions [79, 80], dark matter in form of axions [81], a scenario motivated by the strong QCD problem, or sterile neutrino dark matter with a mass in the keV range, which in combination with other sterile neutrinos could be related to the non-zero masses of the Standard Model neutrinos [82, 83]. However, up to date the true particle nature of dark matter is still obscure, and hence remains as one of the most pressing open questions in modern particle physics.

Thermal freeze-out and the WIMP miracle

In this thesis, we study the viability and detectability of dark matter candidates falling into the class of *weakly interacting massive particles* (WIMPs). These are loosely defined as new elementary particles with masses between a few GeV and tens of TeV, and which interact weakly[4] with Standard Model particles. WIMPs naturally arise as a "by-product" of some of the theories mentioned in the previous paragraph, which often have been proposed for completely different reasons than the dark matter puzzle, making this class of dark matter candidates theoretically appealing and well-motivated. However, probably the most salient feature of WIMPs is related to their production mechanism in the early Universe: the process of *thermal freeze-out* provides a natural way of explaining the observed abundance of dark matter, for generic values of the mass and interaction strength of weakly interacting massive particles. In the following, we present a brief introduction to the main concepts of this mechanism, referring to [14, 84, 85] for more details.

The basic idea behind the freeze-out process is that at sufficiently early times in the Universe, the weak-scale interactions of WIMPs with Standard Model particles led to a chemical and thermal equilibrium of dark matter with the hot plasma of Standard Model

[4] This is to be understood is the general sense, i.e. the interactions are not necessarily related to the weak gauge interaction of the Standard Model.

particles X, via annihilation processes of the form $\mathrm{DM\,DM} \leftrightarrow X\bar{X}$ [5]. Eventually, the expansion rate of the Universe became larger than the annihilation rate of WIMPs, leading to the decoupling of the dark matter particles existing at that point. This population of *frozen-out* particles is then observed today as the dark matter in the Universe.

Quantitatively, this process is described by a Boltzmann equation for the number density n of dark matter [84]:

$$\frac{\mathrm{d}n}{\mathrm{d}t} = -3Hn - \langle\sigma v\rangle \left(n^2 - n_{\mathrm{eq}}^2\right) . \tag{1.6}$$

Here, the first term on the right hand side accounts for the decrease of n due to the expansion of the Universe with a rate given by the Hubble parameter H. Moreover, the annihilation of dark matter particles occurs with a rate $\langle\sigma v\rangle n^2$, where $\langle\sigma v\rangle$ is the *thermally averaged annihilation cross section*, defined as the average of $v\cdot\sigma_{\mathrm{DM\,DM}\to X\bar{X}}$ over the thermal velocity distribution of dark matter particles, with v being the relative velocity of the annihilating particles. Lastly, the creation of WIMPs from annihilations of Standard Model particle pairs $X\bar{X}$ is included via the term $\langle\sigma v\rangle n_{\mathrm{eq}}^2$, using the principle of detailed balance. Here, n_{eq} is the density of dark matter particles at thermal equilibrium, which for non-relativistic species is given by [14]

$$n_{\mathrm{eq}} = g\left(\frac{m_{\mathrm{DM}}T}{2\pi}\right)^{3/2} \exp\left(-\frac{m_{\mathrm{DM}}}{T}\right) , \tag{1.7}$$

with g being the number of degrees of freedom for the dark matter particle.

Eq. (1.6) in general has to be modified in scenarios containing other new particles besides the dark matter candidate. Specifically, if these additional states are kept in equilibrium via annihilations with themselves or with the dark matter particle, and if they eventually decay into dark matter, their abundances obtained via the freeze-out mechanism effectively contribute to the final density of dark matter particles [86]. Formally, these *coannihilations* can be taken into account via a modified Boltzmann equation of the form [14]

$$\frac{\mathrm{d}n}{\mathrm{d}t} = -3Hn - \langle\sigma_{\mathrm{eff}}v\rangle \left(n^2 - n_{\mathrm{eq}}^2\right) , \tag{1.8}$$

where $n = \sum_i n_i$ is defined to be the total density of states eventually decaying into the dark matter particle (including the dark matter particle itself), and $\langle\sigma_{\mathrm{eff}}v\rangle$ denotes the effective thermally averaged annihilation cross section, defined via [14]

$$\langle\sigma_{\mathrm{eff}}v\rangle = \sum_{ij}\langle\sigma_{ij}v_{ij}\rangle\frac{n_{i,\mathrm{eq}}n_{j,\mathrm{eq}}}{n_{\mathrm{eq}}^2} . \tag{1.9}$$

Similar as above, σ_{ij} and v_{ij} are the cross section and relative velocity for the annihilation process involving the states i and j in the initial state. As $n_{i,\mathrm{eq}}/n_{\mathrm{eq}} \propto \exp(-(m_i - m_{\mathrm{DM}})/T)$, in the computation of the effective annihilation cross section it is sufficient to include only the particles i which are rather close in mass to the dark matter particle, i.e. $m_i/m_{\mathrm{DM}} \lesssim 1.2{-}1.5$, with the precise value depending on the detailed characteristics of the model.

Both for scenarios with and without coannihilations, the relic density of dark matter as observed today follows from $\Omega_{\mathrm{DM}} = m_{\mathrm{DM}}n^{(\mathrm{today})}/\rho_c$, where ρ_c is the critical density as

[5] Notice that here $X\bar{X}$ can also be replaced by a final state consisting of three or more Standard Model particles, not affecting anything in the following discussion. In fact, in Sec. 4 we will encounter an explicit scenario where $2 \to 3$ processes dominate the freeze-out process.

introduced in Sec. 1.1.2, and $n^{(\text{today})}$ is given by the solution of the corresponding Boltzmann equation defined in Eq. (1.6) or (1.8), evaluated at present times[6]. Whenever necessary, we employ the micrOMEGAs code [87] for a numerical solution of the Boltzmann equation, in order to obtain a prediction of the dark matter relic density Ω_{DM} for a given particle physics model, i.e. a given set of annihilation cross sections entering the corresponding Boltzmann equation.

Even though in this work we always choose a fully numerical approach for the solution of the Boltzmann equation, it is highly instructive to discuss an approximate analytic solution for the dark matter relic density. For this purpose, we restrict ourselves to the standard scenario without coannihilations, and expand the thermally averaged annihilation cross section as follows:

$$\langle \sigma v \rangle = a + b\langle v^2 \rangle + d\langle v^4 \rangle + \mathcal{O}(\langle v^6 \rangle)\,, \tag{1.10}$$

where the individual terms proportional to a, b and d can be interpreted as the s-, p- and d-wave partial wave contribution to the annihilation process. Assuming furthermore that the annihilation is not mediated by a resonance, nor proceeds close to a kinematical threshold [86], the relic density of dark matter follows from [14, 88]

$$\Omega_{\text{DM}} h^2 \simeq \frac{1.07 \cdot 10^9\,\text{GeV}^{-1}}{M_{\text{Planck}}} \frac{x_F}{\sqrt{g_\star}} \frac{1}{a + 3b/x_F + 20d/x_F^2}\,, \tag{1.11}$$

where $g_\star \simeq 100$ is the number of degrees of freedom in the primordial plasma at the time of dark matter decoupling [84], and $x_F \equiv m_{\text{DM}}/T_F$ parametrizes the *freeze-out temperature* T_F at which the dark matter population falls out of equilibrium and decouples from the thermal bath. Typically, $x_F \simeq 20 - 25$, implying in particular that the dark matter particles are non-relativistic at freeze-out.

From Eq. (1.11), we deduce that in the absence of a suppression of the coefficient a appearing in the expansion of $\langle \sigma v \rangle$ defined in Eq. (1.10), the dark matter relic density is dominantly set by the s-wave contribution to the annihilation cross section. Neglecting the higher-order partial waves, Eq. (1.11) simplifies to [89]

$$\Omega_{\text{DM}} h^2 \simeq 0.12 \cdot \frac{2.2 \cdot 10^{-26}\,\text{cm}^3/\text{s}}{\langle \sigma v \rangle}\,. \tag{1.12}$$

Hence, within the approximations introduced above, the dark matter relic density as observed by Planck is reproduced for a WIMP with a s-wave annihilation cross section of $\simeq 2.2 \cdot 10^{-26}\,\text{cm}^3/\text{s}$, denoted as the *thermal annihilation cross section*[7]. On the other hand, from the particle physics side one can roughly estimate the expected annihilation cross section for a weakly interacting massive particle solely on dimensional grounds:

$$(\sigma v)_{\text{weak}} \sim \frac{g_{\text{DM}}^4}{m_{\text{DM}}^2} \sim \frac{0.1^4}{(200\,\text{GeV})^2} \simeq 2.2 \cdot 10^{-26}\,\text{cm}^3/\text{s}\,, \tag{1.13}$$

where for illustration we assumed a weak coupling ~ 0.1 and a dark matter mass of $\sim 200\,\text{GeV}$. Remarkably, the order of magnitude of a weak scale interaction cross section

[6] Technically, one rewrites the Boltzmann equation as a differential equation for the yield $Y = n/s$, where s is the entropy density per comoving volume, and approximates $n^{(\text{today})}$ via $Y_{t\to\infty} \cdot s^{(\text{today})}$ [14].

[7] This value corresponds to the case in which the dark matter particle is its own antiparticle, e.g. if it is a Majorana fermion. Otherwise, the thermal annihilation cross section is given by $\simeq 4.4 \cdot 10^{-26}\,\text{cm}^3/\text{s}$.

matches the necessary cross section for reproducing the observed relic density, a situation commonly referred to as the *WIMP miracle*. While this of course might simply be an amusing coincidence of nature, the fact that the observed amount of dark matter can naturally be explained by means of this mechanism at least serves as a strong motivation for WIMPs as dark matter candidates.

Most importantly, the WIMP framework leads to the firm and testable prediction that dark matter has weak-scale interactions with Standard Model particles. In view of this, in the last decades a huge effort has been undertaken in designing and constructing experiments searching for these non-gravitational interactions of dark matter, most notably direct, indirect and collider searches. The idea behind these approaches as well as the current experimental status will be discussed in detail in the next section.

2. Detection methods of WIMPs: general concepts

2.1. Direct detection of dark matter

WIMPs, as introduced in the previous section, are expected to interact with particles of the Standard Model with a strength comparable to the weak interaction. If that scenario is indeed realized in nature, dark matter particles present at the location of the Earth will occasionally scatter off ordinary nuclei, via the (hypothetical) weak-scale interactions of WIMPs with quarks and gluons. This prediction of the WIMP framework can be tested with *direct detection* experiments, which aim at observing the nuclear recoil induced by non-relativistic dark matter particles which are bound to our Galaxy and scatter elastically off target nuclei which are initially at rest [90].

In this section, we first review the basic concepts necessary for calculating the expected rate of scattering events at a direct detection experiment, which requires input both from the particle physics as well as from the astrophysics of dark matter. After that, we briefly discuss the current experimental situation as well as the prospects for future developments in the field.

2.1.1. Rate of scattering events expected at a direct detection experiment

The elastic scattering of a dark matter particle with mass $m_{\rm DM}$ and a non-relativistic velocity v off a nucleus with mass m_T, which is assumed to be initially at rest in the laboratory system, gives rise to a recoil of the nucleus with an energy [91]

$$E_R = \frac{\mu_T^2 v^2 \left(1 - \cos\theta^\star\right)}{m_T} \;\in\; \left[0,\, \frac{2\mu_T^2 v^2}{m_T}\right] , \tag{2.1}$$

where $\theta^\star$ is the scattering angle in the center of mass frame, and $\mu_T \equiv m_{\rm DM}\, m_T/(m_{\rm DM} + m_T)$ is the reduced mass of the WIMP-nucleus system. For an exemplary scenario with $m_{\rm DM} \simeq 50\,\text{GeV}$, $m_T \simeq m_{\rm Xe} \simeq 130\,\text{GeV}$, and $v \simeq 10^{-3}$, which is the characteristic velocity for dark matter particles bound to our Galaxy (c.f. Sec. 1.2), the typical recoil energy is of the order of $E_R \simeq 10\,\text{keV}$.

The number of recoil events expected at a direct detection experiment per unit target mass of the isotope T, observation time and recoil energy is given by the product of the flux of dark matter particles at Earth and the cross section for the scattering of dark matter off the nucleus T, integrated over all possible dark matter velocities v:

$$\frac{\mathrm{d}R_T}{\mathrm{d}E_R}(E_R) = \frac{\rho_0}{m_T m_{\rm DM}} \int_{v_{\rm min}(E_R)}^{\infty} \mathrm{d}v\, v f(v) \frac{\mathrm{d}\sigma_T}{\mathrm{d}E_R}(v, E_R) \; . \tag{2.2}$$

Hence, the event rate depends both on astrophysical properties of the Galactic dark matter population, specifically on the local speed distribution $f(v)$ and the local dark matter density ρ_0, as well as on the particle physics of the dark matter, which enters in the differential dark

matter-nucleus scattering cross section $\frac{\mathrm{d}\sigma_T}{\mathrm{d}E_R}$. Furthermore, $v_{\min}(E_R)$ is the minimal velocity of a dark matter particle which allows for a recoil with energy E_R; following Eq. (2.1), it is given by

$$v_{\min}(E_R) = \sqrt{\frac{m_T E_R}{2\mu_T^2}}\,. \tag{2.3}$$

On the one hand, the dependence of the event rate on the astrophysical and particle physics aspects of dark matter constitutes a significant challenge, as most of these properties of dark matter are poorly understood up to date. On the other hand, this implies that by eventually measuring the rate of dark matter induced scattering events in one or more experiments, one can potentially learn a lot about the physics of dark matter. With this situation in mind, we will now discuss the basic concepts as well as the most commonly adopted assumptions regarding the particle- and astrophysics relevant for direct detection experiments.

Scattering rate: particle physics input

Fundamentally, a given extension of the Standard Model containing a dark matter candidate specifies the couplings of the dark matter particle to quarks and gluons. In order to calculate the dark matter-nucleus scattering cross section $\frac{\mathrm{d}\sigma_T}{\mathrm{d}E_R}$ for an underlying theory, one then has to go from the level of dark matter-quark and dark matter-gluon interactions to a description of dark matter-nucleon interactions, and finally it has to be taken into account that nucleons are bound inside the target nucleus.

While this procedure in principle has to be carried out separately for each underlying theory (requiring different input from nuclear physics depending on the scenario), it has been noted that for a large variety of models, though not for all, two types of dark matter-nucleus interactions are sufficient to capture the dominant part of the scattering cross section: *spin-independent* (SI) and *spin-dependent* (SD) interactions [90]. In a SI interaction, the dark matter particle scatters coherently off the complete nucleus, with a cross section given by [92]

$$\left(\frac{\mathrm{d}\sigma_T}{\mathrm{d}E_R}\right)_{\mathrm{SI}} = \left[Z + \frac{f_n}{f_p}(A-Z)\right]^2 \frac{m_T \sigma_p}{2\mu_p^2 v^2}\, F_{\mathrm{SI}}^2(E_R)\,, \tag{2.4}$$

where μ_p is the reduced dark matter-proton mass, $f_p(f_n)$ is the effective SI coupling of dark matter to protons (neutrons) and σ_p is the total scattering cross section for dark matter off a free proton. In particular, if dark matter couples with equal strength to protons and neutrons, SI scattering is enhanced by a factor A^2, favoring heavy nuclei as target material. Furthermore, in Eq. (2.4), $F_{\mathrm{SI}}(E_R)$ is a form factor taking into account the loss of coherence, relevant if the momentum exchange $q = \sqrt{2m_T E_R}$ is comparable to or larger than the inverse size of the nucleus. To first approximation, the form factor is given by the Fourier transform of the spatial distribution of nucleons inside the nucleus; if not specified otherwise, we will use the SI form factor presented in [93]. From the model building perspective, SI scattering arises e.g. in scenarios where dark matter interacts with quarks via the exchange of a heavy CP-even scalar, such as the Standard Model Higgs, or in models where the dark matter particle couples to quarks via a heavy vector mediator. A specific example for a scenario involving SI interactions will be discussed in Sec. 3.2, including more details about the relation of the fundamental couplings of the theory to the effective dark matter-nucleon couplings f_p and f_n and the dark matter-proton scattering cross section σ_p.

On the other hand, SD scattering originates from the interaction of a dark matter particle with the spin J_T of the target nucleus, leading to the cross section [92]

$$\left(\frac{\mathrm{d}\sigma_T}{\mathrm{d}E_R}\right)_{\mathrm{SD}} = \left[\langle S_p\rangle + \frac{a_n}{a_p}\langle S_n\rangle\right]^2 \frac{J_T+1}{J_T}\frac{2m_T\sigma_p}{3\mu_p^2 v^2}\,F^2_{\mathrm{SD}}(E_R)\,, \tag{2.5}$$

where $\langle S_p\rangle$ and $\langle S_n\rangle$ are the expectation values of the spin content of the proton and neutron group in the nucleus, respectively, a_p (a_n) is the effective SD coupling of dark matter to protons (neutrons), and the form factor $F^2_{\mathrm{SD}}(E_R)$ again takes into account the finite size of the nucleus, and can be found in [94] for a large variety of target nuclei[1]. As apparent from Eq. (2.5), SD interactions favor target nuclei with unpaired protons and/or neutrons, and in contrast to SI interactions with $f_p = f_n$, the scattering cross section is not enhanced by the coherence factor A^2. At the fundamental level, SD interactions arise in models where a fermionic dark matter particle couples to quarks via an axial-vector interaction, induced e.g. by the exchange of the Standard Model Z-boson. In Sec. 3.2, we will discuss in more detail the nuclear and particle physics input to Eq. (2.5).

Finally, it is important to remark that there are several models in which the scattering cross section of dark matter with nuclei can not be classified according to the "standard" SI or SD interactions given by Eqs. (2.4) and (2.5). For instance, if the mediator between dark matter and the Standard Model particles is lighter than the typical momentum transfer in scattering events, $q \simeq 50\,\mathrm{MeV}$, or if the mediator is a CP-odd scalar particle, the scattering cross section has additional, non-trivial dependencies on the recoil energy E_R, compared to Eqs. (2.4) and (2.5). Examples of scenarios featuring a non-standard dark matter-nucleus scattering cross section will be discussed in detail in Sec. 3 and 7.

Scattering rate: astrophysical input, annual modulation

Besides the particle physics of dark matter, the recoil rate defined in Eq. (2.2) also depends on astrophysical properties of the dark matter population in our Galaxy. First, the event rate depends linearly on the local dark matter density ρ_0. Following the discussion in Sec. 1.2, we will typically assume values between ~ 0.3 and $\sim 0.4\ \mathrm{GeV/cm^3}$. Secondly, the recoil rate depends on the local speed distribution $f(v)$ of dark matter particles in the rest frame of the detector, which can be written in the form

$$f(v) \equiv f(v,t) = \int_{|\vec{v}|=v} \mathrm{d}\Omega\, v^2 f^{(\mathrm{Earth})}_{\mathrm{3D}}(\vec{v},t) = \int_{|\vec{v}|=v} \mathrm{d}\Omega\, v^2 f^{(\mathrm{Gal})}_{\mathrm{3D}}(\vec{v}+\vec{v}_{\mathrm{Earth}}(t))\,. \tag{2.6}$$

In this expression, $f^{(\mathrm{Gal})}_{\mathrm{3D}}(\vec{v})$ and $f^{(\mathrm{Earth})}_{\mathrm{3D}}(\vec{v},t)$ are the three-dimensional velocity distributions of dark matter particles in the rest frame of the Galaxy and the Earth, respectively. These two distributions are related by a shift $\vec{v}_{\mathrm{Earth}}(t)$ in velocity space, with $\vec{v}_{\mathrm{Earth}}(t)$ being the velocity of the Earth in the Galactic rest frame.

As discussed in Sec. 1.2, the local velocity distribution $f^{(\mathrm{Gal})}_{\mathrm{3D}}(\vec{v})$ corresponding to an isothermal halo of dark matter particles is given by a Maxwell-Boltzmann distribution:

$$f^{(\mathrm{Gal})}_{\mathrm{3D}}(\vec{v}) = \frac{1}{\sqrt{2\pi}\sigma}\exp\left(-\frac{|\vec{v}|^2}{2\sigma^2}\right)\,\theta\left(v_{\mathrm{esc}}-|\vec{v}|\right)\,, \tag{2.7}$$

[1]Note that for SD scattering, the form factor $F^2_{\mathrm{SD}}(E_R)$ also depends explicitly on the ratio a_n/a_p [92, 94].

with a velocity dispersion $\sigma \simeq 270-290\,\mathrm{km/s}$ and a Galactic escape velocity $v_{\mathrm{esc}} \simeq 492-587$ km/s (c.f. Sec. 1.2). Eq. (2.7) is a frequently used assumption in the analysis of direct detection experiments, and it also will be employed in several parts of this work. However, it is important to keep in mind that deviations from the Maxwell-Boltzmann shape are possible, and in fact they are expected from N-body simulations, as discussed in more detail in Sec. 1.2. Consequently, the lack of knowledge of the precise form of the local velocity distribution leads to a significant systematic uncertainty when inferring particle physics properties of dark matter from direct detection experiments.

More specifically, while the uncertainty in the local density of dark matter ρ_0 affects all direct detection experiments in a universal way, the impact of the velocity distribution on the event rate differs from experiment to experiment, which can be seen from Eqs. (2.2) and (2.3): the event rate at a given recoil energy E_R is sensitive to all dark matter velocities above $v_{\mathrm{min}}(E_R)$, which however depends on the mass of the target nucleus. Taking furthermore into account the fact that different experiments are sensitive to different ranges of recoil energies, it follows that in general two direct detection experiments probe different regions in the velocity space of dark matter. However, it has been shown that it is possible to partially circumvent this source of uncertainty with the help of *halo-independent* methods (see e.g. [95–97] for early works), which aim at analyzing data from direct detection experiments without specifying the velocity distribution. In particular, in Sec. 8 we will present a novel halo-independent method, which allows to place upper limits on dark matter properties valid for all possible velocity distributions.

For a fixed velocity distribution $f_{\mathrm{3D}}^{(\mathrm{Gal})}(\vec{v})$ defined in the Galactic rest frame, e.g. the Maxwell-Boltzmann distribution given by Eq. (2.7), the one-dimensional speed distribution $f(v,t)$ relevant for the analysis of direct detection experiments follows from Eq. (2.6), with $\vec{v}_{\mathrm{Earth}}(t)$ given by [98]

$$\vec{v}_{\mathrm{Earth}}(t) = \vec{v}_{\mathrm{LSR}} + \vec{v}_{\odot,\mathrm{pec}} + \vec{V}_{\oplus}(t)\,. \tag{2.8}$$

Here, $\vec{v}_{\mathrm{LSR}} = (0, v_0, 0)$ describes the motion of the Local Standard of Rest in Galactic coordinates, with v_0 being the local circular velocity introduced earlier on. Furthermore, $\vec{v}_{\odot,\mathrm{pec}} = \left(11.1^{+0.69}_{-0.75}, 12.24^{+0.47}_{-0.47}, 7.25^{+0.37}_{-0.36}\right)$ km/s is the velocity of the Solar System with respect to the Local Standard of Rest, with the numerical values corresponding to a recent estimation using stellar kinematics [99]. Finally, $\vec{V}_{\oplus}(t)$ takes into account the orbital motion of the Earth around the Sun with a speed given by $\left|\vec{V}_{\oplus}(t)\right| = 29.8\,\mathrm{km/s}$; we refer to [100] for the full expression of the Earth's velocity vector.

Due to the time dependence of the Earth's motion around the Sun, $f(v,t)$ is changing through the year, leading in particular to an *annually modulating* event rate in direct detection experiments [58]. Specifically, it can be shown [98] that under quite generic assumptions regarding the shape of the Galactic velocity distribution, the time dependence of the event rate defined in Eq. (2.2) is well approximated by

$$\frac{\mathrm{d}R_T}{\mathrm{d}E_R}(E_R,t) \simeq S_0(E_R) + S_m(E_R)\cos\left(\frac{2\pi}{1\,\mathrm{year}}(t-t_0)\right)\,. \tag{2.9}$$

In this expression, $S_0(E_R)$ is the time-averaged event rate, while $S_m(E_R)$ gives the *modulation amplitude* of the signal. The phase of the modulation t_0 in general depends on the velocity distribution; for the Maxwell-Boltzmann distribution it is given by $t_0 \simeq$ June 1, which is the time of the year at which the Earth is moving with maximal velocity through the wind of dark matter particles [98].

Even though the modulation fraction $S_m(E_R)/S_0(E_R)$ is typically only at the level of a few percent (with the precise value depending on both the particle- as well as the astrophysics entering the direct detection rate), annual modulation provides a potentially very clean signature of dark matter, as most sources of background in a direct detection experiment are not expected to modulate in time. Hence, even if the total background rate in a detector is not fully understood, the observation of an annual modulation of the total rate, i.e. the sum of the dark matter induced signal and the various background components, can provide a strong indication for the interaction of dark matter with the target nuclei. Moreover, at least within the framework of the Maxwell-Boltzmann velocity distribution, the phase of the modulation t_0 is a prediction which can be tested experimentally.

2.1.2. Experimental situation

For a given particle physics model and for fixed astrophysical parameters, the methods outlined in the previous section can be employed in order to predict the number of dark matter induced recoil events at a direct detection experiment. For many scenarios, the expected event rates are of the order of only one or even less events per kilogram target material and per day; hence, the main experimental challenge is to distinguish these rare signals from various sources of background. In most of the up-to-date experiments, the backgrounds are typically dominated by nuclear interactions of neutrons arising from radioactive materials inside and around the detector, as well as by electromagnetic interactions of α-particles, muons, electrons and photons induced by either cosmic ray showers or also by radioactivity.

Detecting nuclear recoil events is usually achieved by measuring the ionization, the scintillation, or the small temperature rise in a cryogenic material induced by the primary scattering event. Most experiments then use a combination of two of these strategies, which often permits to discriminate between signal and background on an event-by-event basis. Based on such techniques, over the last decades there has been tremendous progress in the field of direct detection experiments. Results of searches for dark matter induced scattering events have been reported by various collaborations using different target nuclei and detection methods, such as the xenon-based experiments LUX [101–103], XENON100 [104, 105], XENON10 [106], XMASS-I [107], PandaX [108], experiments using a germanium target, such as SuperCDMS [109], CDMS-Ge [110], CDMSlite [111], CoGeNT [112] and EDELWEISS-II [113], the silicon-based experiment DAMIC [114], the NaI experiments DAMA/LIBRA [115] and DM-Ice [116], the CsI experiment KIMS [117], the CRESST-II [118,119] experiment based on a $CaWO_4$ target, the CF_3I-based experiments COUPP [120] and PICO-60 [121], and finally the experiments SIMPLE [122], PICASSO [123] and PICO-2L [124, 125], which are based on bubble chambers containing different carbon-fluorine targets.

Most of these experiments have observed event rates that are consistent with the expected level of background, and hence they can be used to constrain the interaction strength of dark matter with nuclei. Fig. 2.1 shows the upper limits on the dark matter-nucleon scattering cross section for the most sensitive experiments, assuming standard spin-independent scattering (upper panel) or spin-dependent scattering off protons (lower left panel) or off neutrons (lower right panel). In these plots, the velocity distribution of dark matter is fixed to the Maxwell-Boltzmann distribution given by Eq. (2.7). For spin-independent interactions, LUX is currently the most sensitive experiment for dark masses above $\simeq 4$ GeV, while for smaller masses the low-threshold experiments CDMSLite and CRESST-II provide stronger limits. For spin-dependent scattering off protons, PICO-2L is the leading experiments for

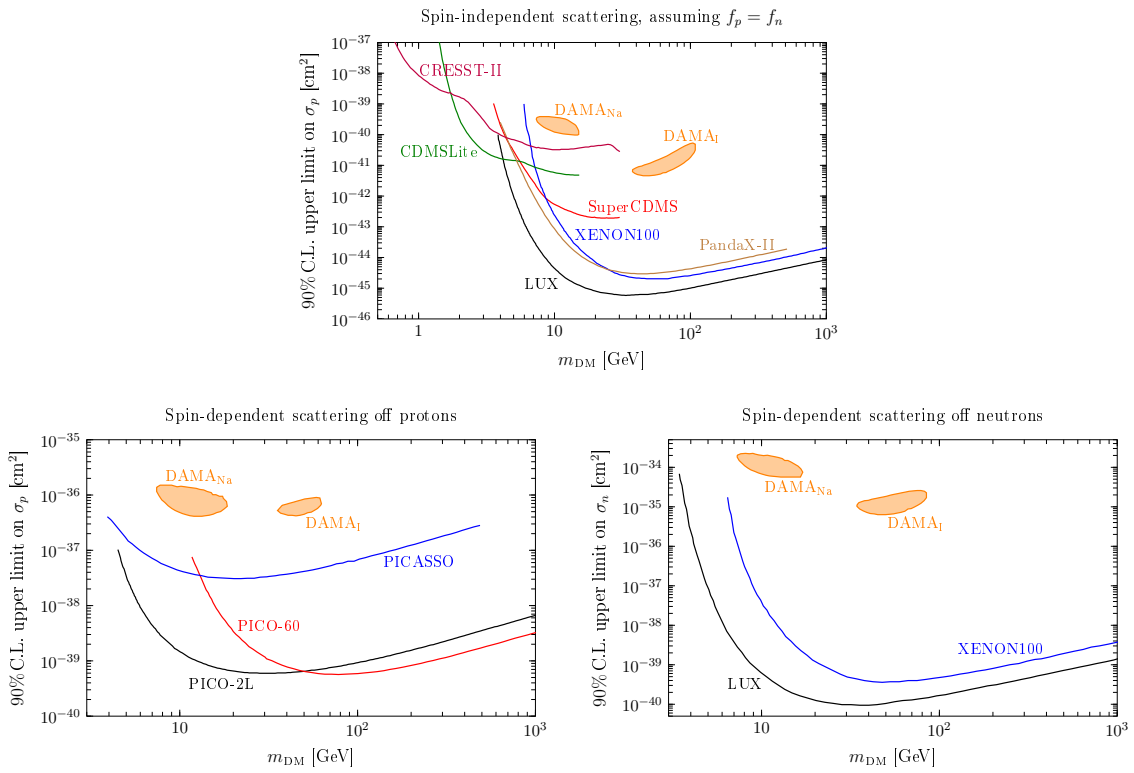

Figure 2.1.: Status of direct detection experiments as of 2016, assuming $\rho_0 = 0.3\,\mathrm{GeV/cm^3}$ as well as a Maxwell-Boltzmann velocity distribution. In all panels, the 3σ-favored regions of the parameter space implied by the DAMA modulation are shown in orange, as calculated in [100] for scattering off Na and I. On the other hand, all solid lines are upper limits on σ_p or σ_n at 90% C.L. *Upper panel:* spin-independent scattering, assuming $f_p = f_n$ (c.f. Eq. (2.4)). Upper limits are shown for LUX [102] in black, for XENON100 [104] in blue, for PandaX-II [108] in brown, for SuperCDMS [109] in red, for CDMSLite [111] in dark green, as well as for CRESST-II [119] in purple. *Lower left panel:* spin-dependent scattering off protons, with the upper limit from PICO-2L [125] shown in black, from PICO-60 [121] shown in red, as well from PICASSO [123] shown in blue. *Lower right panel:* spin-dependent scattering off neutrons, shown for LUX [103] in black and for XENON100 [105] in blue.

$m_{\rm DM} \lesssim 50$ GeV, with PICO-60 taking over at larger masses. Lastly, for spin-dependent scattering off neutrons, LUX is providing the best limits, due to the unpaired neutron in the xenon isotopes ^{129}Xe and ^{131}Xe.

Notably, there is one experiment[2] reporting results that are not in agreement with known sources of background: DAMA and its successor DAMA/LIBRA, based on a NaI scintillator, have observed an annual modulation of the event rate in the energy range between 2 and 6 keV, consistently appearing over 14 annual cycles, with a combined statistical significance of 9.3σ [115]. Intriguingly, the phase t_0 of the modulation signal is compatible with the prediction based on the Maxwell-Boltzmann velocity distribution, as introduced in the previous

[2]We do not discuss other claims of detection by CDMS-Si [126] or CoGeNT [127], as these are statistically not significant, or the excess of events reported by CRESST [128], which eventually has been explained by a novel source of background [118].

section. For this astrophysical setup, the range of parameters within the spin-independent and spin-dependent parameter spaces that can explain this observation are shown in the different panels of Fig. 2.1. Clearly, there is a strong tension of these scenarios with various null results, which have set upper limits on the scattering cross section orders of magnitude below the parameter space favored by DAMA. However, it is important to keep in mind that Fig. 2.1 makes very specific assumptions both about the particle- as well as about the astrophysics of dark matter. In particular, we will discuss in Sec. 7 to what extent the tension between DAMA and the null results can be ameliorated by extending the standard spin-independent and spin-dependent parameter space to a much more general framework of dark matter-nucleon interactions.

Irrespectively of the puzzling situation regarding the apparently conflicting experimental results in the region of low-mass WIMPs, it is very interesting to note that in the next decade a new generation of direct detection experiments will push the sensitivity to even lower cross sections. For dark matter masses above $\simeq 10$ GeV, the most promising future experiments are XENON1T [129], which has been inaugurated in November 2015, as well as the ton-scale experiments LZ [130] and DARWIN [131], which are planned to start running in 2021 and 2024, respectively. These experiments will be able to probe cross sections several orders of magnitude below current bounds, and thus will be sensitive to a large variety of models that remain unexplored up to date. While the main improvement of these experiments compared to the already existing ones is the much larger target mass, which currently is the limiting factor for the sensitivity at large dark matter masses, at the low-mass frontier it is mainly the performance of the detector which limits the capability of detecting smaller and smaller cross sections. In that context, further upgrades of CRESST [132] as well as of SuperCDMS at Snolab [133] are expected to push down the threshold below the keV scale, leading to unprecedented sensitivity to dark matter in the mass range between $\simeq 500$ MeV and $\simeq 10$ GeV.

Ultimately, direct detection experiments will face a source of irreducible background, called the *neutrino floor*: besides dark matter, also solar, atmospheric and diffuse supernova neutrinos can scatter coherently off the target nuclei, giving rise to a nuclear recoil signal mimicking the one of dark matter induced scattering events [58, 134, 135]. For conventional direct detection experiments, this limits the discovery reach to spin-independent scattering cross sections above $3 \cdot 10^{-45}\,\mathrm{cm}^2$ ($10^{-49}\,\mathrm{cm}^2$) for a dark matter particle with mass 5 GeV (30 GeV) [136]. Discovering dark matter with a cross section beyond the neutrino floor would then require detectors that can resolve the *direction* of the recoil track of the nucleus, which can be used to discriminate the dark matter signal from the neutrino induced background [137]. However, the sensitivity of existing prototypes of directional detectors is still orders of magnitude above the neutrino floor; realizing a detection of dark matter beyond it thus requires considerable future experimental efforts [138].

2.2. Capture and annihilation of dark matter in the Sun and in the Earth

In the previous section, we introduced the idea of dark matter direct detection, which is based on observing the nuclear recoil produced by the scattering of a WIMP off a nucleus. Due to this recoil, such a scattering event also leads to an energy loss of the dark matter particle. While irrelevant for direct detection experiments, this energy loss, if large enough, can lead to the capture of the dark matter particle in the gravitational potential of large celestial

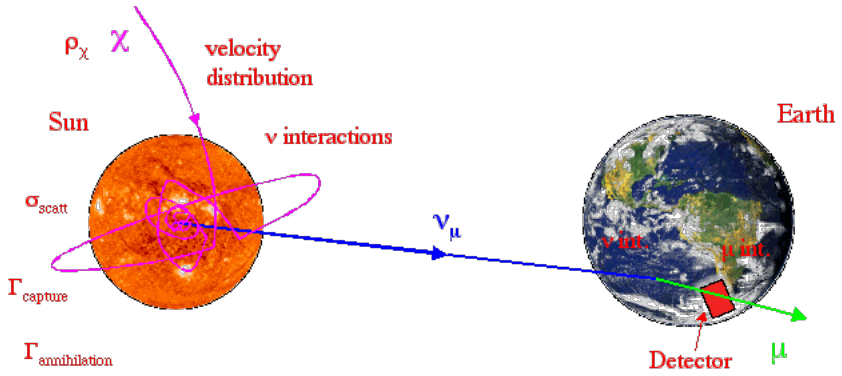

Figure 2.2.: Schematic illustration of the capture and annihilation process of dark matter in the Sun, leading to a flux of high-energetic neutrinos which potentially can be observed at Earth. Figure has been taken from [145].

objects, such as the Sun or the Earth [139]. The captured dark matter particles will then accumulate in the center of the celestial object, and subsequent dark matter annihilations, as suggested by the freeze-out mechanism (c.f. Sec. 1.3), can produce high-energetic neutrinos, which potentially can escape the celestial object and eventually be observed by neutrino telescopes at Earth [140, 141]. This mechanism of dark matter capture and annihilation is illustrated in Fig. 2.2 for the case of the Sun. As ordinary solar neutrinos produced by fusion reactions in the Sun have energies below $\simeq 20$ MeV [142], the observation of a flux of neutrinos with energies $E_\nu \simeq 1 - 100$ GeV which is correlated with the direction of the Sun would provide compelling evidence for the particle nature of dark matter[3]. In this section, we first discuss the basic concepts underlying the physics of capture and annihilation of dark matter in the Sun and in the Earth, before giving an overview of recent results of neutrino telescopes searching for a high-energy neutrino flux from the direction of the Sun.

Capture of dark matter in celestial objects

To begin, let us briefly review the calculation of the capture rate of dark matter in the Sun[4], following [141, 146]. A dark matter particle of the Galactic halo which has a velocity u at large distances from the Sun will have a velocity $w = \sqrt{u^2 + v_{\mathrm{Sun,esc}}(r)^2}$ at a distance r from the center of the Sun, with $v_{\mathrm{Sun,esc}}(r)$ being the escape velocity from the Sun at radius r. Then, in order to be gravitationally captured, the dark matter particle has to undergo a scattering event off a nucleus T, reducing its velocity to a value smaller than $v_{\mathrm{Sun,esc}}(r)$. In other words, it has to transfer a minimal recoil energy $E_R^{(\mathrm{min})} = m_{\mathrm{DM}} u^2/2$ to the nucleus. For a given dark matter particle, this process occurs with a rate per unit time given by

$$\Omega(w) = \eta_T(r)\, w \int_{E_R^{(\mathrm{min})}}^{E_R^{(\mathrm{max})}} \mathrm{d}E_R \frac{\mathrm{d}\sigma_T}{\mathrm{d}E_R}(w, E_R)\,, \tag{2.10}$$

[3]There is only one known source of background which could mimic this signature: high-energetic cosmic rays impinging on the Solar corona produce secondary particles which in turn can decay into neutrinos, leading also to a neutrino flux correlated with the direction of the Sun [143]. However, considering current and near-future sensitivities of neutrino telescopes, this background can safely be neglected [144].

[4]For simplicity, in the following discussion we will focus on the case of the Sun, as the generalization to other celestial objects like the Earth is obvious.

where $\eta_T(r)$ is the number density of the nucleus T at the position r, $E_R^{(\max)} = 2\mu_T^2 w^2/m_T$ is the maximal recoil energy following from Eq. (2.1), and $\frac{\mathrm{d}\sigma_T}{\mathrm{d}E_R}$ is the differential dark matter-nucleus scattering cross section, which already entered the definition of the recoil rate in direct detection experiments, Eq. (2.2). The capture rate per unit volume of solar material then follows from convolving the scattering rate $\Omega(w)$ with the flux of incoming dark matter particles [5] [141]:

$$\frac{\mathrm{d}C}{\mathrm{d}V} = \frac{\rho_0}{m_{\mathrm{DM}}} \int_0^{u_{\max}(r)} \mathrm{d}u \frac{f(u)}{u} w\Omega(w)\,, \tag{2.11}$$

where $f(u)$ is the speed distribution of dark matter particles in the rest frame of the Sun[6], *without* taking into account the Sun's gravitational potential. The capture process is kinematically only possible if $E_R^{(\min)} \leq E_R^{(\max)}$, c.f. Eq. (2.10); this leads to the maximal initial velocity of the dark matter particle $u_{\max}$ entering Eq. (2.11):

$$u_{\max}(r) = v_{\mathrm{Sun,esc}}(r) \cdot \frac{2\sqrt{m_{\mathrm{DM}} m_T}}{|m_{\mathrm{DM}} - m_T|}\,. \tag{2.12}$$

Notice that $u_{\max} \to \infty$ for $m_{\mathrm{DM}} \to m_T$, which in particular leads to a resonant enhancement of the capture rate in the Earth, if the dark matter mass matches e.g. the mass of the iron nucleus [141,148]. Finally, the total capture rate C is obtained by integrating Eq. (2.11) up to the radius R of the Sun (or the Earth, respectively):

$$C = \sum_T \int_0^R \mathrm{d}r\, 4\pi r^2 \frac{\mathrm{d}C}{\mathrm{d}V}\,, \tag{2.13}$$

with the sum including all relevant isotopes of the celestial object.

As discussed in Sec. 2.1.1, in a large variety of particle physics models the scattering dominantly proceeds via a spin-independent and/or spin-dependent interaction, with the cross section defined in Eqs. (2.4) and (2.5), respectively. Assuming furthermore a Maxwell-Boltzmann distribution with $v_0 = 220\,\mathrm{km/s}$ and $v_{\mathrm{esc}} = 544\,\mathrm{km/s}$, the solar capture rate for $m_{\mathrm{DM}} \gtrsim 1$ TeV is approximately given by [7, 149]

$$C \simeq 10^{20}\,\mathrm{s}^{-1} \left(\frac{\rho_0}{0.3\,\mathrm{GeV/cm}^3}\right) \left(\frac{1\,\mathrm{TeV}}{m_{\mathrm{DM}}}\right)^2 \frac{2.77\,\sigma_p^{(\mathrm{SD})} + 4.27 \cdot 10^3\,\sigma_p^{(\mathrm{SI})}}{10^{-40}\,\mathrm{cm}^2}\,, \tag{2.14}$$

assuming $f_p = f_n$ in Eq. (2.4). While we will employ this standard result for the capture rate in Sec. 5 and 6, we will study the capture process of dark matter for different velocity distributions in Sec. 8. To that extent, we calculate the capture rate C for a given velocity distribution $f(v)$ following Eqs. (2.10)−(2.13), using the solar model AGSS09 [150] for the number densities $\eta_T(r)$. For the case of spin-independent interactions, we include the 29 most abundant elements in the Sun, and we assume Gaussian form factors, as parametrized

[5] This step is only valid if the overall probability of capture is much smaller than one, which is indeed the case for most realistic scenarios. However, for very large scattering cross sections, the capture rate is instead simply given by the geometrical cross section of the Sun, taking into account its gravitational potential. For details, we refer to [147].

[6] In Sec. 2.1, $f(v)$ denoted the speed distribution in the rest frame of the Earth, relevant for direct detection. Despite this slight abuse of notation, in the following it always should be clear from the context which speed distribution is to be used.

in [149]. On the other hand, following [151], for the capture rate induced by the spin-dependent coupling to the proton, we take into account scattering off hydrogen and ^{14}N, using the form factor given in [151] for nitrogen.

By studying the dependence of the capture rate on the velocity distribution of dark matter, which according to the discussion in Sec. 1.3 is not necessarily in the form of a Maxwell-Boltzmann distribution, one finds that direct detection experiments and the capture process are sensitive to different parts of the velocity space: for the former, only velocities above a *minimal* velocity $v_{\rm min}$ given by Eq. (2.3) are relevant, while capture is sensitive to all velocities below a *maximal* velocity given by $u_{\rm max}$ in Eq. (2.12). Then, by combining the information from direct detection experiments and neutrino telescopes, one has access to the complete range of dark matter velocities. This will be discussed in more detail in Sec. 8, where we develop a novel halo-independent approach based precisely on this observation.

Annihilation and equilibration of dark matter

Once a dark matter particle has been captured, it will be subject to subsequent scatterings with the solar matter, and for typical weak-scale scattering cross sections the dark matter population reaches thermal equilibrium in a region around the center of the Sun, with a density profile given by [152, 153]

$$n_{\rm DM,Sun}(r) \propto \exp\left(-r^2/R_{\rm DM,Sun}^2\right) \quad \text{with} \quad R_{\rm DM,Sun} \simeq 0.01 R_\odot \left(\frac{100\,\text{GeV}}{m_{\rm DM}}\right)^{1/2}\,, \tag{2.15}$$

with $R_\odot = 7 \cdot 10^8\,$m being the radius of the Sun. For capture in the Earth, the dark matter population has a radial extension of $R_{\rm DM,Earth} \simeq 500\,\text{km}\,(100\,\text{GeV}/m_{\rm DM})^{1/2}$ [153]. Following the paradigm of WIMPs produced by thermal freeze-out, these dark matter particles then start to self-annihilate, with a rate proportional to the square of the number of dark matter particles N present in the core of the celestial object:

$$\Gamma_A = \frac{1}{2} C_A N^2 \quad \text{with} \quad C_A = \langle\sigma v\rangle \frac{\int_0^{R_\odot} \text{d}r\, 4\pi r^2\, n_{\rm DM,Sun}^2(r)}{\left(\int_0^{R_\odot} \text{d}r\, 4\pi r^2\, n_{\rm DM,Sun}(r)\right)^2}\,. \tag{2.16}$$

Numerically, the annihilation constants C_A for the Sun and the Earth are given by [92]

$$C_{A,\odot} \simeq 1.2 \cdot 10^{-52}\,\text{s}^{-1} \left(\frac{\langle\sigma v\rangle}{2.2 \cdot 10^{-26}\,\text{cm}^3\text{s}^{-1}}\right) \left(\frac{m_{\rm DM}}{\text{TeV}}\right)^{3/2}\,, \tag{2.17}$$

$$C_{A,\oplus} \simeq 3.9 \cdot 10^{-49}\,\text{s}^{-1} \left(\frac{\langle\sigma v\rangle}{2.2 \cdot 10^{-26}\,\text{cm}^3\text{s}^{-1}}\right) \left(\frac{m_{\rm DM}}{\text{TeV}}\right)^{3/2}\,. \tag{2.18}$$

The competition between the capture process, which builds up the dark matter population, and the annihilation process depleting it is governed by the differential equation [152]

$$\frac{\text{d}N}{\text{d}t} = C - C_A N^2 - C_E N\,. \tag{2.19}$$

In this equation, the last term additionally takes into account the thermal evaporation of dark matter particles: a solar nucleus with a non-zero velocity can scatter off a dark matter particle which has been previously captured, and potentially transfer an energy large enough such that after this scattering event the velocity of the dark matter particle is again larger

than the escape velocity of the Sun. However, this mechanism of depleting the dark matter population is only efficient for fairly small dark matter masses $m_{\rm DM} \lesssim 4$ GeV [154]; by restricting ourselves to scenarios involving larger dark matter masses, we can safely neglect evaporation in the rest of this work.

In the absence of evaporation, the solution to Eq. (2.19) satisfying the initial condition $N(t=0)=0$ is given by

$$N(t) = \sqrt{\frac{C}{C_A}}\,\tanh\left(\frac{t}{\tau}\right) \quad \text{with} \quad \tau \equiv \frac{1}{\sqrt{C\cdot C_A}}\,. \tag{2.20}$$

In particular, for $t \gg \tau$, the number of dark matter particles stays constant, corresponding to an equilibrium between capture and annihilation. The *equilibration time* τ defined in the previous equation depends on both the scattering as well as on the annihilation cross section of dark matter: the larger these cross sections, the shorter the equilibration time. In Sec. 5, we will calculate τ for a specific dark matter model; in general, it turns out that in many (though not in all) scenarios of weakly interacting dark matter, at present times $t \simeq t_\odot = 4.5\cdot 10^9\,$y, corresponding to the age of the Solar System, the equilibration condition $t \gg \tau$ is indeed satisfied for capture and annihilation in the Sun. On the other hand, for the case of the Earth equilibration typically has not yet been reached, which we will also confirm in the context of a specific model in Sec. 5.

Most importantly, if captures and annihilations are in equilibrium, the annihilation rate defined in Eq. (2.16) is completely determined by the capture rate:

$$\Gamma_A = C/2 \quad \text{for} \quad t \gg \tau\,. \tag{2.21}$$

Physically, this equation simply states that in equilibrium there is one annihilation event for every pair of captured dark matter particles. If that is the case, also the normalization of the neutrino flux produced by the dark matter annihilations is fully specified by the capture rate, in particular it is proportional to the scattering cross section of dark matter with nuclei while being independent of the annihilation cross section, provided the latter is large enough for equilibration to be satisfied. Consequently, the results of neutrino telescopes searching for high-energy neutrinos from the direction of the Sun can be directly compared to direct detection experiments.

Production and propagation of neutrinos

Depending on the annihilation channel, the dark matter particles annihilating in the center of the Sun or the Earth produce a cascade of stable Standard Model particles. Almost all of these are stopped by subsequent interactions with the dense matter of the environment, and never reach the surface. However, depending on their energy, neutrinos can escape the annihilation region, and eventually be detected by neutrino telescopes located at the surface of the Earth. In the rest of this introductory section, we will omit the discussion of dark matter capture and annihilation in the Earth, as the absence of equilibration in almost all viable models (c.f. the previous paragraph) suppresses considerably the neutrino flux, making the observational prospects rather poor.

In order to obtain the spectrum of neutrinos injected at the core of the Sun for a given annihilation channel of dark matter, the first step is to simulate the hadronization process with the help of a Monte Carlo event generator such as PYTHIA [155, 156]. For the subsequent decays of unstable Standard Model particles, the dense environment of the solar

matter has to be taken into account: if the lifetime $\gamma\tau_0$ of a particle, where τ_0 is the proper lifetime and γ is the corresponding Lorentz factor, is comparable to or larger than the typical timescale for interactions with the solar medium $\tau_{\rm int}$, the particle loses a significant part of its initial energy before decaying [157]. In particular, it turns out that muons as well as charged pions and kaons are completely stopped before they decay, and thus do not contribute to the flux of neutrinos at energies $E_\nu \gtrsim 100$ MeV, rendering them irrelevant for searches with neutrinos detectors such as IceCube [158] or ANTARES [159], which are only sensitive to neutrinos with energies $E_\nu \gtrsim (1-10)$ GeV [7]. On the other hand, τ leptons or hadrons consisting of charm or bottom quarks have a lifetime comparable to their interaction time [157], and thus they lose part of their energy before decaying. Other particles as e.g. weak gauge bosons or the Higgs boson have lifetimes much smaller than their inverse interaction rates, and consequently they decay as if they were in vacuum. All these effects can be taken into account on an event-by-event basis in a Monte Carlo event generator, as done e.g. in [153, 162, 163]. In Sec. 5 and 6, we will also use our own implementation of this formalism, by using a properly modified version of PYTHIA 8.1 [156], based on the modeling of the interaction rates of Standard Model particles with the solar matter presented in [157].

Once produced near the center of the Sun, the neutrinos propagate through the solar matter. During that phase, they are subject to matter-enhanced flavor oscillations, described by the following effective Hamiltonian in flavor space [153]:

$$\mathbf{H} = \frac{\mathbf{m}^\dagger \mathbf{m}}{2E_\nu} + \sqrt{2} G_F \left[N_e \, \mathrm{diag}(1,0,0) - \frac{N_n}{2} \, \mathrm{diag}(1,1,1) \right] . \tag{2.22}$$

Here, the first term on the right hand side describes oscillations in vacuum, determined by the 3×3 neutrino mass matrix $\mathbf{m}$, which in turn is specified by the three neutrino masses and the mixing angles in vacuum; see [164] for a recent review on the experimental determination of these parameters. In addition, coherent forward scattering of neutrinos off electrons, protons and neutrons in the Sun, via the exchange of Z and W bosons, leads to an additional matter potential (which in particular can give rise to the MSW effect [165]), described by the second term in the oscillation Hamiltonian (2.22). We refer to [166] for more details on neutrino oscillations in matter. Furthermore, neutrinos can lose energy or disappear completely by scattering off solar nuclei. More precisely, a neutral-current interaction $\overset{(-)}{\nu_i} N \to \overset{(-)}{\nu_i} N$ leads to an energy loss of the (anti-)neutrino, while a charged-current interaction $\overset{(-)}{\nu_i} N \to l_i^\pm N'$ removes the neutrino from the flux, by producing a charged lepton $l_i^\pm$. If the latter is a τ lepton, the decay of it again produces a high-energetic neutrino, denoted as τ regeneration. As the neutrino-nucleus scattering cross section grows with the neutrino energy [166], all these effects are more pronounced for large neutrino energies. In particular, for $E_\nu \gtrsim 1$ TeV, the Sun gets opaque to neutrinos, leading to a cutoff in the neutrino spectrum from annihilations of dark matter particles with masses above a few TeV [153]. The combined problem of matter enhanced neutrino oscillations as well as interactions with solar nuclei can be solved numerically, either using the density matrix formalism [153], or by means of an event-by-event Monte Carlo simulation, as implemented in the WimpSim package [162]. Whenever necessary, we employ the latter in order to propagate a spectrum of neutrinos injected at the core of the Sun.

As soon as the neutrinos reach the surface of the Sun, they propagate through vacuum

[7] Notice however that also the MeV neutrino flux can be used to probe dark matter models, using the Super-Kamiokande detector [160], as discussed in [147, 161].

on their way to Earth, corresponding to only the first term in Eq. (2.22). Depending on the relative orientation of the neutrino telescope to the position of the Sun, they also cross the interior of the Earth before they can finally be detected; however, for the energy range of interest to us, Earth matter effects are negligible [153, 162]. Also for this final part of the neutrino propagation, we employ the WimpSim package [162].

Detection of neutrinos from dark matter annihilations, experimental situation

After reaching the Earth, the neutrinos originating from dark matter annihilations in the Sun can be observed via their interactions with nuclei inside or nearby large-scale neutrino detectors. More specifically, charged-current interactions of muon (anti-)neutrinos produce charged (anti-)muons, which typically move at relativistic velocities and hence induce the emission of Cherenkov light, which in turn can be detected by optical sensors of the corresponding neutrino telescope. Importantly, with this technique it is possible to achieve angular resolutions down to $1 - 10^\circ$ (depending on the instrument and the neutrino energy, see e.g. [167]), facilitating a directional search for a point-like source like the Sun[8]. For the energy range of interest, the dominant sources of background are atmospheric muons and neutrinos, produced by interactions of cosmic rays with the atmosphere of the Earth. However, as mentioned already in the beginning of this section, these processes are not expected to correlate with the direction of the Sun, allowing for a direct off-source measurement of the background.

Several searches for an excess of muon tracks correlated with the direction of the Sun have been undertaken, most notably by the neutrino telescopes IceCube [158, 168, 169], ANTARES [159], Super-Kamiokande [170], Baikal [171], as well as by the Baksan Underground Scintillator Telescope [172]. Up to date, none of these experiments have found a statistically significant excess, and consequently various upper limits on the neutrino flux originating from dark matter annihilations in the Sun have been deduced from the corresponding data sets. For a fixed annihilation channel of dark matter, one can employ the methods introduced in the previous part of this section in order to convert an upper limit on the neutrino flux into an upper limit on the annihilation rate of dark matter. Assuming equilibrium between capture and annihilation of dark matter in the Sun, this in turn implies an upper limit on the capture rate, via Eq. (2.21). Finally, using the formalism of the calculation of the capture rate given at the beginning of this section, one arrives at an upper limit on the scattering cross section of dark matter with nuclei, separately for every possible annihilation channel.

In Fig. 2.3, we show the upper limits on the spin-dependent as well as on the spin-independent scattering cross section with protons following from the currently most sensitive neutrino telescopes. Analogously to Fig. 2.1 showing the upper limits derived from direct detection experiments, these results are based on assuming a Maxwell-Boltzmann velocity distribution, given by Eq. (2.7), and furthermore use $\rho_0 = 0.3\,\mathrm{GeV/cm^3}$. Following common practice by the neutrino telescope collaborations, in these plots we show the upper limits only for two benchmark annihilation channels: W^+W^-(replaced by $\tau^+\tau^-$ for $m_{\mathrm{DM}} < m_W$), corresponding to a rather hard neutrino spectrum due to the prompt decay of the W and τ particles in the Sun (c.f. the previous discussion), as well as $b\bar{b}$, which leads to a softer spectrum of neutrinos, due to the energy loss of B-mesons and -hadrons inside the Sun.

[8] In general, neutrinos can also be detected via electromagnetic or hadronic showers. However, this signature does not allow for a precise reconstruction of the direction of the initial neutrino, and hence is typically not employed for the search for neutrinos from dark matter annihilations in the Sun.

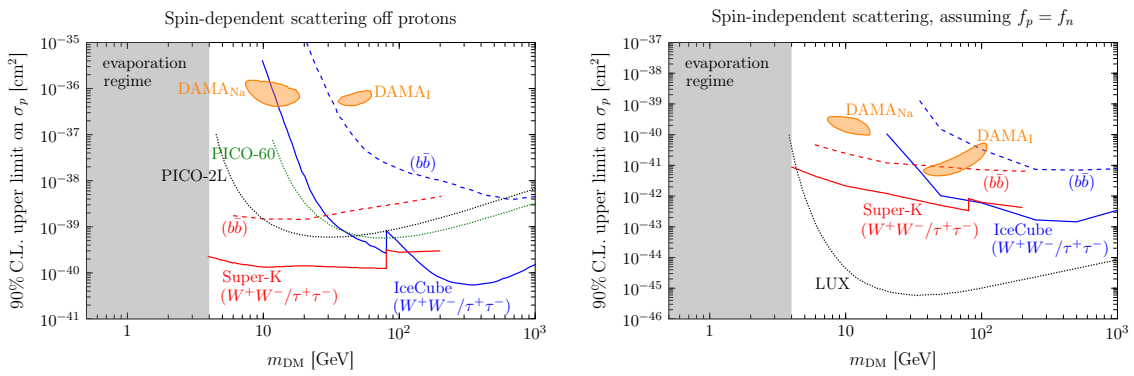

Figure 2.3.: Upper limits from neutrino telescopes searching for a high-energy neutrino flux from the direction of the Sun, compared to the most sensitive direct detection experiments, assuming $\rho_0 = 0.3\,\mathrm{GeV/cm^3}$ as well as a Maxwell-Boltzmann velocity distribution. In both panels, the 3σ-favored regions of the parameter space implied by the DAMA modulation are shown in orange, as calculated in [100] for scattering off Na and I. All other lines are upper limits on σ_p at 90% C.L. *Left panel:* spin-dependent scattering off protons, with the IceCube limits (blue curves) taken from [158], and the Super-Kamiokande limits (red curves) from [170]. The results from PICO-2L [125] and PICO-60 [121] are shown as black and green dotted curves, respectively. *Right panel:* spin-independent scattering, assuming $f_p = f_n$. The IceCube limits (blue curves) are taken from [168], while the Super-Kamiokande results were presented in [170]. For comparison, the upper limit from LUX [102] is shown as the black dotted curve.

As the effective area for neutrino detection rises with energy, the expected muon signal is larger in the former case, leading to more stringent upper limits. In particular, from the left panel of Fig. 2.3, it follows that for the annihilation channel $W^+W^-/\tau^+\tau^-$, the neutrino telescopes provide stronger limits on the spin-dependent scattering cross section with protons than the most sensitive direct detection experiments. For the softer annihilation channel $b\bar{b}$, as well as for spin-independent scattering, direct detection experiments are typically more important, although the neutrino telescopes are still competitive for some ranges of dark matter masses. However, as mentioned already earlier on, it is important to notice that direct detection experiments and the capture process in the Sun are sensitive to different parts of the velocity space. Hence, even for those scenarios in which direct detection limits are stronger than the ones from neutrino telescopes when assuming the Maxwell-Boltzmann distribution, the latter nevertheless provide important complementary information, once astrophysical uncertainties are taken into account.

Finally, we remark that $W^+W^-, \tau^+\tau^-$ and $b\bar{b}$ are of course not the only possible annihilation channels of dark matter. In particular, it is conceivable that dark matter only annihilates into "neutrino-poor" channels, such as e^+e^- or $u\bar{u}$. In Sec. 6, we will derive upper limits on the scattering cross section of dark matter for these and various other annihilation channels, including for the first time higher-order corrections to the annihilation process, which we will show to have a significant impact on the neutrino flux expected from these annihilation channels.

2.3. Indirect dark matter detection with gamma rays and charged cosmic rays

Following the WIMP paradigm, dark matter is expected to annihilate also in today's Universe, most significantly in regions with a high density of dark matter. The idea of *indirect detection* is to observe the Standard Model particles produced in these annihilation events as part of the cosmic rays impinging on Earth[9]. One example of this idea has been introduced in the previous section: captured dark matter particles which are present in the core of the Sun can annihilate, producing a flux of neutrinos potentially detectable at Earth. In this section, we give a brief overview of other important indirect detection channels, namely gamma rays in Sec. 2.3.1 and charged antimatter in Sec. 2.3.2. These messengers will be employed later on in Sec. 3, 4 and 5 in order to confront particle physics models of dark matter to observations from gamma ray instruments such as Fermi-LAT or H.E.S.S., and from experiments searching for antimatter in cosmic rays, such as PAMELA and AMS-02.

2.3.1. Gamma rays from dark matter

Gamma rays constitute an excellent messenger for dark matter annihilations or decays: photons with energies in the GeV to TeV range propagate essentially unhindered through the Universe, and thus both the spectral and directional information can be used to distinguish a dark matter induced component from conventional astrophysical backgrounds. For energies below $\simeq 100 - 500\,\mathrm{GeV}$, gamma rays can be detected by satellite experiments like DAMPE [174] and in particular Fermi-LAT [175], while for larger energies atmospheric Cherenkov telescopes such as H.E.S.S. [176] or MAGIC [177] are the leading technology.

The flux of gamma rays produced from dark matter annihilations within a given angular patch $\Delta\psi$ in the sky is given by [178]

$$\frac{\mathrm{d}\Phi_\gamma}{\mathrm{d}E_\gamma}(E_\gamma) = \frac{1}{8\pi} \underbrace{\int_{\Delta\psi} \frac{\mathrm{d}\Omega}{\Delta\psi} \int_{\mathrm{l.o.s.}} \mathrm{d}l_\psi \, \rho^2(\vec{r})}_{J\text{-factor}} \left(\frac{\langle\sigma v\rangle}{m_{\mathrm{DM}}^2} \sum_f B_f \frac{\mathrm{d}N_\gamma^f}{\mathrm{d}E_\gamma} \right) . \tag{2.23}$$

Here, the J-factor takes into account the information about the spatial distribution of dark matter within the observed angular region $\Delta\psi$, in particular involving an integration of the square of the dark matter density $\rho(\vec{r})$ over the line of sight. The remaining part of Eq. (2.23) depends on the particle physics properties of dark matter, i.e. its mass m_{DM} and velocity averaged annihilation cross section $\langle\sigma v\rangle$, as well as the spectrum of gamma rays $\mathrm{d}N_\gamma^f / \mathrm{d}E_\gamma$ arising from the final state f, which is assumed to occur with a branching fraction B_f.

An important aspect in the search for dark matter annihilations using gamma rays is the choice of the target region in the sky. The scaling of the J-factor with $\rho^2(\vec{r})$ clearly motivates to search for WIMP annihilations in directions containing a large integrated density of dark matter. One widely used target is the region around the Galactic Center (GC), which hosts most of the dark matter population of the Milky Way. However, while potentially luminous in gamma rays from dark matter annihilations, it is also a very active region in

[9] Besides annihilations, dark matter particles might furthermore decay on cosmological time scales, leading also to a potential signature in cosmic rays. However, as only the case of annihilations is relevant for the remaining parts of this work, we will mostly omit the discussion of dark matter decays in the rest of this introductory section, referring to [173] for more details on this topic.

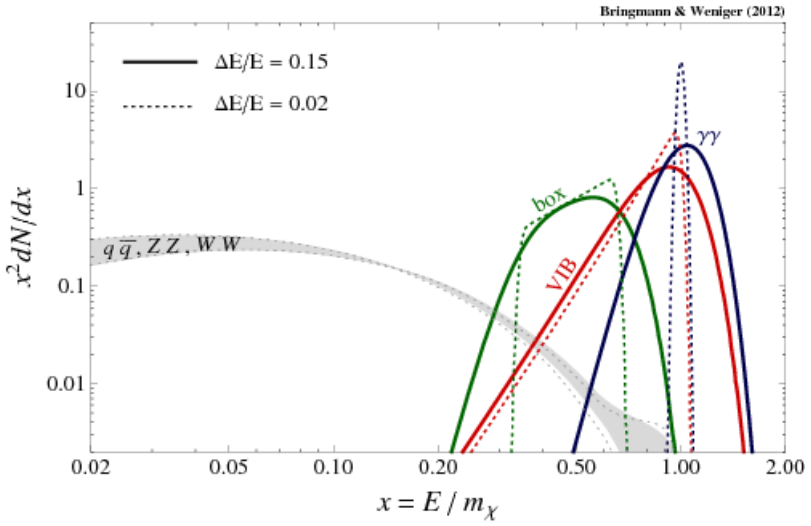

Figure 2.4.: Energy spectrum of gamma rays produced by dark matter annihilations. The gray band brackets the spectra for annihilations into quarks and gauge bosons, while the colored solid and dotted lines correspond to the spectral features mentioned in the text, assuming different energy resolutions of the instrument. Figure taken from [178].

terms of conventional astrophysical processes. Important examples for the latter are spallations of cosmic rays on the interstellar matter, leading to the production of neutral pions that subsequently decay into gamma rays, bremsstrahlung emission of cosmic ray electrons interacting with the interstellar gas, or inverse Compton scattering of low-energy photons with cosmic ray electrons [179]. The modeling of these processes to a precision necessary for extracting a potential dark matter induced signal from the observed data is highly challenging. Furthermore, following the discussion in Sec. 1.2, the density profile $\rho(\vec{r})$ near the GC is only poorly constrained, which results in a significant systematic uncertainty in the relation between the dark matter annihilation cross section $\langle \sigma v \rangle$ and the associated gamma ray flux. Besides the GC, also dwarf spheroidal galaxies (dSphs) orbiting the Milky Way have been employed extensively in the search for the gamma ray emission produced by dark matter annihilations. While their J-factors are typically $\simeq 2$ orders of magnitude smaller than the GC region [180], dSphs are expected to be largely dominated by dark matter, making the problems associated with the subtraction of the astrophysical background much less severe than for the case of the GC. Furthermore, the J-factors of the dSphs can be estimated with reasonable accuracy from data, by inferring their gravitational potential from observations of the stellar density and velocity profiles [181–183]. Lastly, also Galaxy clusters and the gamma ray emission from the extragalactic sky can be employed for indirect searches for dark matter; as these targets are not relevant for the rest of this work, we refer to [184–186] for more details.

From the particle physics side, following Eq. (2.23), the main ingredients in the calculation of the gamma ray flux induced by dark matter annihilations are the dark matter mass and annihilation cross section on the one hand side, affecting the overall normalization of the signal, and on the other hand the spectrum of gamma rays $\mathrm{d}N_\gamma^f / \mathrm{d}E_\gamma$ for a given final state f. Let us first consider the signal produced by annihilations into quark and gauge boson final states, which produce a rather universal and featureless energy spectrum shown as the

gray band in Fig. 2.4. Various authors have analyzed the Fermi-LAT data corresponding to different regions around the GC, allowing for the presence of such an exotic contribution to the total gamma ray spectrum. Interestingly, several works have claimed the existence of an extended diffuse emission of gamma rays on top of the standard astrophysical backgrounds, within a region of a few degrees around the GC [187–192]. In particular, this excess seems to be robust with respect to changes in the modeling of the diffuse gamma ray emission associated to the background processes [192]. When interpreted in terms of dark matter annihilations, the spatial profile is consistent with a slightly contracted NFW profile, and the energy spectrum, peaking at a few GeV, can be well-fitted by a large number of annihilation channels, for dark matter masses in the range of $\simeq 10 - 200\,\text{GeV}$ [193]. Intriguingly, within the astrophysical uncertainties related to the determination of the J-factor corresponding to the region close to the GC, the absolute strength of the signal is compatible with the thermal annihilation cross section $\langle\sigma v\rangle \simeq 2.2 \cdot 10^{-26}\,\text{cm}^3/\text{s}$. In Sec. 3, we will give an explicit interpretation of the GC excess in terms of a simplified model of Dirac dark matter, which we then confront to bounds from direct detection experiments. Finally, it should be mentioned that there are also proposals for explaining the GC excess without invoking dark matter annihilations, such as recent hadronic or leptonic cosmic-ray outbursts [194–196], or the combined emission from a large number of unresolved point sources, in particular millisecond pulsars [197, 198]. Recent analyses claim that the Fermi-LAT data prefers the latter option over the dark matter interpretation [199, 200].

On the other hand, the Fermi-LAT search for a gamma ray emission from 15 dSphs turns out to be consistent with the absence of a dark matter induced signal [180]. This results in stringent and robust upper limits on the annihilation cross section of dark matter; in particular, for annihilations into quark-antiquark pairs or into $\tau^+\tau^-$, the thermal cross section is excluded for $m_{\text{DM}} \lesssim 100\,\text{GeV}$. These bounds pose important constraints on a large variety of dark matter models, which we will specifically study in Sec. 3 and 4 in the context of simplified models. Also, it should be noticed that taken at face value, the upper limits from dSphs are in tension with the dark matter interpretation of the GC excess. However, in view of the uncertainties in extracting the J-factor in regions close to the GC, reconciling both observations is still possible [193].

Finally, let us briefly introduce the search for *gamma ray spectral features* as a complementary strategy for disentangling the dark matter induced gamma ray signal from the astrophysical background processes. This method is based on the observation that in a large variety of models, dark matter can annihilate into final states featuring a hard photon spectrum, with the energy scale set by the dark matter mass. The most prominent example is the annihilation process DM DM $\to \gamma X$ [201–203], where X denotes either another photon, a Z boson or the Higgs particle. For WIMPs with non-relativistic velocities, as it is relevant in particular for the dark matter population in our Galaxy, this process leads to a photon spectrum in form of a gamma ray line with an energy $E_\gamma \simeq m_{\text{DM}}(1 - m_{\text{X}}^2/4m_{\text{DM}}^2)$. As discussed previously, it is difficult to accurately predict the precise normalization and spectral shape of the astrophysical background of gamma rays e.g. from the direction of the GC; however, for the purpose of the search for gamma ray spectral features, it is enough to employ the fact that in the GeV to TeV range all known astrophysical processes lead to smooth, featureless energy spectra. Hence, the observation of a gamma ray line on top of a smooth background is generally expected to be a smoking-gun signal for the annihilation or decay of dark matter. Besides gamma ray lines, the annihilation of dark matter can also result in other spectral features which can be distinguished in this way from the background: *virtual internal bremsstrahlung* (VIB) [204–206], arising from the annihilation

of dark matter into a three-body final state including a hard photon[10], as well as gamma ray boxes [207], triangles [208] or higher-order polynomials [209] which appear in scenarios in which the dark matter particle annihilates into an intermediate particle, which then decays in flight into γX. Examples for the spectra arising from these processes are shown in Fig. 2.4.

Several experiments, most notably Fermi-LAT, H.E.S.S. and MAGIC, have searched for the presence of a gamma ray spectral feature in various regions of the sky, such as in different regions close to the GC [210,211], in nearby galaxy clusters [212], in dwarf galaxies [213,214], or in the extragalactic sky [211]. As of today, no statistically significant gamma ray feature has been found[11], and hence several of these searches lead to stringent bounds on the annihilation cross section of dark matter into a pair of gamma rays or into the other final states involving a spectral feature. In Sec. 4, we will employ these upper limits in the context of a simplified model of real scalar dark matter, showing that large parts of the parameter space are excluded by the observations of Fermi-LAT and H.E.S.S.

2.3.2. Searches for antimatter in cosmic rays

The annihilation of dark matter particles into final states containing e.g. quarks or gauge bosons produces not only gamma rays, as discussed in the previous section, but also stable charged Standard Model particles. Among these, in particular antiprotons, antinuclei and positrons are interesting messengers for dark matter, as their astrophysical background flux is suppressed compared to the more commonly occurring protons, nuclei and electrons.

In contrast to gamma rays, charged cosmic rays with energies in the GeV to TeV range are subject to rather complex propagation effects within the Milky Way. In particular, the presence of inhomogeneous Galactic magnetic fields leads to a diffusion of the particles which smooths out almost all directional information, leading to a flux of antimatter at Earth that is, to first order, isotropic [217, 218]. The fluxes of antiprotons and positrons have been measured by various space-based instruments, most recently by PAMELA [219–222] and AMS-02 [218, 223–225]. We show the recent (but still preliminary) data from AMS-02 on the $\bar{p}/p$ ratio in the left panel of Fig. 2.5, as well as several measurements of the positron fraction $e^+/(e^+ + e^-)$ in the right panel of the same figure.

The left panel of Fig. 2.5 furthermore includes a prediction for the $\bar{p}/p$ ratio arising from spallations of cosmic rays on the interstellar matter [226], constituting the main background for dark matter searches. Here, the blue band brackets the uncertainty on the spallation background resulting from our incomplete knowledge of propagation in the Milky Way. The standard approach for modeling the latter is to describe the effects of diffusion, convection, reacceleration, energy losses, annihilations on the interstellar medium, as well as solar modulation by means of a two-zone diffusion model [229,230]. This model contains a handful of free parameters, which can be constrained by observations of secondary-to-primary ratios such as boron-to-carbon (B/C). The blue band in the left panel of Fig. 2.5 corresponds to the envelope of the expected spallation background obtained by using 500 sets of propagation parameters consistent with the B/C ratio [226] as measured by AMS-02 [231]. Besides, the gray band in that panel additionally takes into account uncertainties in the nuclear cross sections underlying the spallation reactions of cosmic ray protons and helium on the

[10] The phenomenology of this spectral feature will be discussed in detail in Sec. 4.

[11] Several authors have found a line-like feature at $E_\gamma \simeq 130\,\mathrm{GeV}$ [215,216] in the Fermi-LAT data. However, its significance has decreased considerably after using a larger, reprocessed data set, making a dark matter origin unlikely [210].

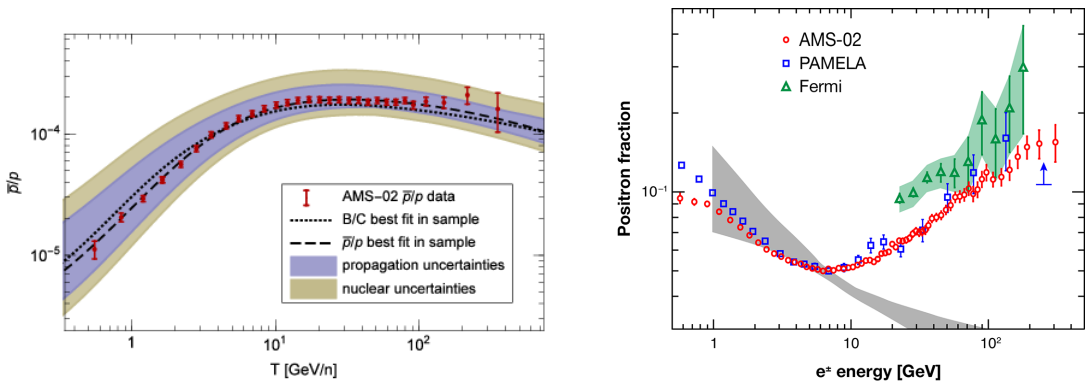

Figure 2.5.: *Left panel:* $\bar{p}/p$ ratio as measured by AMS-02, compared to the expected flux arising from cosmic ray spallations. Figure from [226]. *Right panel:* positron fraction, with data from several experiments, as well as the prediction for the spallation background. Figure has been taken from [227], which is based on [218] and [228].

interstellar matter.

As apparent from the plot, the AMS-02 data on the $\bar{p}/p$ ratio is well compatible with the expected astrophysical background, once all the uncertainties mentioned above are taken into account. This leaves little room for an exotic source of antiprotons, such as dark matter annihilations, and consequently the $\bar{p}/p$ data can be employed in order to derive upper limits on the dark matter annihilation cross section. However, the uncertainties corresponding to the different sets of propagation parameters compatible with the B/C ratio are significantly larger for the antiproton flux expected from dark matter annihilations, compared to the spallation background. Partially, this is because both B/C as well as the spallation antiproton flux are mainly sensitive to the combination K_0/L, where K_0 and L are the normalization of the diffusion coefficient and the half-height of the diffusion zone, respectively, while on the other hand antiprotons originating from dark matter annihilations are produced in the complete halo, and are very sensitive to L directly. Hence, upper limits on $\langle\sigma v\rangle$ vary by up to two orders of magnitude when using different sets of viable propagation parameters [232, 233]. In Sec. 4.3, we will derive constraints arising from the $\bar{p}/p$ ratio as measured by PAMELA in the context of a simplified model of real scalar dark matter, based on the three sets of propagation parameters MIN, MED and MAX which have been derived in [234], and which approximately bracket the propagation uncertainty for antiprotons from dark matter annihilations[12].

Besides antiprotons, also positrons can be used as a messenger for dark matter annihilations or decays. Interestingly, PAMELA [221, 222], Fermi [237] and AMS-02 [218, 224] have observed an increase of the positron fraction at energies $E_{e^+} \gtrsim 10\,\text{GeV}$, as shown in the right panel of Fig. 2.5. As the positrons produced in spallation reactions of cosmic rays on the interstellar matter are expected to lead to a decreasing positron fraction [228], indicated by the gray band in the same plot, the *positron excess* is nowadays widely accepted to be evidence for an additional, primary source of positrons. In particular, it is possible to fit the data with dark matter annihilations or decays [238, 239], although in the case of annihi-

[12]It should be noted however that these propagation parameters are based on old data on the B/C ratio. Furthermore, by now the MIN parameters are excluded on the basis of radio, synchrotron and positron data [235, 236].

lations the cross section necessary for explaining the positron excess is up to three orders of magnitude larger than the thermal value $\langle \sigma v \rangle = 2.2 \cdot 10^{-26}\,\mathrm{cm}^3/\mathrm{s}$. In any case, by now the dark matter interpretation of the positron excess is in strong tension with the absence of signals in other indirect detection channels, most notably antiprotons and gamma rays (see e.g. [240]), as well as by observations of the CMB [241]. Consequently, the currently most plausible option is that the positron excess is dominantly caused by other primary sources, most notably pulsars, which indeed can also provide an excellent fit to the data [242].

Irrespectively of the origin of the positron excess, the data on the positron fraction as well as on the positron flux can nevertheless be used for setting upper limits on the annihilation cross section of dark matter. In particular, analogously to the idea of gamma-ray spectral features introduced in Sec. 2.3.1, one can search for the presence of a spectral feature in the positron flux or fraction on top of the observed smooth spectrum. Such an analysis is particularly interesting for final states leading to a peaked positron spectrum, such as e^+e^- and $\mu^+\mu^-$. This idea has been employed in [243] and [244], based on the AMS-02 data on the positron fraction and flux, respectively. The corresponding upper limits on the annihilation cross section will be employed in Sec. 3, in order to constrain a simplified model of Dirac dark matter coupling to electrons or muons.

Finally, it has been pointed out that also antideuterons [245] (or even antihelium [246,247]) can be used as a messenger for dark matter annihilations or decays. While the overall antideuteron flux expected from dark matter as well as from spallations of cosmic rays is $\simeq 2-3$ orders of magnitude smaller than for antiprotons, the signal-to-background ratio is considerably larger. In particular, the observation of only a few antideuterons would provide a strong indication for the presence of a primary source of antinuclei, such as dark matter [248, 249]. Up to date, no antideuterons have been detected in cosmic rays, but are currently searched for by AMS-02, as well as in the future by the GAPS experiment [250]. More details on this indirect detection channel can be found in the recent review article [251].

2.4. Collider searches for dark matter

Finally, in this section we give a brief overview on the possibility to probe the particle nature of dark matter at colliders. Naturally, the focus of the discussion is on proton-proton collisions at the LHC, operating at center-of-mass energies between $\sqrt{s} = 7-13$ TeV. Furthermore, we remark that for some dark matter models also constraints from LEP can still be relevant, as we will see e.g. in Sec. 4.4.

As weakly interacting dark matter particles themselves do not lead to signals in the LHC detectors, they can only be observed in association with visible Standard Model particles. Hence, the signatures of interest are typically given by one or several hadronic jets or leptons, accompanied by a significant amount of transverse missing energy (see e.g. [252]). Such a topology in general can arise in two ways: first, the dark matter particle itself can be directly produced in the pp collisions, together with e.g. a hard gluon or quark originating from initial or final state radiation. Secondly, in several models also other new heavy states connected to the dark matter particle can be produced (such as a mediator between the dark matter and Standard Model particles), which then subsequently can decay into the dark matter and a visible Standard Model particle, also leading to one of the signatures mentioned above. Notice that this in particular implies that in contrast to direct and indirect detection experiments, the LHC is not only sensitive to the dark matter particle itself, but also to other new states within a possible "dark sector". In run 1 of the LHC,

performed at $\sqrt{s} = 7$ and 8 TeV, no significant excess which can be attributed to the production of dark matter particles has been found.

From the theoretical point of view, a generic problem is that collider searches for dark matter are typically highly model-dependent: there is no straightforward analogue to the way of interpreting the direct and indirect detection experiments in a two-dimensional parameter space spanned by the dark matter mass and its scattering or annihilation cross section. In view of that situation, dark matter searches at colliders are often interpreted within the parameter space of a given UV complete theory containing a dark matter candidate, most notably supersymmetric theories featuring the neutralino as the hypothetical dark matter particle; see e.g. the recent analysis [253]. Obviously, a disadvantage of such an approach is that there is no direct way of translating the results obtained in one particular theory to another scenario, and also a comparison with non-collider experiments can only be done separately for each point in the (typically high-dimensional) parameter space of the model. Hence, in run 1 of the LHC, the dark matter searches also have been interpreted within *effective field theories* (EFTs) [254]. In this framework, one assumes that the production of the dark matter particle can be described by a higher-dimensional contact interaction involving e.g. two quarks and two dark matter particles. A bound on the coefficient of such an operator can then be compared to direct and indirect detection experiments, which allows to study the complementarity of the different approaches [255, 256].

However, various authors have stressed that the assumption of contact interactions can be strongly violated at the LHC, questioning the validity of the EFT at the relevant energy scales, see e.g. [257,258]. In view of that situation, there has emerged the consensus [259–261] to interpret the LHC data in terms of *simplified models* of the dark matter particle and its interactions. As already mentioned in the introduction to this thesis, here the strategy is to include only the degrees of freedom relevant for the description of the dark-matter-related signatures at the LHC, leading to typically two or three free parameters which then can be constrained by the data. These minimal, but still self-consistent particle physics models (as opposed to the EFT description) can then also be confronted to direct and indirect detection searches, allowing for detailed complementarity studies. We will employ precisely this approach in Sec. 4.4, where we interpret an ATLAS search for multiple jets plus missing energy in terms of a simplified model containing a real scalar dark matter particle and a colored fermionic mediator.

Part II

t-CHANNEL SIMPLIFIED MODELS FOR DARK MATTER

3. Dirac dark matter with a charged mediator: a comprehensive analysis of the direct detection phenomenology

In this section, we open the discussion of the phenomenology of dark matter searches within simplified models, by studying the direct detection signals arising in a model of Dirac dark matter. In this framework, the dark matter particle is assumed to be a singlet under the Standard Model gauge group, coupling via a Yukawa interaction to a Standard Model fermion and a charged scalar mediator. Apart from the cases where the dark matter couples directly to a quark of the first generation, there is no tree-level coupling of dark matter to nucleons within this simplified model. Naively, one then might think that in these scenarios the dark matter-nucleus scattering cross section is beyond the reach of current and future direct detection experiments.

However, within the last decades, dark matter direct detection experiments have reached unprecedented sensitivity to ever smaller scattering cross sections, and future experiments such as XENON1T [129] or DARWIN [131] are expected to probe further parts of the dark matter parameter space, as discussed in detail in Sec. 2.1.2. With this development in mind, it is worthwhile to ask whether current or future direct detection experiments are sensitive to models in which there is no tree-level coupling of dark matter to nucleons, but where the scattering can only proceed via one-loop diagrams. The simplified model of Dirac dark matter introduced in the previous paragraph is a prime example to study this question: if the dark matter particle couples via the Yukawa coupling to a Standard Model lepton or a heavy quark, the tree-level coupling to nucleons vanishes, however, due to the non-vanishing interactions of all Standard Model fermions with gauge bosons and/or the Higgs boson, there are one-loop diagrams which can nevertheless induce the scattering of dark matter off nuclei. Examples of such processes include the one-loop exchange of a Higgs, a Z-boson and a photon, as discussed partially in [262–270], or the one-loop coupling of dark matter to gluons [271–273]. Taking into account all relevant tree-level and one-loop processes, in the following we present a comprehensive calculation of the scattering cross section of dark matter with nucleons, and discuss the phenomenological implications for current and future direct detection experiments, separately for all Standard Model fermions that can couple to the dark matter particle.

This section is organized as follows: In Sec. 3.1, we define the simplified model, and subsequently discuss the constraint imposed on the model by requiring that the Dirac dark matter candidate accounts for all of the observed relic density. Then, in Sec. 3.2 we discuss the effective Lagrangian for dark matter-nucleon interactions induced by the coupling of dark matter to a given Standard Model fermion. Finally, in Sec. 3.3 we determine the expected scattering rate in xenon-based direct detection experiments, confronting it to existing upper limits from LUX, as well as comparing it with the projected reach of the future experiments XENON1T and DARWIN.

3.1. Singlet Dirac dark matter with a charged mediator

The simplified model discussed in this section is defined by extending the Standard Model by a Dirac fermion χ, which is a singlet under the Standard Model gauge group, and a charged scalar particle η, with gauge quantum numbers depending on the fermion coupling to χ and η, as it will be discussed later on. By imposing a discrete $\mathbb{Z}_2$ symmetry under which χ and η are odd, while all Standard Model particles are even, and by additionally demanding $m_\chi < m_\eta$, the Dirac fermion χ is guaranteed to be stable, and thus can potentially constitute the dark matter observed in the Universe. Then, the most general renormalizable Lagrangian is given by

$$\mathcal{L} = \mathcal{L}_{\text{SM}} + \mathcal{L}_\chi + \mathcal{L}_\eta + \mathcal{L}_{\text{int}}^{\text{fermion}} + \mathcal{L}_{\text{int}}^{\text{scalar}} \,. \tag{3.1}$$

In this equation, $\mathcal{L}_{\text{SM}}$ is the Lagrangian for the Standard Model, including in particular the scalar potential $V = m_1^2 \Phi^\dagger \Phi + \frac{1}{2}\lambda_1 (\Phi^\dagger \Phi)^2$ for the Higgs doublet Φ. Moreover, $\mathcal{L}_\chi$ and $\mathcal{L}_\eta$ contain the kinetic, mass and self-interaction terms for the dark matter particle χ and the scalar mediator η:

$$\mathcal{L}_\chi = \bar{\chi} i \partial\!\!\!/ \chi - m_\chi \bar{\chi}\chi \quad \text{and} \tag{3.2}$$

$$\mathcal{L}_\eta = (D_\mu \eta)^\dagger (D^\mu \eta) - m_2^2 \eta^\dagger \eta - \frac{1}{2}\lambda_2 (\eta^\dagger \eta)^2 \,. \tag{3.3}$$

In Eq. (3.3), the covariant derivative D^μ is specified by the gauge quantum numbers of η, which will be discussed below.

The interactions between the dark matter particle χ and the Standard Model sector are governed by $\mathcal{L}_{\text{int}}^{\text{fermion}}$, which consists of a Yukawa interaction between χ, η and one Standard Model fermion f. The latter can be either a right-handed quark or lepton, i.e. $f_R \in \left\{u_R^i, d_R^i, e_R^i\right\}$, with $i = 1, 2, 3$ labeling the generations of Standard Model fermions, or a left-handed quark or lepton doublet $f_L \in \left\{Q_L^i, L_L^i\right\}$. In the first case, the Yukawa interaction is given by

$$\mathcal{L}_{\text{int}}^{\text{fermion}} = -y\, \eta^\dagger \bar{\chi} f_R + \text{h.c.} \,, \tag{3.4}$$

while in the latter case it reads

$$\mathcal{L}_{\text{int}}^{\text{fermion}} = -y\, \eta^\dagger \bar{\chi} f_L + \text{h.c.} = \begin{cases} -y\, \eta_0^\dagger \bar{\chi} \nu_L - y\, \eta_-^\dagger \bar{\chi} e_L + \text{h.c.} & \text{for coupling to } L_L \,, \text{ and} \\ -y\, \eta_u^\dagger \bar{\chi} u_L - y\, \eta_d^\dagger \bar{\chi} d_L + \text{h.c.} & \text{for coupling to } Q_L \,. \end{cases} \tag{3.5}$$

Eqs. (3.4) and (3.5) specify the gauge quantum numbers of the mediator η; in particular, it is color neutral for dark matter coupling to a lepton, and a color triplet for coupling to a Standard Model quark.

Finally, the last term in the Lagrangian defined in Eq. (3.1) is a scalar potential leading to the interaction between the scalar mediator η and the Standard Model Higgs boson:

$$\mathcal{L}_{\text{int}}^{\text{scalar}} = \begin{cases} -\lambda_3 (\Phi^\dagger \Phi)(\eta^\dagger \eta) & \text{for coupling to } f_R \,, \text{ and} \\ -\lambda_3 (\Phi^\dagger \Phi)(\eta^\dagger \eta) - \lambda_4 (\Phi^\dagger \eta)(\eta^\dagger \Phi) & \text{for coupling to } f_L \,. \end{cases} \tag{3.6}$$

Large parts of the phenomenology of the model do not depend critically on this part of the Lagrangian, and thus we will set the couplings λ_3 and λ_4 to zero in the following discussion.

Nevertheless, we will comment briefly in Sec. 3.2 on the impact of this assumption on the effective dark matter-nucleon Lagrangian. Finally, we note that by neglecting the terms in $\mathcal{L}_{\rm int}^{\rm scalar}$, the neutral and charged components of the SU(2) doublet $\eta = (\eta_0, \eta_-)$ appearing in Eq. (3.5) have a common mass, which in the following will be denoted by m_η.

As discussed in Sec. 1.3, the relic density of dark matter particles is determined by the thermally averaged annihilation cross section $\langle\sigma v\rangle$ at the time of dark matter freeze out, which in general receives contributions from the self-annihilation of dark matter as well as from coannihilation processes involving other particles in the dark sector. For the model discussed in this section, the only relevant self-annihilation process is $\chi\bar{\chi} \to f\bar{f}$, with f being the Standard Model fermion coupling to χ via the Yukawa interaction specified by Eq. (3.4) or (3.5). Due to the small velocity of dark matter particles during the freeze-out process, the thermally averaged annihilation cross section is well approximated by the s-wave contribution:

$$\langle\sigma v\rangle_{\chi\bar{\chi}} \simeq (\sigma v)_{\chi\bar{\chi}}\big|_{v\to 0} = \frac{y^4 N_c}{32\pi}\,\frac{m_\chi^2\sqrt{1-(m_f/m_\chi)^2}}{\left(m_\chi^2+m_\eta^2-m_f^2\right)^2}\,, \tag{3.7}$$

with $N_c = 3\,(1)$ for coupling to quarks (leptons). If the dark matter particle couples to a fermion doublet f_L, $\langle\sigma v\rangle_{\chi\bar{\chi}}$ is given by the sum of the annihilation cross sections into both fermion states, with each one given by Eq. (3.7).

Besides the self-annihilation of the dark matter particle χ, in certain parts of the parameter space also coannihilations of χ with the scalar mediator η, as well as self-annihilations of η have to be taken into account in the computation of the dark matter relic density. Following the discussion in Sec. 1.3, these processes are only expected to be relevant if χ and η are nearly degenerate in mass, due to the exponential suppression of the contribution of coannihilation processes with the mass splitting $m_\eta - m_\chi$. Specifically, if this is the case, the processes $\chi\eta \to qg$, $\eta\eta^\dagger \to gg$, and $\eta_u\eta_d^\dagger \to W^+g$, if χ couples to quarks, as well as $\chi\eta \to e^-\gamma$, $\eta\eta^\dagger \to \gamma\gamma, \gamma Z, ZZ, W^+W^-$, or $\eta_0\eta_-^\dagger \to W^+\gamma$, if χ couples to leptons contribute to the effective annihilation cross section. For the calculation of the relic density at a given point in the parameter space of the model, we fully take into account all annihilation and coannihilation channels, by solving numerically the corresponding Boltzmann equation with the help of micrOMEGAs [87], interfaced with FeynRules [274] and CalcHEP [275]. Using this procedure, we find that the coannihilation processes contribute significantly to the relic density for $m_\eta \lesssim 1.2\,m_\chi$.

In the following discussion, for every value of m_χ and m_η, we fix the Yukawa coupling y entering Eqs. (3.4) and (3.5) by requiring that all of the dark matter observed in the Universe has been produced by the thermal freeze-out of the dark matter candidate χ; for this, we use the measurement of the relic density by Planck, given by $\Omega_{\rm DM}h^2 = 0.1198 \pm 0.0015$ [32]. Consequently, there are only two parameters of the model left which are relevant for the phenomenological analysis, and which can be chosen to be e.g. the dark matter mass m_χ and the relative mass splitting between the dark matter particle and the scalar mediator, $(m_\eta - m_\chi)/m_\chi$. We finally note that outside the coannihilation regime, i.e. for $m_\eta \gtrsim 1.2\,m_\chi$, the above-mentioned condition on the Yukawa coupling y is equivalent to demanding that the self-annihilation cross section $\langle\sigma v\rangle_{\chi\bar{\chi}}$ defined in Eq. (3.7) is equal to the value $\langle\sigma v\rangle_{\rm thermal} \simeq 4.4\times 10^{-26}\,{\rm cm}^3/{\rm s}$, as discussed in Sec. 1.3.

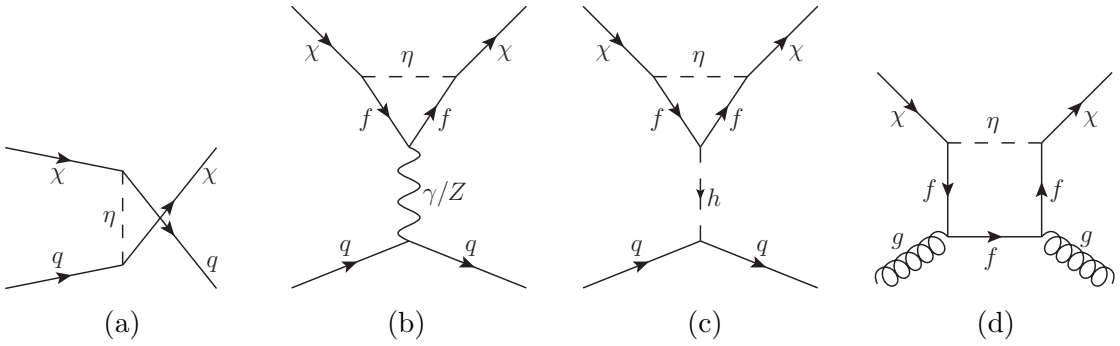

Figure 3.1.: Representative Feynman diagrams leading to dark matter-nucleon scattering: (a) tree-level scattering, (b) one-loop scattering via the exchange of a photon or a Z boson, (c) one-loop scattering via the exchange of a Higgs boson, (d) dark matter-gluon scattering at one loop.

3.2. Effective Lagrangian for dark matter-nucleon scattering

Depending on the fermion f that couples to the dark matter particle χ via the Yukawa interaction given by Eqs. (3.4) or (3.5), different processes contribute to the dark matter-nucleon scattering amplitude. We show one representative Feynman diagram for each possible process in Fig. 3.1. If dark matter couples to a quark q, it can scatter off nucleons at tree-level, as shown in panel (a). On the other hand, panels (b) and (c) show the scattering of dark matter off a quark at the one-loop level, mediated by a photon, a Z-boson or a Higgs boson, which is present for all possible choices of the fermion f coupling to the dark matter particle. Finally, panel (d) is an example for a box-diagram with two external gluons, again only relevant if dark matter couples to quarks. In the following, we discuss the effective Lagrangians corresponding to each of the processes shown in Fig. 3.1.

If the dark matter particle χ couples directly to a quark q, it can scatter off nucleons at tree-level via the diagram shown in panel (a) of Fig. 3.1. In that case, similar to the scattering of χ, also the antiparticle $\bar{\chi}$ can scatter off a quark q, by exchanging the colored mediator η in the s-channel. The effective interaction between dark matter and quarks then follows from a Fierz rearrangement of the corresponding matrix elements, resulting in a vector and an axialvector coupling[1]:

$$\mathcal{L}_{\text{eff,tree}}^{(\chi\text{-q})} = \lambda_V \left(\bar{\chi}\gamma^\mu \chi \, \bar{q}\gamma_\mu q - \bar{\chi}\gamma^\mu\gamma^5 \chi \, \bar{q}\gamma_\mu\gamma^5 q \right) , \tag{3.8}$$

with $\lambda_V \equiv y^2 / \left[8(m_\eta^2 - m_\chi^2)\right]$. In order to go from the level of dark matter-quark interactions to a description of dark matter-nucleon interactions, one then has to evaluate the matrix elements of the corresponding quark currents inside a nucleon $N \in \{p, n\}$. For the vector interaction, they are given by [92]

$$\langle p|\bar{q}\gamma_\mu q|p\rangle = \begin{cases} 2\,\bar{p}\gamma_\mu p & \text{if } q = u \\ \bar{p}\gamma_\mu p & \text{if } q = d \\ 0 & \text{otherwise} \end{cases} \quad \text{and} \quad \langle n|\bar{q}\gamma_\mu q|n\rangle = \begin{cases} \bar{n}\gamma_\mu n & \text{if } q = u \\ 2\,\bar{n}\gamma_\mu n & \text{if } q = d \\ 0 & \text{otherwise} \end{cases} . \tag{3.9}$$

[1] We omit terms leading to a scattering cross section suppressed by v^2, with v being the velocity of the dark matter particle.

These relations simply reflect the fact that even in the presence of non-perturbative QCD effects, the vector current is a conserved quantity, and hence the contributions of the valence quarks contained in the proton and neutron add coherently. In particular, the nucleon matrix element of the vector current vanishes identically for $q \notin \{u, d\}$. Using Eqs. (3.8) and (3.9), the vector interaction leads to an effective dark matter-nucleon Lagrangian describing a spin-independent interaction (c.f. the general discussion in Sec. 2.1.1):

$$\mathcal{L}_{\text{eff,tree}} = f_{V,\text{tree}}^{(N)}\, \bar{\chi}\gamma^\mu\chi\, \bar{N}\gamma_\mu N \quad , \quad \text{with} \tag{3.10}$$

$$f_{V,\text{tree}}^{(p)} = \begin{cases} 2\,\lambda_V & \text{for coupling to } u_R \\ \lambda_V & \text{for coupling to } d_R \\ 3\,\lambda_V & \text{for coupling to } (u_L, d_L) \end{cases} \quad \text{and} \quad f_{V,\text{tree}}^{(n)} = \begin{cases} \lambda_V & \text{for coupling to } u_R \\ 2\,\lambda_V & \text{for coupling to } d_R \\ 3\,\lambda_V & \text{for coupling to } (u_L, d_L) \end{cases} . \tag{3.11}$$

On the other hand, the axialvector current is not conserved, and consequently the corresponding nucleon matrix elements are not perturbatively calculable. Following [92], we parametrize them in the form

$$\langle N|\bar{q}\gamma_\mu\gamma^5 q|N\rangle = 2 s_\mu^{(N)} \Delta_q^{(N)} , \tag{3.12}$$

where $s_\mu^{(N)}$ is the spin of the nucleon, and $\Delta_q^{(N)}$ parametrizes the quark spin content of the nucleon N, which can be estimated from lepton-nucleon scattering experiments. $\Delta_q^{(N)}$ turns out to be essentially zero for $q \in \{c, t, b\}$; for $q \in \{u, d, s\}$ we employ the numerical values given in [276]. From Eq. (3.12), it follows that the axialvector part of the dark matter-quark Lagrangian leads to a spin-dependent interaction. As the experimental sensitivity to spin-independent scattering is orders of magnitude better than to the spin-dependent one [102,103], the spin-dependent part of the scattering cross section is always subdominant in the simplified model of Dirac dark matter discussed in this section. Hence, we will disregard it in the rest of the discussion, while still taking it into account in our numerical analysis.

Besides the tree-level scattering, which is only relevant if dark matter couples to $f \in \{u, d\}$, the Yukawa interactions defined through Eqs. (3.4) or (3.5) necessarily lead to dark matter-nucleon scattering at the one-loop level via the penguin diagrams depicted in panels (b) and (c) of Fig. 3.1, regardless of the choice of the Standard Model fermion f. In particular, the exchange of a photon induces electromagnetic moments for the dark matter particle χ, which are described by means of an effective Lagrangian for dark matter-photon interactions:[2]

$$\mathcal{L}_{\text{eff},\gamma} = \frac{\mu_{\chi,\text{magn.}}}{2}\bar{\chi}\sigma^{\mu\nu}\chi F_{\mu\nu} + b_\chi \bar{\chi}\gamma^\mu\chi\partial^\nu F_{\mu\nu} , \tag{3.13}$$

with $\mu_{\chi,\text{magn.}}$ and b_χ being the dark matter magnetic dipole moment and charge radius, respectively. These electromagnetic moments are obtained by matching an explicit calculation of the relevant loop diagrams to the effective Lagrangian given by Eq. (3.13), working

[2] The photon exchange furthermore leads to an anapole moment of the dark matter particle, given by the effective operator $\bar{\chi}\gamma^\mu\gamma^5\chi\partial^\nu F_{\mu\nu}$. In the non-relativistic limit, this operator leads to a scattering cross section which is suppressed by the square of the dark matter velocity, and hence can be safely neglected with respect to the other electromagnetic moments. Nevertheless, we include it for completeness in our numerical calculations.

in the limit where the transferred momentum q^2 goes to zero. For dark matter coupling to a right-handed Standard Model fermion f_R, we obtain[3]

$$\mu_{\chi,\text{magn.}} = \frac{-Q_f e N_c y^2}{32\pi^2 m_\chi}\left[\frac{-\Delta+1-\mu-\epsilon}{\Delta^{1/2}}\operatorname{arctanh}\left(\frac{\Delta^{1/2}}{\mu+\epsilon-1}\right)+\frac{1}{2}(\epsilon-\mu)\log\left(\frac{\epsilon}{\mu}\right)-1\right], \tag{3.14}$$

$$\begin{aligned} b_\chi = \frac{-Q_f e N_c y^2}{384\pi^2 m_\chi^2}\Bigg[&\frac{2}{\Delta^{3/2}}\left(8\Delta^2+(9\mu+7\epsilon-5)\Delta-4\epsilon(3\mu+\epsilon-1)\right)\operatorname{arctanh}\left(\frac{\Delta^{1/2}}{\mu+\epsilon-1}\right) \\ &+(8\mu-8\epsilon+1)\log\left(\frac{\epsilon}{\mu}\right)+4\left(4+\frac{\mu+3\epsilon-1}{\Delta}\right)\Bigg]. \end{aligned} \tag{3.15}$$

In these expressions, Q_f is the charge of the fermion f_R in units of $|e|$, N_c is a color factor given by 3 (1) for coupling to quarks (leptons), and Δ is defined through

$$\Delta \equiv \mu^2+(\epsilon-1)^2-2\mu(\epsilon+1)\,, \tag{3.16}$$

with $\mu = m_\eta^2/m_\chi^2$ and $\epsilon = m_f^2/m_\chi^2$. Furthermore, if dark matter couples to a left-handed Standard Model fermion doublet via Eq. (3.5), $\mu_{\chi,\text{magn.}}$ and b_χ are given by the sum of the corresponding expressions for both components of the doublet.

By taking the limit $\epsilon \to 0$ in Eq. (3.15), one realizes that the charge radius b_χ suffers from an infrared logarithmic divergence $\propto \log\left(m_f^2/m_\eta^2\right)$ in the limit of small fermion masses, questioning the validity of our fixed-order calculation. However, in that context it is important to note that Eq. (3.15) has been derived in the limit of vanishing momentum transfer, which is an invalid assumption if the momentum transfer is not the smallest energy scale in the process. Namely, for a scattering event off a xenon nucleus with a recoil energy $E_R \sim 10$ keV, the typical momentum transfer is given by $\sqrt{-q^2} \sim 50$ MeV, which is substantially larger than the fermion mass m_f, if dark matter couples to a first generation quark or to an electron. Hence, for these scenarios we replace m_f by 50 MeV in our numerical analysis, in order to cut-off the divergence at the relevant energy scale. Due to the logarithmic nature of the divergence, the precise value of the cut-off does not significantly affect our results.

Similar to the photon exchange described in the previous paragraph, χ can also interact with nucleons via penguin diagrams involving a Z boson, as shown in panel (b) of Fig. 3.1. Neglecting the subdominant spin-dependent contribution, this process leads to a vector interaction between dark matter and quarks $\propto \bar{\chi}\gamma^\mu\chi\,\bar{q}\gamma_\mu q$; using the nucleon matrix elements (3.9), we obtain the following effective dark matter-nucleon Lagrangian:

$$\mathcal{L}_{\text{eff},Z} = f_{V,Z}^{(N)}\,\bar{\chi}\gamma^\mu\chi\,\bar{N}\gamma_\mu N\,, \tag{3.17}$$

$$\text{with}\quad f_{V,Z}^{(p)} = \left(4s_W^2-1\right)\frac{G_F a_Z}{\sqrt{2}}\quad,\quad f_{V,Z}^{(n)} = \frac{G_F a_Z}{\sqrt{2}}\,. \tag{3.18}$$

Similar to the calculation of the electromagnetic moments, a_Z is obtained by matching the effective Lagrangian to an explicit loop calculation, with the result being

$$a_Z^{(f_R)} = \frac{T_3^f N_c y^2 \epsilon}{16\pi^2}\left[\frac{1}{2}\log\left(\frac{\epsilon}{\mu}\right)+\frac{1+\mu-\epsilon}{\Delta^{1/2}}\operatorname{arctanh}\left(\frac{\Delta^{1/2}}{\mu+\epsilon-1}\right)\right], \tag{3.19}$$

$$a_Z^{(u_L,d_L)} = -a_Z^{(u_R)} - a_Z^{(d_R)}\quad,\quad a_Z^{(\nu_L,e_L)} = -a_Z^{(e_R)}\,, \tag{3.20}$$

[3] We have employed FeynCalc [277] for parts of the calculation. Furthermore, we checked that our result numerically agrees with the semi-analytical expressions given in [265].

for dark matter coupling to a right-handed fermion f_R, a left-handed quark doublet (u_L, d_L) and a left-handed fermion doublet (ν_L, e_L), respectively, and with Δ given by Eq. (3.16). Notice that for $m_f \ll m_\chi$, the effective coupling of dark matter to the Z boson, parametrized by a_Z, scales as $(m_f/m_\chi)^2$. Hence, the contribution of the Z exchange to the total scattering cross section is strongly suppressed with respect to e.g. the contribution arising from photon exchange, except for the scenarios where χ couples to t_R or (t_L, b_L).

Furthermore, the dark matter particle can scatter off quarks via the exchange of the Standard Model Higgs h, shown by the one-loop diagram in panel (c) of Fig. 3.1, leading to a scalar interaction $\propto \bar{\chi}\chi\bar{q}q$. Analogously to Eqs. (3.9) and (3.12), one then has to evaluate the nucleon matrix elements of the scalar quark current $\bar{q}q$ [92]:

$$\langle N|\bar{q}q|N\rangle \equiv \frac{m_N}{m_q} f_q^{(N)}\,, \tag{3.21}$$

where the nuclear parameters $f_q^{(N)}$ can be estimated from chiral perturbation theory [278], pion-nucleon scattering [279] and lattice simulations [280]. For our purposes, the relevant quantity is the effective Higgs-nucleon coupling $f_N^{(0)}$, given by [281, 282]

$$f_N^{(0)} = \sum_q f_q = \frac{2}{9} + \frac{7}{9}\sum_{q=u,d,s} f_q \;\simeq\; 0.345\,. \tag{3.22}$$

With that, the effective dark matter-nucleon Lagrangian describing the Higgs exchange contribution can be written as

$$\mathcal{L}_{\text{eff,Higgs}} = f^{(N)}_{\text{S,Higgs}}\,\bar{\chi}\chi\,\bar{N}N\,, \tag{3.23}$$

where $f^{(N)}_{\text{S,Higgs}}$ is given by

$$f^{(N)}_{\text{S,Higgs}} = \frac{-\sqrt{2}G_F m_\chi m_N f_N^{(0)}}{m_h^2}\,\frac{3\epsilon}{32\pi^2\Delta^{1/2}}\left[\Delta^{1/2}\left(2+(\mu-\epsilon)\log\left(\frac{\epsilon}{\mu}\right)\right)+ 2\left(\epsilon^2+\mu\,(\mu-1)-\epsilon\,(1+2\mu)\right)\operatorname{arctanh}\left(\frac{\Delta^{1/2}}{\mu+\epsilon-1}\right)\right]. \tag{3.24}$$

As the Higgs couples to Standard Model fermions with a strength proportional to their mass, this contribution to the dark matter-nucleon Lagrangian is suppressed by $\epsilon = m_f^2/m_\chi^2$, making it clearly subdominant for scenarios in which the dark matter particle couples to a light Standard Model fermion. For dark matter coupling to a third-generation quark, we find that the contribution from Z exchange, given by Eq. (3.17), is always significantly larger than the one arising from Higgs exchange, rendering the latter irrelevant for all scenarios discussed in this work. Nevertheless, for completeness we include it in our numerical analysis. Furthermore, we notice that the effective dark matter-Higgs interaction would receive additional contributions from non-zero values of the quartic couplings λ_3 and λ_4, c.f. Eq. (3.6). However, we find that even when allowing for $\mathcal{O}(1)$ values of these couplings, the Higgs interaction is still subdominant compared to the scattering induced by the exchange of the Z boson.

Finally, if the dark matter couples at tree level to a quark, one-loop box diagrams such as the one shown in panel (d) of Fig. 3.1 induce an effective coupling of χ to gluons, which

in turn leads to an effective scalar interaction of the dark matter particle to nucleons, given by

$$\mathcal{L}_{\text{eff,gluon}} = f^{(\text{N})}_{S,\text{gluon}} \bar{\chi}\chi\bar{N}N \,. \tag{3.25}$$

The effective coupling $f^{(\text{N})}_{S,\text{gluon}}$ has been studied in detail for a simplified model in which the Dirac dark matter particle χ studied in this section is replaced by a Majorana fermion [271–273]. In particular, it has been shown in [273] that only the heavy quarks c, b and t contribute to the effective dark matter-gluon coupling, as the box-diagrams containing light quarks are already included in the non-perturbative matrix elements $f_q^{(N)}$, c.f. Eq. (3.21). By inspecting all relevant diagrams, we find that $f^{(\text{N})}_{S,\text{gluon}}$ is exactly the same for Majorana and for Dirac dark matter, and we refer to [273] for the full expression of the effective coupling.

3.3. Event rate for dark matter-nucleus scattering and experimental limits

3.3.1. Scattering cross section and event rate

Starting from the effective Lagrangians describing the interaction of dark matter with nucleons and photons, given by Eqs. (3.8), (3.13), (3.17), (3.23) and (3.25), we now compute the scattering cross section of dark matter with a nucleus T. For elastic and non-relativistic scattering, it generally follows from

$$\frac{\mathrm{d}\sigma_T}{\mathrm{d}E_R} = \frac{1}{32\pi v^2 m_\chi^2 m_T} \left|\mathcal{M}_{\chi+\text{T}\to\chi+\text{T}}\right|^2 \,, \tag{3.26}$$

where m_T is the nucleus mass. Assuming coherent scattering off the individual constituents of the nucleus, the scattering amplitude $\mathcal{M}_{\chi+\text{T}\to\chi+\text{T}}$ is simply obtained by replacing the nucleon spinors N in the effective dark matter-nucleon Lagrangians presented in the previous section by a spinor describing the nucleus T. As the typical momentum transfer in a scattering event is of the same order as the inverse size of the nucleus, one additionally has to take into account the loss of coherence by means of an appropriate form factor. Finally, for scattering mediated by a photon, one has to decompose the nuclear current $\bar{T}\gamma^\mu T$ into a term describing the interaction of the photon with the charge Z of the nucleus, and a term taking into account the coupling to the nuclear magnetic dipole moment $\mu_{T,\text{magn.}}$, using the Gordon identity [283]. Including only the leading terms in an expansion in $1/E_R$ and $1/v^2$, we obtain:

$$\begin{aligned}\frac{\mathrm{d}\sigma_T}{\mathrm{d}E_R} =& \alpha_{\text{em}}\mu^2_{\chi,\text{magn.}} Z^2 \left(\frac{1}{E_R} - \frac{m_T}{2\mu_T^2 v^2}\right) \left[F_{\text{SI}}\left(E_R\right)\right]^2 \\ &+ \frac{\mu^2_{T,\text{magn.}}\mu^2_{\chi,\text{magn.}} m_T}{\pi v^2} \frac{J_T+1}{3J_T} \left[F_{\text{dipole}}\left(E_R\right)\right]^2 \\ &+ \frac{m_T}{2\pi v^2}\left(f^{(T)}\right)^2 \left[F_{\text{SI}}\left(E_R\right)\right]^2 \,,\end{aligned} \tag{3.27}$$

where J_T is the spin of the nucleus, μ_T is the dark matter-nucleus reduced mass, $F_{\text{SI}}(E_R)$ is the Helm form factor for spin-independent scattering given in [93], $F_{\text{dipole}}(E_R)$ is the form

factor for dipole-dipole scattering taken from [284], and $f^{(T)}$ is the effective scalar dark matter-nucleus coupling, defined as

$$f^{(T)} = Z\left(f^{(p)}_{S,\text{gluon}} + f^{(p)}_{V,\text{tree}} + f^{(p)}_{V,Z} - eb_\chi - \frac{e\mu_{\chi,\text{magn.}}}{2m_\chi}\right) + (A-Z)\left(f^{(n)}_{S,\text{gluon}} + f^{(n)}_{V,\text{tree}} + f^{(n)}_{V,Z}\right). \tag{3.28}$$

Finally, using Eq. (2.2), we convert the scattering cross section given by Eq. (3.27) into a differential event rate $\frac{\mathrm{d}R_T}{\mathrm{d}E_R}$ in a xenon experiment. Following the discussion in Sec. 1.2, we assume that the velocity distribution of dark matter is given by a Maxwell-Boltzmann distribution, as defined in Eq. (2.7), with parameters $v_0 = \sqrt{2/3}\sigma = 220$ km/s, $|\vec{v}_{\text{Earth}}| = 233$ km/s (neglecting the small time dependence, which is unimportant for the results discussed in this section), and $v_{\text{esc}} = 533$ km/s. Furthermore, we use $\rho_0 = 0.3\,\text{GeV/cm}^3$ for the local dark matter density. We then confront the expected event rate to the results of the LUX experiment [101], which has the strongest sensitivity to the model discussed in this section. To this end, we determine the total number of expected scattering events N_T in LUX for every point in the parameter space, by integrating the differential event rate $\frac{\mathrm{d}R_T}{\mathrm{d}E_R}$ over the relevant range of recoil energies, taking into account the exposure and efficiency of the detector. If N_T is larger than the 90% C.L. upper limit following from the non-observation of an excess in LUX, the corresponding set of model parameters is considered to be excluded. Details of our procedure of obtaining upper limits can be found in Appendix A[4].

Besides considering the results from LUX, we will also discuss to what extent the future xenon-based experiments XENON1T [129] and DARWIN [131] (c.f. Sec. 2.1.2) can further probe the parameter space of the Dirac dark matter model discussed in this section[5]. Following [136], we derive prospects for XENON1T by assuming that this experiment will be sensitive to scattering cross sections σ_p^{SI} which are a factor of 40 below the limits from LUX [101]; this translates into a rescaling of the upper limits on the Yukawa coupling y following from the LUX data by a factor of $40^{1/4} \simeq 2.5$. We only apply this procedure for sufficiently large dark matter masses, $m_{\text{DM}} \gtrsim 30$ GeV, as the prospected upper limit at smaller masses depends critically on details of the detector performance near threshold, which are not yet known for XENON1T. Analogously, we derive prospects for DARWIN by assuming a gain of sensitivity to the Yukawa coupling y by a factor of $1800^{1/4} \simeq 6.5$, corresponding to the most optimistic scenario in which the experiment will be able to probe cross section as small as $\simeq 10^{-48}\,\text{cm}^2$ [131]. As for XENON1T, we do not attempt to derive prospects for scenarios involving a low-mass dark matter particle.

Before presenting the existing and prospected limits on the model arising from LUX, XENON1T and DARWIN, we first discuss the relative importance of the different contributions to the scattering rate, which have been introduced in Sec. 3.2, and which are schematically shown in Fig. 3.1. To this end, we show in Figs. 3.2 and 3.3 which of these processes lead to the largest contribution to the total number of events N_T expected at LUX, and correspondingly also at XENON1T and DARWIN, for a given coupling scheme, dark matter mass m_χ and mediator mass m_η. The left panels of Fig. 3.2 correspond to the three

[4] It is important to remark that it is not possible to simply employ the limits on σ^p_{SI} published by the experimental collaboration for constraining the model discussed in this section: the scattering cross section given by Eq. (3.27) has a different dependence on the recoil energy E_R compared to the standard spin-independent case, c.f. Eq. (2.4), due to the long-range force induced by the magnetic dipole moment of dark matter.

[5] For simplicity, we assume that DARWIN will consist only of xenon, although liquid argon is also discussed as a possible target material.

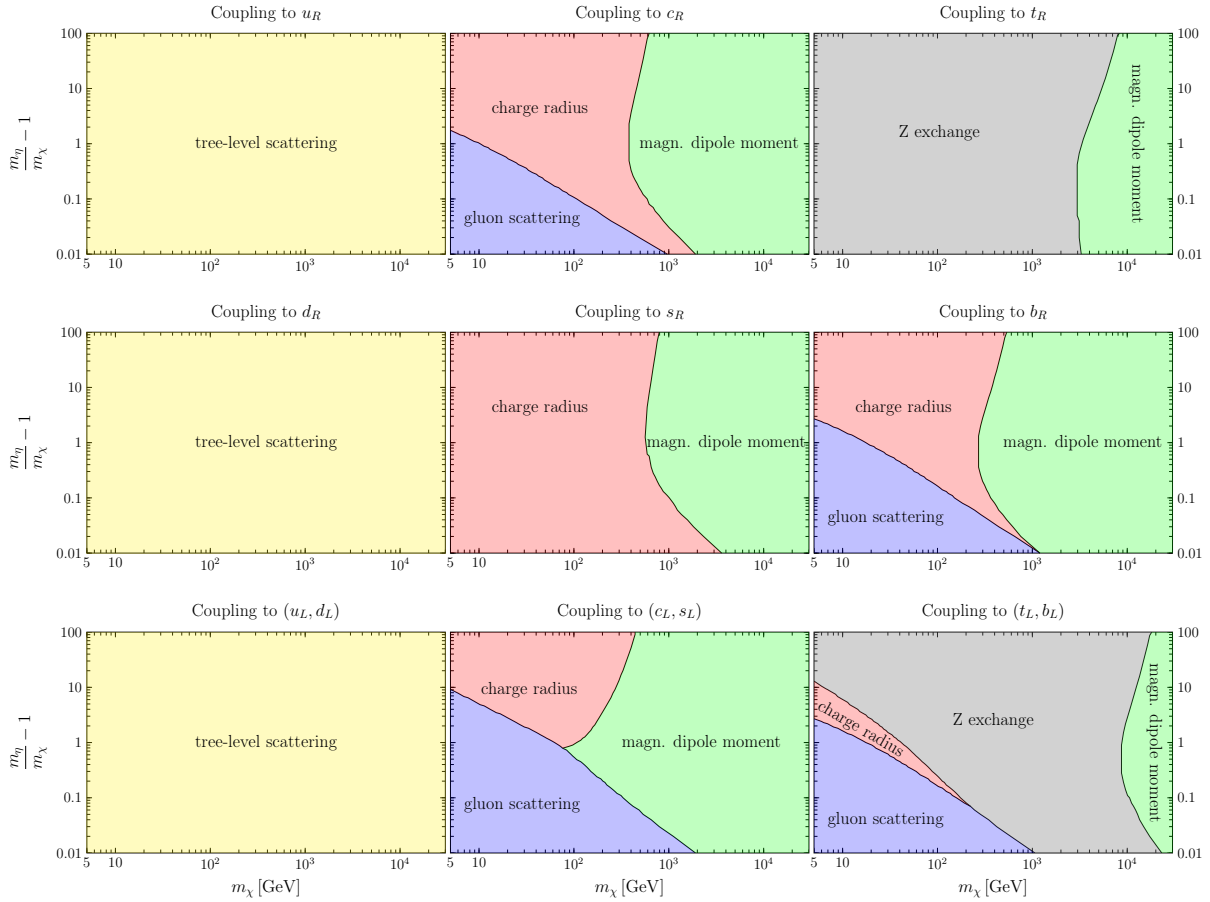

Figure 3.2.: Dominant contributions to the scattering rate of dark matter in LUX. *Upper panels:* coupling to right-handed up-type quarks. *Central panels:* coupling to right-handed down-type quarks. *Lower panels:* coupling to left-handed quark doublets.

cases of dark matter coupling at tree-level to first generation quarks (from top to bottom: u_R, d_R and (u_L, d_L)). As expected, in these scenarios the tree-level scattering shown in panel (a) of Fig. 3.1 dominates the event rate, rendering all one-loop processes irrelevant. However, as discussed in Sec. 3.2, the spin-independent scattering cross section induced by the vector interaction, Eq. (3.10), is identically zero for all other coupling schemes, and hence in all these scenarios the one-loop processes dominate the event rate.

In particular, for dark matter coupling to second generation quarks, b_R or any of the Standard Model leptons, it follows from the corresponding panels of Figs. 3.2 and 3.3 that for large parts of the parameter space, the most important process is the scattering via photon exchange. More precisely, for dark matter masses below $\simeq 1$ TeV, the contribution induced by the charge radius dominates, while for larger masses the magnetic dipole moment of dark matter is more important. This behavior can be understood from the dimensions of the effective operators appearing in Eq. (3.13): while the charge radius operator is of dimension six, the magnetic dipole moment already arises at dimension five, leading to the asymptotic behaviors $b_\chi \sim m_\chi^{-2}$ and $\mu_{\chi,\text{magn.}} \sim m_\chi^{-1}$, respectively. Consequently, for large dark matter masses, scattering via the magnetic dipole moment dominates over the charge radius of dark matter. Moreover, if the dark matter particle couples at tree-level to a charm,

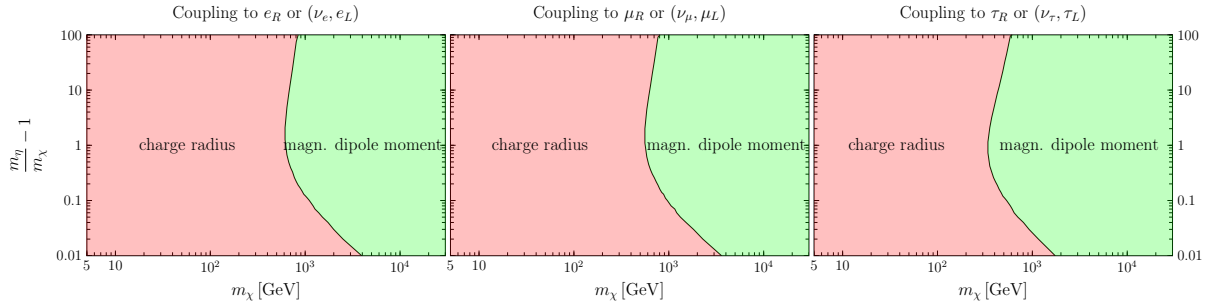

Figure 3.3.: Same as Fig. 3.2, for coupling to leptons.

top or bottom quark, also the one-loop coupling to gluons can contribute significantly to the scattering rate in some parts of the parameter space. In particular, for dark matter coupling to c_R, (c_L, s_L), b_R or (t_L, b_L), it is the dominant process for small dark masses and mass splittings m_η/m_χ.

Lastly, if dark matter couples to the top quark, corresponding to the coupling schemes t_R or (t_L, b_L) shown in the upper right and lower right panel of Fig. 3.2, it is the one-loop exchange of a Z boson which dominates the event rate in large parts of the parameter space. Following the discussion in Sec. 3.2, this is due to the fact that the effective coupling of dark matter to the Z boson, parametrized by a_Z, is suppressed by m_f^2/m_χ^2 in the limit $m_f \ll m_\chi$, c.f. Eqs. (3.19) and (3.20). For dark matter coupling to the top quark, this suppression is absent (or at least less severe), enlarging the corresponding contribution to the scattering rate with respect to all other scenarios.

3.3.2. Limits on the model from current and future experiments

In this section we finally determine, separately for each coupling scheme, the parts of the parameter space which are ruled out by the LUX experiment, as well as the regions that are within the reach of the future experiments XENON1T and DARWIN. As mentioned already at the end of Sec. 3.1, to this end we fix the Yukawa coupling y at each point of the parameter space to the value y_{thermal} leading to the observed relic density of dark matter. The result is shown in Fig. 3.4 for the various scenarios of dark matter coupling to quarks, and in Fig. 3.5 for coupling to leptons. In each case, the dark gray shaded regions are theoretically inaccessible, as for these dark matter and mediator masses the coannihilation processes discussed in Sec. 3.1 are effective enough to deplete the dark matter density below the observed value, irrespectively of the value of the Yukawa coupling y. Also the parts of the parameter space shown in light gray, corresponding to large dark matter and mediator masses are theoretically not viable, as they correspond to Yukawa couplings $y_{\text{thermal}} > \sqrt{4\pi}$, which we consider to be the maximal value of y compatible with a perturbative theory[6]. In particular, this condition limits the parameter space of the model to dark matter masses below $\simeq 20$ TeV (15 TeV), for coupling to quarks (leptons).

As expected, the direct detection constraints are most stringent for scenarios in which the dark matter particle couples at tree-level to first generation quarks, as shown in the left panels of Fig. 3.4, for coupling to right-handed up-quarks (top panel), right-handed down-quarks (central panel), and to the first generation left-handed quark doublet (lower

[6]This condition follows from the requirement that the expansion parameter $\alpha_y \equiv y^2/4\pi$ for higher-order processes is smaller than one.

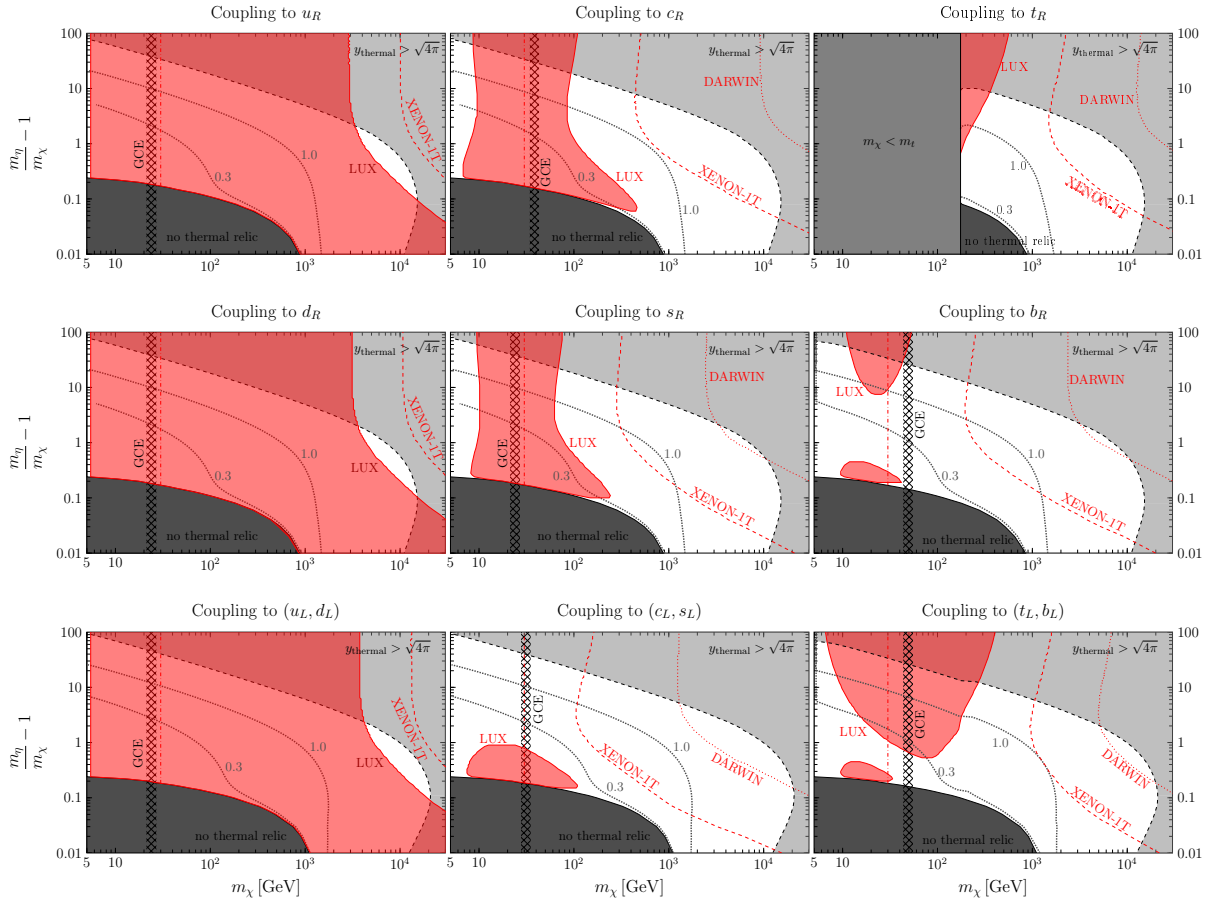

Figure 3.4.: Regions of the parameter space of the Dirac dark matter model which are excluded by the LUX experiment (red shaded regions, enclosed by red solid curves), or which are within the reach of XENON1T or DARWIN, shown as red dashed and red dotted curves, respectively. The upper (central) panels correspond to coupling to right-handed up-type quarks (right-handed down-type quarks), while the lower panels show the results for coupling to left-handed quark doublets. In all plots, the Yukawa coupling y is fixed to its thermal value $y_{\rm thermal}$, with the dotted black lines corresponding to $y_{\rm thermal} = 0.3$ and 1.0, respectively. The dark gray shaded regions in the lower left corners of each panel show the regions for which coannihilations suppress the dark matter relic density below the observed value, irrespectively of the value of y, making these parts of the corresponding parameter space theoretically inaccessible. Moreover, in the light gray shaded regions our perturbativity condition $y_{\rm thermal} < \sqrt{4\pi}$ is violated.

panel). As it can be seen from the plots, practically the whole thermal parameter space is excluded by LUX, and already XENON1T will completely close in on these scenarios. In particular, it is worthwhile mentioning that in this model, LUX is sensitive to dark matter masses up to tens of TeV. The enhanced sensitivity of direct detection experiments to these scenarios with respect to other dark matter models can be traced back to the unsuppressed vector interaction between dark matter and quarks given by Eq. (3.8); this is in contrast to e.g. the scalar singlet model, where the scattering proceeds via a scalar interaction $\propto \bar{\chi}\chi\bar{q}q$, which has a much smaller nuclear matrix element, leading to a less stronger upper limit $m_{\rm DM} \lesssim 100$ GeV arising from the LUX data [285].

On the other hand, as discussed in Sec. 3.2 and as shown in Fig. 3.2, for coupling to quarks of the second generation, the scattering proceeds dominantly via the dark matter electromagnetic moments, which are suppressed by a loop factor, and hence lead to considerably weaker constraints from LUX. This can be seen from the plots in the second column of Fig. 3.4 for dark matter coupling to c_R (top panel), s_R (central panel), and (c_L, s_L) (lower panel). Nevertheless, it is remarkable to notice that even though the scattering proceeds only at the one-loop level, LUX already excludes dark matter masses up to $\simeq 100-500$ GeV, with the precise value depending on the coupling scheme as well as on the mass splitting between η and χ [7]. Furthermore, there are excellent prospects that the next generation of direct detection experiments will further probe the parameter space of the model: as it follows from the plots, already XENON1T will be sensitive to dark matter masses of up to $\simeq 1$ TeV or more, and DARWIN could even cover practically the whole thermal parameter space compatible with the condition on perturbativity, despite the fact that all scattering processes only arise at the one-loop level.

Moreover, the right panels of Fig. 3.4 show the constraints on the parameter space for dark matter coupling to third-generation quarks. In the scenario where χ couples to the right-handed top quark, shown in the upper right panel, we restrict our analysis to $m_\chi > m_t \simeq 175$ GeV, as for smaller dark matter masses the tree-level annihilation process $\bar{\chi}\chi \to \bar{t}t$ is kinematically forbidden. While in principle it is also possible to have a thermal relic in that part of the parameter space, e.g. by means of one-loop induced annihilation processes such as $\bar{\chi}\chi \to gg$, this would substantially modify the phenomenology of the model and is beyond the scope of this work. We refer to [286] for an extensive discussion in that direction. The constraints on scenarios where dark matter couples to a top quark, i.e. either to t_R (upper right panel) or (t_L, b_L) (lower right panel) are dominated by the one-loop exchange of a Z boson, as shown in Fig. 3.2, or by the dark matter magnetic dipole moment for masses above $\simeq 3-20$ TeV. In these two scenarios, LUX excludes dark matter masses below $\lesssim 200-400$ GeV. On the other hand, the constraints are weaker in the case of coupling to b_R (central right panel of Fig. 3.4), as in this case the effective coupling of dark matter to the Z boson is suppressed by m_b^2/m_χ^2, as discussed above. However, in all cases in which dark matter couples to third-generation quarks, XENON1T and eventually DARWIN will probe large parts of the remaining parameter space; in particular, similar as for the scenarios with coupling to second-generation quarks, these experiments will be sensitive to dark matter masses well above the TeV scale.

Finally, Fig. 3.5 shows the results for the scenarios in which the dark matter particle couples at tree level to one of the Standard Model leptons. The dark and light gray shaded regions again show the theoretically inaccessible parameter space, as in Fig. 3.4. As it follows from the plots, the region of the parameter space for which no thermal relic exists due to efficient coannihilations is smaller for dark matter coupling to leptons than for coupling to quarks. This can be understood from the fact that for leptonic couplings, the coannihilation channels such as $\eta\eta^\dagger \to \gamma\gamma$ are induced by the electromagnetic coupling, while for colored mediators they are driven by QCD processes (e.g. $\eta\eta^\dagger \to gg$), leading to a stronger suppression of the cross sections in the former case. Besides, for the scenarios with coupling to leptons, the coannihilation process $\eta\eta^\dagger \to f\bar{f}$ with a Z boson exchanged in the s-channel is resonantly enhanced for $m_\chi \simeq m_\eta \simeq m_Z/2 \simeq 45$ GeV, which is clearly visible in the various panels of Fig. 3.5. As for coupling to the second- or third-generation quarks, also in these

[7] We notice that the sensitivity of direct detection experiments is enhanced for mass-degenerate scenarios, i.e. $m_\eta/m_\chi \simeq 1$, which is due to the parametric dependence of the charge radius of dark matter, $b_\chi \propto 1/((m_\eta/m_\chi)^2 - 1)$, c.f. Eq. (3.15).

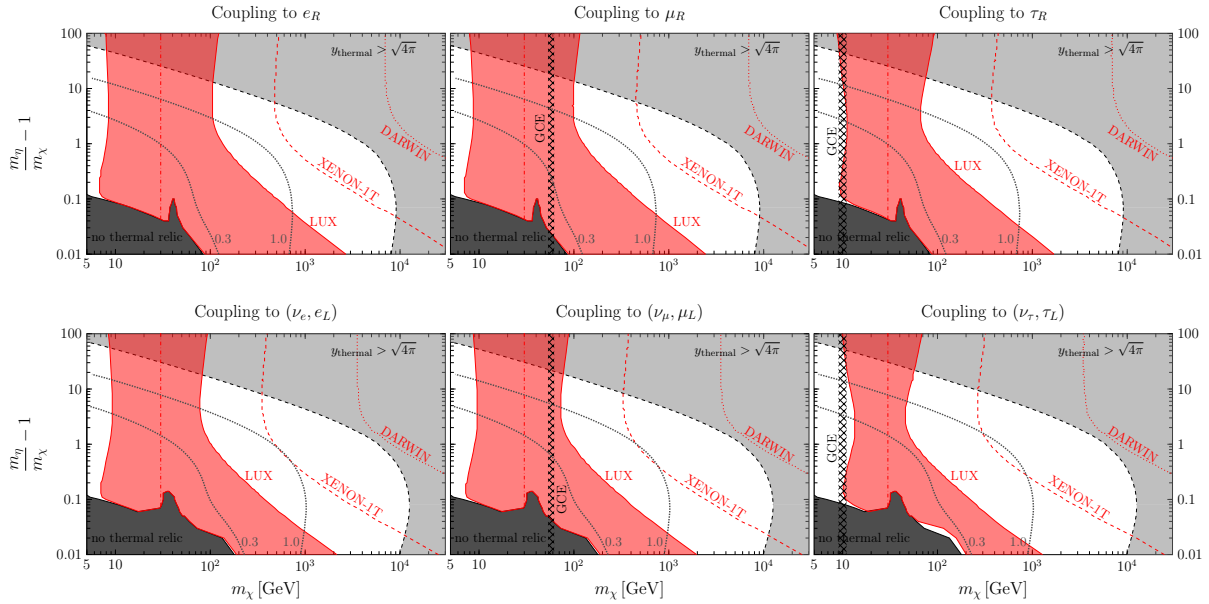

Figure 3.5.: Same as Fig. 3.4, but for dark matter coupling to right-handed charged leptons (upper panels) and to left-handed lepton doublets (lower panels).

scenarios the direct detection signal is induced only at the one-loop level, as discussed in Sec. 3.2 and shown in Fig. 3.3. We show the constraints from LUX, as well as the potential reach of XENON1T and DARWIN, for coupling to right-handed leptons (left-handed lepton doublets) in the upper (lower) panels, with each generation of leptons corresponding to one column of the Figure. As apparent from the plots, the range of masses which is excluded by LUX, or which will be probed by the future experiments, is very similar for the different scenarios involving coupling to leptons. For large mass splittings m_η/m_χ, LUX excludes dark matter masses between $8\,\text{GeV} \lesssim m_\chi \lesssim 100\,\text{GeV}$, while XENON1T (DARWIN) will probe the parameter space up to dark masses of $\simeq 500$ GeV (7 TeV). For smaller mass splittings, the experiments are even more sensitive, again due to the fact that the charge radius operator b_χ is parametrically enhanced in the limit $m_\eta/m_\chi \to 1$, c.f. the discussion in the previous paragraphs.

3.3.3. Complementary information from indirect detection and collider searches

In the previous section, we found that direct detection experiments have a remarkable sensitivity to the simplified model of Dirac dark matter, even in the cases where there is no tree-level coupling of χ to a light quark. However, as discussed in Sec. 2.1, direct searches are subject to astrophysical uncertainties, i.e. the local dark matter density as well as the local velocity distribution of dark matter particles. One possibility to handle this source of uncertainty is to use halo-independent methods for analyzing direct detection data, for which we refer to Sec. 8. Instead, in the rest of this section, we will qualitatively discuss complementary constraints on the model arising from indirect detection experiments and collider searches (see also the general introduction to these topics in Sec. 2.3 and 2.4), which are mostly sensitive to different systematic uncertainties, and hence can be used together with the direct detection constraints to robustly exclude parts of the parameter space.

To begin, for the case of dark matter coupling to quarks, the colored mediator η can

be pair-produced at the LHC, provided that it has a mass below a few TeV. Assuming furthermore that the absolute mass splitting between m_η and m_χ is larger than $\simeq 100$ GeV, the subsequent decays $\eta \to \chi q$ and $\bar{\eta} \to \bar{\chi}\bar{q}$ produce a characteristic signal consisting of two jets plus missing energy, which is a well-studied event topology in dark matter searches, e.g. in the context of simplified supersymmetric models [287–290]. On the other hand, when the mass difference is small, the jets are too soft in order to be observed at the LHC, and higher-order diagrams involving the additional emission of one or more hard jets is required for the visibility of the event. This strategy has been employed in monophoton [291] or monojet searches [292], which also can be used in parts of the parameter space where the colored mediator is too heavy to be kinematically accessible at the LHC, and in which one has to search for the pair-production of the dark matter particles themselves, accompanied e.g. by a hard jet, a photon or a W or Z boson [255, 256, 293]. While a full analysis of these signatures in the context of the Dirac dark matter model discussed in this section is beyond the scope of this work[8], a qualitative comparison with the works mentioned above suggests that present collider limits can constrain some regions of the parameter space with $m_\chi \lesssim 200$ GeV, with the details depending on the specific scenario. Besides the searches at the LHC, additional constraints arise from electroweak precision observables such as the Z boson decay width [294], which excludes the existence of charged scalar mediators with masses below $m_\eta \lesssim 40$ GeV.

On the other hand, in the scenarios in which the dark matter particle couples to leptons, the charged (but not colored) scalar mediator η can be pair-produced via the Drell-Yan process in colliders. The subsequent decay into the Standard Model lepton and the dark matter particle gives rise to a signature consisting of opposite-sign, same-flavor leptons, plus missing transverse momentum due to the escaping dark matter particle. Searches of this kind have been undertaken in the context of slepton searches (i.e. searches for the scalar partners of Standard Model leptons predicted by supersymmetric models), both at the LHC by the ATLAS [289] and CMS [290] collaborations, as well as at LEP II by the ALEPH, DELPHI, L3 and OPAL collaborations [295]. In [296], a compilation of the corresponding limits has been applied to the parameter space of a simplified model featuring a Majorana dark matter particle, which also couples to Standard Model leptons via a charged scalar mediator. In that work, it has been found that some regions of the parameter space with $m_\chi \lesssim 100$ GeV are excluded by collider searches; as the decay modes of the charged mediator in that simplified model are very similar to the ones appearing in the model discussed in this section, this is also a reasonable estimate for the sensitivity of collider searches to the scenarios discussed here.

Finally, we discuss the indirect detection signatures predicted by the simplified model of Dirac dark matter. The only relevant self-annihilation channel of dark matter, both during freeze-out as well as today, is the tree-level annihilation $\bar{\chi}\chi \to \bar{f}f$, where f is the Standard Model fermion coupling to the dark matter particle. Fixing the Yukawa coupling to the value imposed by the constraint on the relic density, the annihilation cross section of this process in the relevant astrophysical environments (e.g. in the Galactic center) is then simply given by the thermal value $\simeq 4.4 \cdot 10^{-26}\,\mathrm{cm}^3/\mathrm{s}$ (c.f. Sec. 1.3), except in regions of the parameter space where coannihilations are relevant, where the annihilation cross section is suppressed today. The predicted imprint of dark matter annihilations in cosmic rays then leads to significant constraints on the model. In particular, for all coupling schemes discussed in

[8] We note, however, that we will discuss in detail the collider constraints in a simplified model of real scalar dark matter in Sec. 4.4, using event topologies very similar to the ones mentioned above.

this section, the non-observation of an excess of gamma rays from the direction of dwarf galaxies excludes relevant parts of the parameter space: employing a recent analysis by the Fermi-LAT collaboration which is based on a stacked analysis of 15 dwarf spheroidal galaxies, dark matter masses below $\simeq 100$ GeV (80 GeV) are excluded for coupling to b_R (τ_R) [180]. For the other coupling schemes, the constraints are either of similar order or less stringent, e.g. for coupling to e_R, for which the Fermi-LAT data only excludes dark matter masses $m_\chi \lesssim 15$ GeV [180]. However, the latter scenario can be efficiently probed using AMS-02 data on the positron fraction [218, 224] or on the positron flux [225]. More specifically, as already introduced in Sec. 2.3.2, the annihilation of dark matter into e^+e^- pairs, and, to a lesser extent also the annihilation into $\mu^+\mu^-$ and into $\tau^+\tau^-$, would produce a sharp spectral feature in both the positron fraction as well as in the positron flux, for which there is no indication in the data. Using the limits derived in [243] based on the positron fraction, one can exclude $m_\chi \lesssim 120$ GeV for coupling to e_R, $m_\chi \lesssim 70$ GeV for coupling to μ_R, and $m_\chi \lesssim 30$ GeV for coupling to τ_R. Employing instead the more conservative limits from [244], which are based on the positron flux measurement, dark matter masses below 100 GeV (40 GeV) are excluded for coupling to e_R (μ_R).

Lastly, the model discussed in this section also gives rise to a diffuse gamma ray signal associated with the direction of the center of our Galaxy. Interestingly, as mentioned already in Sec. 2.3.1, various authors have claimed evidence for an excess of gamma rays in that region of the sky over the known astrophysical backgrounds [187–192]. The spectral shape of this signal can be well fitted by the gamma ray spectrum expected from dark matter annihilations, for a dark matter mass of $\simeq 10 - 100$ GeV, with the precise value depending on the annihilation channel [193]. Most remarkably, the overall normalization of the signal is compatible with a Dirac dark matter particle annihilating with a thermal cross section $\langle \sigma v \rangle \simeq 4.4 \cdot 10^{-26}\,\mathrm{cm}^3/\mathrm{s}$, once astrophysical uncertainties are taken into account [193]. Consequently, our simplified model of Dirac dark matter in principle provides an excellent particle physics framework to explain the Galactic center excess (GCE), for all possible coupling schemes discussed in this work, except for dark matter coupling to e_R or (ν_e, e_L), for which the corresponding gamma ray flux can not fit the observed spectrum. For all other coupling schemes, we show the mass ranges favored by the dark matter interpretation of the GCE in the corresponding panels of Figs. 3.4 and 3.5 as vertical hatched bands, using the results presented in [193]. As it can be seen from the plots, for dark matter coupling to first generation quarks, c_R, s_R or μ_R, the non-observation of an excess in LUX is in strong tension with the dark matter origin of the GCE. On the other hand, for the scenarios in which dark matter couples to (c_L, s_L), b_R, (t_L, b_L), τ_R or (ν_τ, τ_L), the dark matter interpretation of the GCE is still allowed by direct detection experiments, at least for some values of the mass splitting between η and χ.

4. Complementary searches in a model of real scalar dark matter

In the previous section, we have considered a simplified model consisting of a Dirac dark matter particle coupling to a Standard Model fermion via a scalar mediator. This scenario is part of the more general class of *t-channel simplified models*, i.e. models in which the dark matter particle can annihilate into Standard Model fermions via the exchange of a mediator in the t-channel. Within this class of simplified models, another viable possibility is a scenario featuring a scalar dark matter particle and a vector-like Dirac fermion serving as the mediator. In the following, we will discuss in detail the phenomenology of this model, focussing for definiteness on the case of a *real* scalar dark matter particle, coupling either to a right-handed Standard Model lepton, e_R, μ_R or τ_R, or to a light quark, u_R or d_R.

This section is organized as follows: in Sec. 4.1, after defining the model, we discuss the effect of *helicity suppression* in the annihilation of a dark matter pair into $f\bar{f}$, which turns out to have important consequences for the phenomenology of the model. In that context, we also introduce the higher-order effects which are relevant for the calculation of the total annihilation cross section of dark matter. Equipped with that, we present the calculation of the dark matter relic density within this scenario in Sec. 4.2. Afterwards, in Sec. 4.3 we investigate the phenomenology of the model for the case of dark matter coupling to a Standard Model lepton, with an emphasis on gamma-ray spectral features, while in Sec. 4.4 we consider the scenario in which the dark matter couples to a light Standard Model quark, focussing in particular on the direct detection and collider phenomenology.

4.1. General properties of the model

Definition of the model

In a similar fashion as in the previous section, we now extend the Standard Model by a real scalar S, which is a singlet under the Standard Model gauge group, as well as by a vector-like Dirac fermion ψ. In order to allow for a Yukawa interaction between S, ψ and a right-handed Standard Model fermion f_R, which we consider to be either a lepton or a light quark, the gauge quantum numbers of ψ are chosen to be identical to those of f_R. We again impose a $\mathbb{Z}_2$ symmetry, under which S and ψ are odd, while all Standard Model particles are even. Then, by assuming $m_\psi > m_S$, the scalar S is a stable dark matter candidate. We furthermore note that from a more fundamental perspective, this model can be understood as a simplified version of a scenario with large extra dimensions, see e.g. [297].

With this particle content of the model, the most general renormalizable Lagrangian can be written as

$$\mathcal{L} = \mathcal{L}_{\rm SM} + \mathcal{L}_S + \mathcal{L}_\psi + \mathcal{L}_{\rm int}^{\rm fermion} + \mathcal{L}_{\rm int}^{\rm scalar}\,, \tag{4.1}$$

which is similar to the Lagrangian given in Eq. (3.1) for the simplified Dirac dark matter model. In Eq. (4.1), $\mathcal{L}_{\rm SM}$ denotes the Standard Model Lagrangian, while $\mathcal{L}_S$ and $\mathcal{L}_\psi$ contain

the kinetic, mass and self-interaction terms for S and ψ, respectively:

$$\mathcal{L}_S = \frac{1}{2}\left(\partial_\mu \phi\right)^2 - \frac{1}{2} m_S^2 S^2 - \frac{\kappa}{4!} S^4 \quad , \quad \mathcal{L}_\psi = \bar{\psi}\left(i \not{D} - m_\psi\right)\psi \,. \tag{4.2}$$

The quartic coupling κ is irrelevant for the phenomenology of the model (as long as it does not lead to strong self-interactions of S), and hence will be ignored in the following. On the other hand, the interactions of dark matter with the Standard Model particles are induced by the Lagrangians

$$\mathcal{L}_{\text{int}}^{\text{fermion}} = -y\, S \bar{\psi} f_R \; + \text{h.c.} \tag{4.3}$$

$$\text{and} \quad \mathcal{L}_{\text{int}}^{\text{scalar}} = -\frac{\lambda}{2} S^2\, \Phi^\dagger \Phi \,. \tag{4.4}$$

Here, the first equation defines a Yukawa interaction between the dark matter particle S, the mediator ψ, and one right-handed Standard Model fermion f_R, analogously to Eq. (3.4). Note that in contrast to Sec. 3, here for simplicity we do not consider the case of coupling to left-handed Standard Model fermions. Furthermore, Eq. (4.4) describes the interaction of S to the Standard Model Higgs doublet Φ. Within the simplified models discussed in this work, the existence of this term, which leads to a tree-level interaction of dark matter with the Higgs boson, is unique to the scalar dark matter case: the corresponding operator $\bar{\psi}\psi\, \Phi^\dagger \Phi$ for the case of a fermionic dark matter particle ψ does not arise at the level of renormalizable interactions.

Broadly speaking, the parameter space of the model can be divided in two regions, one of them corresponding to the dominance of the "vector-like portal" given by Eq. (4.3) over the "Higgs-portal" defined through Eq. (4.4), and the other one vice versa. In particular, in the limit $y \to 0$, the model discussed in this section is identical to the *singlet scalar model* [298–301], which has already been discussed extensively in the literature [282,302–307]. Hence, in this work, we will mostly focus on the opposite limit, in which the scalar interaction given by Eq. (4.4) is subdominant compared to the Yukawa interaction, Eq. (4.3), a scenario which has partially been discussed in [8,88,265,297,308–312]. However, in Sec. 4.3, we also discuss to some extent the phenomenology of the model when both y and λ are significantly different from zero.

Helicity suppression and higher-order annihilations

Assuming a vanishing Higgs portal interaction, i.e. setting $\lambda \equiv 0$ in Eq. (4.4), the lowest-order dark matter annihilation channel is $SS \to f\bar{f}$, proceeding via the Yukawa interaction defined through Eq. (4.3). A straightforward calculation of the annihilation cross section for this process yields

$$(\sigma v)_{f\bar{f}} \simeq \frac{N_c\, y^4}{4\pi m_S^2 (1+r^2)^2} \left(\frac{m_f^2}{m_S^2} - \frac{2}{3} \frac{m_f^2 v^2 (1+2r^2)}{m_S^2 (1+r^2)^2} + \frac{v^4}{15\,(1+r^2)^2} \right) \underset{m_f/m_S \to 0}{\propto} v^4 \,, \tag{4.5}$$

with $N_c = 3\,(1)$ for coupling to quarks (leptons), $r \equiv m_\psi / m_S$, and keeping only the leading terms in an expansion in m_f/m_S and in the relative dark matter velocity v. Crucially, in the limit $m_f/m_S \to 0$, as it is relevant for dark matter coupling to leptons or light quarks, the annihilation cross section is suppressed by the fourth power of the dark matter velocity [88, 311]. In other words, in the expansion of σv introduced in Eq. (1.10) of Sec. 1.3, the first non-vanishing term corresponds to the d-wave part of the cross section. This peculiar

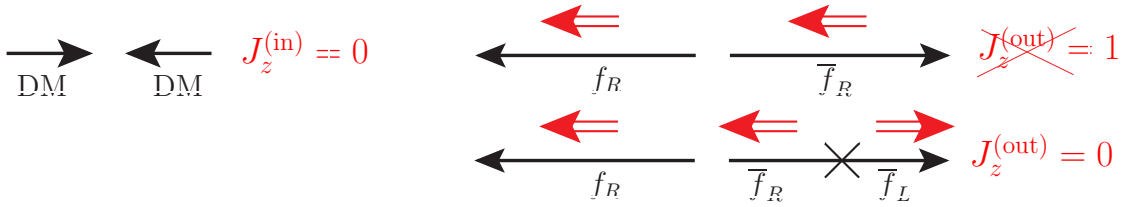

Figure 4.1.: Illustration of the helicity suppression of the annihilation cross section of real scalar or Majorana dark matter coupling chirally to a massless Standard Model fermion f_R.

behavior of the annihilation cross section has profound implications for the phenomenology of the model, which will be discussed in detail in the rest of this section.

However, first let us give a physical explanation for the suppression of the cross section by v^4 for the case of a massless Standard Model fermion f. The vanishing of the s-wave component a appearing the expansion $\sigma v = a + b\,v^2 + d\,v^4 + \mathcal{O}(v^6)$ can be understood from simple helicity arguments, illustrated in Fig. 4.1: the s-wave part of the cross section corresponds to an angular momentum $L^{(\mathrm{in})} = 0$ of the initial state, implying $J^{(\mathrm{in})} = 0$ for scalar dark matter. Moreover, by defining the z-axis to be the direction of motion of the outgoing fermions f and $\bar{f}$, and using the fact that the Yukawa interaction given by Eq. (4.3) only involves the right-handed fermion f_R as well as the left-handed antifermion $\bar{f}_R$, the only possible spin configuration in the limit $m_f = 0$ is given by $J_z^{(\mathrm{out})} = S_z^{(\mathrm{out})} = 1$, as shown in Fig. 4.1. Hence, by angular momentum conservation, the s-wave annihilation of dark matter is forbidden. A mass insertion flips the helicity of one of the fermions, explaining the scaling $a \propto m_f^2$ in Eq. (4.5). This *helicity suppression* of the annihilation cross section is also present for the annihilation of Majorana dark matter particles coupling chirally to a massless Standard Model fermion f_R: the argument above is equally valid, after realizing that in that case the implication $L^{(\mathrm{in})} = 0 \to J^{(\mathrm{in})} = 0$ follows from the Pauli exclusion principle for identical fermions, requiring a spin singlet initial state. On the other hand, for the Dirac dark matter scenario discussed in Sec. 3, the argument does not hold, and indeed, the annihilation cross section given by Eq. (3.7) is non-zero in the limit $v \to 0$ and $m_f \to 0$. In the case of real scalar dark matter (but not for Majorana dark matter, see Sec. 5), in addition also the p-wave contribution of the cross section is zero for $m_f = 0$, as it can be seen from Eq. (4.5). This can be understood from the fact that there is no bilinear current for real scalars transforming as a vector, and hence also the $L^{(\mathrm{in})} = 1$ state is forbidden by angular momentum conservation [88, 313].

The suppression of $SS \to f\bar{f}$ by the fourth power of the dark matter velocity naturally asks for the inclusion of higher-order processes, which are not necessarily d-wave suppressed, and thus can be relevant both for the calculation of the relic density, as well as for the indirect detection phenomenology. One way of lifting the helicity suppression is to emit an additional gauge boson[1] in the annihilation process, i.e. $SS \to f\bar{f}V$, with $V = \gamma, Z, g$, known as *virtual internal bremsstrahlung* (VIB) [204–206], for which one representative Feynman diagram is shown in the central panel of Fig. 4.2. While being suppressed by a gauge coupling as well as by the additional phase space required for the final state, this process features a non-vanishing s-wave component in the limit $m_f \to 0$. Besides this $2 \to 3$ process, the dark

[1] Also the additional emission of a Higgs boson can lift the helicity suppression [314]; however, due to the small Standard Model Yukawa couplings of the fermions discussed in this section, this process is irrelevant for our purposes.

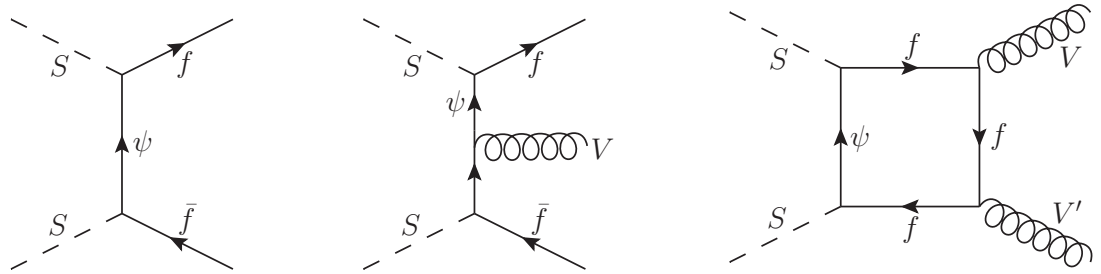

Figure 4.2.: Annihilation channels of the scalar dark matter particle S, with only one representative diagram shown for each process. In the limit $m_f \to 0$, the lowest order annihilation channel $SS \to f\bar{f}$, shown in the left panel, is d-wave suppressed, and the higher-order diagrams shown in the central and right panel can contribute significantly to the total annihilation cross section. See text for details.

matter particle S can annihilate via one-loop diagrams into a pair of gauge bosons V and V', as illustrated in the right panel of Fig. 4.2. Like VIB, this channel proceeds without helicity suppression, in that case at the price of two additional gauge couplings as well as a loop factor $\simeq 1/16\pi^2$. The analytical results for all relevant cross sections are provided in Appendix B.1; for large mass splittings $r \gg 1$ they are approximately given by

$$\begin{aligned}
(\sigma v)_{f\bar{f}g} &\simeq 1.6 \times 10^{-24}\,\mathrm{cm^3 s^{-1}} \frac{y^4}{r^8} \left(\frac{100\,\mathrm{GeV}}{m_S}\right)^2 \quad \text{(only for } f = q\text{)} \\
(\sigma v)_{f\bar{f}\gamma} \simeq 3.3 \cdot (\sigma v)_{f\bar{f}Z} &\simeq 3.0 \times 10^{-26}\,\mathrm{cm^3 s^{-1}} \frac{N_c Q_f^2 y^4}{r^8} \left(\frac{100\,\mathrm{GeV}}{m_S}\right)^2 \\
(\sigma v)_{gg} &\simeq 4.7 \times 10^{-26}\,\mathrm{cm^3 s^{-1}} \frac{y^4}{r^4} \left(\frac{100\,\mathrm{GeV}}{m_S}\right)^2 \quad \text{(only for } f = q\text{)} \\
(\sigma v)_{\gamma\gamma} \simeq 1.7 \cdot (\sigma v)_{\gamma Z} &\simeq 1.3 \times 10^{-28}\,\mathrm{cm^3 s^{-1}} \frac{N_c^2 Q_f^4 y^4}{r^4} \left(\frac{100\,\mathrm{GeV}}{m_S}\right)^2 ,
\end{aligned} \tag{4.6}$$

where for the final states involving a Z boson these results additionally assume $m_S \gg m_Z$. From Eq. (4.6) one can in particular infer that for $r \gg 1$, the VIB cross sections scale as $1/r^8$, while the one-loop annihilations into gauge bosons are proportional to $1/r^4$. Hence, the relative importance of the one-loop processes with respect to the $2 \to 3$ annihilations increases with the mass ratio of the mediator ψ and the dark matter particle S. A similar behavior arises in scenarios with a Majorana dark matter particle coupling to a Standard Model fermion via a charged scalar mediator, as we will discuss in more detail in Sec. 5.

4.2. Dark matter relic density

Perturbative analysis and Sommerfeld corrections to the coannihilation processes

In the following, we discuss the constraint on the real scalar dark matter model arising from the requirement that S accounts for all of the observed dark matter in the Universe. To this end, we take into account the processes induced by the Yukawa coupling shown in Fig 4.2; in addition, if the scalar coupling λ of the dark matter particle to the Higgs doublet, defined by

Eq. (4.4), is non-zero, also annihilation processes of the form $SS \to h \to XX'$ are possible, with X, X' being any Standard Model particles. Besides, similar to the discussion of the Dirac dark matter model in Sec. 3, for mass splittings $m_\psi/m_S \lesssim 1.5$ also the coannihilation processes $\psi\psi \to ff$, $\psi\bar{\psi} \to F\bar{F}$, $\psi\bar{\psi} \to VV'$, $\psi\bar{\psi} \to Zh$ as well as $S\psi \to fV$ can play a significant role in the calculation of the relic density, with V, V' and F being any Standard Model gauge boson and fermion, respectively.

As first noted by Sommerfeld [315], the non-relativistic annihilation of two particles which interact with each other via the exchange of a light or massless mediator can receive significant non-perturbative corrections, induced by the multiple exchange of the corresponding mediator. For our purposes, this is most relevant for the coannihilation processes involving the colored initial states $\psi\psi$, $\psi\bar{\psi}$ or $\bar{\psi}\bar{\psi}$ interacting via gluon exchange, as in contrast to the equivalent process including photons, the corresponding diagrams are only suppressed by the strong coupling, and not by the electromagnetic one. In the following, we briefly recapitulate the formalism of the Sommerfeld effect, following closely the method presented in [296, 316].

Similar as in Eq. (1.10), the perturbative annihilation cross section can be expanded as

$$\sigma_{\text{pert.}} = \frac{a}{v} + bv + \mathcal{O}(v^3)\,. \tag{4.7}$$

The presence of the Sommerfeld effect is taken into account by introducing an individual Sommerfeld factor S_l for each partial wave l [317, 318]:

$$\sigma_{\text{Somm.}} = S_0 \frac{a}{v} + S_1 bv + \mathcal{O}(v^3)\,, \quad \text{with} \tag{4.8}$$

$$S_0 = \frac{-2\pi\alpha/v}{1-\exp(2\pi\alpha/v)} \quad \text{and} \quad S_{l>0} = S_0 \times \prod_{k=1}^{l} \left(1 + \frac{\alpha^2}{v^2 k^2}\right)\,. \tag{4.9}$$

Here, v is the relative velocity between the two particles of the initial state, while α is the coupling strength of the effective abelian potential between the annihilating particles. The latter depends on the individual $SU(3)_c$ representations R and R' of the initial state particles, as well as on the $SU(3)_c$ representation Q of the coupled initial state, which in general is one of the irreducible components of $R \otimes R'$. Then, the interaction can be effectively described by the Coulomb-like potential [316]

$$V(r) = \frac{\alpha}{r} = \frac{\alpha_s}{r}\frac{1}{2}\left(C_Q - C_R - C_{R'}\right)\,, \tag{4.10}$$

where C_i is the quadratic Casimir invariant of the representation i, and α_s is the strong coupling constant evaluated at the energy scale $p = mv/2$. We are interested in the annihilations $\psi\psi$, $\psi\bar{\psi}$, $\bar{\psi}\bar{\psi}$, corresponding to either $\mathbf{3} \otimes \bar{\mathbf{3}} = \mathbf{1} \oplus \mathbf{8}$ or $\mathbf{3} \otimes \mathbf{3} = \mathbf{6} \oplus \bar{\mathbf{3}}$; the relevant Casimir invariants are given by $C_{\mathbf{1}} = 0, C_{\mathbf{3}} = C_{\bar{\mathbf{3}}} = 4/3, C_{\mathbf{6}} = 10/3$ and $C_{\mathbf{8}} = 3$. With that, the effective potentials read

$$V_{\mathbf{3}\otimes\bar{\mathbf{3}}} = \frac{\alpha_s}{r}\begin{cases} -\frac{4}{3} & (\mathbf{1}) \\ \frac{1}{6} & (\mathbf{8}) \end{cases} \qquad \text{and} \qquad V_{\mathbf{3}\otimes\mathbf{3}} = \frac{\alpha_s}{r}\begin{cases} -\frac{2}{3} & (\bar{\mathbf{3}}) \\ \frac{1}{3} & (\mathbf{6}) \end{cases}\,. \tag{4.11}$$

For the following discussion, we define $S_l^{(\mathbf{1})}$, $S_l^{(\mathbf{8})}$, $S_l^{(\bar{\mathbf{3}})}$, $S_l^{(\mathbf{6})}$ to be the Sommerfeld factors defined in Eq. (4.9), using the couplings $\alpha = \alpha_s \times \{-4/3, 1/6, -2/3, 1/3\}$ following from these potentials. Notice that Eq. (4.11) implies that depending on the initial color state, the Sommerfeld effect can either lead to an attractive or to a repulsive potential.

With the Sommerfeld factors S_l being calculated, we are left with determining the relative probabilities for the annihilation in a given color state, separately for every annihilation channel. For $\psi\bar{\psi} \to gg$, we obtain

$$S_l^{(gg)} = \frac{2}{7} S_l^{(\mathbf{1})} + \frac{5}{7} S_l^{(\mathbf{8})} \,, \tag{4.12}$$

as for this process the probability of annihilation in a singlet (octet) state is 2/7 (5/7), consistent with the results of [316][2]. Next, for the annihilation channel $\psi\psi \to qq$ induced by the Yukawa coupling of S to the quark q, the Sommerfeld factor is given by

$$S_l^{(qq)} = \frac{1}{3} S_l^{(\bar{\mathbf{3}})} + \frac{2}{3} S_l^{(\mathbf{6})} \,. \tag{4.13}$$

Moreover, the annihilations of $\psi\bar{\psi}$ into $\gamma g, Zg$ ($\gamma\gamma, \gamma Z, ZZ, WW, Zh$) proceed via a pure octet (singlet) state, a result that directly follows from color conservation. Hence, the corresponding Sommerfeld factors read

$$S_l^{(\gamma g, Zg)} = S_l^{(\mathbf{8})} \quad \text{and} \quad S_l^{(\gamma\gamma, \gamma Z, ZZ, WW, Zh)} = S_l^{(\mathbf{1})} \,. \tag{4.14}$$

Lastly, we take into account the coannihilation channel $\psi\bar{\psi} \to q\bar{q}$. If the final state quark q is *not* the fermion coupling to the dark matter particle via the Yukawa interaction defined in Eq. (4.3), the only contribution to the process is the s-channel exchange of a gluon. In that case, the initial color state is a pure octet. On the other hand, if the Yukawa coupling involves the final state quark q, the annihilation additionally receives a contribution from the exchange of the mediator ψ in the t-channel. In that case, the s- and t-channel processes interfere, and the initial state is a combination of singlet and octet representations. Hence, the total Sommerfeld factor can not be expressed in the concise form of Eqs. (4.12)-(4.14); in our numerical calculations, we decompose the squared matrix element in the parts corresponding to singlet and octet initial states, multiplying each contribution with $S_l^{(\mathbf{1})}$ and $S_l^{(\mathbf{8})}$, respectively.

Results of the relic density calculation

We calculate the relic density by employing the micrOMEGAs code [87] for the solution of the Boltzmann equation, thereby taking into account all of the (co)annihilation processes listed above[3], including the Sommerfeld corrections where applicable. Then, for a fixed value of λ, we determine the value $y = y_{\text{thermal}}$ of the Yukawa coupling leading to $\Omega_{\text{DM}} h^2 \simeq 0.12$ as required by the PLANCK data [32]. The result for y_{thermal} as a function of the dark matter mass is shown in the left panel (right panel) of Fig. 4.3 for dark matter coupling to a right-handed lepton (quark), adopting several different choices for the mass splitting $r = m_\psi / m_S$. For concreteness, here we assume $\lambda = 0$; setting $\lambda > 0$ leads to a decrease of y_{thermal} with respect to the values shown in the plots, which will be further discussed in Sec. 4.3. We also remark that due to the dominance of either the Yukawa interaction or the QCD processes in the (co)annihilation processes, y_{thermal} is identical for the scenarios of coupling to u_R and to d_R, up to sub-percent corrections arising from diagrams involving electromagnetic or weak couplings. Notice however that we fully include all these sub-leading effects in the numerical calculation.

[2] These probabilities, as well as the corresponding values for the other annihilation channels have been calculated in the limit $v \to 0$, and hence are strictly only applicable for $S_{l=0}$. However, we have checked that the error arising from using the same probabilities also for $S_{l>0}$ is negligible.

[3] For the higher-order processes, we only take into account the s-wave contribution to the total annihilation cross section.

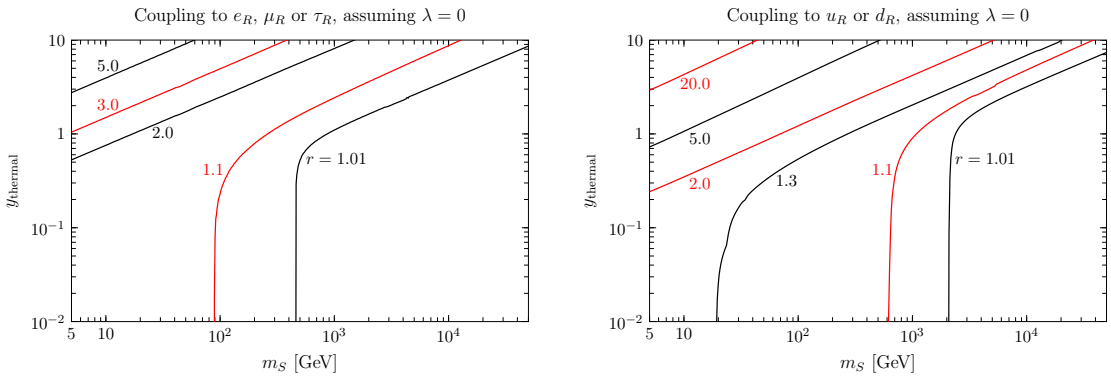

Figure 4.3.: Thermal value y_{thermal} of the Yukawa coupling entering Eq. (4.3), defined as the coupling leading to the observed relic density, as a function of the dark matter mass. The left panel corresponds to setting $f_R = e_R, \mu_R$ or τ_R in Eq. (4.3), while the right panel assumes coupling to a light quark, i.e. u_R or d_R. In both panels, each curve corresponds to a different value of the mass ratio m_ψ/m_S.

Generally speaking, one can infer from Fig. 4.3 that in the scenario discussed in this section, the values of the Yukawa coupling $y = y_{\text{thermal}}$ necessary for matching the observed relic density are quite large, compared to many other simplified models of WIMP dark matter. As discussed above, this can be traced back to the d-wave suppression of the lowest-order $2 \to 2$ annihilation channel, which is a specific feature of the real scalar dark matter model. This has important consequences for the phenomenology of the model, as large couplings in general lead to enhanced signal rates in direct, indirect and collider experiments, as it will be investigated in detail in the following sections. It is also important to note that several of the coannihilation channels, such as $\psi\bar{\psi} \to gg$, are purely driven by gauge interactions, and thus are independent of the Yukawa coupling y. In particular, if $r \lesssim 1.2$ (or $r \lesssim 1.4$ for the case of dark matter coupling to quarks), there is a lower limit on the dark matter mass below which these annihilation channels suppress the relic density to values smaller than the observed one, irrespectively of the choice of y, as it can be seen from Fig. 4.3.

By investigating the relative importance of the different contributions to the total annihilation cross section at freeze-out, we find that for the case of dark matter coupling to a Standard Model lepton, the VIB and one-loop processes introduced in Sec. 4.1 contribute up to $\simeq 10\%$ to the total annihilation cross section, with the remaining part given either by the d-wave suppressed channel $SS \to f\bar{f}$, or by the Higgs-mediated annihilations. Moreover, for dark matter coupling to a light Standard Model quark, we obtain the result that for $\lambda = 0$ the higher-order processes give a larger contribution to the total annihilation cross section than the annihilation into $q\bar{q}$, reinforcing the importance of including these additional annihilation channels in the computation of the relic density[4]. The difference between the cases of coupling to leptons and quarks can be understood from the fact that in the former case, the higher-order processes are suppressed by one or two powers of α_{em}, while for the

[4]Using a model-independent approach based on effective operators, the possibility that annihilations into gg dominate the dark matter freeze-out process has been previously considered in [319]. The model of real scalar dark matter coupling to a quark as discussed in this section provides an explicit realization of that scenario.

latter scenario the suppression by one or two powers of the strong coupling is less severe, c.f. Eq. (4.6). From this equation, we also infer that due to the different scaling of the VIB and one-loop cross sections with the mass ratio $r = m_\psi/m_S$, namely $(\sigma v)_{f\bar{f}V} \propto 1/r^8$ and $(\sigma v)_{VV'} \propto 1/r^4$, the $2 \to 3$ annihilations are more important for small mass splittings (concretely, $r \lesssim 2.5$), while the one-loop processes are relevant for larger values of r. Finally, we find that for the most degenerate scenario discussed in this work, $r = 1.01$, the Sommerfeld corrections lead to a change of the relic density of up to 15%; notice that this change can be in either direction, depending on the dark matter mass and the mass splitting, as it follows from the different signs of the effective couplings α for various initial color states, c.f. Eqs. (4.10) and (4.11).

4.3. Real scalar dark matter coupling to leptons

Based on the calculation of the dark matter relic density discussed in the previous section, we now investigate the detectability of the real scalar dark matter model for the case of coupling to a lepton e_R, μ_R or τ_R. In Sec. 4.3.1, we discuss the sharp gamma-ray features arising from the higher-order annihilation processes, while complementary constraints from other indirect searches, as well as from direct detection and collider experiments will be covered in Sec. 4.3.2. Taking together all of the relevant search strategies, we then identify the remaining viable regions of the parameter space of the model in Sec. 4.3.3, and also discuss the prospects to probe them with future experiments.

4.3.1. Sharp gamma-ray features from scalar dark matter annihilations

As discussed in Sec. 4.1, the annihilation of the real scalar dark matter candidate S can proceed both via the d-wave suppressed lowest-order process $SS \to f\bar{f}$, as well as by VIB and one-loop annihilations into gauge bosons. The typical velocity for the galactic dark matter population is $v \simeq 10^{-3}$ (c.f. Sec. 1.2); hence, the $2 \to 2$ process $SS \to f\bar{f}$ is completely negligible for dark matter annihilations in our Galaxy. Consequently, for dark matter coupling to leptons, the dominant annihilation channels are given by $SS \to f\bar{f}\gamma$, $SS \to f\bar{f}Z$, $SS \to \gamma\gamma$, $SS \to \gamma Z$ and $SS \to ZZ$.

The gamma-ray spectrum produced by these annihilations reads[5]

$$\frac{\mathrm{d}N_\gamma}{\mathrm{d}x} = \frac{1}{(\sigma v)_{\mathrm{total}}} \left[\frac{\mathrm{d}(\sigma v)_{f\bar{f}\gamma}}{\mathrm{d}x} + 2\frac{\mathrm{d}(\sigma v)_{\gamma\gamma}}{\mathrm{d}x} + \frac{\mathrm{d}(\sigma v)_{Z\gamma}}{\mathrm{d}x} \right], \tag{4.15}$$

with $x = E_\gamma/m_S$, and all relevant cross sections given in Appendix B.1. The rescaled gamma-ray spectrum $x^2\,\mathrm{d}N_\gamma/\,\mathrm{d}x$ is shown in Fig. 4.4 for several choices of the mass splitting $r = m_\psi/m_S$, assuming for concreteness $m_S = 500\,\mathrm{GeV}$ [6], and including a 10% gaussian energy resolution, as roughly appropriate for instruments like Fermi-LAT or H.E.S.S. As it can be seen from the plot, not only the annihilations into $\gamma\gamma$ and γZ, but also the VIB process $f\bar{f}\gamma$ can lead to a sharp gamma-ray spectral feature, which, as introduced in more detail in Sec. 2.3.1, allows for an efficient discrimination of the dark matter induced signal from the smooth astrophysical background. The sharpness of the VIB feature close to the

[5] For the purpose of the following discussion, we neglect the contribution arising from the decay and hadronization of the Z bosons produced in the annihilations of S, as these do not lead to a sharp feature in the gamma-ray spectrum.

[6] Notice that for $m_S \gg m_Z$, the gamma ray spectrum $\mathrm{d}N_\gamma/\,\mathrm{d}x$ is independent of m_S.

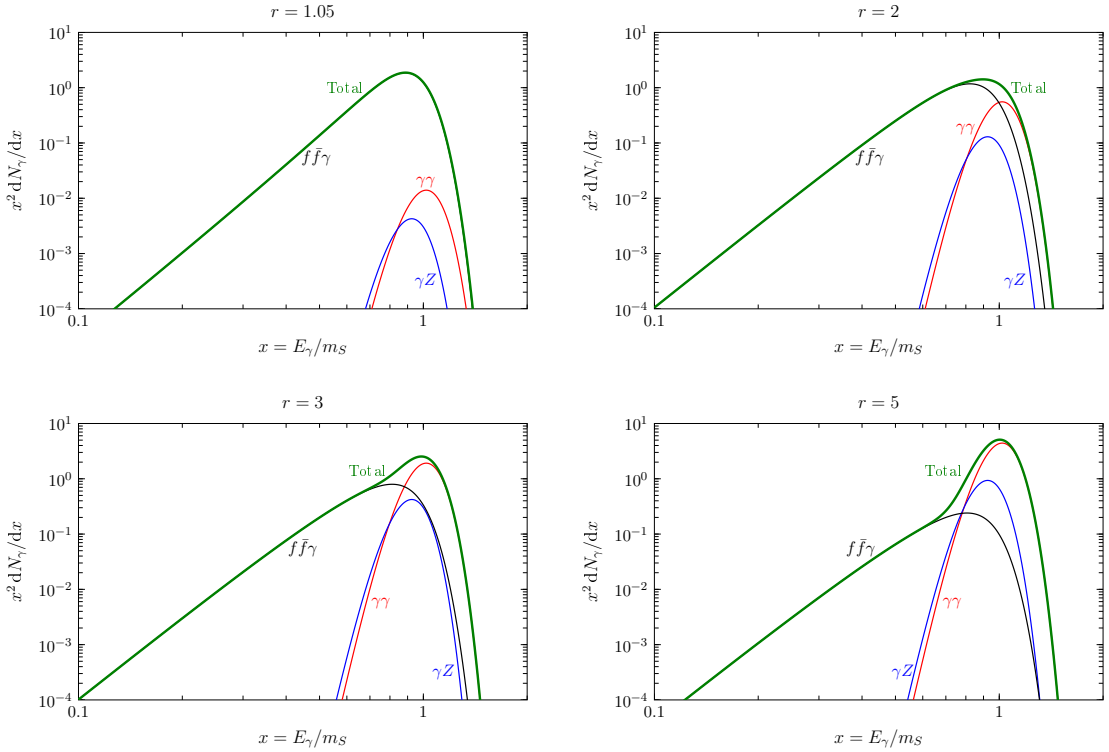

Figure 4.4.: Energy spectra of gamma rays produced in the annihilations of the real scalar dark matter particle into $f\bar{f}\gamma$ (black curves), $\gamma\gamma$ (red curves) and γZ (blue curves), for several different values of the mass splitting $r = m_\psi/m_S$. For concreteness, these spectra assume an energy resolution of 10%, as well as $m_S = 500\,\mathrm{GeV}$ (or, equivalently, any $m_S \gg m_Z$).

kinematical endpoint, $x = 1$, is most pronounced for small and intermediate mass splittings $r \lesssim 2$, while for larger values of r the spectrum becomes softer, analogously to the well-known case of Majorana dark matter annihilating into $f\bar{f}\gamma$ [206]. It also follows from the plot that for an energy resolution of 10%, experiments can not distinguish between the spectra of the different annihilation channels; this might change with the next generation of gamma-ray telescopes, such as GAMMA-400 [320] and DAMPE [174], which are expected to reach an energy resolution of $\simeq 1\%$ at $E_\gamma > 10\,\mathrm{GeV}$.

Furthermore, Fig. 4.4 implies that depending on the mass splitting r, either the VIB process or the one-loop annihilations into gauge bosons can dominate the total gamma-ray spectrum at large x. The relative importance of the three processes leading to a sharp gamma-ray feature is further investigated in Fig. 4.5, again assuming $m_S = 500\,\mathrm{GeV}$. For $r = 1$, the cross section for $SS \to f\bar{f}\gamma$ is $1.6 \cdot 10^3$ ($2.9 \cdot 10^3$) times larger than for the annihilation into $\gamma\gamma$ (γZ). Increasing r leads to a further decrease of $(\sigma v)_{\gamma\gamma}$ and $(\sigma v)_{\gamma Z}$, and eventually the amplitude for annihilation into $\gamma\gamma$ changes sign at $r - 1 \simeq 4.0 \cdot 10^{-3}$, leading to a vanishing of the cross section at that value of the mass splitting. For $r \gg 1$, the relative importance of the one-loop annihilations increases again, and dominates the total cross section for $r \gtrsim 3$ (c.f. also Eq. (4.6) for the asymptotic behavior of the cross sections at large mass splittings).

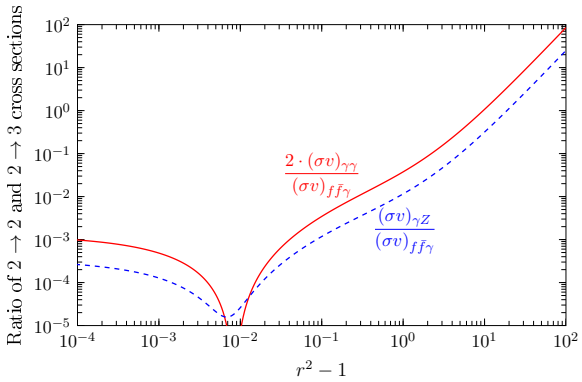

Figure 4.5.: Ratio between the cross sections for the one-loop induced annihilations into gauge bosons and the VIB process $SS \to f\bar{f}\gamma$, as a function of $r^2 - 1$. For the ratio $(\sigma v)_{\gamma Z}/(\sigma v)_{f\bar{f}\gamma}$, this assumes $m_S = 500\,\text{GeV}$; however, notice that this curve is independent of m_S in the limit $m_S \gg m_Z$.

Fixing $y = y_{\text{thermal}}$ (and $\lambda = 0$) by means of the discussion in Sec. 4.2, the total cross sections for annihilations of dark matter into $f\bar{f}\gamma$ and $\gamma\gamma$ are shown in Fig. 4.6, for $r = 1.1\,(3)$ in the left (right) panel. As introduced in Sec. 2.3.1, several experiments have searched for the presence of a gamma-ray spectral feature on top of the smooth astrophysical background, most notably Fermi-LAT [322] and H.E.S.S. [211], employing a target region close to the Galactic center. Based on these results, upper limits on the combined annihilation cross section $(\sigma v)_{f\bar{f}\gamma} + 2(\sigma v)_{\gamma\gamma}$ have been derived in [321], for a simplified model of Majorana dark matter coupling to a scalar mediator and a right-handed Standard Model lepton f_R via a Yukawa coupling. As the gamma-ray spectrum induced by the VIB process (and, of course, by the one-loop annihilations) in the scenarios of Majorana and real scalar dark matter is identical up to a global rescaling factor, we adopt those limits for our analysis[7]. The corresponding upper limits on the cross sections are shown in Fig. 4.6, together with the prospected sensitivity for the future Cherenkov telescope array CTA [323], which we also take from [321].

From Fig. 4.6, it follows that already current experimental searches for sharp gamma-ray features are highly sensitive to the model of real scalar dark matter coupling to a Standard Model lepton, and in fact exclude significant parts of the parameter space. This will be discussed in more detail in Sec. 4.3.3, where we compare the upper limits from Fermi-LAT and H.E.S.S. with complementary bounds from direct detection and collider searches. In Fig. 4.6, we also show the annihilation cross sections into $f\bar{f}\gamma$ and $\gamma\gamma$ for the analogous simplified model of Majorana dark matter, discussed in detail in [321], fixing again the Yukawa coupling y to the value implied by the relic density constraint. Clearly, the expected cross sections are considerably smaller than for the case of real scalar dark matter, and are out of the reach of current and future gamma-ray instruments, unless fairly large boost factors are adopted [321]. The reason for the difference between the scenarios involving a

[7] Strictly speaking, adopting these limits for our scenario of real scalar dark matter is only valid if either the VIB process *or* the annihilation into $\gamma\gamma$ dominates the high-energy gamma-ray spectrum. In principle, this assumption is not fulfilled for intermediate values of the mass splitting r, where both processes contribute with comparable strength, c.f. Fig. 4.4. However, due to the only mild dependence of the upper limits on (σv) on the mass splitting r [321], we estimate that this level of approximation changes the actual upper limits for the real scalar dark matter model by at most a factor of two.

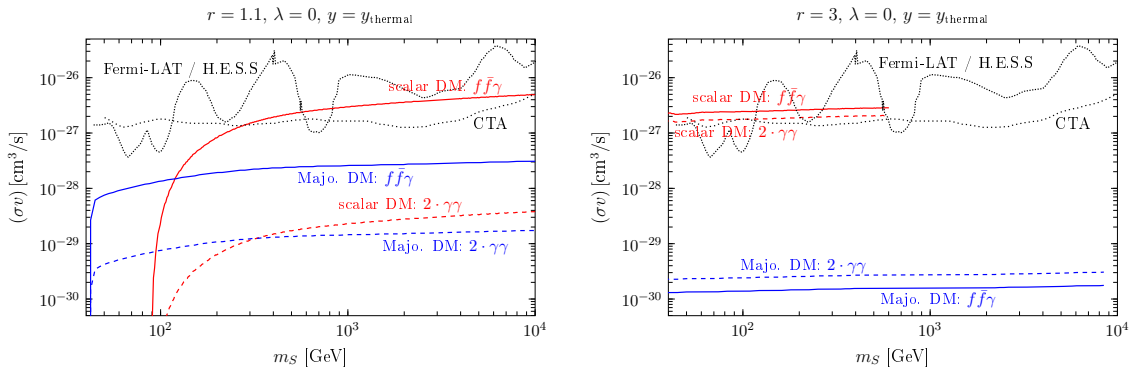

Figure 4.6.: Cross sections (σv) for dark matter annihilations into $f\bar{f}\gamma$ (solid curves) and $\gamma\gamma$ (dashed curves), for the simplified model of real scalar dark matter (red curves) and Majorana dark matter (blue curves). In each case, for a given dark matter mass m_S, the Yukawa coupling y is fixed to the value $y_{\rm thermal}$ implied by the constraint on the relic density, following the discussion in Sec. 4.2. All lines are only shown for the cases corresponding to $y_{\rm thermal} < 4\pi$, as required by our perturbativity condition, c.f. Sec. 4.3.2. Furthermore, the black dashed line shows the upper limit on $(\sigma v)_{f\bar{f}\gamma} + 2(\sigma v)_{\gamma\gamma}$ deduced from Fermi-LAT and H.E.S.S. data, as derived in [321], while the black dotted line depicts the reach of CTA.

real scalar and a Majorana dark matter particle is twofold: first, for fixed masses and a fixed value of y, the total cross section into $f\bar{f}\gamma$ is a factor of 8 larger for a real scalar dark matter particle compared to the case of Majorana dark matter [88]. Secondly, the annihilation of a pair of Majorana dark matter particles into $f\bar{f}$ is only p-wave suppressed, in contrast to the d-wave suppression implied by Eq. (4.5), leading to significantly enhanced values of $y_{\rm thermal}$ for the scenario of real scalar dark matter.

4.3.2. Complementary constraints

In addition to the gamma-ray spectral features discussed in the previous section, the model of real scalar dark matter coupling to a lepton can also be probed by means of other indirect detection techniques as well as by direct detection and collider experiments, and it is furthermore subject to theoretical restrictions such as perturbativity. In the following, we discuss each of the constraints resulting from these considerations individually, before investigating their complementarity with the gamma-ray searches in Sec. 4.3.3.

Perturbativity

As we have seen in Sec. 4.2, the constraint from the relic density of dark matter typically implies rather large values of the Yukawa coupling $y_{\rm thermal}$. On the other hand, perturbativity of the model leads to an upper bound on this coupling, for which we will mainly use the common and conservative condition $y_{\rm thermal} < 4\pi$. However, in Sec. 4.3.3, we will also present our results employing a more stringent upper limit on the size of the coupling, given by $y_{\rm thermal} < \sqrt{4\pi}$, motivated by the observation that the perturbative calculations of the annihilation and scattering cross sections are based on an expansion in $\alpha_y \equiv y^2/(4\pi)$. Notice that by assumption, for the scalar coupling λ we anyway only consider values $\ll 1$,

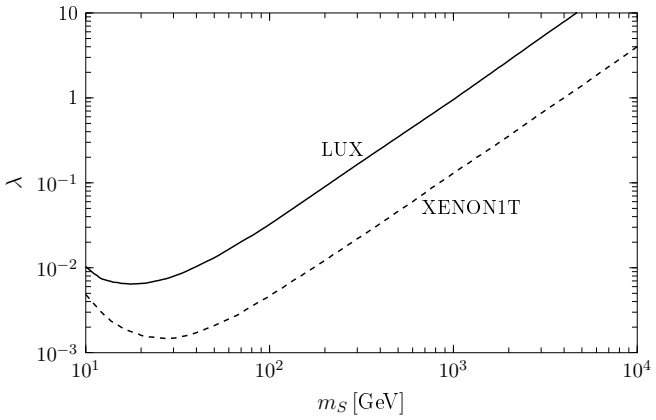

Figure 4.7.: Upper limit on the scalar coupling λ following from the LUX data [101] (solid line), as well as the projected reach of XENON1T (dashed line).

compatible with perturbativity.

Direct detection

The rate for scatterings of the scalar dark matter particle off nucleons in principle receives two contributions: the first one is induced by the Yukawa coupling of S to the Standard Model fermion f defined in Eq. (4.3), while the second contribution arises from the scalar coupling λ given by Eq. (4.4). However, for the scenario of dark matter coupling to a Standard Model lepton as discussed in this section, the former appears only at the two-loop level [324], rendering it completely irrelevant for current and future direct detection experiments. On the other hand, a non-zero value of the scalar coupling λ induces the tree-level scattering of S off nucleons via the exchange of the Higgs boson in the t-channel, leading to the spin-independent cross section

$$\sigma_p^{\mathrm{SI}} = \frac{\lambda^2 \left(f_N^{(0)}\right)^2}{4\pi} \frac{\mu_N^2 m_N^2}{m_h^4 m_S^2}\,, \tag{4.16}$$

where $\mu_N = m_N m_S / (m_N + m_S)$ is the dark matter-nucleon reduced mass, $m_h \simeq 125\,\mathrm{GeV}$ is the Higgs mass, and $f_N^{(0)} \simeq 0.345$ is the effective Higgs-nucleon coupling defined in Eq. (3.22), with the numerical value taken from [282].

As introduced in Sec. 2.1.2, the strongest constraint on the spin-independent scattering cross section follows from the LUX experiment [101], leading to an upper limit on the scalar coupling λ via Eq. (4.16), which is independent of the values of y and m_ψ. This upper bound on λ is shown in Fig. 4.7 as a function of the dark matter mass[8], together with the projected reach of the XENON1T experiment. For the latter, we assume a gain in sensitivity by a factor of 100 with respect to the XENON100 results [104, 325].

[8] After the results of this study have been first published [8], the LUX collaboration has updated their limits on σ_p^{SI} [102]. However, the improvement is mainly relevant for dark matter masses below $\simeq 20\,\mathrm{GeV}$, which is not the focus of the discussion in this section; in particular, we confirmed that all of our qualitative results stay unchanged with the new limits.

Indirect detection using cosmic ray antimatter and the continuum gamma-ray spectrum

The annihilation of S not only produces sharp gamma-ray features as discussed in Sec. 4.3.1, but also contributes to the antimatter and continuum gamma-ray flux. Based on the general introduction to these indirect detection techniques given in Sec. 2.3, in the following we discuss the resulting constraints on the model of real scalar dark matter coupling to a Standard Model lepton. To this end, we will first consider the case of a vanishing scalar coupling λ, and subsequently discuss the impact of a non-zero value of this coupling on the cosmic ray fluxes.

To begin, the annihilations of dark matter into $f\bar{f}Z$, γZ and ZZ, which are present also for $\lambda = 0$, lead to the production of antiprotons via the decay and hadronization of the Z boson[9]. The cross section for $SS \to f\bar{f}Z$ is given in Eq. (B.3); the annihilations into gauge bosons are only relevant for mass splittings $r \gtrsim 3$ (c.f. Eq. (4.6)), for which the antiproton flux turns out to be too small to be observable. Hence, in the following we neglect the contribution of the one-loop annihilations to the production of antiprotons.

In order to obtain a prediction for the flux of antiprotons produced by the VIB of a Z boson, we first calculate the injected spectrum of antiprotons by employing CalcHEP [330, 331], interfaced with PYTHIA 8 [156]. After being produced by dark matter annihilations, antiprotons are subject to propagation effects in the Galaxy, as introduced in more detail in Sec. 2.3.2. Following that discussion, we employ the standard two-zone diffusion model, neglecting energy losses and reacceleration, and using the MIN, MED and MAX propagation parameters [234] for bracketing the propagation uncertainty in the final antiproton flux (see Sec. 2.3.2 as well as [329] for all relevant details). For definiteness, the Galactic dark matter distribution is assumed to follow a NFW profile as defined in Eq. (1.3); however, other profiles are known to yield very similar results for the antiproton flux [329]. Finally, we convert the interstellar antiproton flux to a top-of-atmosphere flux by including the effect of solar modulation, employing the force-field approximation [332] with $\Phi_F = 500\,\mathrm{MeV}$. The sum of the resulting exotic contribution to the $\bar{p}/p$ ratio and the expected spallation background (c.f. Sec. 2.3.2), which we take from [333], is then compared to the PAMELA $\bar{p}/p$ data [219] [10]. We derive upper limits on the normalization of the dark matter induced signal, and hence on the Yukawa coupling y, by means of a χ^2-test at 95% C.L. In Fig. 4.8, we show these upper bounds as a function of the dark matter mass for three different choices of the mass splitting r. In each panel, the three blue dashed lines depict (from top to bottom) the upper limits deduced from the PAMELA data for the MIN, MED and MAX propagation parameters. For comparison, the black solid line shows the Yukawa coupling y_{thermal} required by the constraint on the dark matter relic density, as discussed in Sec. 4.2. From these plots, it follows that even for the most optimistic propagation setup, the antiproton data is not able to constrain the model of real scalar dark matter coupling to leptons, at least for the choice $\lambda = 0$ used in the preceding discussion.

Furthermore, if the dark matter particle S couples to an electron via the Yukawa interaction given by Eq. (4.3), and if the mass splitting between S and ψ is small enough, i.e. $r \lesssim 2$, the annihilation processes $SS \to e^-e^+\gamma$ and $SS \to e^-e^+Z$ lead to a sharp feature in the positron spectrum towards the kinematical end point. As explained in more

[9] For the corresponding simplified model of Majorana dark matter, the associated phenomenology has been studied in detail in [326–329].

[10] For the purpose of this section, we do not employ the preliminary AMS-02 data on the $\bar{p}/p$ ratio [223]. This choice has a negligible impact on our results.

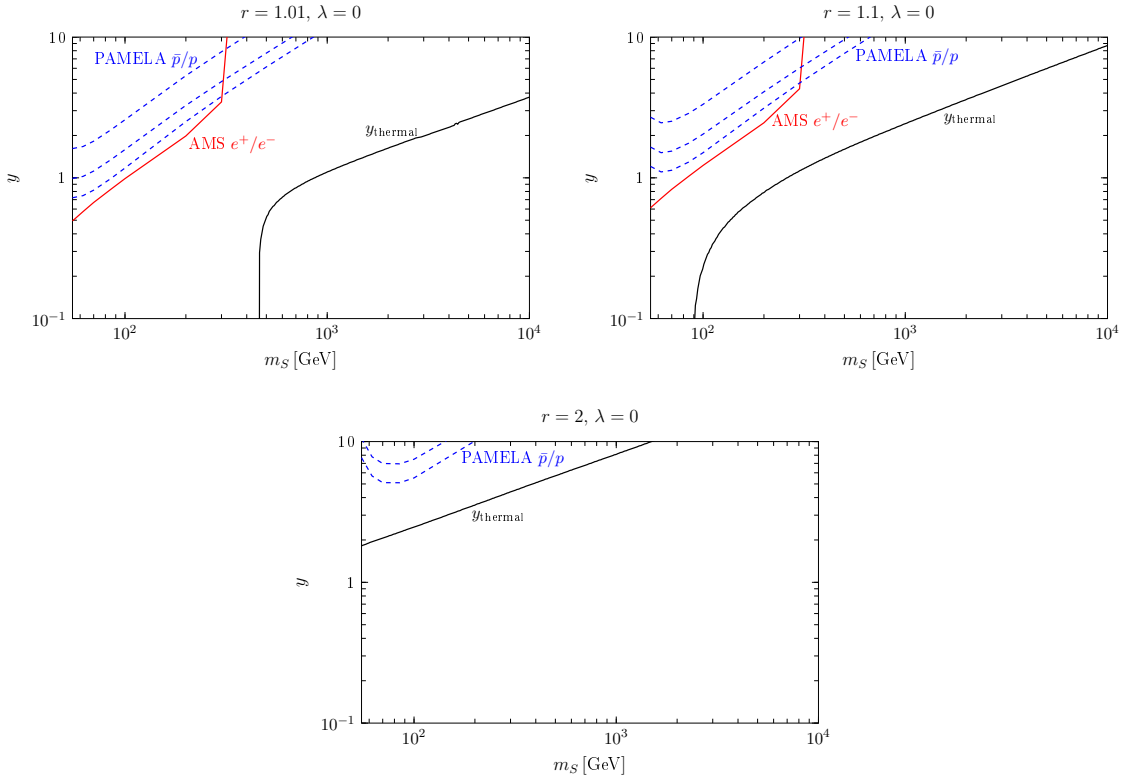

Figure 4.8.: 95% C.L. upper bounds on the Yukawa coupling y arising from searches for antimatter in cosmic rays, as a function of the dark matter mass m_S, for $r = 1.01, 1.1$ and 2 in the upper left, upper right and lower panel, respectively. The blue dashed curves show the upper limits derived from the PAMELA $\bar{p}/p$ data for three different sets of propagation parameters, while the red solid curves correspond to the non-observation of a sharp feature in the AMS-02 positron fraction, and are only applicable for dark matter coupling to electrons (see text for details). For comparison, the black solid line shows the value of the Yukawa coupling necessary for matching the observed relic density. In these plots, we assume $\lambda = 0$.

detail in Sec. 2.3.2, this allows for an efficient subtraction of the astrophysical background of positrons, similar to the search for gamma-ray spectral features. For the following discussion, we employ the limits on $(\sigma v)_{e^-e^+\gamma}$ derived in [243] from the AMS-02 data on the positron fraction [218], and convert them to upper limits on the Yukawa coupling y [11]. In [243], the limits arising from the positron fraction have only been derived for a mass splitting $r = 1$; up to mass ratios $r \lesssim 1.2$, we confirmed that the spectrum of positrons only changes marginally, allowing for the applicability of these constraints. The corresponding upper bounds on y are shown in Fig. 4.8 together with the $\bar{p}/p$ constraints, for the cases of $r = 1.01$ (upper left panel) and $r = 1.1$ (upper right panel). As apparent from these plots, also the positron data is not able to constrain the thermal values of the Yukawa coupling of the real scalar dark matter model.

So far, in the discussion of the indirect detection phenomenology of the model, we assumed a vanishing scalar coupling λ. For $\lambda > 0$, there are additional tree-level annihilation channels

[11] Notice that here we neglect the subdominant contribution from $SS \to e^-e^+Z$ to the positron spectrum.

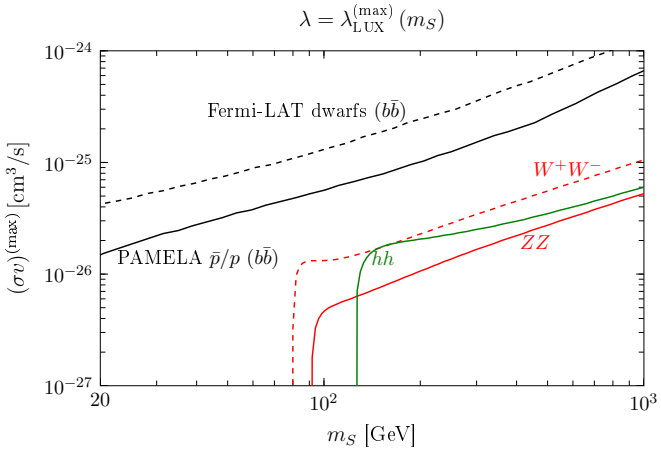

Figure 4.9.: Maximally allowed annihilation cross sections $(\sigma v)^{(\rm max)}$ into W^+W^- (red dashed line), ZZ (red solid line), and hh (green solid line), after imposing the upper limit on the scalar coupling λ deduced from the LUX data. The black solid and dashed curves show the upper limits on (σv) arising from the PAMELA measurement of the $\bar{p}/p$ ratio [232] and from the Fermi-LAT observations of dwarf galaxies [334], respectively.

mediated by the Standard Model Higgs boson in the s-channel, the most important ones being $SS \to W^+W^-$, $SS \to ZZ$ and $SS \to hh$. In the limit $v \to 0$, the corresponding annihilation cross sections are given by

$$
\begin{aligned}
(\sigma v)_{ZZ} &= \frac{\lambda^2 \left(4m_S^4 - 4m_S^2 m_Z^2 + 3m_Z^4\right)\sqrt{m_S^2 - m_Z^2}}{16\pi m_S^3 \left(m_h^2 - 4m_S^2\right)^2}\,, \\
(\sigma v)_{W^+W^-} &= \frac{\lambda^2 \left(4m_S^4 - 4m_S^2 m_W^2 + 3m_W^4\right)\sqrt{m_S^2 - m_W^2}}{8\pi m_S^3 \left(m_h^2 - 4m_S^2\right)^2}\,, \\
(\sigma v)_{hh} &= \frac{\sqrt{m_S^2 - m_h^2}}{16\pi m_S^3 \left(8m_S^4 - 6m_S^2 m_h^2 + m_h^4\right)^2}\,\lambda^2 \left(4m_S^4 + 4\lambda m_S^2 v_{\rm EW}^2 - m_h^2\left[m_h^2 + \lambda v_{\rm EW}^2\right]\right)^2 .
\end{aligned}
\tag{4.17}
$$

Here, $v_{\rm EW} = 246$ GeV is the vacuum expectation value of the Higgs field. These annihilation channels lead to an additional exotic source of antiprotons, and also contribute to the featureless gamma-ray spectrum. However, the upper limit on λ following from direct detection experiments severely constrains the magnitude of the antiproton and gamma-ray fluxes arising from these processes. This is illustrated in Fig. 4.9, which shows the maximally allowed annihilation cross sections $(\sigma v)^{(\rm max)}$ for the Higgs-mediated processes, fixing λ to the upper limit from LUX given in Fig. 4.7, separately for each dark matter mass. In Fig. 4.9, we also show the upper limits derived in [232] from the PAMELA data on the $\bar{p}/p$ ratio, as well as the Fermi-LAT bounds on the annihilation cross section deduced from the non-observation of a gamma-ray flux correlated with the direction of dwarf spheroidal galaxies [334] (c.f. the discussion in Sec. 2.3.1 for details). It follows from the plot that the LUX bounds are stronger than the indirect detection limits arising from PAMELA and Fermi-LAT, for all values of the dark matter mass. Note that for simplicity, the upper limits

shown in Fig. 4.9 assume annihilations of dark matter into $b\bar{b}$; however, the antiproton and gamma-ray constraints for the annihilation channels W^+W^-, ZZ and hh are expected to be very similar [232, 334], and thus our conclusion regarding the comparison of the direct and indirect detection limits is not affected by that approximation.

Collider constraints

We conclude this section by briefly commenting on the possibility to probe the real scalar dark matter model with coupling to leptons at colliders (see also the general introduction into searches for dark matter at colliders in Sec. 2.4). A full analysis of the corresponding constraints is beyond the scope of this work; notice however that for the case of dark matter coupling to quarks, we will present a dedicated study of the collider signatures in Sec. 4.4.2.

Here, we focus on the Drell-Yan production of a pair of heavy fermions, $\psi\bar{\psi}$, at the LHC. The subsequent decays into the dark matter particle S and the lepton f (or the antilepton $\bar{f}$) lead to a signature consisting of two oppositely charged, same-flavor lepton jets plus missing energy. This type of signal is very similar to the one appearing in the search for supersymmetric sleptons, i.e. charged scalar particles decaying into missing energy and a Standard Model lepton. However, the production cross section for ψ is about one order of magnitude larger than for the case of the sleptons [264], leading to more stringent constraints for the scenario discussed in this work. We estimate the production cross section for $pp \to \psi\bar{\psi}$ at leading order using CalcHEP [330,331], and confront it to the upper limits on the production cross section presented in [265], which are based on the ATLAS search [335] at $\sqrt{s} = 8\,\text{TeV}$, using an integrated luminosity of $20.3\,\text{fb}^{-1}$. Furthermore, we estimate a bound from the LEP experiment by reinterpreting a search for the right-handed selectron in the MSSM, undertaken at $\sqrt{s} = 183 - 208\,\text{GeV}$ [336]. We remark that this search is not exactly applicable to the scenario of real scalar dark matter discussed in this section, and hence is only meant to serve as an order-of-magnitude estimation.

The results of the estimation of the collider bounds will be presented in Fig. 4.10, together with the complementary information from direct and indirect searches.

4.3.3. Combined constraints on thermally produced dark matter

Finally, in this section we discuss which parts of the parameter space of the real scalar dark matter model coupling to a Standard Model lepton are excluded by the combination of the constraints presented in the previous sections. To this end, each panel of Fig. 4.10 shows the parameter space of the model spanned by the dark matter mass m_S and the mass splitting $r = m_\psi/m_S$, fixing the Yukawa coupling to the value y_{thermal} implied by the requirement of reproducing the observed relic density, separately at each point in the parameter space. The left panels correspond to existing constraints, while the right panels show the reach of future experiments (see the discussion below for details). Furthermore, in the upper panels we assume a vanishing scalar coupling λ, while the central and lower panels show our results for $\lambda = 0.03$ and 0.1, respectively.

The dark gray shaded regions in the upper right part of each plot correspond to values of the parameters not fulfilling our conservative perturbativity requirement, $y_{\text{thermal}} < 4\pi$, while the dotted black lines show the combination of masses leading to the more stringent condition $y_{\text{thermal}} = \sqrt{4\pi}$. Moreover, the light gray shaded regions appearing in particular in the lower left part of each panel are theoretically inaccessible, as for these choices of the parameters there is no value of y leading to the observed relic density. This can be either

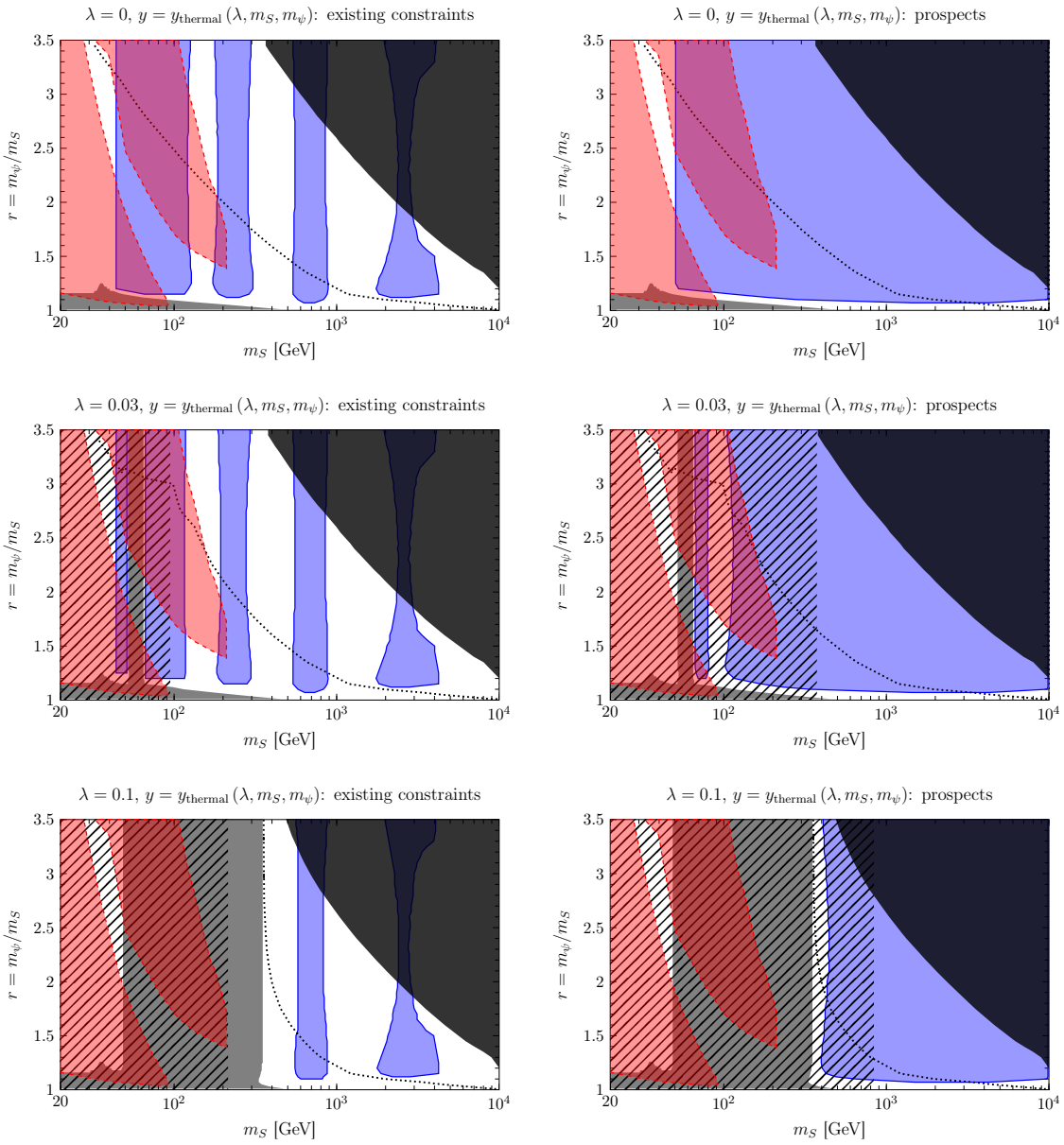

Figure 4.10.: Regions of the parameter space of real scalar dark matter coupling to a Standard Model lepton for $\lambda = 0$, 0.03 and 0.1 in the upper, central and lower panels, respectively, fixing at each point the Yukawa coupling to the value y_{thermal} implied by the relic density constraint. The blue shaded regions in the left panels show the constraints from Fermi-LAT and H.E.S.S., while in the right panels they show the reach of CTA. The constraints from collider searches are shown as red shaded regions. Furthermore, in the dark gray shaded regions one has $y_{\text{thermal}} > 4\pi$, while the black dotted lines correspond to $y_{\text{thermal}} = \sqrt{4\pi}$. Finally, the light gray shaded parts of the parameter space in the lower left corner of each panel, and in case of $\lambda > 0$ also in the nearly vertical strips, show the values of the parameters for which either the coannihilations or the Higgs-mediated annihilations suppress the relic density below the observed value, irrespectively of the value of y.

due to efficient coannihilations as discussed in Sec. 4.2 (see in particular Fig. 4.3), or because the Higgs-mediated annihilation channels are sufficiently strong to suppress the relic density below the observed value, independently of the value of y, leading to the nearly vertical light gray shaded strips in the central and lower panels of Fig. 4.10. In particular, even for small values of λ, the region of the parameter space around $m_S \simeq m_h/2 \simeq 63\,\text{GeV}$ is not compatible with the relic density requirement, due to the resonantly enhanced annihilation channels involving the Higgs particle in the s-channel.

In the case of a vanishing scalar coupling λ, corresponding to the upper panels of Fig. 4.10, the real scalar dark matter model is significantly constrained by the non-observation of gamma-ray spectral features, as discussed in detail in Sec. 4.3.1. In the upper left panel of Fig. 4.10, we show the parts of the parameter space which are excluded by the Fermi-LAT and H.E.S.S. searches as the blue shaded regions enclosed by the blue solid lines. It follows from the plot that these experiments already rule out large parts of the parameter space, and in particular, depending on the mass splitting r, can exclude dark matter masses up to $\simeq 4$ TeV. On the other hand, as discussed above, other indirect detection channels such as antiprotons or continuum gamma rays are not able to rule out the thermal values of the Yukawa coupling, and hence are not shown in the figure. However, the collider constraints introduced in Sec. 4.3.2 can probe some parts of the parameter space for $m_S \lesssim 200$ GeV, shown as the red shaded regions enclosed by the red dashed curves. In particular, it is worth noting that the indirect and collider searches are partially complementary, i.e. they exclude different regions in the parameter space. Furthermore, the blue shaded region in the right upper panel shows the reach of CTA, again following the discussion in Sec. 4.3.1. Remarkably, CTA has good prospects to completely close in on the whole parameter space of the model, and in particular it could probe dark matter masses up to $\simeq 10\,\text{TeV}$, which are inaccessible to present and near-future collider searches.

Finally, let us discuss the combined constraints on the model for a non-zero value of the scalar coupling λ, concretely for $\lambda = 0.03$ (0.1) in central (lower) panels of Fig. 4.10. The presence of new annihilation channels mediated by the Higgs boson leads to a smaller value of y_{thermal} compared to the case of $\lambda = 0$, and thus the intensity of the gamma-ray spectral features is expected to be smaller. This can be seen e.g. by comparing the upper right and central right panel of Fig. 4.10: increasing λ from 0 to 0.03 diminishes (slightly) the prospects to observe gamma-ray spectral features with CTA, in particular for $m_S \lesssim 100\,\text{GeV}$. Additionally, as discussed in Sec. 4.3.2, for $\lambda > 0$ there are stringent constraints on the scenario arising from direct detection experiments. The ranges of m_S and r which are excluded by LUX are shown as a hatched region in the central and lower left panels of Fig. 4.10, while the prospected reach of XENON1T is shown in the same way in the central and lower right panels. It follows from the corresponding plots in Fig. 4.10 that there is an interesting complementarity between the direct detection experiments, the gamma ray searches and the collider constraints: while LUX and the LHC mainly exclude regions of the parameter space with $m_S \lesssim 100 - 200$ GeV (depending on the precise value of λ), Fermi-LAT and H.E.S.S. can test the model for larger dark matter masses. We also observe that some regions of the parameter space are ruled out by *both* direct and indirect searches (and in some cases also by collider searches), which is interesting in view of the different systematical uncertainties inherent to these search strategies. Moreover, from Fig. 4.10 it follows that there are parts of the parameter space which are still allowed by current experiments, but which could be detected in the future both by XENON1T and CTA, e.g. the region around $\lambda = 0.03$ and $m_S \simeq 350\,\text{GeV}$.

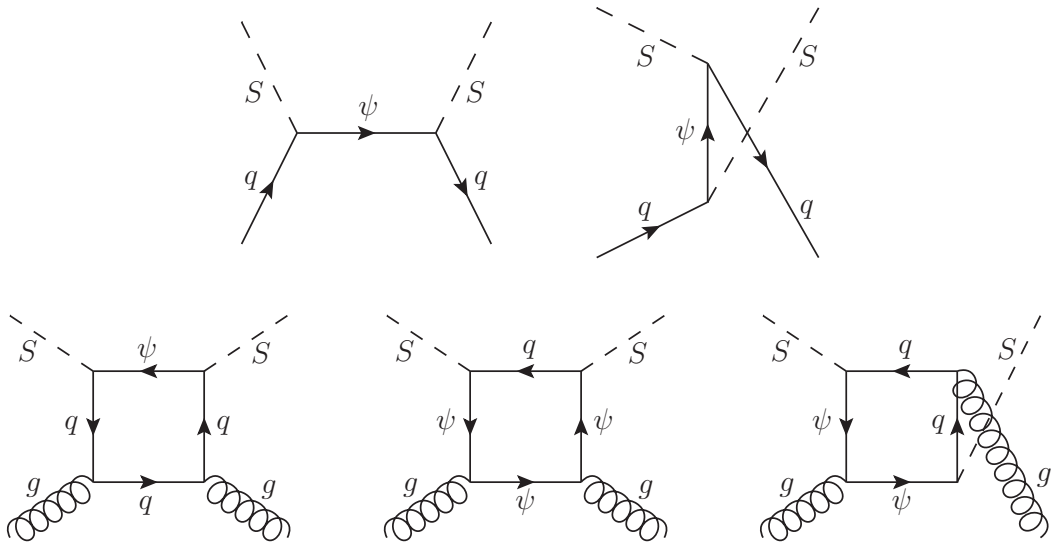

Figure 4.11.: Feynman diagrams visualizing the different contributions to the dark matter-nucleon scattering process, with q being either u or d. Additional diagrams corresponding to the crossing of initial or final state particles are not shown.

4.4. Real scalar dark matter coupling to a light quark

We now turn to the discussion of the phenomenology of the model of real scalar dark matter coupling to a light right-handed Standard Model quark, i.e. u_R or d_R. For simplicity, in this section we only discuss the case of a vanishing Higgs-portal interaction, i.e. we set $\lambda = 0$. The constraints arising from direct detection experiments are discussed in Sec. 4.4.1, while in Sec. 4.4.2 we confront the simplified model to an ATLAS search for multiple jets plus missing energy. Finally, we include constraints from indirect detection in Sec. 4.4.3, before taking together all relevant search strategies in order to determine the excluded regions in the parameter space of the model in Sec. 4.4.4.

4.4.1. Direct detection constraints

The dark matter particle S can scatter off nuclei via the Feynman diagrams shown in Fig. 4.11. In the upper row, we show the diagrams corresponding to the tree-level scattering off a light quark $q = u, d$, via the exchange of the fermionic mediator ψ in the s- or t-channel. After integrating out the mediator, as appropriate for the small momentum transfer relevant in direct detection experiments, the effective interaction of S with a light quark q is given by the sum of a scalar and a twist-2 contribution [271]:

$$\mathcal{L}_q = C_S^q \, m_q S^2 \bar{q} q \;+\; C_T^q \, (\partial_\mu S)(\partial_\nu S) \mathcal{O}^{\mu\nu}_{q,\text{twist-2}} \,, \tag{4.18}$$

$$\text{with} \quad \mathcal{O}^{\mu\nu}_{q,\text{twist-2}} \equiv \frac{i}{2} \left(\bar{q}\gamma^\mu \partial^\nu q + \bar{q}\gamma^\nu \partial^\mu q - \frac{g^{\mu\nu}}{2} \bar{q} \partial\!\!\!/ q \right) . \tag{4.19}$$

For the coefficients of these effective interactions, we obtain

$$C_S^q = \frac{y^2}{4m_S^2} \frac{2r^2 - 1}{(r^2-1)^2} \;,\; C_T^q = \frac{y^2}{m_S^4} \frac{1}{(r^2-1)^2} \,, \tag{4.20}$$

with $q = u$ ($q = d$) for dark matter coupling to u_R (d_R).

Furthermore, the dark matter particle can scatter off nucleons via the diagrams shown in the lower row of Fig. 4.11, which describe the interaction of S with gluons induced at the one-loop level. A conceptual complication in the evaluation of these diagrams is that the loop integrals receive significant contributions both from small momentum scales of the order of $k \sim m_q$, as well as from large momenta $k \sim m_\psi$, denoted as the long-distance and short-distance contributions, respectively, similar to the corresponding scenario of Majorana dark matter with a colored scalar mediator [271–273]. The long-distance contribution involves values of the strong coupling constant at an energy scale $k \ll \Lambda_{\rm QCD} \simeq 250\,\text{MeV}$, questioning the validity of the perturbative expansion of the scattering process. However, as recently discussed in [337], one can argue that the non-perturbative part of the amplitude is already implicitly contained in the parton distribution functions of the light quarks in the nucleon, which in turn enter the nuclear matrix elements of the effective dark matter-quark interaction given by Eq. (4.18). Consequently, for the dark matter-gluon interaction, only the short-distance contribution has to be taken into account, leading to the effective Lagrangian

$$\mathcal{L}_g = C_S^g \frac{\alpha_S}{\pi} S^2 G^{\mu\nu} G_{\mu\nu} \,, \tag{4.21}$$

where in the limit $m_q \ll m_\psi - m_S$ the coefficient C_S^g is given by [337]

$$C_S^g = \frac{y^4}{24 m_S^2} \frac{1}{r^2 - 1} \,. \tag{4.22}$$

Similar as in the discussion of the simplified model of Dirac dark matter in Sec. 3, the next step is to evaluate the nuclear matrix elements of the dark matter-quark and dark matter-gluon Lagrangians given by Eq. (4.18) and (4.21), respectively. This leads to a spin-independent interaction of dark matter with nucleons, $\mathcal{L}_{\rm eff} = f^{(N)} S^2 \bar{N} N$, with $f^{(N)}$ given by [271]

$$\frac{f^{(N)}}{m_N} = C_S^q f_q^{(N)} + \frac{3}{4} C_T^q m_S^2 (q^{(N)}(2) + \bar{q}^{(N)}(2)) - \frac{8}{9} C_S^g f_g^{(N)} \,. \tag{4.23}$$

Here, $f_q^{(N)}$ is the mass fraction of the quark q in the nucleon N as introduced in Eq. (3.21), $f_g^{(N)} \equiv 1 - \sum_{q=u,d,s} f_q^{(N)}$ parametrizes the gluon contribution to the nucleon mass [92], and $q^{(N)}(2)$ and $\bar{q}^{(N)}(2)$ are the second moments of the parton distribution functions. The numerical values for all of these parameters are taken from [337]. In the left panel of Fig. 4.12, we show the effective dark matter-proton coupling f_p/m_p in units of y^4/m_S^2 (which appears as a prefactor in all terms of Eq. (4.23)) as a function of $r - 1$, assuming for concreteness dark matter coupling to u_R. Besides the total f_p shown as the solid black curve, we indicate the individual contributions defined in Eq. (4.23) by the colored dashed lines. It follows from the plot that there is a destructive interference of the dark matter-gluon scattering with the scalar and twist-2 quark contributions, leading in particular to a vanishing dark matter-proton coupling for $r \simeq 3.0$. Similarly, we find that the dark matter-neutron coupling f_n is zero at a mass splitting $r \simeq 2.3$.

Finally, the total spin-independent cross section for the scattering of S off a target nucleus T at zero momentum transfer is given by the coherent sum of f_p and f_n:

$$\sigma_T^{(\rm SI)} = \frac{m_T^2}{\pi (m_S + m_T)^2} \left[Z f_p + (A - Z) f_n \right]^2 \,, \tag{4.24}$$

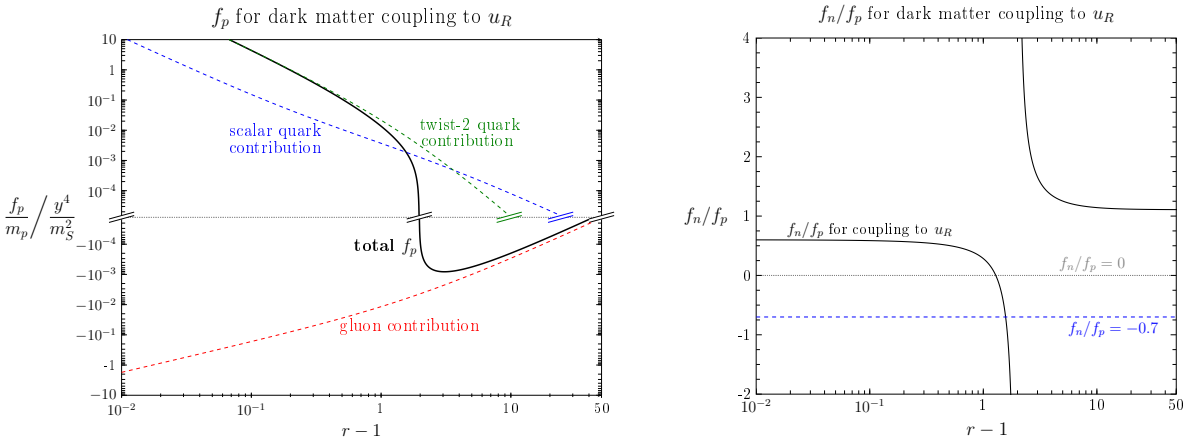

Figure 4.12.: *Left panel*: effective dark matter-proton coupling f_p/m_p, expressed in units of y^4/m_S^2, for the case of coupling to u_R. *Right panel*: ratio of the neutron-to-proton coupling of dark matter, also for coupling to u_R.

where Z and A are the charge and mass number of the nucleus T, respectively (see also Sec. 2.1.1, in particular Eq. (2.4)). Most experiments analyze their data by assuming isospin conserving interactions, i.e. $f_p = f_n$, and then present the resulting limit on the spin-independent scattering cross section with protons, $\sigma_p^{(\mathrm{SI})}$. However, as shown in the right panel of Fig. 4.12, we find that the model discussed in this section in general can lead to strong violations of that assumption: the ratio f_n/f_p calculated from Eq. (4.23) for the case of dark matter coupling to u_R can be drastically different from 1, depending on the mass splitting r. In particular, for $r \simeq 2.6$, one has $f_n/f_p \simeq -0.7$, leading to "maximal isospin violation" at a xenon target, i.e. a strong cancellation in Eq. (4.24) for the case of scattering off xenon nuclei. Analogously, for dark matter coupling to d_R, this occurs at $r \simeq 3.3$. When confronting the model of real scalar dark matter to the results of the LUX experiment [101], which provides the currently best limits on spin-independent interactions[12] for $m_S \gtrsim 4\,\mathrm{GeV}$ (see also Sec. 2.1.2), we take into account the fact that $f_n \neq f_p$ by defining the *effective dark matter-proton cross section* $\sigma_p^{(\mathrm{eff})}$ via

$$\sigma_p^{\mathrm{eff}} \equiv \sigma_p \cdot \frac{\sum_{i\in\mathrm{isotopes}} \xi_i \left(Z + (A_i - Z) f_n/f_p\right)^2}{\sum_{i\in\mathrm{isotopes}} \xi_i A_i^2} \,. \tag{4.25}$$

In this equation, the sum runs over all xenon isotopes i occurring with natural relative abundances ξ_i. With that definition, one can interpret σ_p^{eff} as the dark matter-proton scattering cross section which, under the common assumption $f_p = f_n$, would lead the same expected number of events in LUX as the actual cross section σ_p of the model. Hence, a given point in the parameter space is excluded by LUX if and only if σ_p^{eff} is larger than the upper limit on the dark matter-proton scattering cross section presented by the collaboration in [101].

Based on this formalism, we show in Fig. 4.13 the effective dark matter-proton scattering cross section σ_p^{eff} in two different projections of the parameter space of the model, each time

[12] After this work has been first published, LUX updated its upper limits on the spin-independent scattering cross section in [102]. We have checked that none of our conclusion change qualitatively when using these new results.

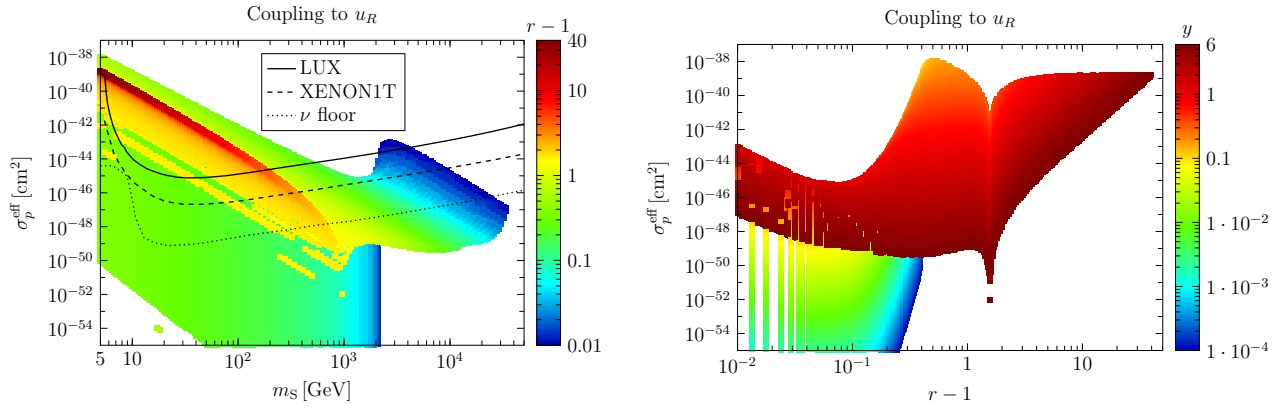

Figure 4.13.: Effective spin-independent dark matter-proton scattering cross section $\sigma_p^{\rm eff}$, defined via Eq. (4.25), as a function of the dark matter m_S (the relative mass splitting $r-1$) in the left (right) panel. In the left panel, the color gradient corresponds to different values of $r-1$, fixing the Yukawa coupling y to $y_{\rm thermal}$, while in the right panel the color coding stands for the Yukawa coupling y, fixing the dark matter mass m_S to the value imposed by the relic density constraint. Furthermore, the black solid, dashed and dotted curves in the left panel show the upper limit on $\sigma_p^{\rm eff}$ from LUX, the projected sensitivity of XENON1T and the neutrino floor, respectively. See text for details.

imposing the constraint that the abundance of S generated by the freeze-out mechanism accounts for all of the observed dark matter, following the discussion in Sec. 4.2. For simplicity, in these plots we only consider the case of dark matter coupling to u_R; the results for coupling to d_R will be discussed in Sec. 4.4.4 together with the complementary constraints from collider and indirect searches. Furthermore, we only consider points in the parameter space with $y \leq 6$, which we choose as perturbativity limit[13]. In the left panel of Fig. 4.13, we present $\sigma_p^{\rm eff}$ as a function of m_S, with the color gradient corresponding to different values of the mass splitting r, and fixing the Yukawa coupling to the value $y_{\rm thermal}$ implied by the relic density requirement. It follows from this plot that depending on the mass of the dark matter particle and the fermionic mediator, $\sigma_p^{\rm eff}$ can vary by several orders of magnitude. Generally speaking, we find that for fixed m_S, the scattering cross section is enhanced for degenerate scenarios, i.e. $r \to 1$, which is due to the resonant behavior of the dark matter-nucleon coupling $f^{(N)}$ in that limit, as it follows from Eqs. (4.20), (4.22) and (4.23). On the other hand, for small r there is a lower limit on the dark matter mass, below which the coannihilation processes suppress the dark matter relic density below the observed value, irrespectively of the value of y; this can also be inferred from the right panel of Fig. 4.3. This behavior is visible in the left panel of Fig. 4.13 as a turnaround of the points corresponding to a fixed, small value of the mass splitting, e.g. $r = 1.01$ shown in dark blue, towards arbitrarily small values of the effective cross section. Furthermore, we observe that when fixing m_S to a value $\lesssim 200\,\text{GeV}$ and increasing the mass splitting r to larger and larger values, $\sigma_p^{\rm eff}$ converges to a finite value, visible in form of the line containing the dark red points. This feature can be understood by noting that for $r \gg 1$, the total

[13]This is motivated by the observation that the loop process $SS \to gg$, which is relevant for the relic density calculation and for indirect detection constraints, scales as $y^2 g_s^2/(16\pi^2)$. Requiring that this combination of parameters is $\lesssim 1$, such that the one-loop calculation is reliable, one obtains the condition $y \lesssim 6$.

annihilation cross section relevant for the freeze-out process scales as $1/r^4$ (c.f. Eq. (4.6)), which is precisely the same asymptotic behavior of the effective scattering cross section in the limit of large r, as it follows from Eqs. (4.20), (4.22), (4.23) and (4.24).

The left panel of Fig. 4.13 also includes the upper limit on the spin-independent dark matter-proton scattering cross section from LUX [101], the projected sensitivity of XENON1T [325], as well as the values of the cross section corresponding to the neutrino floor [135], constituting the ultimate reach of non-directional direct detection experiments, as explained in Sec. 2.1. Interestingly, the LUX experiment already excludes significant parts of the parameter space for $m_S \lesssim 200-300\,\text{GeV}$; furthermore, for highly mass-degenerate scenarios, even dark matter masses around 2 TeV are already ruled out. During the next years, XENON1T will be able to probe further parts of the parameter space of the model, and in particular it is expected to have sensitivity to dark matter masses up to $\simeq 10\,\text{TeV}$, which will not be accessible to any near-future collider experiment. On the other hand, Fig. 4.13 also implies that for several choices of m_S and r, the expected scattering cross section is well below the neutrino floor, leading to the conclusion that direct detection experiments alone will not be able to fully rule out this model of real scalar dark matter.

Finally, the right panel of Fig. 4.13 shows the effective dark matter scattering cross section as a function of $r-1$. In this plot, the color gradient corresponds to different values of the Yukawa coupling y, while we fix the dark matter mass m_S by the requirement of reproducing the relic density via the freeze-out mechanism. This projection of the parameter space clearly shows the loss of sensitivity of xenon-based direct detection experiments at $r \simeq 2.6$, due to the maximal isospin violation occurring at this value of the mass splitting, c.f. Fig. 4.12.

4.4.2. Constraints from searches at the LHC

Besides direct detection, the model of real scalar dark matter coupling to a Standard Model quark can also be probed at the LHC, in particular through the production of the colored fermionic mediator ψ. After being produced, ψ decays into the dark matter particle S and the quark q via the Yukawa coupling defined in Eq. (4.3). Consequently, the signature associated to the production of a mediator pair[14] is given by at least two jets plus missing transverse energy $\not{E}_T$, which is a typical signal topology in dark matter searches at the LHC, as introduced in Sec. 2.4.

In the following, we first discuss the production cross section for a pair of mediators in proton-proton collisions, and then derive constraints on the real scalar dark matter model by carefully reinterpreting an ATLAS search for multiple jets plus $\not{E}_T$.

Production of mediator pairs

The production of a mediator pair $\psi\psi$, $\psi\bar{\psi}$ or $\bar{\psi}\bar{\psi}$ in a proton-proton collision arises from the Feynman diagrams shown in Fig. 4.14. The diagrams in the upper row describe the QCD induced production of $\psi\bar{\psi}$ from a $q\bar{q}$ or gg initial state, which is independent of the dark matter mass and the Yukawa coupling y. On the other hand, the processes in the lower row of Fig. 4.14 correspond to the production of $\psi\psi$, $\psi\bar{\psi}$ or $\bar{\psi}\bar{\psi}$ via the exchange of the dark matter particle S in the t-channel, involving the Yukawa interaction defined in Eq. (4.3).

[14] In addition to the production of mediator pairs considered in this section, also the processes $pp \to S\psi$ and $pp \to S\bar{\psi}$ contribute to the signature of jets plus missing energy. However, we have checked that $\sigma(pp \to SX) < \sigma(pp \to XX)$, with $X = \psi, \bar{\psi}$, and hence including these production channels does not significantly affect the final results shown in Fig. 4.17.

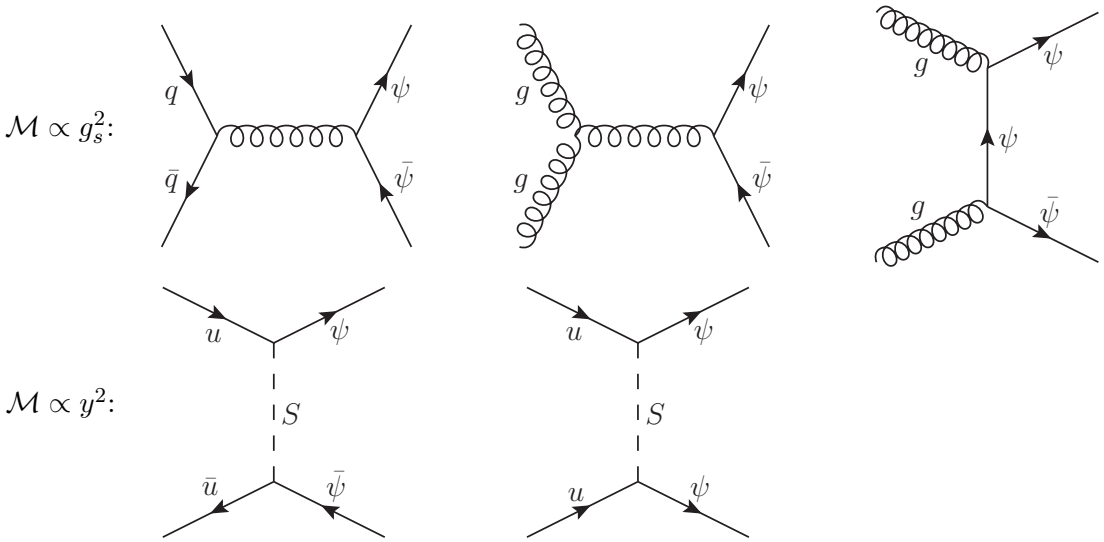

Figure 4.14.: Feynman diagrams contributing to the production of mediator pairs in proton-proton collisions, for dark matter coupling to u_R. Additional diagrams corresponding to crossing or charge conjugation of the initial or final state are not shown.

Notice that for the case of dark matter coupling to u_R, the Yukawa induced processes are only possible for a uu, $u\bar{u}$ or $\bar{u}\bar{u}$ initial state, respectively. An analogous statement holds for dark matter coupling to d_R.

Usually, the production of a heavy colored state at the LHC is dominated by QCD processes, such as the ones shown in the upper row of Fig. 4.14. However, in the model of real scalar dark matter discussed in this section, the requirement of correctly reproducing the observed relic density of dark matter via thermal freeze-out implies rather large Yukawa couplings y_{thermal}, c.f. Fig. 4.3, leading to a significant enhancement of the Yukawa induced processes shown in the lower row of Fig. 4.14. Furthermore, for the scenario of dark matter coupling to u_R (d_R), the production process $uu \to \psi\psi$ ($dd \to \psi\psi$), which is driven solely by the Yukawa coupling, is favored compared to processes involving a $q\bar{q}$ initial state by the large parton distribution function of the u (d) quark in the proton. All in all, we find that depending on the masses of S and ψ, either the QCD or the Yukawa induced processes can dominate the production of mediator pairs; hence, we carefully take into account all relevant contributions (including interference terms) in our numerical analysis. To this end, we calculate the leading-order cross section σ^{LO} for $pp \to \psi\psi$, $\psi\bar{\psi}$, $\bar{\psi}\bar{\psi}$ at $\sqrt{s} = 8\,\text{TeV}$ using CalcHEP [275], employing the `cteq6l` parton distribution function. Furthermore, we parametrize higher-order corrections to the production cross section by defining

$$\sigma^{\text{full}} = K\,\sigma^{\text{LO}}\,. \tag{4.26}$$

A full calculation of the relevant K-factor is beyond the scope of this work; consequently, we treat K as a source of uncertainty by varying it in the range $[0.5, 2]$ [15].

The result for σ^{LO} is shown in Fig. 4.15 as a function of the relative mass splitting $r - 1$, choosing for illustration $m_\psi = 500\,\text{GeV}$, and assuming that dark matter couples

[15] This choice is motivated by $K \simeq 1.7$ for $t\bar{t}$ production [338], which resembles the QCD induced processes shown in the upper row of Fig. 4.14.

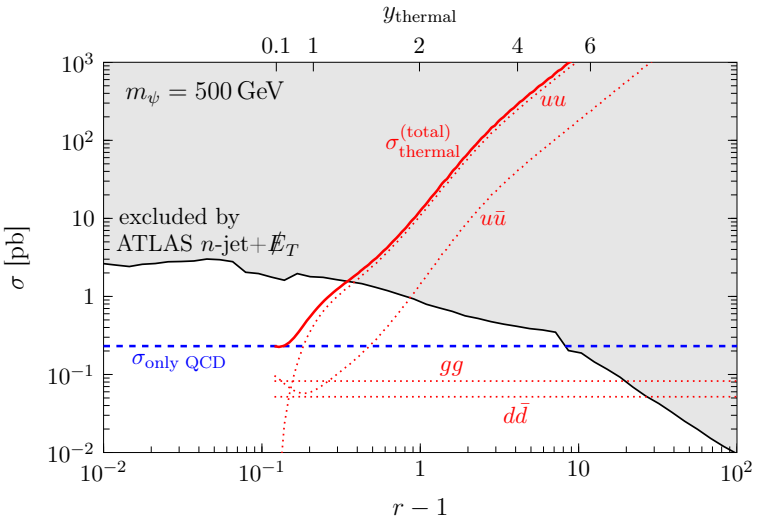

Figure 4.15.: Production cross section of mediator pairs $\psi\psi$, $\psi\bar{\psi}$ and $\bar{\psi}\bar{\psi}$ in proton-proton collisions at $\sqrt{s} = 8\,\text{TeV}$, assuming $m_\psi = 500\,\text{GeV}$ and dark matter coupling to u_R. For the red curves, the Yukawa coupling is fixed to the value y_{thermal} following from the constraint on the dark matter relic density, while the blue dashed line corresponds to the production induced solely by the QCD processes.

to u_R. The red solid curve shows the total production cross section, while the red dashed curves correspond to the individual contributions from the different initial states, in all cases fixing the Yukawa coupling to the value y_{thermal} implied by the relic density constraint. For comparison, the blue dashed curve shows the production cross section induced only by the QCD interaction. It follows from the plot that for intermediate and large mass splittings, the production of mediator pairs is dominated by the Yukawa induced process $uu \to \psi\psi$; as discussed above, this is due to the large value of y_{thermal} as well as due to the large parton distribution function of the up-quark in the proton.

Reinterpreting an ATLAS search for multiple jets plus missing transverse energy

After being produced, ψ can be detected via its decay into the light quark q and the dark matter particle S. At leading order, the relevant signal topology thus consists of two jets plus missing energy[16]. However, the radiation of quarks or gluons from the initial, final or an intermediate state can lead to additional jets which potentially can be observed at the detector. Even though the cross sections for these processes are suppressed by one or several powers of α_s, including these extra jets can be important for two reasons: first, if $m_\psi - m_S \lesssim 50 - 100\,\text{GeV}$, the jets arising from the decays of the mediators are too soft in order to pass the basic p_T-cut of the ATLAS detector, requiring the presence of additional jets for the visibility of the event. Secondly, even for larger mass splittings the signal-to-background ratio of the signature consisting of three or more jets plus $\not{E}_T$ can be larger compared to the lowest-order 2-jet + $\not{E}_T$ process, leading to potentially more stringent constraints arising from the former signal topology.

[16] Constraints on the model of real scalar dark matter based on this signature have also been obtained in [339]. However, in that work neither coannihilations nor the higher-order annihilation channels of S have been taken into account in the freeze-out process.

In order to confront the multiple jet + $\not{E}_T$ signature predicted by the model to available LHC data, we employ the ATLAS search `ATLAS-CONF-2013-047` [340] for 2-6 jets + $\not{E}_T$, undertaken at $\sqrt{s} = 8\,\text{TeV}$ with a luminosity of $20.3\,\text{fb}^{-1}$. For the analysis of the data, the collaboration has defined ten different signal regions, each of them specified by a set of cuts on the number of jets and the minimally required $\not{E}_T$. All of the signal regions receive background contributions from Standard Model processes, most notably the production of jets in association with weak gauge bosons, which can decay into (invisible) neutrinos leading to the $\not{E}_T$ signature. By extrapolating the number of events observed in separate control regions into the signal regions, the ATLAS collaboration has estimated the number of background events in each signal region [340]. These predictions have also been cross checked with a direct Monte Carlo evaluation of the expected background rates. After comparing to the actually observed number of events, no significant excess in any of the signal regions over the Standard Model background expectation has been found, leading to 95 % C.L. upper bounds $S^{95}_{\text{obs},i}$ on the number of signal events in each signal region i, which can be found in [340]. Similarly, we denote the upper bounds expected in the absence of a signal contribution as $S^{95}_{\text{exp},i}$, and also take them from [340].

For a given signal region i, the upper limit $S^{95}_{\text{obs},i}$ or $S^{95}_{\text{exp},i}$ can then be compared to the expected number of signal events predicted by the model of real scalar dark matter, which we calculate from

$$S_i = \sigma \cdot \epsilon_i \cdot \mathcal{L}\,, \tag{4.27}$$

with σ being the total production cross section for a pair of mediators, as discussed earlier on in this section, and $\mathcal{L} = 20.3\,\text{fb}^{-1}$ being the luminosity relevant for the ATLAS search. Furthermore, ϵ_i is the *efficiency* corresponding to the signal region i, which is defined as the probability that a given event leads to a signature that passes all the selection cuts, i.e. gives rise to the required number of jets and amount of missing energy. As the probability of emitting additional quarks or gluons explicitly depends on the Feynman diagrams underlying the production process of the mediators, the efficiencies ϵ_i have to be recalculated for a given model. To this end, we implement the model of real scalar dark matter in FeynRules [274], and then simulate events for the production of mediator pairs using MadGraph [341], taking into account all diagrams involving the emission of up to two additional jets. The showering and hadronization of the partonic events is then simulated using PYTHIA 6 [155]. A well-known complication arising in that step is that the additional jets produced by the radiative emissions of the quarks and/or gluons can both be considered as being part of the underlying partonic event as well as being due to the showering process. In order to avoid a possible double counting, one then defines a minimal transverse momentum k_T of the corresponding jet, above which it is considered to be part of the partonic event, while for smaller values of k_T it is described by means of the showering process. Technically, this is implemented by employing the MLM matching scheme which ensures a smooth transition between both regimes, using the parameters `Qcut` $= m_\psi/4$ and `SHOWERKT=T`. We also validate this approach by checking that the differential jet distributions are indeed smooth, indicating a physically meaningful matching scheme. Lastly, we employ CheckMATE [342] for the detector simulation and the implementation of the cuts corresponding to the ATLAS search. More precisely, for a given point in the parameter space of the model, we simulate N_{ev} events as described above, and then use CheckMATE in order to determine the number of events $N^{(i)}_{\text{after cuts}}$ passing all the cuts for a given signal region i. Then, the efficiency follows from $\epsilon_i = N^{(i)}_{\text{after cuts}}/N_{\text{ev}}$, which allows us to obtain S_i as defined in Eq. (4.27).

Finally, by comparing the expected number of signal events S_i with the observed (expected) upper limit $S^{95}_{\text{obs},i}$ ($S^{95}_{\text{exp},i}$), we calculate the observed and expected 95% C.L. upper limit on the production cross section of mediator pairs from

$$\sigma^{(95)}_{\text{obs},i} = \sigma \cdot \frac{S^{95}_{\text{obs},i}}{S_i - 1.96\Delta S_i} \quad , \quad \sigma^{(95)}_{\text{exp},i} = \sigma \cdot \frac{S^{95}_{\text{exp},i}}{S_i - 1.96\Delta S_i} \, , \tag{4.28}$$

respectively. Here, we additionally have taken into account in a conservative way the Monte Carlo uncertainties associated to the finite number of simulated events N_{ev}, by replacing $S_i \to S_i - 1.96\Delta S_i$, with ΔS_i being the 1σ statistical error on the number of expected signal events, and hence $S_i - 1.96\Delta S_i$ being the 95% C.L. lower limit on S_i. In order to ensure that $\Delta S_i / S_i \lesssim 0.1 - 0.2$, we have generated up to $N_{\text{ev}} = 5 \cdot 10^6$ events per point in the parameter space. We find that depending on m_S and m_ψ, a different signal region i provides the most stringent constraint on the model, i.e. the lowest value of the excluded cross section σ. As the choice of the optimal signal region should not depend on the actual data in order to avoid artificially stringent constraints based on an underfluctuation of the background rate, we proceed as follows: for a given point in the parameter space, we determine the signal region i_{optimal} leading to the smallest *expected* upper limit among all $\sigma^{(95)}_{\text{exp},i}$, and then define our final upper limit on the production cross section via $\sigma^{(95)}_{\text{obs},i_{\text{optimal}}}$. For illustration, this upper limit is shown in Fig. 4.15 for $m_\psi = 500\,\text{GeV}$, which then can be compared to the production cross section expected within the model. In Sec. 4.4.4, we will determine in detail which parts of the parameter space are ruled out by the ATLAS search, comparing it to complementary constraints from direct and indirect detection.

4.4.3. Probing the model with indirect detection

In this section we discuss one more class of constraints on the model of real scalar dark matter coupling to a quark: indirect searches for dark matter annihilations using gamma-rays and antiprotons.

Gamma-ray spectral features

Fully analogous to the gamma-ray spectral features appearing in the scenario of real scalar dark matter coupling to a lepton, as discussed in Sec. 4.3.1, also for the case of coupling to a Standard Model quark the annihilation of S gives rise to sharp gamma-ray features. As it follows from Eq. (4.6), for small mass splittings r the gamma ray spectrum at the kinematical endpoint $E_\gamma \simeq m_S$ is dominated by the VIB process $SS \to q\bar{q}\gamma$, while for larger mass splittings the one-loop annihilations into $\gamma\gamma$ and γZ are more important. We again refer to Appendix B.1 for the full expressions of the corresponding cross sections. For the scenario of dark matter coupling to u_R, the combined annihilation cross section $(\sigma v)_{q\bar{q}\gamma} + 2(\sigma v)_{\gamma\gamma}$, which acts as the normalization of the total gamma ray flux containing sharp features, is shown in the left panel of Fig. 4.16 as a function of m_S, with the color gradient corresponding to different values of the mass splitting r, and fixing again the Yukawa coupling to the value y_{thermal} following from the relic density requirement. Furthermore, in this plot we show the observational upper limits from Fermi-LAT and H.E.S.S. on $(\sigma v)_{q\bar{q}\gamma}$ as derived in [321], as well as the upper limits on $2(\sigma v)_{\gamma\gamma}$ derived by the Fermi-LAT collaboration in [210] and by the H.E.S.S. collaboration in [211]. For a given dark matter mass, the upper limits on $(\sigma v)_{q\bar{q}\gamma}$ and $2(\sigma v)_{\gamma\gamma}$ bracket the actual upper limit on the combination $(\sigma v)_{q\bar{q}\gamma} + 2(\sigma v)_{\gamma\gamma}$, and hence can be used as an estimation of the limits on the model. As apparent from the

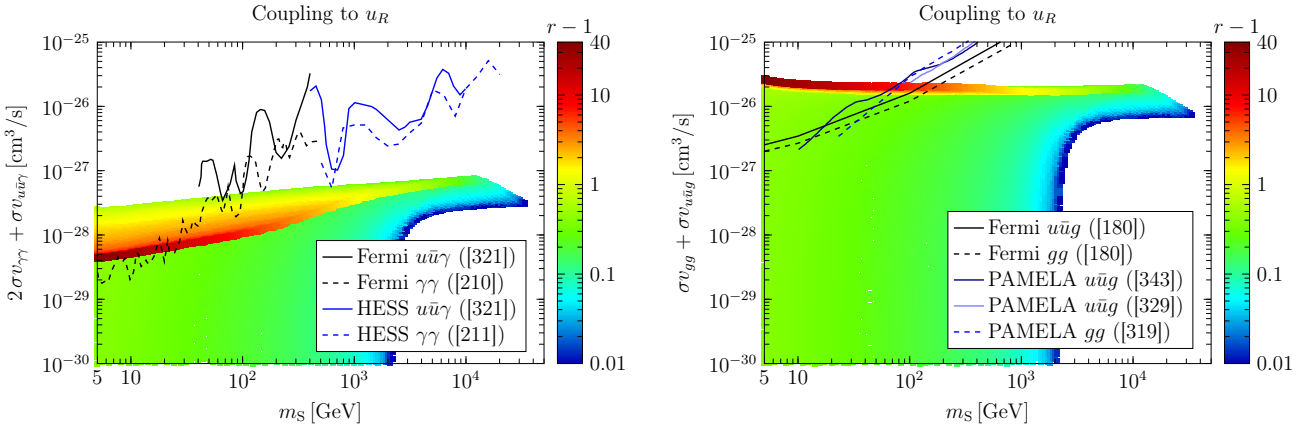

Figure 4.16.: Cross section $(\sigma v)_{q\bar{q}\gamma} + 2(\sigma v)_{\gamma\gamma}$ (left panel) and $(\sigma v)_{gg} + (\sigma v)_{q\bar{q}g}$ (right panel) in the scenario of thermally produced dark matter coupling to u_R, as a function of the dark matter mass. The color gradient corresponds to different values of the mass splitting r. The solid and dashed curves show various upper limits on the corresponding cross sections arising from gamma-ray and antiproton searches; see text for details.

figure, the present limits on sharp gamma-ray spectral features probe the model of real scalar dark matter coupling to u_R only for $m_S \lesssim 40\,\text{GeV}$; for coupling to d_R we obtain very similar results. This is in strong contrast to the case of dark matter coupling to a Standard Model lepton: from Fig. 4.6, we concluded that in that scenario Fermi-LAT and H.E.S.S. are sensitive to dark matter masses up to several TeV. The reason for this difference is the relative enhancement of y_{thermal} in the case of dark matter coupling to e_R, μ_R or τ_R compared to the scenario involving a Yukawa interaction with u_R or d_R, due to the additional annihilation channels involving the strong coupling in the latter scenarios, reducing the value of the Yukawa coupling necessary for reproducing the observed relic density.

Continuum gamma rays

In contrast to the scenario in which S couples to a lepton, the presence of the annihilation channels $SS \to q\bar{q}g$ and $SS \to gg$ in the model discussed in this section also leads to a significant continuum spectrum of gamma-rays produced by dark matter annihilations, which can be constrained by observations of dwarf spheroidal galaxies, as introduced in Sec. 2.3.1. The right panel of Fig. 4.16 shows the total annihilation cross section $(\sigma v)_{gg} + (\sigma v)_{q\bar{q}g}$ for these two processes for the case of dark matter coupling to u_R, as a function of the dark matter mass, and again fixing y by the relic density requirement. As for the gamma-ray spectral features, for an intermediate mass splitting r the total photon spectrum is a superposition of the spectra for pure annihilations into $q\bar{q}g$ and gg, and hence we can again bracket the upper limit on $(\sigma v)_{gg} + (\sigma v)_{q\bar{q}g}$ by considering the upper limits derived for the single annihilation channels. These are shown in the right panel of Fig. 4.16 as the solid and dashed black curves, based on the dSph observations by Fermi-LAT [180] [17]. As it

[17] The Fermi-LAT collaboration has not published upper limits on (σv) for the annihilation channels $q\bar{q}g$ and gg. Hence, following [215], we estimate these via $(\sigma v)^{\text{upper limit}}_{q\bar{q}g,\,gg} \simeq (\sigma v)^{\text{upper limit}}_{q\bar{q}} \cdot N_\gamma^{q\bar{q}} / N_\gamma^{q\bar{q}g,\,gg}$, where $(\sigma v)^{\text{upper limit}}_{q\bar{q}}$ is the upper limit for the annihilation channel $q\bar{q}$ given in [180]. Furthermore, N_γ^X is defined as the number of gamma rays per annihilation into the final state X within the energy range of Fermi-LAT, $0.5\,\text{GeV} < E_\gamma < 500\,\text{GeV}$, which we obtain by using PYTHIA 8.1 [156].

can be seen from the figure, this indirect detection channel probes the model of real scalar dark matter coupling to a quark for dark matter masses $\lesssim 150\,\text{GeV}$, for a large range of mass splittings r.

Antiprotons

Finally, the annihilations $SS \to q\bar{q}g$ and $SS \to gg$ also produce a flux of antiprotons, which can be constrained by the PAMELA $\bar{p}/p$ data, as explained in more detail in Sec. 2.3.2 [18]. Analogously to the continuum gamma rays, we show in the right panel of Fig. 4.16 the band bracketing the upper limit on the combined annihilation cross section $(\sigma v)_{gg}+(\sigma v)_{q\bar{q}g}$, based on the upper limits on $(\sigma v)_{q\bar{q}g}$ and $(\sigma v)_{gg}$ derived in [329,343] and [319] from the PAMELA data [220], respectively. It follows from the plot that the non-observation of an excess in the $\bar{p}/p$ ratio leads to constraints on the model for $m_S \lesssim 100\,\text{GeV}$; however, it is important to keep in mind that these limits are rather sensitive to propagation uncertainties, c.f. Sec. 2.3.2. Hence, we will conservatively not include the antiproton limits when discussing the combined constraints on the parameter space of the model in Sec. 4.4.4.

4.4.4. Combined constraints on thermally produced dark matter

We conclude this chapter by discussing the combined constraints on the model of real scalar dark matter coupling to u_R or d_R, taking into account direct, indirect and collider searches as discussed in the previous sections. To this end, Fig. 4.17 shows the parameter space of the model for coupling to u_R (d_R) in the upper (lower) panel, fixing the Yukawa coupling to the value y_{thermal} resulting from the relic density constraint, separately for each m_S and r. Similar to the case of real scalar dark matter coupling to a lepton, as shown in Fig. 4.10, or to the scenario involving Dirac dark matter presented in Figs. 3.4 and 3.5, the dark gray shaded regions in the lower left corners of the two panels in Fig. 4.17 show the regions of the parameter space, where coannihilations suppress the dark matter relic density below the observed value, irrespectively of the value of y. On the other hand, large values of m_S and/or r violate our perturbativity condition $y_{\text{thermal}} < 6$, as shown by the light gray regions enclosed by the black dashed curves. Besides, we include in the plots the limits from the LUX experiment as a red shaded region enclosed by the red solid curve, following the results obtained in Sec. 4.4.1. Moreover, the constraints from the ATLAS search for multiple jets plus $\not{E}_T$ discussed in Sec. 4.4.2 are shown as a blue shaded region enclosed by the solid blue line, adopting $K = 1$ in Eq. (4.26), i.e. neglecting the higher-order corrections to the production cross section of mediator pairs. The dependence of the limits on the unknown K-factor is indicated by the dashed and dotted blue lines, which show the ATLAS excluded region for $K = 0.5$ and $K = 2$, respectively. We also show for completeness an estimation of the limits arising from a search for vector-like quarks at the Z-resonance at LEPI as the yellow dotted curve, which follows from requiring $m_\psi \gtrsim m_Z/2$, as well as an approximate bound from LEPII (yellow solid), corresponding to $m_\psi \gtrsim 100\,\text{GeV}$ [344]. Lastly, the constraints arising from the dSph searches by Fermi-LAT discussed in Sec. 4.4.3 are shown as the green shaded region enclosed by the green solid curve.

As apparent from the plots, both for dark matter coupling to u_R and d_R, large parts of the parameter space with $m_S \lesssim 1\,\text{TeV}$ are excluded by one or multiple searches. The ATLAS limits are most stringent for $r \simeq 1.5$, excluding masses between $\simeq 20\,\text{GeV}$ and $1\,\text{TeV}$ for coupling to u_R. For dark matter coupling to d_R, the constraints are slightly weaker, due to

[18] We do not consider the preliminary data on the $\bar{p}/p$ ratio from AMS-02 [223].

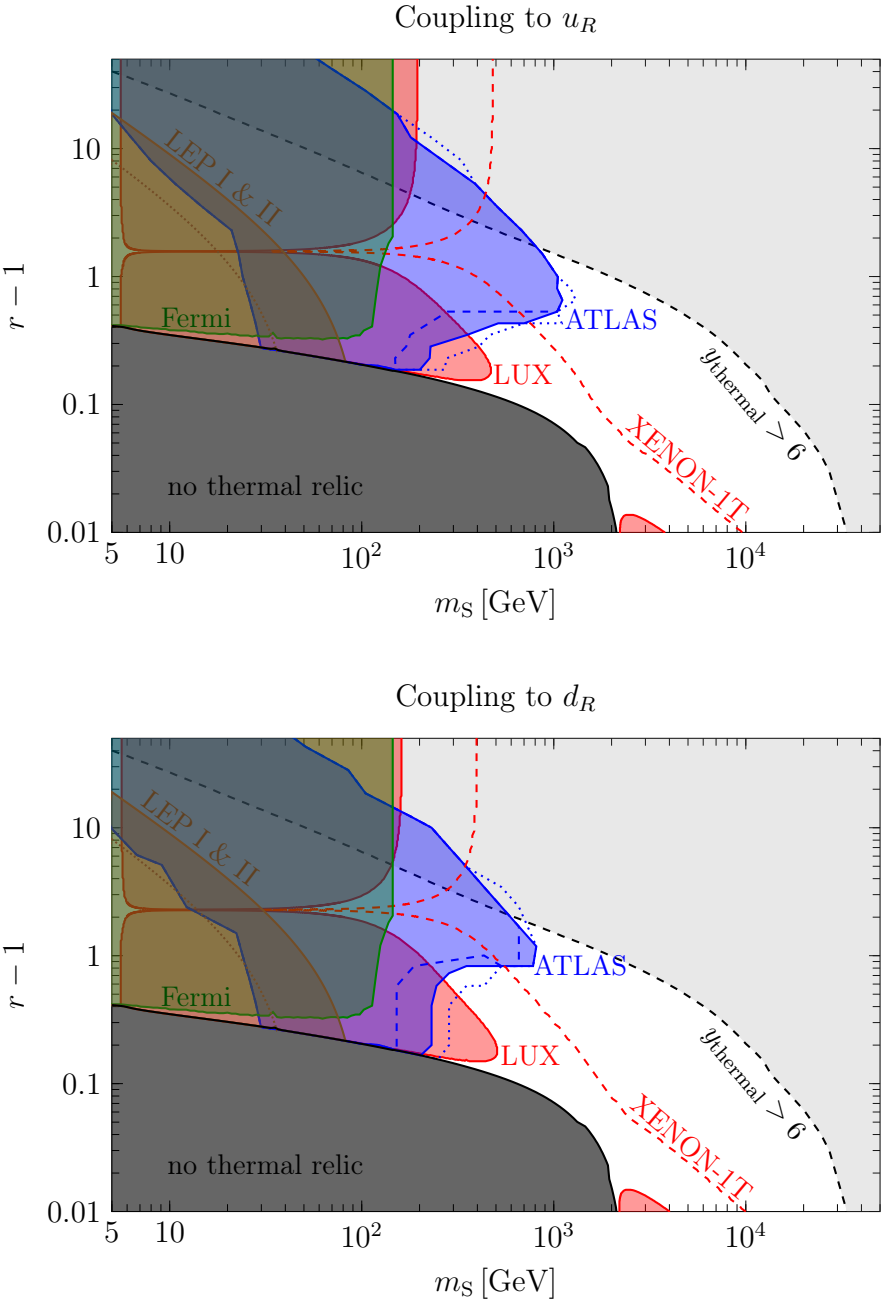

Figure 4.17.: Combined constraints on the model of real scalar dark matter coupling to u_R or d_R, shown in the upper and lower panel, respectively. For a given dark matter mass m_S and mass splitting $r = m_\psi/m_S$, we fix the Yukawa coupling to the value implied the relic density constraint. See text for details.

the smaller parton distribution function of the down-quark in the proton. We also notice that the ATLAS excluded region is only mildly sensitive to the choice of the K-factor, making our results robust against the uncertainties related to the next-to-leading-order corrections of the mediator production cross section. Furthermore, from the plots one can infer an interesting complementarity between the LUX constraints and the collider limits: on the one hand, direct detection is very sensitive to very small mass splittings, excluding e.g. the region around $m_S = 300\,\text{GeV}$ and $r = 1.2$ which is not covered by the ATLAS search. On the other hand, the LUX limits are significantly worsened at $r \simeq 2.6\,(3.0)$ for dark matter coupling to u_R (d_R), due to the maximal isospin violation occurring at that value of the mass splitting, as discussed in detail in Sec. 4.4.1. However, that part of the parameter space is covered by the ATLAS and LEP searches, excluding this "blind spot" of direct detection. Lastly, also the Fermi-LAT limits shown in green are partially complementary to the other approaches, excluding in particular very small values of the dark matter mass which are inaccessible to both LUX and the ATLAS search.

Finally, in both panels of Fig. 4.17 we show as a red dashed line the prospected reach of the XENON1T experiment, which will be able to probe dark matter masses up to $\simeq 10\,\text{TeV}$ for small mass splittings $r - 1 \ll 1$. We also remark that a future 100 TeV proton-proton collider (not shown in the figure) would perfectly complement the next-generation direct detection experiments by being sensitive to scenarios with intermediate and large values of r. Altogether, the simplified model discussed in this section constitutes a prime example of a scenario which might be completely probed by future experiments, however, requiring the complementary interplay of various search strategies, such as direct detection experiments and high-energy collider searches.

5. Neutrinos from the Sun in a model of Majorana dark matter

Having discussed the model of Dirac dark matter and a scalar mediator in Sec. 3, and the scenario involving a real scalar dark matter particle interacting via a fermionic mediator in Sec. 4, we now turn to one more example of a t-channel simplified model: a Majorana dark matter particle χ interacting via a Yukawa interaction with a scalar mediator η and a right-handed Standard Model quark q [1].

The phenomenology of this model in the context of direct and collider searches, as well as of indirect detection using gamma-rays and antiprotons has already been extensively discussed in the literature [215, 296, 321, 328, 329, 343, 345–348]. In this section, we will consider a so far unexplored avenue to probe the scenario of Majorana dark matter, namely via the capture and annihilation process of dark matter particles in the Sun, an idea introduced in detail in Sec. 2.2. Previous analyses of dark matter annihilations in the Sun have focused on computing and constraining the neutrino flux arising from the lowest-order $2 \to 2$ processes; however, similar to the scenario of real scalar dark matter discussed in Sec. 4, also in the simplified model of Majorana dark matter the tree-level $2 \to 2$ annihilation turns out to be heavily suppressed, requiring the consideration of higher-order processes such as virtual internal bremsstrahlung of a gauge boson. After introducing the simplified model in Sec. 5.1, we will analyze the capture and equilibration process in Sec. 5.2, where we in particular show that the spectrum of neutrinos is significantly affected by the higher-order annihilations. In Sec. 5.3, we then use recent data from the IceCube telescope in order to place an upper bound on the normalization of the neutrino flux and employ these limits in order to derive constraints on the parameter space of the Majorana dark matter model, comparing our results to complementary information from direct and other indirect searches.

5.1. Definition of the model and discussion of the dark matter annihilation process

The simplified model studied in this section is defined in an analogous way to the scenarios discussed in Sec. 3 and 4. We extend the Standard Model by a Majorana fermion χ, singlet under the Standard Model gauge group, and by a charged and colored scalar η. The latter particle has gauge quantum numbers $(3, 1, -q_f)$ under $SU(3)_c \times SU(2)_L \times U(1)_Y$, with q_f being the electric charge of the quark coupling to χ and η via a Yukawa interaction. Both of the newly introduced particles are assumed to be odd under a $\mathbb{Z}_2$ symmetry, guaranteeing the stability of the dark matter candidate χ, as long as $m_\chi < m_\eta$. Then, the most general renormalizable Lagrangian is identical to the case of the simplified Dirac dark matter scenario coupling to $f_R = q_R$ as defined in Eqs. (3.1)-(3.6), except that the kinetic and mass

[1] This scenario is closely related to a specific realization of the Minimal Supersymmetric Standard Model (MSSM), namely when the neutralino is a pure bino; in that case, the mediator η can be identified with a corresponding squark. However, in the simplified model approach, the strength of the Yukawa coupling is taken to be a free parameter, while in the MSSM it is fixed by the Standard Model $U(1)_Y$ gauge coupling.

term of a Majorana fermion reads $\frac{1}{2}\bar{\chi}^c i\partial\!\!\!/\chi - \frac{1}{2}m_\chi \bar{\chi}^c\chi$. Most important for the phenomenology of the model, the Yukawa interaction of χ, η and the Standard Model quark q_R is given by

$$\mathcal{L}_{\rm int}^{\rm fermion} = -y\,\eta^\dagger \bar{\chi} q_R + \text{h.c.} \tag{5.1}$$

For concreteness, in the following we focus on the scenarios $q_R = u_R$, representative for dark matter coupling to a light quark, and $q_R = b_R$ as an example for dark matter coupling to a third-generation quark.

The lowest-order annihilation channel of the dark matter candidate is the t-channel mediated process $\chi\chi \to q\bar{q}$, with a cross section given by [347]

$$(\sigma v)_{q\bar{q}} \simeq \frac{3y^4 m_q^2}{32\pi(m_\chi^2 + m_\eta^2)^2} + v^2 \cdot \frac{y^4}{16\pi m_\chi^2}\frac{1 + m_\eta^4/m_\chi^4}{(1 + m_\eta^2/m_\chi^2)^4}\,, \tag{5.2}$$

where we kept only the leading terms in an expansion in m_q^2 and v^2. As for the case of real scalar dark matter discussed in Sec. 4, the s-wave component is helicity suppressed, i.e. it vanishes in the limit $m_q \to 0$. For the physical explanation of this suppression, we refer to Sec. 4.1. On the other hand, in contrast to the scenario involving a real scalar dark matter particle, the p-wave component given by Eq. (5.2) is non-zero in the limit of a vanishing quark mass, leading to qualitative differences between the two models when computing the total annihilation cross section during freeze-out, as we will discuss below.

Analogous to the case of real scalar dark matter, the suppression of the annihilation channel $\chi\chi \to q\bar{q}$ asks for the inclusion of higher-order processes, given by the virtual internal bremsstrahlung (VIB) of a gauge boson, $\chi\chi \to q\bar{q}V$, as well as by the one-loop annihilations into a pair of gauge bosons, $\chi\chi \to VV'$. The cross sections for all relevant processes are summarized in Appendix B.2; most importantly, all of these higher-order annihilation channels feature a s-wave component which is not suppressed by m_q^2/m_χ^2, making them typically dominant over the lowest order $2 \to 2$ process for velocities $v \simeq 10^{-3}$ relevant for dark matter annihilations in our Galaxy. In this section, we mostly focus on the case of small and intermediate mass splittings m_η/m_χ, and hence we will only take into account the VIB processes in the discussion of the dark matter annihilation process[2], as the one-loop annihilations are only relevant for larger mass splittings.

The relative importance of the different VIB processes compared to the lowest-order $2 \to 2$ annihilation channel is illustrated in Fig. 5.1 for the case of dark matter coupling to u_R (b_R) in the upper (lower) panels, employing for concreteness the two exemplary mass splittings $m_\eta/m_\chi = 1.01$ (left panels) and $m_\eta/m_\chi = 2.0$ (right panels). In these plots, we have assumed $v \simeq 10^{-3}$ for the p-wave suppressed annihilation channel $\chi\chi \to q\bar{q}$, appropriate for dark matter annihilations in the galactic halo or in the Sun. Clearly, if χ couples to the up-quark, the $2 \to 2$ annihilation is completely negligible, due to the large suppression of the s-wave component by m_u^2/m_χ^2, c.f. Eq. (5.2). The total annihilation cross section is dominated by the VIB processes, which in the limit $m_\chi \gg m_Z$ are related via

$$\begin{array}{rcccccl} (\sigma v)_{u_R\bar{u}_R g} & : & (\sigma v)_{u_R\bar{u}_R\gamma} & = & 3\alpha_s(m_{\rm DM})/\alpha_{\rm em} & \simeq & 32.2\,, \\ (\sigma v)_{u_R\bar{u}_R Z} & : & (\sigma v)_{u_R\bar{u}_R\gamma} & = & \tan^2(\theta_W) & = & 0.30\,, \end{array} \tag{5.3}$$

as it follows from the cross section expressions presented in Appendix B.2. On the other hand, for dark matter coupling to b_R, the helicity suppression by m_b^2/m_χ^2 is somewhat

[2] We notice, however, that we include the one-loop annihilations into gauge bosons in Sec. 6.2, where we discuss the simplified model of Majorana dark matter in a different context.

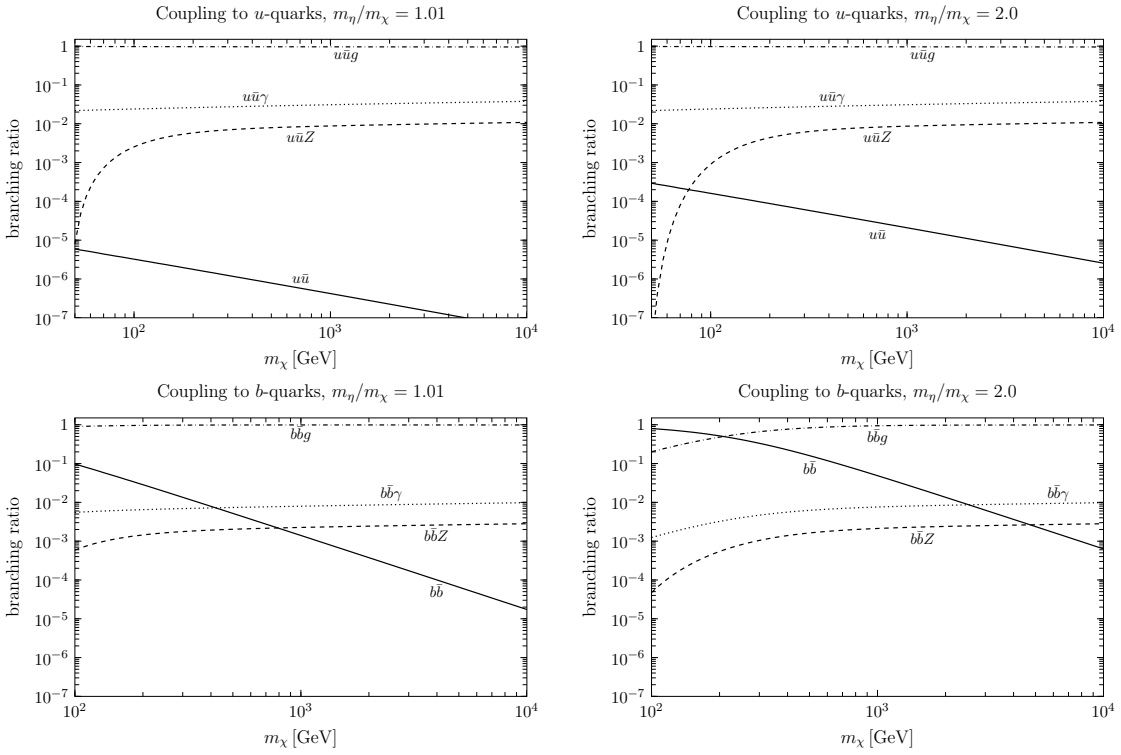

Figure 5.1.: Branching ratios of the annihilation channels $\chi\chi \to q\bar{q}(V)$, with $V \in \{g, \gamma, Z\}$, for q being an up-quark (upper panels) or bottom-quark (lower panels). The left and right panels correspond to a mass ratio $m_\eta/m_\chi = 1.01$ and 2.0, respectively.

alleviated at dark matter masses $\lesssim 100\,\text{GeV}$; still, in most parts of the parameter space, the VIB processes are dominant, with the relative strengths

$$\begin{aligned} (\sigma v)_{b_R\bar{b}_R g} \;&:\; (\sigma v)_{b_R\bar{b}_R\gamma} \;=\; 12\alpha_s(m_\chi)/\alpha_{\text{em}} \;\simeq\; 129\,, \\ (\sigma v)_{b_R\bar{b}_R Z} \;&:\; (\sigma v)_{b_R\bar{b}_R\gamma} \;=\; \tan^2(\theta_W) \;=\; 0.30\,. \end{aligned} \tag{5.4}$$

For concreteness, in Eqs. (5.3) and (5.4) the numerical values of the cross section ratios have been obtained for a strong coupling constant evaluated at the scale $m_\chi \simeq 1\,\text{TeV}$.

During freeze-out, the annihilation channel $\chi\chi \to q\bar{q}$ is suppressed by $\langle v^2 \rangle \simeq 0.2$. Then, for the total annihilation cross section of dark matter entering the Boltzmann equation, we find that in contrast to the scenario of real scalar dark matter in which the lowest-order annihilation process occurs only via the d-wave contribution, the milder suppression in the case of Majorana dark matter makes the higher-order annihilation channels subdominant compared to the tree-level $2 \to 2$ process. Hence, in this section we employ the results of the relic density calculation obtained in [347], which takes into account the annihilation channel $\chi\chi \to q\bar{q}$ as well as all relevant coannihilation processes, analogous to the discussion in Sec. 4.2 [3].

[3] For the calculations in the current section, the Sommerfeld corrections to the coannihilation channels are not included.

5.2. Capture, annihilation and equilibration in the Sun and Earth

Capture rate of dark matter and the equilibrium coupling constant

Both the event rate at a direct detection experiment as well as the capture rate of dark matter particles in the Sun or the Earth depend on the scattering cross section of χ with a nucleon N. Starting from the Yukawa interaction defined in Eq. (5.1), the scattering cross sections for the model of Majorana dark matter have been calculated in [271,272,276], using a similar approach as the one employed in Sec. 3 and 4 for the other t-channel simplified models. The result for the spin-dependent scattering cross section with a nucleon N reads

$$\sigma_{\mathrm{SD}}^{(N)} = \frac{12\mu_N^2}{\pi}\left(\Delta_q^{(N)}\right)^2 \frac{y^4}{64\left[m_\eta^2-(m_\chi+m_q)^2\right]^2}\,, \tag{5.5}$$

where μ_N is the dark matter-nucleon reduced mass, and $\Delta_q^{(N)}$ parametrizes the contribution of the quark $q \in \{u,b\}$ to the spin of the nucleon, as already introduced in Eq. (3.12), with the numerical values given in [276]. In particular, we notice that $\Delta_b^{(N)} \simeq 0$. Furthermore, the spin-independent cross section is given by

$$\sigma_{\mathrm{SI}}^{(N)} = \frac{4\mu_N^2}{\pi}\left(f^{(N)}\right)^2\,, \tag{5.6}$$

with

$$\begin{aligned} f^{(N)} = m_N\Bigg(& f_q^{(N)}\frac{m_\chi}{2}\frac{y^2}{8\left[m_\eta^2-(m_\chi+m_q)^2\right]^2} \\ &+ \frac{3}{2}m_\chi\frac{y^2}{8\left[m_\eta^2-(m_\chi+m_q)^2\right]^2}\left[q^{(N)}(2)+\bar{q}^{(N)}(2)\right]-\frac{8}{9}\pi b f_g^{(N)}\Bigg)\,. \end{aligned} \tag{5.7}$$

Here, b is a function of m_χ, m_η and m_q specified in [92,271]. Moreover, the nuclear parameters $f_q^{(N)}$, $f_g^{(N)}$, $q^{(N)}(2)$ and $\bar{q}^{(N)}(2)$ are the same as those appearing in Eq. (4.23). We remark that in the limit $m_\eta \gg m_\chi$, the spin-dependent cross section scales as $1/m_\eta^4$, while $\sigma_{\mathrm{SI}}^{(N)}$ is suppressed by $1/m_\eta^8$. This is due to the fact that the lowest-order spin-independent operator $\chi\chi\bar{q}q$ vanishes for a chiral coupling of a Majorana fermion [271], and correspondingly the leading-order spin-independent contribution arises from a twist-2 operator similar to the one defined in Eq. (4.19) for the scenario of scalar dark matter. Furthermore, we notice that both the spin-dependent as well as the spin-independent cross section are enhanced for mass-degenerate scenarios, i.e. when the mediator η is only slightly heavier than the dark matter particle χ. We avoid complications arising from the apparent divergence of $f^{(N)}$ at $m_\eta = m_\chi + m_q$, which would require the modeling of the width of the exchanged scalar, by restricting our analysis to values of the model parameters satisfying $m_\eta - m_\chi \geq 2m_q$.

As introduced in detail in Sec. 2.2, the scattering process with a nucleus can lead to the capture of the dark matter particle in a celestial object like the Sun or the Earth. For given values of $\sigma_{\mathrm{SI}}^{(N)}$ and $\sigma_{\mathrm{SD}}^{(N)}$, we calculate the capture rate C using DarkSUSY [149], adopting for concreteness the local dark matter density $\rho_0 = 0.4\,\mathrm{GeV/cm^3}$, as well as a Maxwell-Boltzmann velocity distribution with the most probable speed $v_0 = 230 \pm 30\,\mathrm{km/s}$, c.f. Sec. 1.2. For the case of capture in the Sun, an approximate expression for C valid

for $m_\chi \gtrsim 1\,\text{TeV}$ is given in Eq. (2.14). Following the discussion in Sec. 2.2, observing the neutrino flux produced by the annihilations of dark matter particles accumulated the center of the Sun or the Earth is only feasible if captures and annihilations have reached equilibrium. This is the case if the age of the solar system $t_\odot = 4.5 \cdot 10^9\,\text{y}$ is sufficiently larger than the equilibration time $\tau \equiv 1/\sqrt{C \cdot C_A}$, where C_A is the annihilation constant given in Eq. (2.17) and (2.18) for the case of the Sun and the Earth, respectively. For the total annihilation cross section (σv) entering the expressions for C_A, we use the sum of the lowest-order $2 \to 2$ and the various $2 \to 3$ annihilation channels discussed in the previous section.

In order to quantify whether equilibrium has been reached within the simplified model of Majorana dark matter, one can make use of the fact that both C and C_A are proportional to y^4, allowing us to define the *equilibrium coupling constant* y_{eq} via

$$t_\odot \sqrt{C\big|_{y=1} C_{\text{A}}\big|_{y=1}}\, y_{\text{eq}}^4 \stackrel{!}{=} 1\,. \tag{5.8}$$

In that way, the ratio between the annihilation rate Γ_A, which sets the normalization of the neutrino flux, and the capture rate C is given by

$$\frac{2\Gamma_{\text{A}}}{C} = \tanh^2\left[\left(\frac{y}{y_{\text{eq}}}\right)^4\right]\,. \tag{5.9}$$

Hence, the equilibrium coupling constant serves as a lower limit on the coupling strength following from the requirement of equilibration: for $y \gtrsim y_{\text{eq}}$, the annihilation rate Γ_A reaches exponentially fast the maximal value $C/2$, while for $y \lesssim y_{\text{eq}}$ it decreases as $(y/y_{\text{eq}})^8$. For example, for $y = y_{\text{eq}}/2$, the signal strength is about 0.4 % of the maximal value.

The upper and lower panels of Fig. 5.2 show the values of the equilibrium coupling constant y_{eq} relevant for capture and annihilation in the Sun and in the Earth, respectively, with the left (right) panels corresponding to the scenario of dark matter coupling to u_R (b_R). In each plot, the red curves show the dependence of y_{eq} on the dark matter mass, for a few exemplary choices of the mass ratio m_η/m_χ. If the scattering process is dominated by the spin-independent interaction, as it is the case for coupling to b_R, the equilibrium coupling constant scales as $m_\chi^{17/16}$ for a fixed mass splitting m_η/m_χ, while it is proportional to $m_\chi^{13/16}$ for a scenario in which the spin-dependent scattering is more important, relevant for coupling to u_R [4]. For comparison, we also show in the figure the values of the coupling y_{thermal} implied by the constraint of matching the observed relic density via the freeze-out mechanism, following the discussion in Sec. 5.1. Similar as in the corresponding models involving Dirac or real scalar dark matter, for mass-degenerate scenarios there is a lower limit on the dark matter mass below which coannihilations suppress the relic density to values smaller than the observed one, irrespectively of the choice of y.

For the case of thermally produced dark matter coupling to u_R, it follows from the upper left panel of Fig. 5.2 that equilibration of capture and annihilation in the Sun is only reached within certain ranges of dark matter masses. Concretely, the requirement of equilibrium leads to the lower limit $m_\chi \gtrsim 1\,\text{TeV}$ and $m_\chi \gtrsim 200\,\text{GeV}$ for $m_\eta/m_\chi = 1.01$ and

[4] These scalings with m_χ follow from $(\sigma v) \propto m_\chi^{-2}$, leading to $C_{\text{A}}\big|_{y=1} \propto m_\chi^{-1/2}$, as well as from $\sigma_{\text{SD}}^{(N)} \propto m_\chi^{-4}$, $\sigma_{\text{SI}}^{(N)} \propto m_\chi^{-6}$, implying $C\big|_{y=1} \propto m_\chi^{-6}$ and $C\big|_{y=1} \propto m_\chi^{-8}$ for the spin-dependent and spin-independent capture rate, respectively. Together with the definition of y_{eq} in Eq. (5.8), we obtain $y_{\text{eq}} \simeq m_\chi^{13/16}$ and $y_{\text{eq}} \simeq m_\chi^{17/16}$ for a scenario in which the capture is dominated by spin-dependent and spin-independent scatterings, respectively.

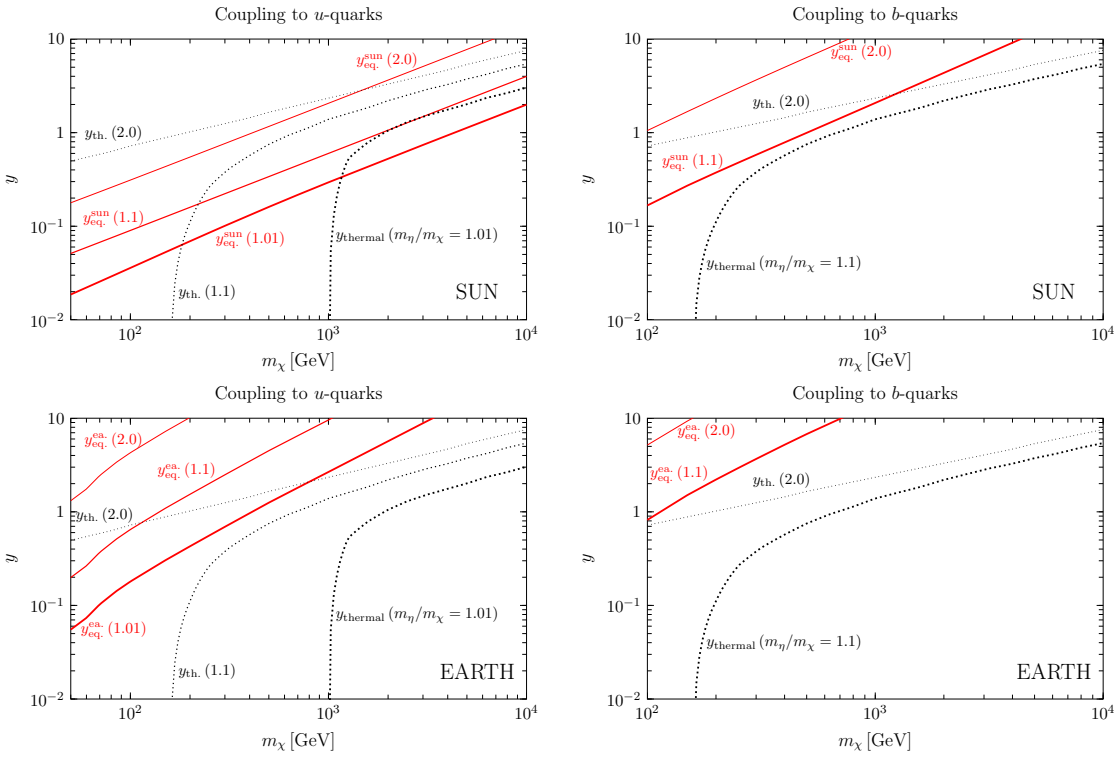

Figure 5.2.: The red curves show the equilibrium coupling constant $y_{\rm eq}$, defined as the lower limit on the Yukawa coupling arising from the requirement of equilibration between capture and annihilation in the Sun and in the Earth, shown in the upper and lower panels, respectively, for coupling to u_R (left panels) and to b_R (right panels). Also, the black dashed curves indicate the values of the Yukawa coupling $y_{\rm thermal}$ following from the relic density constraint.

1.1, respectively, while for a mass splitting $m_\eta/m_\chi = 2.0$, equilibrium is only achieved for $m_\chi \lesssim 1\,\text{TeV}$. For dark matter masses not fulfilling these conditions, the annihilation rate Γ_A and consequently also the neutrino flux observable at Earth is significantly suppressed, c.f. Eq. (5.9). Similarly, the upper right panel of Fig. 5.2 shows the relation between $y_{\rm eq}$ and $y_{\rm thermal}$ for the scenario of dark matter coupling to b_R, again for capture and annihilation in the Sun. Interestingly, the absence of a spin-dependent scattering cross section arising from a coupling to the bottom quark leads to the conclusion that thermally produced dark matter is *not* in equilibrium in the Sun in that scenario (at least for the choices of the mass splitting shown in the figure). Consequently, the simplified model of Majorana dark matter coupling to b_R is a concrete example in which the common assumption $\Gamma_A = C/2$ is not fulfilled.

Finally, the lower panels of Fig. 5.2 show the equilibrium coupling constant relevant for capture and annihilation in the Earth, which we again compare to the thermal value of the Yukawa coupling. As apparent from the plots, within the framework discussed in this section, thermally produced dark matter can never be in equilibrium in the Earth, making the prospects to observe the corresponding neutrino flux rather poor. Consequently, in the following we will not further discuss the case of capture and annihilation of Majorana dark matter in the Earth, and instead focus on the more promising possibility to observe the

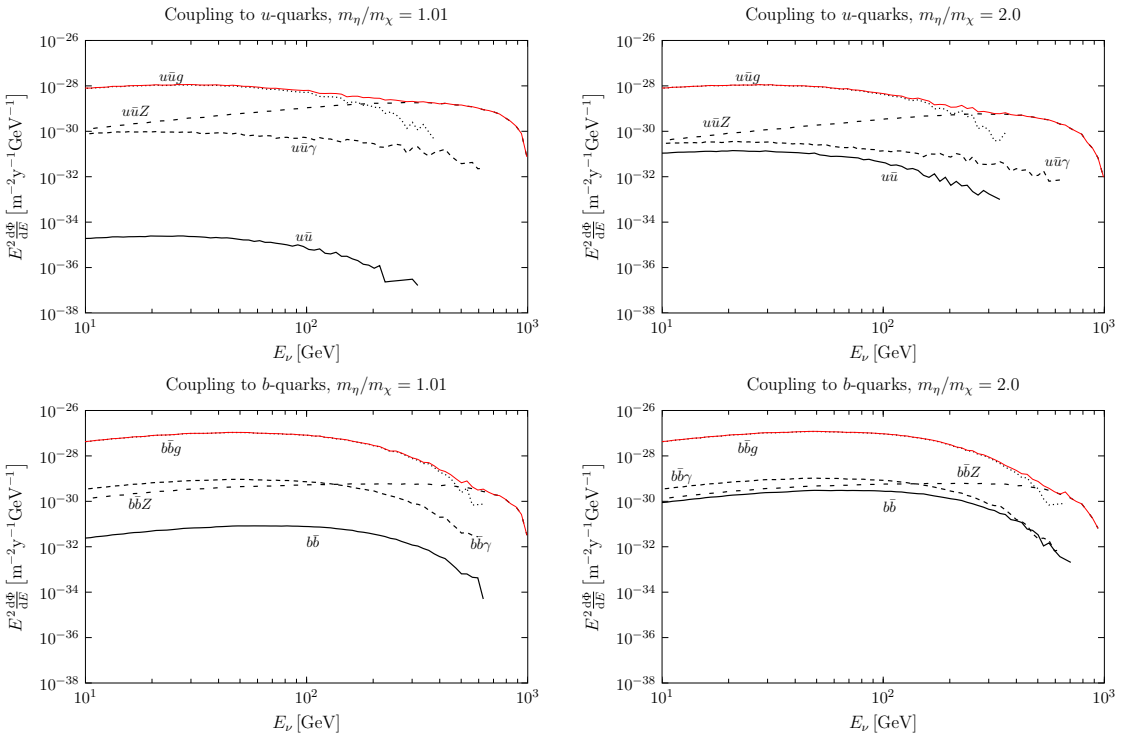

Figure 5.3.: Sum of the differential ν_μ and $\bar{\nu}_\mu$ flux at Earth, produced by annihilations of dark matter particles with $m_\chi = 1\,\mathrm{TeV}$. The upper (lower) panels correspond to coupling to u_R (b_R), while the left and right panels show the results for two different mass ratios, $m_\eta/m_\chi = 1.01$ and 2.0, respectively.

high-energy neutrinos arising from dark matter annihilations in the Sun.

High-energy neutrino flux from the Sun

According to the previous discussion, at least in parts of the parameter space of the model, captures and annihilations of thermally produced Majorana dark matter are in equilibrium in the Sun, leading to a high-energy neutrino flux potentially observable at Earth, with a normalization proportional to the dark matter-nucleon scattering cross section. The neutrinos arise from the hadronization and decays of the quarks and gauge bosons produced in the annihilation channels $\chi\chi \to q\bar{q}(V)$; c.f. Sec. 5.1 for a discussion of the branching ratios. For the modeling of this process in the dense environment of the Sun, as well as of the subsequent propagation of the neutrinos from the point of annihilation to the location of the Earth, we refer to the detailed discussion in Sec. 2.2. We show in Fig. 5.3 the resulting differential flux of muon neutrinos and antineutrinos at Earth, produced by the annihilation of Majorana dark matter particles with a mass $m_\chi = 1\,\mathrm{TeV}$, for coupling to u_R (b_R) in the upper (lower) panels, and for the exemplary mass splittings $m_\eta/m_\chi = 1.01$ and 2.0 in the left and right panels, respectively. In each case, the total flux is shown as the red solid curve, while the various black lines correspond to the contributions of the individual annihilation channels.

For the case of dark matter coupling to u_R, the neutrino flux at energies $E_\nu \lesssim 200\,\mathrm{GeV}$ is dominated by the gluon bremsstrahlung process, due to the large branching fraction of this

annihilation channel, c.f. Fig. 5.1. However, it follows from the upper panels of Fig. 5.3 that for larger neutrino energies, the dominant contribution arises from annihilations into $u\bar{u}Z$, even though this channel has a significantly smaller branching fraction than the $u\bar{u}g$ final state. This can be understood by recalling from the discussion in Sec. 2.2 that the baryons and mesons produced by the hadronization of quarks or gluons lose a significant amount of their energy before decaying (or are even stopped completely), leading to a suppressed flux of neutrinos with the highest kinematically allowed energies. On the other hand, the Z boson produced in the annihilation process $\chi\chi \to u\bar{u}Z$ can decay promptly into a pair of neutrinos, leading to the dominant contribution to the total flux at large E_ν. As we will see below, the IceCube detector is mainly sensitive to large neutrino energies, making the VIB of a Z boson particularly important in the calculation of the limits on the model.

From the lower panels of Fig. 5.3, it follows that also for dark matter coupling to b_R, the virtual internal bremsstrahlung of a Z boson dominates the spectrum at the highest possible neutrino energies. However, in that case the annihilation into $q\bar{q}g$ gives a larger contribution compared to the case of coupling to u_R, as there are significantly more high-energetic neutrinos produced by the hadronization of the bottom-quark than of the up-quark, c.f. the discussion in Sec. 2.2. In addition, we remark that the ratio of the branching fractions of the $q\bar{q}Z$ and $q\bar{q}g$ channels is smaller for coupling to b_R than for coupling to u_R, as it follows from Eqs. (5.3) and (5.4).

5.3. Constraints on the parameter space of Majorana dark matter

The flux of muon (anti-)neutrinos produced by the annihilations of dark matter particles in the Sun gives rise to an (anti-)muon signal in a neutrino telescope, via the charged current interaction $\overset{(-)}{\nu}_\mu N \to \mu^\pm N'$ (see also the discussion in Sec. 2.2). For a given neutrino spectrum derived by means of the methods presented in the previous section, we compute the number of induced (anti-)muon events in the IceCube detector following the approach of [349], and using the effective area given in [167]. The expected number of signal events is then compared to the actual data [168], thereby taking into account the background induced by the atmospheric neutrino flux, which we also take from [168]. We refer to Appendix C for further details regarding our method of calculating limits from the IceCube data.

For given values of m_χ and m_η, we convert the upper limit on the normalization of the neutrino flux into a constraint on the Yukawa coupling y. For the scenario of dark matter coupling to u_R, the resulting limits are shown in Fig. 5.4 as a function of the dark matter mass, with each panel corresponding to a different value of the mass splitting, $m_\eta/m_\chi = 1.01$, 1.1 and 2.0. The width of each light red band corresponds to the systematic uncertainties relevant for the calculation of the upper limit following from the IceCube data: first, the dependence of the capture rate on the abundances and spatial distributions of the solar nuclei leads to an uncertainty of $\simeq 3\%\,(25\%)$ in the determination of the spin-dependent (spin-independent) capture rate [167]. Moreover, following [347], we take into account uncertainties related to the parameter v_0 of the Maxwell-Boltzmann velocity distribution, as well as the nuclear parameters $\Sigma_{\pi n}$, σ_0, $q(2)$ and $\bar{q}(2)$.

Furthermore, in Fig. 5.4 we compare the upper limits arising from the non-observation of an excess of high-energy neutrinos from the direction of the Sun by the IceCube telescope with complementary searches for dark matter studied in [347]. Namely, the upper limits

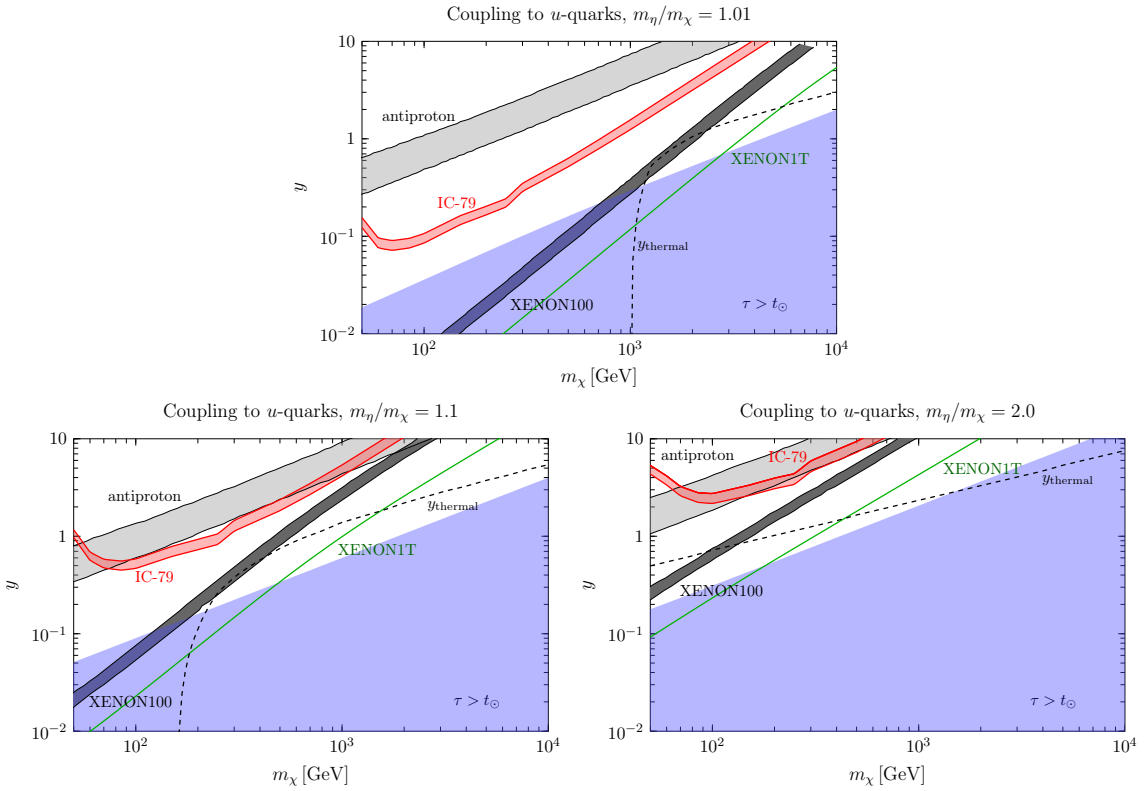

Figure 5.4.: Upper limits on the Yukawa coupling y, for a scenario of Majorana dark matter coupling to u_R, and for a mass splitting $m_\eta/m_\chi = 1.01$ (upper panel), 1.1 (lower left panel) and 2.0 (lower right panel). The constraints from IceCube are shown in light red, from XENON100 in dark gray, and from the PAMELA $\bar{p}/p$ data in light gray. In each case, the width of the band indicates the level of systematic uncertainties in deriving the limits. The shaded blue region shows the region of the parameter space where captures and annihilations are not in equilibrium in the Sun, while the black dashed curves depict the values of the Yukawa coupling leading to the observed relic abundance via dark matter freeze-out. Finally, the prospected reach for XENON1T is shown as a green line.

on y resulting from the XENON100 experiment are shown as the dark gray shaded bands[5], while the constraints following from the non-observation of an excess in the PAMELA $\bar{p}/p$ ratio correspond to the light gray shaded bands. Again, the width of each band shows the impact of the astrophysical and nuclear uncertainties. It follows from the three different panels of Fig. 5.4 that the IceCube constraints derived in this work are competitive, or in the case of small mass splittings m_η/m_χ even better than the PAMELA antiproton limits. On the other hand, XENON100 provides stronger limits in all of the parameter space, which can be explained by the significant spin-independent scattering cross section induced by the Majorana dark matter model, c.f. Sec. 5.2, which is known to be better constrained by direct detection experiments than by neutrino telescopes.

Besides, the shaded blue region in each panel of Fig. 5.4 corresponds to the values of the

[5] After the results of this section have first been published, the XENON100 limits were superseded by the LUX results [101, 102]. These would lead to (slightly) stronger direct detection constraints, but we have checked that the qualitative conclusions remain unchanged.

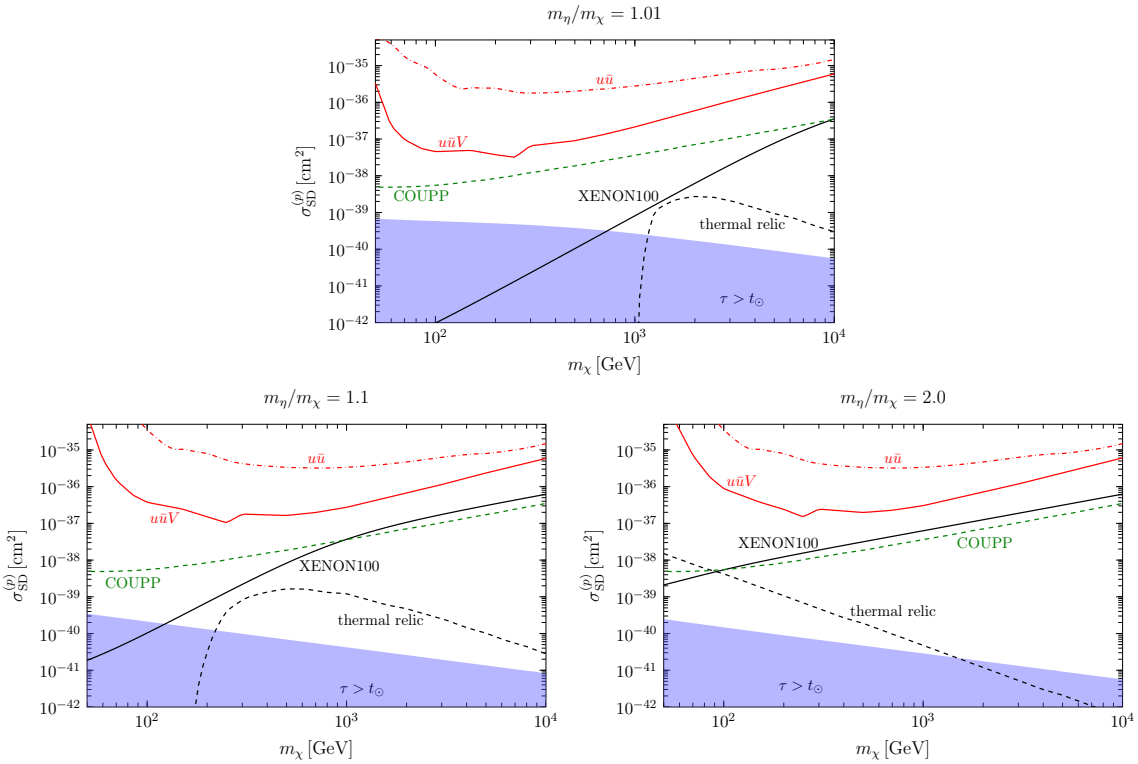

Figure 5.5.: Upper limits on the spin-dependent cross section with protons, following from the corresponding constraints on the Yukawa coupling y presented in Fig. 5.4. The full results from the IceCube analysis (including the higher-order annihilation channels) are shown as red solid curves, while the red dashed curves correspond to a calculation only taking into account the lowest-order annihilation channel $\chi\chi \to u\bar{u}$. Furthermore, the upper limit on $\sigma_{\rm SD}^{(p)}$ arising from the COUPP data is shown as a green dashed line. All other curves are analogous to the ones shown in Fig. 5.4.

Yukawa coupling for which captures and annihilations of dark matter particles in the Sun are not in equilibrium, based on the definition of the equilibrium coupling constant $y_{\rm eq}$ in Sec. 5.2. In these parts of the parameter space, the annihilation rate is highly suppressed with respect to the equilibrium value, c.f. Eq. (5.9), and hence observing the neutrino flux is very challenging both for current and future experiments. As it can be seen from the plots, in particular the XENON100 experiment already probes a significant fraction of the parameter space in which dark matter is in equilibrium in the Sun, and in some cases it actually excludes the equilibrium coupling constant $y_{\rm eq}$. This conclusion will be further strengthened by future direct detection experiments such as XENON1T, which will be able to probe Yukawa couplings smaller by a factor $\simeq 60^{1/4} = 2.78$ compared to the ones constrained by the XENON100 experiment. Lastly, we remark that from comparing Fig. 5.2 and Fig. 5.4 it follows that XENON100 excludes all values of the Yukawa coupling leading to equilibration in the Earth, making the observation of a high-energy neutrino flux from dark matter annihilations in Earth very unlikely within this scenario.

The results of neutrino telescopes searching for a dark matter induced flux from the direction of the Sun are typically presented in the parameter space spanned by the dark matter mass and the spin-dependent scattering cross section with protons. Hence, for illustration

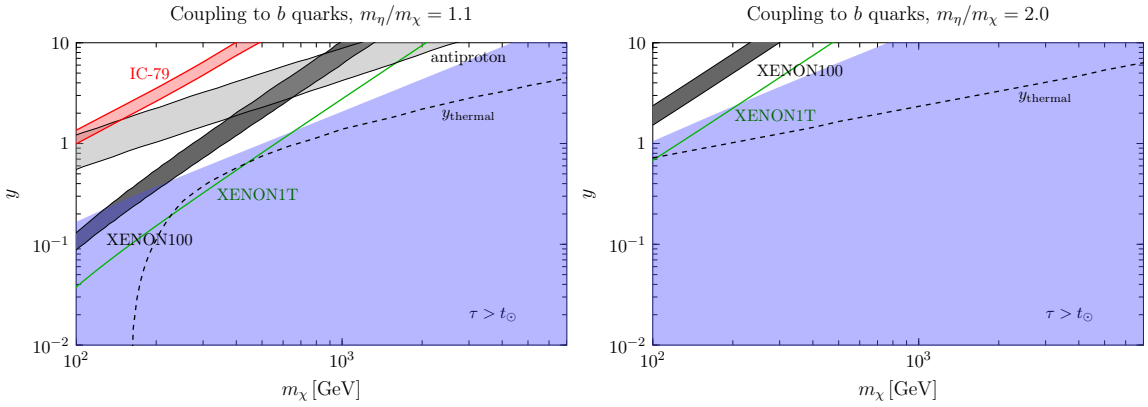

Figure 5.6.: Same as Fig. 5.4, but for dark matter coupling to b_R.

we translate the upper limits on y presented in Fig. 5.4 into upper limits on $\sigma_{\rm SD}^{(p)}$, using Eq. (5.5), and show the results in the different panels of Fig. 5.5. In order to highlight the importance of including the higher-order corrections to the annihilation process, we show both the upper limit obtained from the full calculation including all annihilation channels $\chi\chi \to u\bar{u}V$ (red solid curves), as well as the upper limit that would follow from assuming a 100% branching fraction of the lowest-order channel $\chi\chi \to u\bar{u}$ (red dashed curves). Evidently, the presence of the $2 \to 3$ processes significantly improves the sensitivity of IceCube to the model of Majorana dark matter, for all vales of m_χ and m_η. For comparison, we also show the upper limits on the spin-dependent cross section following from the COUPP [120] and XENON100 experiments, thereby choosing the astrophysical and nuclear parameters among those suggested in [347] leading to the most conservative constraints[6].

Analogously to Fig. 5.4 showing the constraints for dark matter coupling to u_R, we present in Fig. 5.6 the upper limits on y for coupling to b_R. As discussed in Sec. 5.2, we restrict our analysis to $m_\eta - m_\chi > 2m_q$, in order to avoid the modeling of the resonant behavior of the scattering cross section at $m_\eta = m_\chi + m_q$. Hence, in Fig. 5.6 we only show our results for $m_\eta/m_\chi = 1.1$ and 2.0, and for $m_\chi > 100\,\text{GeV}$. It follows from the plots that compared to the scenario of dark matter coupling to the up-quark, the IceCube limits are significantly weaker for coupling to the bottom-quark, which can be explained by the absence of a spin-dependent coupling to protons, c.f. Sec. 5.2. In particular, the upper limits on y following from the PAMELA measurement of $\bar{p}/p$ as well as from the null results of the XENON100 experiment are always stronger than the constraints arising from the IceCube data.

Finally, we compare the various upper limits on the Yukawa coupling y to the values $y_{\rm thermal}$ following from the requirement of correctly reproducing the observed relic density via the freeze-out mechanism, c.f. Sec. 5.1. To this end, all panels of Figs. 5.4, 5.5 and 5.6 include a black dashed curve indicating the coupling (or scattering cross section) expected for a thermal relic. These figures suggest that the results from IceCube are not (yet) constraining the thermal parameter space of the model, while for some values of m_χ and m_η, XENON100 already excludes Yukawa couplings smaller than $y_{\rm thermal}$.

[6] We stress that the XENON100 limits in Fig. 5.5 correspond to the upper limit on $\sigma_{\rm SD}^{(p)}$ within the specific scenario discussed in this section, which also leads to a spin-independent scattering cross section, c.f. Eq. (5.6). Hence, the corresponding curves differ from those reported in [105, 350], which implicitly assume $\sigma_{\rm SI}^{(N)} \equiv 0$.

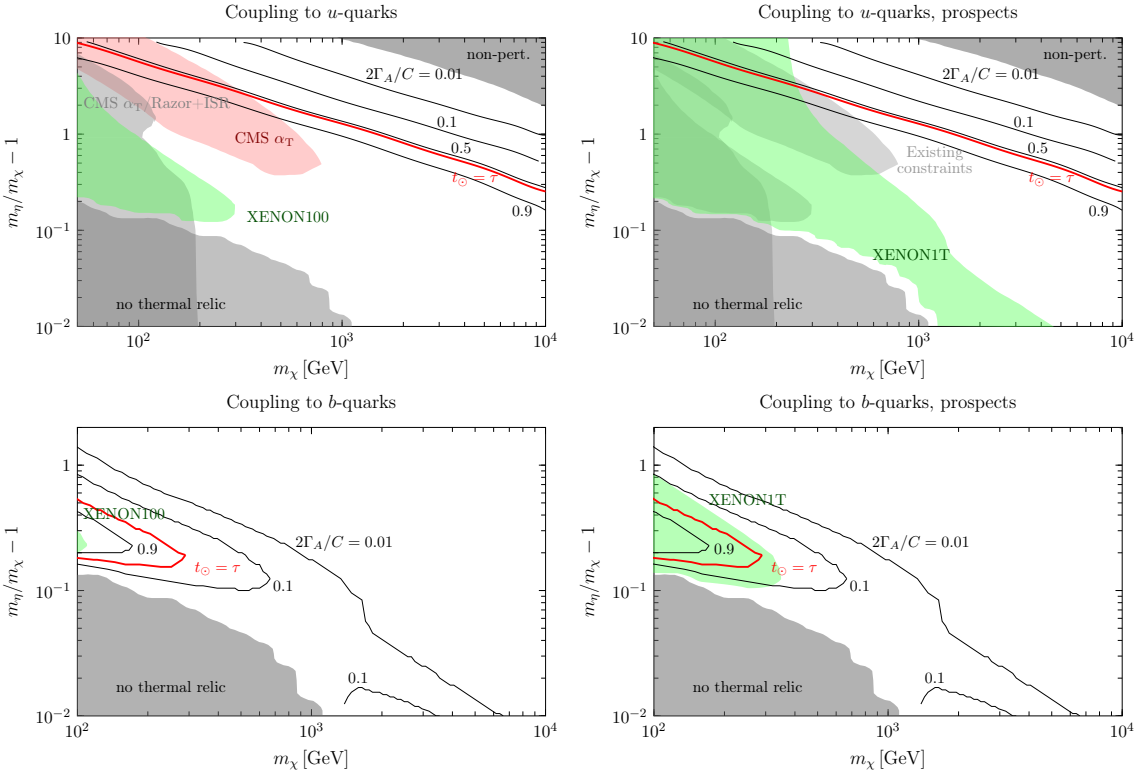

Figure 5.7.: Thermal parameter space of the simplified model of Majorana dark matter, for coupling to u_R (upper panels) and to b_R (lower panels). The light gray shaded regions are theoretically inaccessible, either due to efficient coannihilations for small values of m_χ and m_η/m_χ, or because the model becomes non-perturbative at large values of the masses. In the left panels, we show the constraints from XENON100 (light green) and from CMS (light red), as well as contours of constant $2\Gamma_A/C$, determining whether captures and annihilations are in equilibrium in the Sun, c.f. the discussion in the text. In addition, the right panels show the reach of XENON1T.

We further investigate the thermal parameter space of the model in Fig. 5.7, for dark matter coupling to u_R (b_R) in the upper (lower) panels, with the left panels corresponding to constraints from existing searches, while the right panels show the prospects to probe the model with future experiments. Similar to the related figures for Dirac dark matter and real scalar dark matter shown in Figs. 3.4, 3.5 and Figs. 4.10, 4.17, respectively, we fix the Yukawa coupling y to the thermal value y_{thermal} separately for each dark matter mass m_χ and mass splitting m_η/m_χ. As for the other t-channel simplified models, the region of the parameter space corresponding to small m_χ and m_η/m_χ is theoretically inaccessible due to efficient coannihilations, while for large values of the dark matter and mediator mass, the model becomes non-perturbative. These parts of the parameter space are shown as the gray shaded regions in each panel of Fig. 5.7. Besides, the green shaded regions in the left panels show the parts of the parameter space which are excluded by the XENON100 analysis presented in [321], while they correspond to the reach of XENON1T in the right panels. Furthermore, also following [321], in the upper left panel we include as a light red region the constraints on the parameter space arising from the search of a colored scalar by the CMS collaboration, using the α_T analysis at $\sqrt{s} = 8\,\text{TeV}$ [351]. Indirect searches

for antiprotons or neutrinos are not able to constrain the thermal values of the Yukawa coupling, c.f. Figs. 5.4 and 5.6, and are hence not included in Fig. 5.7. Furthermore, we show in the plots contours of constant values of $2\Gamma_A/C$ (black curves), and in particular the curve corresponding to $t_\odot = \tau$ (red curve), marking our definition of the boundary between equilibrium and non-equilibrium of captures and annihilations in the Sun.

As apparent from the upper left panel of Fig. 5.7, the XENON100 experiment provides the strongest limit on the scenario of Majorana dark matter coupling to u_R for small values of the mass splitting m_η/m_χ, while for larger mass splittings the CMS search gives rise to the most important constraint. Qualitatively, this is similar to the complementarity found for real scalar dark matter coupling to quarks, as shown in Fig. 4.17. Moreover, the upper right panel shows that the XENON1T experiment will probe a significant part of the remaining thermal perturbative parameter space; again, this is a similar conclusion as for the related simplified models of Dirac and real scalar dark matter. Furthermore, it follows from the lower left panel of Fig. 5.7 that for coupling to bottom quarks, present experiments are largely insensitive to the thermal values of the Yukawa coupling, except for the XENON100 experiment at small dark masses and $m_\eta/m_\chi \simeq 1.15$. However, it is worth noting that the XENON1T experiment will probe precisely the parts of the parameter space in which dark matter is in equilibrium in the Sun, as it can be seen from the lower right panel of the same figure. Consequently, within the scenario of dark matter coupling to b_R, the non-observation of a signal at XENON1T would make the possibility of detecting a high-energy neutrino signal with future upgrades of the IceCube detector (or any other neutrino telescope) highly unlikely.

Interlude: t-channel simplified models and beyond

The preceding part of this thesis has been devoted to the study of direct, indirect and collider searches for dark matter in the context of *t-channel simplified models*, i.e. scenarios in which the dark matter particle interacts with a Standard Model fermion f and a mediator particle via a Yukawa interaction. Concretely, we have investigated Dirac dark matter interacting with a charged scalar mediator in Sec. 3, real scalar dark matter coupling to a vector-like fermionic mediator in Sec. 4, and lastly a scenario of Majorana dark matter involving a charged scalar mediator in Sec. 5.

Despite being quite similar in their basic structure, we have learned that the phenomenologies of these models differ significantly from case to case. In order to facilitate a simple comparison between some of the most important features of the different scenarios, we present in Table 5.1 a schematic overview of the three t-channel simplified models listed above, working for simplicity in the limit $m_f \equiv 0$. Concretely, in the column labeled by $(\sigma v)_{f\bar{f}}$, we indicate whether in the corresponding model the tree-level annihilation $\mathrm{DM}\,\mathrm{DM} \to f\bar{f}$ is p- or d-wave suppressed, corresponding to $(\sigma v)_{f\bar{f}} \propto v^2$ and v^4, respectively, or whether it features a non-vanishing s-wave component $\propto v^0$. As discussed in the previous sections, this behavior can be crucial both for the physics of dark matter freeze-out as well as for the total annihilation cross section in today's Universe (c.f. the fourth column of Table 5.1).

Moreover, in the table we summarize (in a simplified fashion) the feasibility of probing the simplified models with direct detection experiments as well as with indirect searches using gamma-ray spectral features. To this end, we specify the most important process(es) contributing to the dark matter-nucleon scattering rate in a xenon experiment, and classify each resulting constraint from the LUX or XENON100 experiment as follows: a "strong" constraint corresponds to a situation in which thermally produced dark matter with $m_{\mathrm{DM}} = 1\,\mathrm{TeV}$ is already excluded for some values of the mass splitting between the dark matter particle and the mediator. On the other hand, the label "intermediate" implies that at least one point of the thermal parameter space is ruled out, while "no constraint" means that currently no direct detection experiment can probe the model. Lastly, we illustrate the relevance of searches for gamma-ray spectral features in each simplified model by quoting a representative value of the annihilation cross section for the VIB process $\mathrm{DM}\,\mathrm{DM} \to f\bar{f}\gamma$, choosing for concreteness $m_{\mathrm{DM}} = 600\,\mathrm{GeV}$ and a mass splitting of 1.2, again employing the relic density requirement for fixing the value of the Yukawa coupling. If the value for $(\sigma v)_{f\bar{f}\gamma}$ is written in red color, that point of the parameter space is ruled out by the H.E.S.S. analysis [211, 321], while it is shown in green if it is still allowed by the data.

For the case of Dirac and real scalar dark matter, all the results employed in Table 5.1 are taken from Sec. 3 and 4 of this work[7]. Moreover, for the simplified model of Majorana dark matter, we partially use the results of [321, 347].

[7] For simplicity, here we set the coupling of the real scalar dark matter particle to the Standard Model Higgs doublet to zero. Furthermore, we remark that we have not analyzed the scenario of a real scalar dark matter particle coupling to $f \in \{c, s, b\}$, and hence omit this case in Table 5.1.

	coupling to	$(\sigma v)_{f\bar{f}}$	dominant annihilation mode		direct detection		$\frac{(\sigma v)_{f\bar{f}\gamma}}{10^{-28}\,\mathrm{cm}^3/\mathrm{s}}$
			at freeze-out	today	contributing processes	resulting constraint	
Dirac DM	$f \in \{u, d\}$	$\propto v^0$	$f\bar{f}$		vector coupling (tree level)	strong	–
	$f \in \{c, s, b\}$				magnetic dipole mom., charge radius (one loop)	intermediate	–
	$f \in \{e^-, \mu^-, \tau^-\}$					strong	–
Majorana DM	$f \in \{u, d\}$	$\propto v^2$	$f\bar{f}$	$f\bar{f}V$ or VV'	scalar, axial-vector and twist-2 quark coupling (tree level),	intermediate	**0.63**
	$f \in \{c, s, b\}$				scalar gluon coupling (one loop)		**0.16**
	$f \in \{e^-, \mu^-, \tau^-\}$				anapole moment (one loop)	no constraint	**1.6**
Real scalar DM	$f \in \{u, d\}$	$\propto v^4$	$f\bar{f}V$ or VV'	$f\bar{f}V$ or VV'	scalar and twist-2 quark coupling (tree level), scalar gluon coupling (one loop)	strong	**3.5**
	$f \in \{e^-, \mu^-, \tau^-\}$		$f\bar{f}$		two-loop suppressed	no constraint	**72**

Table 5.1.: Summary of important properties of the simplified models of Dirac, Majorana and real scalar dark matter, coupling to a Standard Model fermion f via a Yukawa interaction. In the columns specifying the dominant annihilation modes, V and V' denote Standard Model gauge bosons. In the last column, we quote the annihilation cross section for the VIB process $\mathrm{DM\,DM} \to f\bar{f}\gamma$ with f being either u, b or e^-, choosing for concreteness $m_{\mathrm{DM}} = 600\,\mathrm{GeV}$ and a mass splitting of 1.2. See the text for other details relevant for the content of this table.

As it can be seen from Table 5.1, the t-channel simplified models discussed in this work already capture a large variety of non-trivial features in the phenomenology of dark matter searches, such as p- or d-wave suppressed $2 \to 2$ annihilations, the importance of higher-order corrections to the annihilation process both today and at freeze-out, strong constraints from direct detection experiments induced solely by one-loop diagrams, and a large spread of the annihilation cross section into final states involving a gamma ray spectral feature. By employing data from future experiments, all of these differences potentially allow for a discrimination between the corresponding scenarios.

Nevertheless, it is clear that by no means all of the possible models involving a WIMP as the dark matter candidate are described by a t-channel simplified model. For example, dark matter could annihilate into Standard Model particles via the exchange of a scalar or a vector boson in the s-channel, or it could be part of a much more complicated "dark sector", including potentially many more particles relevant for the phenomenology of direct, indirect and collider searches. Obviously, it is impossible to extend the model-specific studies undertaken in the previous sections of this thesis to all conceivable scenarios of dark matter. In view of that situation, we will now turn away from the approach of interpreting experimental data in terms of simplified models, and perform a series of investigations which all aim at extracting as much *model-independent* information as possible from the results of direct and indirect detection experiments.

To this end, we reinvestigate in Sec. 6 the higher-order effects to the annihilation process of dark matter in the Sun, which already have been studied in Sec. 5 in the context of the simplified Majorana dark matter model. We will derive constraints on the scattering cross section of dark matter for a large variety of possible annihilation channels, this time without specifying an underlying particle physics model. Afterwards, in Sec. 7, we study the (almost) model-independent non-relativistic effective theory for dark matter-nucleon interactions, which can be seen as a generalization of the standard spin-independent or spin-dependent interactions. Concretely, we employ this framework in order to evaluate the compatibility of the DAMA modulation signal with the null results of (in)direct searches. Lastly, in Sec. 8, we develop a novel method for analyzing data from direct detection experiments and neutrino telescopes, which, while still referring to a specific model of dark matter-nucleon interactions, is model-independent from the point of view of astrophysics, i.e. it does not refer to a particular velocity distribution of dark matter.

Part III

MODEL-INDEPENDENT METHODS

6. General analysis of higher-order effects in dark matter annihilations in the Sun

We start the discussion of model-independent methods in the phenomenology of dark matter searches by a general analysis of the higher-order effects in the annihilation process of dark matter particles captured in the Sun. One concrete example for the importance of taking into account these processes has been discussed in Sec. 5: in the simplified model of Majorana dark matter coupling chirally to a Standard Model fermion, the virtual internal bremsstrahlung of a Z boson constitutes the dominant source of neutrinos at the largest possible energies. Despite being suppressed by a weak gauge coupling and the three-body phase space, this process turned out to be important, as the baryons and mesons produced in the hadronization of up-quarks and gluons are mostly stopped in the dense environment of the Sun before they decay (c.f. the discussion in Sec. 2.2), and hence lead to a suppressed high-energy neutrino flux.

More generally speaking, it is well known that there are actually several lowest-order $2 \to 2$ annihilation channels for which the limits on the dark matter scattering cross section deduced from neutrino telescopes are either absent or very weak: besides the light quark final states $q\bar{q}$, with $q = u, d, s$, also annihilations into e^+e^- or $\mu^+\mu^-$ only produce a flux of neutrinos with energies in the MeV range, well below the detection threshold of IceCube[1], as discussed in Sec. 2.2. However, as all Standard Model fermions carry non-zero hypercharge, the annihilation into a light fermion-antifermion pair is necessarily accompanied by the emission of Z bosons, either via final state radiation, virtual internal bremsstrahlung, or by means of one-loop annihilations into gauge boson pairs. Additionally, if the corresponding fermion is part of a $SU(2)_L$ doublet, also final states involving $W^\pm$ bosons are present. The prompt decays of the weak gauge bosons into neutrinos or tau leptons then lead to a high-energy flux of neutrinos potentially observable at instruments like IceCube, hence opening a new door for probing models of dark matter where the annihilation is driven by couplings to electrons, muons or light quarks. In this section we will investigate this possibility, and in particular, by assuming equilibrium between captures and annihilations of dark matter in the Sun, we will employ recent data from the IceCube neutrino detector in order to derive for the first time model-independent upper bounds on the scattering cross section of dark matter with nucleons from the neutrino flux generated by these higher-order processes.

This section is organized as follows: in Sec. 6.1, we consider a general setup of dark matter annihilations into a light fermion-antifermion pair mediated by a contact interaction (without referring to a specific model), and investigate the phenomenology of the higher-order annihilation channels leading to a high-energy neutrino flux. More precisely, the relevant processes are either the final state radiation of gauge bosons, discussed in Sec. 6.1.1, or the one-loop annihilation into gauge bosons, which we investigate in Sec. 6.1.2. Subsequently, in Sec. 6.2 we discuss the interplay of the model-independent approach with a full analysis of the simplified model of Majorana dark matter introduced in Sec. 5.

[1] These neutrinos, however, can potentially be observed by Super-Kamiokande [147, 161].

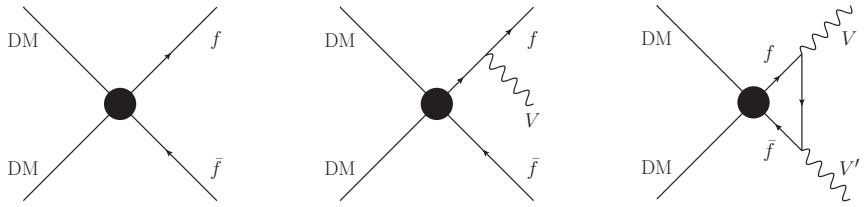

Figure 6.1.: Feynman diagrams showing the annihilation of dark matter into a fermion-antifermion pair via a contact interaction (left panel), as well as the associated higher-order processes relevant for the calculation of the high-energy neutrino flux: the final state radiation of a gauge boson V (central panel), and the one-loop annihilation into a pair of gauge bosons VV' (right panel).

6.1. Contact interactions

In this section, we investigate scenarios in which the unique lowest-order annihilation channel of dark matter is given by DM DM $\to f\bar{f}$, with f being an electron, a muon or a light quark. The only assumption we are making about the nature of the corresponding interaction between the dark matter particle and the Standard Model fermion f is that the mediating particles are sufficiently heavy, allowing for a description of the process by a contact interaction, as illustrated in the left panel of Fig. 6.1. The relevant classes of higher-order annihilations which generate a flux of high-energy neutrinos are shown in the central and right panel of Fig. 6.1. To begin, for all possible choices of f, a soft Z boson can be radiated off the final state fermion, provided that $m_{\rm DM} > m_Z$ [326, 352]. Additionally, if the Standard Model fermion coupling to the dark matter particle is left-handed, also the annihilation into $f\bar{f}'W^\pm$ is possible, with f and f' being the states forming a $SU(2)_L$ doublet[2]. Furthermore, if f is a quark, also the final state radiation of a gluon contributes to the annihilation process. Besides these $2 \to 3$ annihilations, the contact interaction inducing the tree-level annihilation into $f\bar{f}$ in general also leads to the annihilation into a pair of gauge bosons VV' via the one-loop diagram shown in the right panel of Fig. 6.1. Depending on whether f is a $SU(2)_L$ singlet or doublet and whether it carries color charge or not, the possible final states are given by $\gamma\gamma$, γZ, ZZ, W^+W^- and/or gg.

The expected flux of neutrinos is then given by the sum of the fluxes induced by the individual final states, weighted by the corresponding branching fractions. Remarkably, it turns out that within the framework of contact interactions, it is possible to divide all conceivable underlying models in only two classes, and to evaluate the branching fractions (and hence the neutrino flux) in each of these categories without specifying the concrete model. The distinction between these two classes of models is made according to whether the total annihilation cross section is dominated by DM DM $\to f\bar{f}$ or whether the one-loop annihilation into gauge bosons is most important. In the following sections 6.1.1 and 6.1.2, we will separately discuss these two classes of models, i.e. in particular we determine the corresponding branching fractions and the expected neutrino fluxes. For both cases, we then derive bounds on the normalization of the neutrino flux from the IceCube data, and, assuming equilibrium between captures and annihilations, convert them into upper limits on the spin-dependent and spin-independent dark matter scattering cross section with protons.

[2]For dark matter charged under $SU(2)_L$, also the initial state radiation of weak gauge bosons would be allowed. However, our assumption that the single lowest-order annihilation channel is given by DM DM $\to f\bar{f}$ automatically implies that dark matter is a Standard Model singlet, as otherwise also the final states ZZ and W^+W^- would occur at tree level.

To this end, we employ DarkSUSY [149] for the calculation of the capture rate, assuming $\rho_0 = 0.3\,\mathrm{GeV/cm^3}$ and a Maxwell-Boltzmann velocity distribution with $\sigma = 270\,\mathrm{km/s}$, c.f. the discussion in Sec. 2.2.

6.1.1. Case a: total cross section is dominated by DM DM $\to f\bar{f}$

First, let us discuss the class of models in which the dominant annihilation channel of dark matter is the lowest-order $2 \to 2$ process DM DM $\to f\bar{f}$. This is the case, for example, in the simplified model of Dirac dark matter coupling to f_R or f_L discussed in Sec. 3, or for a Majorana fermion that annihilates into $f_L\bar{f}_R$ or $f_R\bar{f}_L$; in both cases, the annihilation proceeds in the s-wave, neither with helicity nor velocity suppression. In such a scenario, the dominant source of high-energy neutrinos is given by the final state radiation (FSR) of gauge bosons V (shown in the central panel of Fig. 6.1), which is suppressed only by two powers of the corresponding gauge coupling, as opposed to the loop annihilations (right panel of Fig. 6.1), which are proportional to g^4.

The quantitative description of the FSR of a gauge boson V is based on the parton distribution function $D_{f\to V}(x)$, which is defined to be the probability for radiating V off a final state fermion f, with a fraction $x = E_V/E_f$ of the energy of the fermion. For a fermion with electric charge q_f and weak isospin $T_{3,f}$, the lowest-order parton distribution functions corresponding to $V = Z, W$ are given by [352–354]

$$D_{f\to Z}\,(x) = \frac{\alpha_{\mathrm{em}}\,(T_{3,f} - q_f \sin^2\theta_{\mathrm{W}})^2}{2\pi \sin^2\theta_{\mathrm{W}} \cos^2\theta_{\mathrm{W}}} P_{f\to V}\,(x)\ , \tag{6.1}$$

$$D_{f\to W}\,(x) = \frac{\alpha_{\mathrm{em}}\,T_{3,f}^2}{\pi \sin^2\theta_{\mathrm{W}}} P_{f\to V}\,(x)\ . \tag{6.2}$$

Moreover, if the fermion f is a Standard Model quark, one also has [355]

$$D_{f\to g}\,(x) = \frac{\alpha_{\mathrm{s}}}{2\pi} P_{f\to V}(x)\,. \tag{6.3}$$

In these equations, the splitting functions $P_{f\to V}\,(x)$ are given by

$$P_{f\to V}\,(x) = \begin{cases} \dfrac{1+(1-x)^2}{x}\left[\ln\dfrac{x^2 m_{\mathrm{DM}}^2}{M_V^2} + 2\ln\left(1+\sqrt{1-\dfrac{M_V^2}{x^2 m_{\mathrm{DM}}^2}}\right)\right] & \text{for } V = Z, W\,, \\ \dfrac{4}{3}\dfrac{1+(1-x)^2}{x} & \text{for } V = g\,. \end{cases} \tag{6.4}$$

We do not implement the formalism of the parton distribution functions ourselves, but use PYTHIA 8.176 [155, 156], which includes the possibility to allow for the emission of (soft) weak gauge bosons and gluons from the final state, c.f. [356] for more information. As described in detail in Sec. 2.2, we then take into account the energy losses of the hadrons induced by their interactions with the solar matter, as well as the propagation effects of neutrinos on their way from the center of the Sun to the location of the Earth[3]. Finally, we

[3] We have confirmed that for $m_{\mathrm{DM}} \gtrsim 300\,\mathrm{GeV}$ our neutrino spectra from the FSR processes are in good agreement with the results presented in [163].

convert the neutrino flux at the position of the detector into a number of (anti)muon events following the approach of [349], and derive upper bounds on the normalization of the neutrino flux from the IceCube 79-string analysis, using the method presented in Appendix C. Under the assumption of equilibrium between capture and annihilation, in this way we obtain upper limits on the scattering cross section of dark matter with protons, separately for each annihilation channel $f\bar{f}(V)$.

We show the resulting upper limits on the spin-dependent and spin-independent scattering cross section in the left and right panels of Fig. 6.2, respectively, for dark matter annihilating into first or second generation leptons (top plots), first generation quarks (central plots), or second generation quarks (bottom plots). For comparison, we also include the upper limits on the scattering cross section arising from the direct detection experiments COUPP [120] and SIMPLE [122] for the case of spin-dependent interactions with protons, as well as from XENON100 [104] and LUX [101] for the spin-independent case. Lastly, we show the upper limits obtained in [147] from considering the MeV neutrinos produced by the corresponding lowest-order $2 \to 2$ final state. Generally speaking, one can infer from the various panels of Fig. 6.2 that when taking into account the FSR processes, the IceCube experiment can probe interesting regions of the parameter space of dark matter annihilating solely into light fermions. In particular, in some cases the limits on the spin-dependent scattering cross section derived in this section are comparable to, or even more stringent than the ones following from the most sensitive direct detection searches, which is remarkable in view of the fact that this sometimes occurs in situations in which the high-energy neutrino flux is solely induced by higher-order annihilation processes. In the following, let us discuss the IceCube upper limits for the different possible annihilation channels in more detail.

To begin, we infer from Fig. 6.2 that the bounds on the cross section for annihilations into $e_R\bar{e}_R$, $\mu_R\bar{\mu}_R$, $u_R\bar{u}_R$, $d_R\bar{d}_R$ and $s_R\bar{s}_R$ are all comparable. For the first two final states, this is easily understood by noting that in these cases all high-energy neutrinos originate from the decay of the Z-boson produced in the FSR process DM DM $\to f_R\bar{f}_R Z$, which occurs with equal probability for electron and muon final states. In the scenarios of annihilations into light right-handed quarks, the cross section for the FSR of a Z-boson is modified with respect to the case of annihilations into leptons due to the different hypercharges of the involved quarks, and additionally the high-energy neutrino flux receives a contribution from the process DM DM $\to f_R\bar{f}_R g$, which we find to be comparable to the flux induced by the weak FSR. Taken together, the differences in the fluxes (and hence in the upper limits) for $f = e, \mu, u, d, s$ are of $\mathcal{O}(1)$. Lastly, the limits for annihilation into $c_R\bar{c}_R$ are significantly stronger than for all other $f_R\bar{f}_R$ final states, due to the production of charmed baryons and mesons: in contrast to the pions and kaons produced by the hadronization of light quarks, these can decay into high-energetic neutrinos before being stopped completely.

On the other hand, if the total annihilation cross section is dominated by DM DM $\to f_L\bar{f}_R$ (or DM DM $\to f_R\bar{f}_L$), the upper limits arising from the IceCube data differ significantly depending on whether f is a Standard Model lepton or a quark. Compared to the scenario of annihilation into $f_R\bar{f}_R$, the final state involving a left-handed fermion now additionally allows for the FSR of a $W^\pm$ boson. For the case of annihilation into leptons, a soft $W^\pm$ boson is automatically accompanied by a hard neutrino, highly favorable for a neutrino detector such as IceCube, which has an effective area that strongly rises with energy. Consequently, the upper limits on the scattering cross section for annihilation into $e_L\bar{e}_R$ or $\mu_L\bar{\mu}_R$ are significantly stronger than the bounds for the corresponding final states involving light quarks. We furthermore remark that the limits for the channels $q_L\bar{q}_R$ turn out to be stronger than for $q_R\bar{q}_R$, which can be explained by the larger hypercharge of left-handed quarks

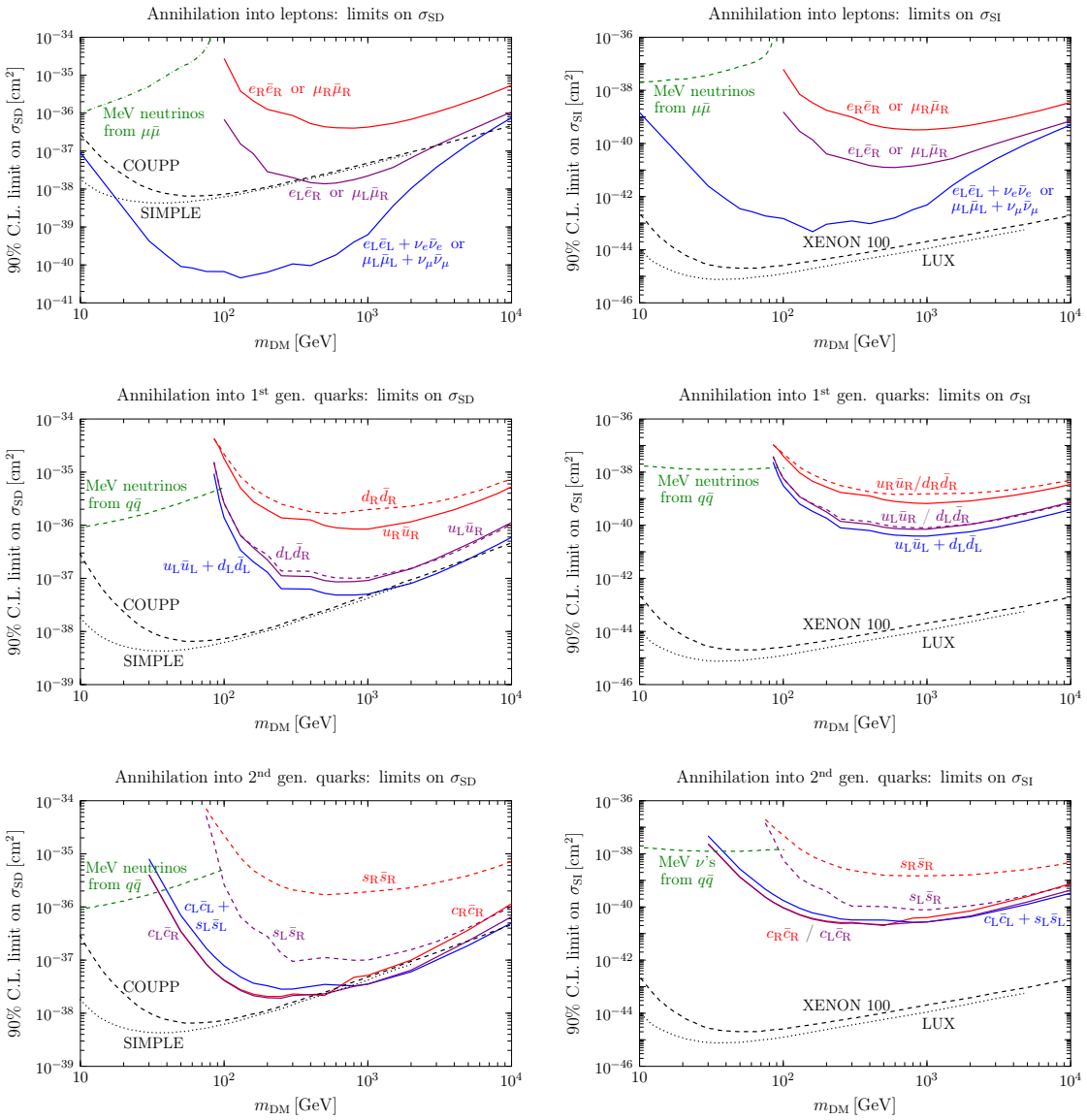

Figure 6.2.: 90% C.L. upper limits on the spin-dependent (spin-independent) scattering cross section of dark matter with protons, shown in the left (right) panels, for dark matter annihilating via a contact interaction into first or second generation leptons (upper row), first generation quarks (central row), or second generation quarks (bottom row). The various red, blue and purple lines show the bounds deduced from our reanalysis of the IceCube 79-string data, taking into account the FSR of weak gauge bosons and gluons, while the green dashed line represents the limit derived in [147] from the MeV neutrino flux. For comparison, the most stringent upper limits arising from direct detection experiments are shown as black dashed and dotted curves.

compared to right-handed quarks, as well as by the existence of the additional FSR process $q_L\bar{q}_R W$ in the former case.

Finally, the limits from IceCube on the annihilation channels $f_L\bar{f}_L$ are again much stronger for f being a lepton compared to annihilations into left-handed quarks. This is related to

the fact that due to $SU(2)_L$ invariance, both components of a weak isospin doublet are necessarily produced with comparable rates, with the relative difference being suppressed by the ratio of the scale of electroweak symmetry breaking and the energy scale of the contact interaction. Hence, the possible final states involving light left-handed leptons or quarks are given by $e_L\bar{e}_L + \nu_e\bar{\nu}_e$, $\mu_L\bar{\mu}_L + \nu_\mu\bar{\nu}_\mu$, $u_L\bar{u}_L + d_L\bar{d}_L$ and $c_L\bar{c}_L + s_L\bar{s}_L$. Among these annihilation channels, the first two clearly give rise to the strongest upper limits on the scattering cross section, due to the presence of hard neutrinos in the lowest-order final state. Also for annihilation into $c_L\bar{c}_L + s_L\bar{s}_L$, the high-energy neutrino flux is dominated by the tree-level contribution, due to the neutrinos produced in the decays of charmed hadrons. On the other hand, the upper limits for annihilations into first generation left-handed quarks are again dominated by the FSR of weak gauge bosons, leading to somewhat less stringent bounds, especially at low dark matter masses.

6.1.2. Case b: total cross section is dominated by loop annihilations

The discussion in the previous section was based on the assumption that the dominant annihilation mode of dark matter is the lowest-order process DM DM $\to f\bar{f}$, which is then accompanied by the FSR of weak gauge bosons and gluons leading to the high-energy neutrino flux potentially observable at IceCube. However, there are several known scenarios in which the tree-level annihilation into a fermion-antifermion pair suffers from a helicity suppression: in these cases, the s-wave component is proportional to $m_f^2/m_{\rm DM}^2$ and hence negligibly small for annihilations into light fermions considered in this section, while all higher-order terms in the partial wave expansion are suppressed by the small velocity of dark matter particles in the Sun. In Sec. 4 and 5, we studied two concrete simplified models where this is realized, namely the scenarios of real scalar and Majorana dark matter coupling chirally either to f_R or f_L. We demonstrated that in these models the dominant annihilation channels of dark matter for $v \to 0$ are given by higher-order processes which are not helicity suppressed, namely the virtual internal bremsstrahlung (VIB) of a gauge boson or the one-loop annihilations into gauge bosons. Under the assumption of contact interactions between dark matter and the fermion f, the mediating particle can be integrated out and hence only the latter class of processes contributes to the annihilation cross section. In the language of the simplified models, this amounts to say that the mediating particle is sufficiently heavier than the dark matter particle, which we will assume in the remainder of this section[4].

The total one-loop annihilation cross section into gauge bosons depends on the strength and the Lorentz structure of the contact interaction. However, under the assumption of equilibrium between captures and annihilations of dark matter in the Sun, the neutrino flux only depends on the *branching ratios* into the various possible final states $\gamma\gamma$, γZ, ZZ, W^+W^- and gg. In the limit $m_{\rm DM} \gg m_f$, these are independent of the nature of the underlying contact interaction, as they only depend on the gauge quantum numbers of f as well as on phase space suppression factors. In Table 6.1, we list the cross sections for the annihilation into each gauge boson final state, with $C_{\rm loop}$ denoting the common model-dependent normalization of each one-loop process, which factors out in the computation of the branching fractions. Furthermore, $\Sigma_{\gamma Z}$, Σ_{ZZ} and Σ_{WW} are phase space suppression factors, which in principle can be important if the dark matter particle is only slightly heavier than the Z or W boson. These quantities depend on the underlying effective operator responsible for the contact interaction; the only relevant cases for the s-wave annihilation

[4]However, we will come back to the full discussion of the VIB and one-loop processes in the context of the simplified model of Majorana dark matter in Sec. 6.2.

	(σv)
$\gamma\gamma$	$N_C^2\,\alpha_{\rm em}^2\,(2I+1)^2\,\left(I^2+Y^2\right)^2\cdot C_{\rm loop}$
γZ	$2N_C^2\,\alpha_{\rm em}^2\,\left[(2I+1)\,Y^2\tan(\theta_{\rm W})-2I^2\cot(\theta_{\rm W})\right]^2\cdot C_{\rm loop}\cdot\Sigma_{\gamma Z}$
ZZ	$N_C^2\,\alpha_{\rm em}^2\,\left[(2I+1)\,Y^2\tan^2(\theta_{\rm W})+2I^2\cot^2(\theta_{\rm W})\right]^2\cdot C_{\rm loop}\cdot\Sigma_{ZZ}$
W^+W^-	$2N_C^2\,\alpha_{\rm em}^2\,\left[I^2/\sin^4(\theta_{\rm W})\right]\cdot C_{\rm loop}\cdot\Sigma_{WW}$
gg	$(N_C-1)\,\alpha_S^2\,(2I+1)^2\cdot C_{\rm loop}$

Table 6.1.: One-loop annihilation cross sections (σv) into gauge boson pairs, for scenarios in which the dark matter particle couples to a fermion-antifermion pair $f\bar{f}$ via a contact interaction. $C_{\rm loop}$ denotes the common model-dependent normalization of each cross section, $N_C=3\,(1)$ for quarks (leptons), $I=1/2\,(0)$ for coupling to $SU(2)_L$ doublets (singlets), and Y is the hypercharge of the Standard Model fermion f.

of a Majorana fermion[5] into gauge bosons are given by [357]

$$\Sigma_{\gamma Z}=\left(1-\frac{m_Z^2}{4m_{\rm DM}^2}\right)^3 \quad \text{for all operators}\,,$$

$$\Sigma_{VV}=\begin{cases}\left(1-\dfrac{m_V^2}{m_{\rm DM}^2}\right)^{1/2}\left(1-\dfrac{m_V^2}{m_{\rm DM}^2}+\dfrac{3m_V^4}{8m_{\rm DM}^4}\right) & \text{for } \bar{\chi}i\gamma^5\chi B_{\mu\nu}B^{\mu\nu} \text{ or } \bar{\chi}i\gamma^5\chi W^a_{\mu\nu}W^{a\mu\nu}\,,\\ \left(1-\dfrac{m_V^2}{m_{\rm DM}^2}\right)^{3/2} & \text{for } \bar{\chi}i\gamma^5\chi B_{\mu\nu}\widetilde{B}^{\mu\nu} \text{ or } \bar{\chi}i\gamma^5\chi W^a_{\mu\nu}\widetilde{W}^{a\mu\nu}\,,\end{cases} \tag{6.5}$$

with V being either a Z or a W boson.

Once the branching fractions BF_i into the various gauge boson final states i are determined, one can evaluate the upper limit on the scattering cross section, $\sigma^{\rm max}_{\rm SD/SI}$, from

$$\frac{1}{\sigma^{\rm max}_{\rm SD/SI}(m_{\rm DM})}\simeq\sum_i\frac{\mathrm{BF}_i}{\sigma^{{\rm max},i}_{\rm SD/SI}(m_{\rm DM})}\,, \tag{6.6}$$

where $\sigma^{{\rm max},i}_{\rm SD/SI}(m_{\rm DM})$ is the upper limit from IceCube at the dark matter mass $m_{\rm DM}$ assuming 100% annihilation into the final state i [6]. This expression can be further simplified by approximating $\sigma^{{\rm max},W^+W^-}_{\rm SD/SI}(m_{\rm DM})\simeq\sigma^{{\rm max},ZZ}_{\rm SD/SI}(m_{\rm DM})$ (which is fulfilled with $\simeq 10\%$ accuracy), and by realizing that the upper limit on the scattering cross section for the γZ channel can be obtained from the limit for the ZZ channel via

$$\sigma^{{\rm max},\gamma Z}_{\rm SD/SI}\,(m_{\rm DM})=\frac{2\,C\left(m_{\rm DM}+\frac{m_Z^2}{4m_{\rm DM}}\right)}{C\,(m_{\rm DM})}\sigma^{{\rm max},ZZ}_{\rm SD/SI}\left(m_{\rm DM}+\frac{m_Z^2}{4m_{\rm DM}}\right)\,, \tag{6.7}$$

[5] For simplicity, here we focus on Majorana dark matter. As we find that the phase space suppression modifies the upper limits only marginally, we expect small changes in our conclusions for scalar or vector dark matter.

[6] Due to the different cone angles employed in the calculation of the limits corresponding to each of the annihilation channels, the upper bound obtained from Eq. (6.6) can differ from the exact result obtained directly from the total neutrino flux. All results shown in this section have been obtained by using the full numerical calculation; however, we have confirmed that the difference with respect to the approximation defined through Eq. (6.6) is at most 30%.

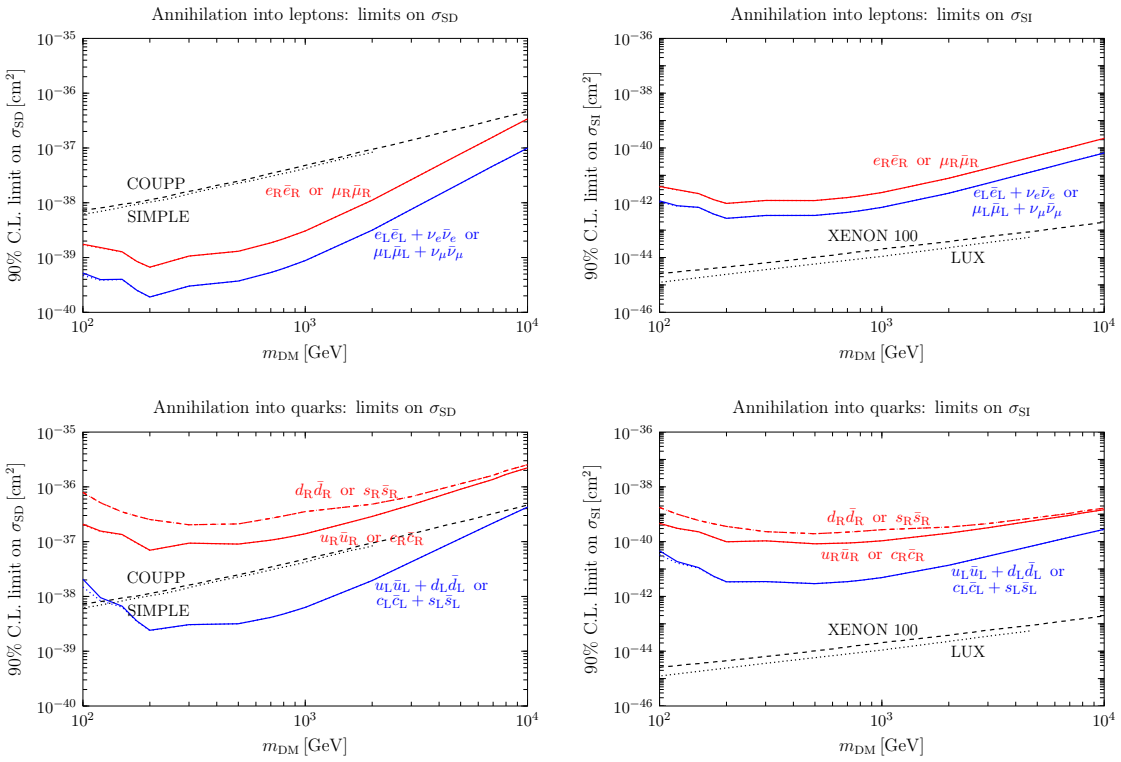

Figure 6.3.: 90% C.L. upper limits on the spin-dependent and spin-independent scattering cross section of dark matter with protons, shown in the left and right panels, respectively, arising from the IceCube data on a high-energy neutrino flux from the direction of the Sun. These results assume that dark matter dominantly annihilates into gauge bosons at one loop, induced by a contact interaction of dark matter to leptons (top plots) or to quarks (bottom plots). For comparison, the dashed and dotted black curves show the most competitive direct detection bounds.

with $C(m_{\rm DM})$ being the capture rate for a dark matter mass $m_{\rm DM}$, using an arbitrary reference cross section. The latter relation follows from the fact that the spectrum of neutrinos originating from the decay of the Z boson produced in the annihilation of dark matter with mass $m_{\rm DM}$ into γZ is related to the spectrum corresponding to the annihilation into ZZ of dark matter particles with a mass $m_{\rm DM} + m_Z^2/(4m_{\rm DM})$ simply by a multiplicity factor of two. These considerations allow us to rewrite Eq. (6.6) in the form

$$\frac{1}{\sigma^{\rm max}_{\rm SD/SI}\left(m_{\rm DM}\right)} = \frac{{\rm BF}_{ZZ} + {\rm BF}_{W^+W^-}}{\sigma^{{\rm max},ZZ}_{\rm SD/SI}\left(m_{\rm DM}\right)} + \frac{1}{2}\frac{C\left(m_{\rm DM}\right)}{C\left(m_{\rm DM} + \frac{m_Z^2}{4m_{\rm DM}}\right)}\frac{{\rm BF}_{\gamma Z}}{\sigma^{{\rm max},ZZ}_{\rm SD/SI}\left(m_{\rm DM} + \frac{m_Z^2}{4m_{\rm DM}}\right)} + \frac{{\rm BF}_{gg}}{\sigma^{{\rm max},gg}_{\rm SD/SI}\left(m_{\rm DM}\right)}\,. \tag{6.8}$$

The upper limits on the cross section for annihilations into ZZ and gg are reported in Appendix C.

We present in Fig. 6.3 the resulting upper limits on the spin-dependent and spin-independent scattering cross section with protons in the left and right panels, respectively. Here, the upper (lower) panels correspond to scenarios in which the annihilation is induced by a contact

interaction of dark matter to leptons (quarks). Each upper limit is shown for the two possible phase space suppression factors for Majorana dark matter defined in Eq. (6.5); evidently, our results are almost insensitive to this model-dependent factor, even for dark matter masses only slightly above the production threshold. Furthermore, for comparison we include in the plots the most constraining results from direct detection experiments.

From comparing the different panels of Fig. 6.3, it follows that the upper limits on the scattering cross section are more stringent for scenarios in which the annihilation of dark matter is driven by a coupling to leptons, compared to the case of quarks. This is straightforwardly understood from the fact that in the former case, the branching fractions into final states involving weak gauge bosons (which produce a significant high-energy neutrino flux) are rather large, while in the latter scenarios the total annihilation cross section is dominated by annihilations into gluon pairs, which produce a much softer spectrum of neutrinos. Furthermore, one can infer from the plot that the limits are stronger for dark matter coupling to left-handed fermions than for coupling to right-handed fermions, due to the additional annihilation channel W^+W^- as well as due to the larger hypercharge of the fermion f in the former case, c.f. Table 6.1. Interestingly, for the leptonic case the upper limits on the spin-dependent scattering cross section following from the IceCube data are stronger than the direct detection bounds; for annihilations driven by couplings to quarks, the two methods of probing σ_{SD} are of similar power. On the other hand, for spin-independent interactions, the direct detection experiments always provide the strongest limits, irrespectively of the final state of dark matter annihilations in the Sun.

6.2. Comparison with the simplified Majorana dark matter model

Lastly, in this section we compare the model-independent approach based on contact interactions with one specific realization falling into the class of scenarios covered in Sec. 6.1.2, i.e. a model in which dark matter dominantly annihilates into a pair of gauge bosons. To this end, we (re)consider the simplified model of Majorana dark matter coupling to a Standard Model fermion via a Yukawa interaction with a charged scalar mediator, which already has been defined and discussed in detail in Sec. 5. In particular, the relevant interaction Lagrangian reads

$$\mathcal{L}_{\mathrm{int}}^{\mathrm{fermion}} = -y\,\eta^\dagger \bar{\chi} f_R + \mathrm{h.c.}\,, \tag{6.9}$$

where χ is the Majorana dark matter candidate, singlet under the Standard Model gauge group, and η is a $SU(2)_L$ singlet scalar particle, with the same hypercharge as the right-handed Standard Model fermion f_R, which we choose to be either e_R, u_R or d_R. As it can be seen from Eq. (5.2), the annihilation cross section for the lowest-order process DM DM $\to f\bar{f}$ is helicity- and velocity suppressed, and hence negligible for dark matter annihilations in the Sun.

The most relevant final states in the self-annihilation of the Majorana particle χ are given by the virtual internal bremsstrahlung (VIB) of a gauge boson, $\chi\chi \to f\bar{f}V$, or by the one-loop annihilation into a pair of gauge bosons, $\chi\chi \to VV'$, both of which feature a non-vanishing s-wave component in the limit $v \to 0$. The full expressions for the corresponding annihilation cross sections are provided in Appendix B.2; the total annihilation cross section

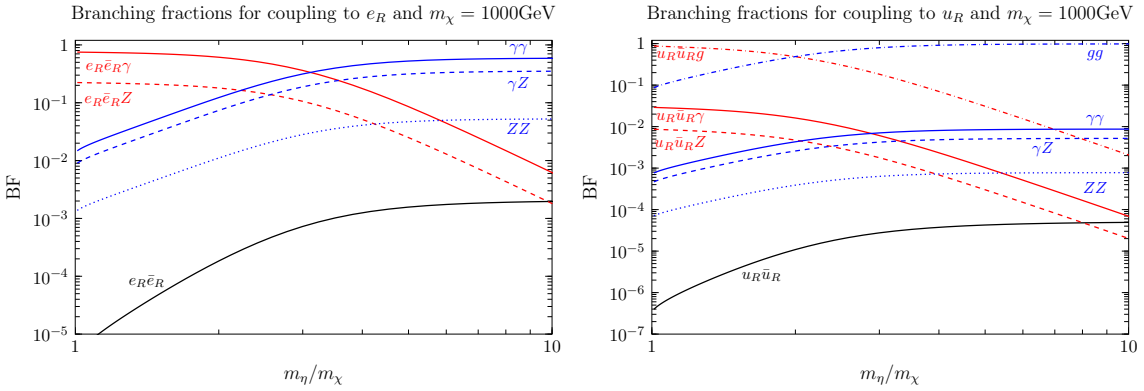

Figure 6.4.: Branching ratios of the various tree-level and one-loop annihilation channels for the simplified model of Majorana dark matter coupling to e_R (left panel) or to u_R (right panel), as a function of the mass splitting m_η/m_χ between the dark matter particle and the scalar mediator, and choosing for concreteness $m_\chi = 1\,\text{TeV}$.

can be approximated to $\simeq 40\%$ accuracy by

$$(\sigma_{\text{ann}} v) \approx \begin{cases} \left(\dfrac{37.6}{(m_\eta/m_\chi)^8} + \dfrac{0.62}{(m_\eta/m_\chi)^4}\right) y^4 \left(\dfrac{\text{TeV}}{m_\chi}\right)^2 \times 10^{-30}\,\text{cm}^3\text{s}^{-1}\,, & \text{for couplings to } e_R, \\ \left(\dfrac{1.2\times 10^3}{(m_\eta/m_\chi)^8} + \dfrac{74.4}{(m_\eta/m_\chi)^4}\right) y^4 \left(\dfrac{\text{TeV}}{m_\chi}\right)^2 \times 10^{-30}\,\text{cm}^3\text{s}^{-1}\,, & \text{for couplings to } u_R, \\ \left(\dfrac{1.2\times 10^3}{(m_\eta/m_\chi)^8} + \dfrac{73.3}{(m_\eta/m_\chi)^4}\right) y^4 \left(\dfrac{\text{TeV}}{m_\chi}\right)^2 \times 10^{-30}\,\text{cm}^3\text{s}^{-1}\,, & \text{for couplings to } d_R. \end{cases} \tag{6.10}$$

Here, the terms scaling as $(m_\eta/m_\chi)^{-8}$ correspond to the $2 \to 3$ annihilations, while the ones proportional to $(m_\eta/m_\chi)^{-4}$ arise from the one-loop processes. In particular, this implies that for small mass splittings, $m_\eta/m_\chi \simeq 1$, the VIB processes dominate the total annihilation cross section, while in the limit of large mediator masses the loop annihilations into gauge bosons are most important. Notice that in the latter case, we recover the framework of contact interactions discussed in the previous section.

We further illustrate this point in Fig. 6.4 by showing the branching fractions into the various two- and three-body final states as a function of the mass splitting m_η/m_χ, for dark matter coupling to e_R (u_R) in the left (right) panel. For concreteness, this plot assumes $m_\chi = 1\,\text{TeV}$, although we find that these curves are nearly independent of the dark matter mass, as long as $m_\chi \gg m_Z$. Additionally, we present analytical results for the branching fractions in Table 6.2, in the limit of complete degeneracy of the dark matter particle and the scalar mediator, $m_\eta = m_\chi$, as well as in the hierarchical limit corresponding to $m_\eta \gg m_\chi$. In the latter case, for the one-loop annihilations into gauge bosons we recover the values given in Table 6.1, which were obtained under the assumption of contact interactions.

Assuming equilibrium between captures and annihilations of dark matter particles in the Sun, these branching fractions can be employed for evaluating the expected flux of neutrinos, as well as the corresponding upper limits on the scattering cross section of dark

	BF	$f = e$			$f = u$		
degenerate limit	$\mathrm{BF}_{f_R\bar{f}_R Z}$	$\sin^2\theta_\mathrm{W}$	$\simeq$	0.23	$\frac{\alpha_\mathrm{em}\tan^2\theta_\mathrm{W}}{3\alpha_\mathrm{s}(m_\chi)}$	$\simeq$	10^{-2}
	$\mathrm{BF}_{\gamma Z}$	$\frac{\pi^3\alpha_\mathrm{em}\sin^2\theta_\mathrm{W}}{32(7/2-\pi^2/3)}$	$\simeq$	$8\cdot10^{-3}$	$\frac{\pi^3\alpha_\mathrm{em}^2\tan^2\theta_\mathrm{W}}{72(7/2-\pi^2/3)\alpha_\mathrm{s}(m_\chi)}$	$\simeq$	$5\cdot10^{-4}$
	BF_{ZZ}	$\frac{\pi^3\alpha_\mathrm{em}\sin^2\theta_\mathrm{W}\tan^2\theta_\mathrm{W}}{64(7/2-\pi^2/3)}$	$\simeq$	10^{-3}	$\frac{\pi^3\alpha_\mathrm{em}^2\tan^4\theta_\mathrm{W}}{144(7/2-\pi^2/3)\alpha_\mathrm{s}(m_\chi)}$	$\simeq$	$7\cdot10^{-5}$
	BF_{gg}		–		$\frac{\pi^3\alpha_\mathrm{s}(m_\chi)}{128(7/2-\pi^2/3)}$	$\simeq$	$9\cdot10^{-2}$
	$\mathrm{BF}_{f_R\bar{f}_R g}$		–			$\simeq$	1
hierarchical limit	$\mathrm{BF}_{f_R\bar{f}_R Z}$		$\simeq$	0		$\simeq$	0
	$\mathrm{BF}_{\gamma Z}$	$\frac{2\tan^2\theta_\mathrm{W}}{(1+\tan^2\theta_\mathrm{W})^2}$	$\simeq$	0.38	$\frac{16\alpha_\mathrm{em}^2\tan^2\theta_\mathrm{W}}{9\alpha_\mathrm{s}^2(m_\chi)}$	$\simeq$	$5\cdot10^{-3}$
	BF_{ZZ}	$\frac{\tan^4\theta_\mathrm{W}}{(1+\tan^2\theta_\mathrm{W})^2}$	$\simeq$	$5.6\cdot10^{-2}$	$\frac{8\alpha_\mathrm{em}^2\tan^4\theta_\mathrm{W}}{9\alpha_\mathrm{s}^2(m_\chi)}$	$\simeq$	$8\cdot10^{-4}$
	BF_{gg}		–			$\simeq$	1
	$\mathrm{BF}_{f_R\bar{f}_R g}$		–			$\simeq$	0

Table 6.2.: Branching fractions of the different VIB and one-loop annihilation channels, for the degenerate limit $m_\eta/m_\chi = 1$ in the upper part, and for the hierarchical limit $m_\eta \gg m_\chi$ in the lower part, assuming $m_\chi \gg m_Z$. The numerical values were obtained by evaluating the strong coupling constant at a momentum scale of $m_\chi \simeq 1\,\mathrm{TeV}$.

matter following from the IceCube 79-string data, by applying the same method as in the previous section. We show the resulting limits on the spin-dependent (left panel) and spin-independent cross section (right panel) in Fig. 6.5, for dark matter annihilations mediated by couplings to right-handed electrons in the upper panels, and to right-handed up- or down-quarks in the lower panels. The solid lines correspond to $m_\eta/m_\chi = 1.01$ and 10, while the dotted curves show our results for eight different values of the mass splitting ranging between those two values. As expected, for $m_\eta/m_\chi = 10 \gg 1$, the upper limits are identical to the ones shown in Fig. 6.3, corresponding to the model-independent results assuming contact interactions.

Furthermore, it follows from Fig. 6.5 that for small and intermediate values of the mass splitting, the upper limits on the scattering cross section differ from the ones corresponding to the limit of contact interactions only by a factor of $\mathcal{O}(1)$. More precisely, for couplings to e_R, the limits for $m_\eta/m_\chi = 1$ and $m_\eta/m_\chi \to \infty$ differ by a factor of 2, and by a factor ranging from 1 to 1.5 (1 to 1.8) for couplings to u_R (d_R). In the first case, this can be understood as follows: for small mass splittings, the dominant source of hard neutrinos is the $2 \to 3$ annihilation channel $e_R\bar{e}_R Z$ (c.f. Fig. 6.4). The spectrum of Z bosons in this final state is strongly peaked towards $E_Z \simeq m_\mathrm{DM}$, and hence the corresponding spectrum of neutrinos is very similar to the one arising from the annihilation of dark matter with the same mass into ZZ, aside from a multiplicity factor of two. Hence, by employing Eq. (6.8) we obtain

$$\sigma_\mathrm{SD/SI}^{\mathrm{max,\,deg}} \simeq \frac{2\sigma_\mathrm{SD/SI}^{\mathrm{max},ZZ}}{\mathrm{BF}_{e_R\bar{e}_R Z}} \simeq \frac{2\sigma_\mathrm{SD/SI}^{\mathrm{max},ZZ}}{\sin^2(\theta_W)}\,, \tag{6.11}$$

where we additionally used Table 6.2. On the other hand, for $m_\eta \gg m_\chi$ it follows from Fig. 6.4 and Table 6.2 that the most important final states for the production of neutrinos are

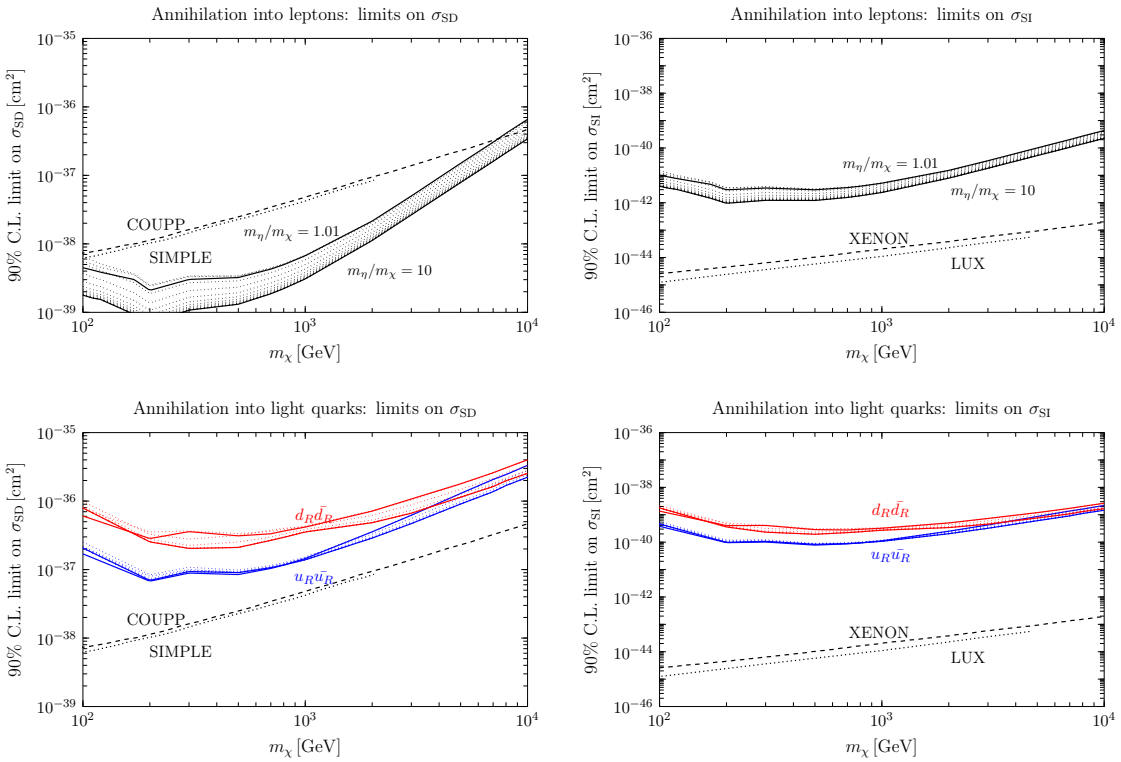

Figure 6.5.: 90% C.L. upper limits on the spin-dependent (left panels) and spin-independent scattering cross section (right panels), for a Majorana dark matter particle annihilating via a coupling to e_R or u_R/d_R, shown in the top and bottom plots, respectively. The various dotted curves correspond to different values of the mass splitting m_η/m_χ between 1.01 and 10. The most stringent constraints from direct detection experiments are shown as black dashed and dotted curves.

ZZ and γZ. Employing again Eq. (6.8) and Table 6.2, and working in the limit $m_\chi \gg m_Z$, we find

$$\sigma^{\text{max, hier}}_{\text{SD/SI}} \simeq \frac{\sigma^{\text{max},ZZ}_{\text{SD/SI}}}{\text{BF}_{ZZ} + \text{BF}_{\gamma Z}/2} = \frac{\sigma^{\text{max},ZZ}_{\text{SD/SI}}}{\sin^2(\theta_W)} \,, \tag{6.12}$$

which differs from Eq. (6.11) by a factor of two.

If the Majorana dark matter particle couples to u_R or d_R, both the channels involving a Z boson as well as the final states including a gluon contribute to the total neutrino flux. Using a similar argument as above, we find for the case of coupling to u_R the approximate results

$$\sigma^{\text{max, deg}}_{\text{SD/SI}} \simeq \frac{2\sigma^{\text{max},gg}_{\text{SD/SI}}}{1 + \text{BF}_{u_R\bar{u}_R Z} \cdot \xi_{\text{SD/SI}}(m_\chi)} \simeq \frac{2\sigma^{\text{max},gg}_{\text{SD/SI}}}{1 + 10^{-2} \cdot \xi_{\text{SD/SI}}(m_\chi)} \,, \tag{6.13}$$

and

$$\sigma^{\text{max, hier}}_{\text{SD/SI}} \simeq \frac{\sigma^{\text{max},gg}_{\text{SD/SI}}}{1 + (\text{BF}_{ZZ} + \text{BF}_{\gamma Z}/2) \cdot \xi_{\text{SD/SI}}(m_\chi)} \simeq \frac{\sigma^{\text{max},gg}_{\text{SD/SI}}}{1 + 3.5 \cdot 10^{-3} \cdot \xi_{\text{SD/SI}}(m_\chi)} \,, \tag{6.14}$$

where we defined $\xi_{\mathrm{SD/SI}}(m_\chi) \equiv \sigma^{\max,gg}_{\mathrm{SD/SI}}(m_\chi)/\sigma^{\max,ZZ}_{\mathrm{SD/SI}}(m_\chi)$. From Appendix C it follows that $\xi_{\mathrm{SD/SI}}(m_\chi)$ is a decreasing function of m_χ, and hence the relative contribution to the upper limits of the annihilation channels involving a Z boson, which correspond to the second term in each denominator of Eqs. (6.13) and (6.14), gets smaller for increasing dark matter masses. Hence, for sufficiently large values of m_χ, the upper limits dominantly arise from the annihilation channels $u\bar{u}g$ (gg) in the degenerate (hierarchical) case, leading again to the ratio $\sigma^{\max,\,\mathrm{deg}}_{\mathrm{SD/SI}}/\sigma^{\max,\,\mathrm{hier}}_{\mathrm{SD/SI}} = 2$ as for the scenario of coupling to e_R. On the other hand, for small values of the dark matter mass, also the annihilation channels involving a Z boson contribute significantly; due to $\mathrm{BF}_{u_R\bar{u}_R Z} > \mathrm{BF}_{ZZ} + \mathrm{BF}_{\gamma Z}/2$, we find that the upper limits improve to a larger extent in the degenerate case compared to the hierarchical scenario when lowering m_χ, c.f. Eqs. (6.13) and (6.14). Consequently, the upper limits are even more insensitive to the mass splitting at small dark matter masses compared to the factor of two found in the limit of large m_χ, which clearly can be seen in Fig. 6.5. A similar rationale can be applied to the case of coupling to d_R.

Let us finally compare the upper limits on the scattering cross section derived from the IceCube analysis to the most stringent bounds from direct detection experiments, shown as black dashed and dotted curves in Fig. 6.5. For annihilations mediated by couplings to electrons, the neutrino limits on the spin-dependent scattering cross section are significantly stronger than the results from COUPP and SIMPLE, while for couplings to quarks they are weaker by $\simeq 1-2$ orders of magnitude. This difference is due to the fact that in the former case, dark matter dominantly annihilates into final states involving a Z boson, leading to a hard neutrino spectrum, while in the latter case the neutrinos mostly arise from the hadronization of gluons, corresponding to a softer spectrum of neutrinos. On the other hand, for spin-independent interactions the constraints from XENON100 and LUX are significantly stronger than the upper limits from IceCube, both for annihilations mediated by leptons as well as by quarks.

7. DAMA confronts null searches in the effective theory of dark matter-nucleon interactions

So far, in this thesis we have employed null results from direct, indirect and collider searches in order to set constraints on the parameter space of dark matter, either in the context of simplified models in Sec. 3, 4 and 5, or in a model-independent way in Sec. 6. However, as already mentioned in Sec. 2.1.2, there is one direct detection experiment which observes a signal that is *not* consistent with the known sources of background: the DAMA collaboration has reported a statistically significant annual modulation of the event rate over 14 annual circles [115], which can naturally be explained by a dark matter signal modulated by the rotation of the Earth around the Sun (c.f. Sec. 2.1.1 for more details). However, when employing the standard assumptions about the astro- and particle physics of dark matter, i.e. a Maxwell-Boltzmann velocity distribution and standard spin-independent or spin-dependent scattering, the upper bounds from direct detection experiments such as LUX [102] or PICO [125] exclude the dark matter interpretation of DAMA by several orders of magnitude, as it can be seen in Fig. 2.1.

Broadly speaking, this tension can be resolved in three possible ways (including of course any combination of them): first, the DAMA modulation might be caused by a so far unknown source of background which also modulates in time with a period of one year, peaking around June 1st. Several attempts have been made in this direction [358–361], however so far there is no generally accepted scenario explaining the DAMA data without invoking a dark matter signal. Secondly, going beyond the vanilla assumptions about the velocity distribution of dark matter can reduce the tension between DAMA and the null searches [95–97]. Lastly, a non-standard interaction between dark matter and nucleons, i.e. anything which is not captured by the framework of (isospin-conserving) spin-independent or spin-dependent scattering, can in principle reconcile DAMA with the other direct detection experiments, as discussed e.g. in [362–366] and many other works. In fact, in Sec. 3 and 4.4 we have already encountered a few simplified models in which the scattering cross section can not be described by means of the standard spin-independent or spin-dependent coupling, e.g. due to a magnetic dipole moment of dark matter, or due to a isospin-violating spin-independent coupling, i.e. $f_p/f_n \neq 1$. Other important examples are dark matter-quark interactions mediated by a pseudoscalar particle [365, 366] or dark matter interacting via an anapole moment [265, 367].

When investigating the compatibility of DAMA with the null searches in the context of non-standard dark matter-nucleon interactions, most previous works have focused on one specific scenario at a time, with a few examples given above. In contrast to that approach, and in the spirit of the second part of this thesis, in this section we will investigate the problem from an (almost) model-independent point of view, by studying the (in)compatibility of DAMA within the non-relativistic effective theory of dark matter-nucleon interactions [362]. In this framework, scattering can be induced by 28 non-relativistic operators constructed

solely from the requirement of Galilean invariance, which by definition describe the most general theory for one-body interactions between a dark matter particle with spin 0 or 1/2 and a nucleon, for mediators with masses $\gtrsim 100\,\mathrm{MeV}$ and spin less or equal to 1 [368–384]. In order to efficiently probe the 28-dimensional parameter space of the theory, we will develop a novel semi-analytical method for comparing a positive signal with a given set of null searches, allowing simultaneously for the presence of all 28 operators without any a priori restrictions on their relative strengths. Most importantly, this approach fully takes into account the interferences between the various operators, which in general can lead to a large variation in the relative rates of different experiments. We will then apply this method to the concrete case of the DAMA modulation, confronting it to both direct detection results as well as to the non-observation of a high-energy neutrino flux from the direction of the Sun.

The rest of this section is organized as follows: in Sec. 7.1, we define the non-relativistic effective theory for dark matter-nucleon interactions, before introducing in Sec. 7.2 our method of comparing the results of different experiments in the parameter space of this theory. Lastly, in Sec. 7.3 we present the results of applying this approach to the case of DAMA, thereby answering the question whether such a generalized particle physics framework allows for a consistent dark matter interpretation of the observed modulation signal.

7.1. Effective theory of dark matter-nucleon interactions

The amplitude for the non-relativistic scattering of a dark matter particle χ off a nucleon N has to be invariant under transformations of the Galilean symmetry group. The most general (quantum mechanical) Hamiltonian density compatible with this restriction can be written as [362]

$$\hat{\mathcal{H}}_{\mathrm{N}}(\mathbf{r}) \;=\; \sum_{\tau=0,1} \sum_{k} c_k^\tau \, \hat{\mathcal{O}}_k(\mathbf{r}) \, t^\tau \,, \tag{7.1}$$

where $t^0 = 1$ and $t^1 = \tau_3$ denote the identity and the third Pauli matrix in isospin space, respectively, and $\mathbf{r}$ is the relative distance between the dark matter particle and the nucleon. Furthermore, each $\hat{\mathcal{O}}_k$ is a Galilean invariant operator constructed from the momentum transfer operator $\hat{\mathbf{q}}$, the transverse relative velocity operator $\hat{\mathbf{v}}^\perp$, as well as from the nucleon and dark matter particle spin operators $\hat{\mathbf{S}}_N$ and $\hat{\mathbf{S}}_\chi$, respectively. For dark matter particles with spin 0 or 1/2 interacting with nucleons via a heavy mediator with spin 1 or less, these operators have been constructed in [362,368], and are listed in Table 7.1. We remark that for simplicity we do not consider two additional operators that can arise for dark matter with spin 1 [379]. In Eq. (7.1), each operator $\hat{\mathcal{O}}_k$ appears both in combination with the isoscalar and isovector coupling constants c_k^0 and c_k^1, respectively, which are related to the coupling constants for protons c_k^p and for neutrons c_k^n by $c_k^p = (c_k^0 + c_k^1)/2$ and $c_k^n = (c_k^0 - c_k^1)/2$.

In the next step, one can construct the most general Hamiltonian density for the interaction of dark matter with a target nucleus T. Under the assumption of one-body dark matter-nucleon interactions, it can be written as [362]

$$\hat{\mathcal{H}}_{\mathrm{T}}(\mathbf{r}) = \sum_{\tau=0,1} \left[\hat{\ell}_{\mathrm{V}}^\tau \hat{\rho}_{\mathrm{V}}^\tau(\mathbf{r}) + \hat{\ell}_{\mathrm{A}}^\tau \hat{\rho}_{\mathrm{A}}^\tau(\mathbf{r}) + \hat{\boldsymbol{\ell}}_{\mathrm{S}}^\tau \cdot \hat{\boldsymbol{\jmath}}_{\mathrm{S}}^\tau(\mathbf{r}) + \hat{\boldsymbol{\ell}}_{\mathrm{C}}^\tau \cdot \hat{\boldsymbol{\jmath}}_{\mathrm{C}}^\tau(\mathbf{r}) + \hat{\boldsymbol{\ell}}_{\mathrm{SV}}^\tau \cdot \hat{\boldsymbol{\jmath}}_{\mathrm{SV}}^\tau(\mathbf{r}) \right] , \tag{7.2}$$

$\hat{\mathcal{O}}_1 = \mathbb{1}_{\chi N}$	$\hat{\mathcal{O}}_9 = i\hat{\mathbf{S}}_\chi \cdot \left(\hat{\mathbf{S}}_N \times \frac{\hat{\mathbf{q}}}{m_N}\right)$
$\hat{\mathcal{O}}_3 = i\hat{\mathbf{S}}_N \cdot \left(\frac{\hat{\mathbf{q}}}{m_N} \times \hat{\mathbf{v}}^\perp\right)$	$\hat{\mathcal{O}}_{10} = i\hat{\mathbf{S}}_N \cdot \frac{\hat{\mathbf{q}}}{m_N}$
$\hat{\mathcal{O}}_4 = \hat{\mathbf{S}}_\chi \cdot \hat{\mathbf{S}}_N$	$\hat{\mathcal{O}}_{11} = i\hat{\mathbf{S}}_\chi \cdot \frac{\hat{\mathbf{q}}}{m_N}$
$\hat{\mathcal{O}}_5 = i\hat{\mathbf{S}}_\chi \cdot \left(\frac{\hat{\mathbf{q}}}{m_N} \times \hat{\mathbf{v}}^\perp\right)$	$\hat{\mathcal{O}}_{12} = \hat{\mathbf{S}}_\chi \cdot \left(\hat{\mathbf{S}}_N \times \hat{\mathbf{v}}^\perp\right)$
$\hat{\mathcal{O}}_6 = \left(\hat{\mathbf{S}}_\chi \cdot \frac{\hat{\mathbf{q}}}{m_N}\right)\left(\hat{\mathbf{S}}_N \cdot \frac{\hat{\mathbf{q}}}{m_N}\right)$	$\hat{\mathcal{O}}_{13} = i\left(\hat{\mathbf{S}}_\chi \cdot \hat{\mathbf{v}}^\perp\right)\left(\hat{\mathbf{S}}_N \cdot \frac{\hat{\mathbf{q}}}{m_N}\right)$
$\hat{\mathcal{O}}_7 = \hat{\mathbf{S}}_N \cdot \hat{\mathbf{v}}^\perp$	$\hat{\mathcal{O}}_{14} = i\left(\hat{\mathbf{S}}_\chi \cdot \frac{\hat{\mathbf{q}}}{m_N}\right)\left(\hat{\mathbf{S}}_N \cdot \hat{\mathbf{v}}^\perp\right)$
$\hat{\mathcal{O}}_8 = \hat{\mathbf{S}}_\chi \cdot \hat{\mathbf{v}}^\perp$	$\hat{\mathcal{O}}_{15} = -\left(\hat{\mathbf{S}}_\chi \cdot \frac{\hat{\mathbf{q}}}{m_N}\right)\left[\left(\hat{\mathbf{S}}_N \times \hat{\mathbf{v}}^\perp\right) \cdot \frac{\hat{\mathbf{q}}}{m_N}\right]$

Table 7.1.: List of non-relativistic operators compatible with Galilean symmetry, constructed in [368]. By introducing the nucleon mass m_N in several of the $\hat{\mathcal{O}}_k$, one ensures that all operators have the same mass dimension.

where the operators

$$
\begin{aligned}
\hat{\rho}^\tau_{\mathrm{V}}(\mathbf{r}) &= \sum_{i=1}^{A} \delta(\mathbf{r}-\mathbf{r}_i) t_i^\tau \,, \\
\hat{\rho}^\tau_{\mathrm{A}}(\mathbf{r}) &= \sum_{i=1}^{A} \frac{1}{2m_N}\left[i\overleftarrow{\nabla}_{\mathbf{r}} \cdot \boldsymbol{\sigma}_i \delta(\mathbf{r}-\mathbf{r}_i) - i\delta(\mathbf{r}-\mathbf{r}_i)\, \boldsymbol{\sigma}_i \cdot \overrightarrow{\nabla}_{\mathbf{r}} \right] t_i^\tau \,, \\
\hat{\boldsymbol{\jmath}}^\tau_{\mathrm{S}}(\mathbf{r}) &= \sum_{i=1}^{A} \boldsymbol{\sigma}_i \delta(\mathbf{r}-\mathbf{r}_i) t_i^\tau \,, \\
\hat{\boldsymbol{\jmath}}^\tau_{\mathrm{C}}(\mathbf{r}) &= \sum_{i=1}^{A} \frac{1}{2m_N}\left[i\overleftarrow{\nabla}_{\mathbf{r}} \delta(\mathbf{r}-\mathbf{r}_i) - i\delta(\mathbf{r}-\mathbf{r}_i)\overrightarrow{\nabla}_{\mathbf{r}} \right] t_i^\tau \,, \\
\hat{\boldsymbol{\jmath}}^\tau_{\mathrm{SV}}(\mathbf{r}) &= \sum_{i=1}^{A} \frac{1}{2m_N}\left[\overleftarrow{\nabla}_{\mathbf{r}} \times \boldsymbol{\sigma}_i \delta(\mathbf{r}-\mathbf{r}_i) + \delta(\mathbf{r}-\mathbf{r}_i)\, \boldsymbol{\sigma}_i \times \overrightarrow{\nabla}_{\mathbf{r}} \right] t_i^\tau
\end{aligned}
\tag{7.3}
$$

correspond to the nuclear vector and axial charges, as well as to the nuclear spin, convection and spin-velocity currents. Here, $\mathbf{r}_i$ and $\mathbf{r}$ denote the position vector of the i-th nucleon and the dark matter particle, respectively, in both cases defined in the nucleus center-of-mass reference frame. Furthermore, $\boldsymbol{\sigma}_i$ is the vector of Pauli matrices acting on the i-th nucleon, and t_i^τ is the previously defined operator t^τ, now acting on the nucleon i.

The model-dependent couplings of dark matter to nucleons enter the Hamiltonian density in Eq. (7.2) via the operators $\hat{\ell}^\tau_{\mathrm{V}}$, $\hat{\ell}^\tau_{\mathrm{A}}$, $\hat{\boldsymbol{\ell}}^\tau_{\mathrm{S}}$, $\hat{\boldsymbol{\ell}}^\tau_{\mathrm{C}}$, and $\hat{\boldsymbol{\ell}}^\tau_{\mathrm{SV}}$, which are given by

$$
\begin{aligned}
\hat{\ell}^\tau_{\mathrm{V}} &= c_1^\tau + i\left(\frac{\hat{\mathbf{q}}}{m_N} \times \hat{\mathbf{v}}^\perp_T\right) \cdot \hat{\mathbf{S}}_\chi\, c_5^\tau + \hat{\mathbf{v}}^\perp_T \cdot \hat{\mathbf{S}}_\chi\, c_8^\tau + i\frac{\hat{\mathbf{q}}}{m_N} \cdot \hat{\mathbf{S}}_\chi\, c_{11}^\tau \,, \\
\hat{\boldsymbol{\ell}}^\tau_{\mathrm{S}} &= \frac{1}{2}\left[i\frac{\hat{\mathbf{q}}}{m_N} \times \hat{\mathbf{v}}^\perp_T\, c_3^\tau + \hat{\mathbf{S}}_\chi\, c_4^\tau + \frac{\hat{\mathbf{q}}}{m_N}\, \frac{\hat{\mathbf{q}}}{m_N} \cdot \hat{\mathbf{S}}_\chi\, c_6^\tau + \hat{\mathbf{v}}^\perp_T\, c_7^\tau + i\frac{\hat{\mathbf{q}}}{m_N} \times \hat{\mathbf{S}}_\chi\, c_9^\tau + i\frac{\hat{\mathbf{q}}}{m_N}\, c_{10}^\tau \right. \\
&\quad + \left. \hat{\mathbf{v}}^\perp_T \times \hat{\mathbf{S}}_\chi\, c_{12}^\tau + i\frac{\hat{\mathbf{q}}}{m_N}\hat{\mathbf{v}}^\perp_T \cdot \hat{\mathbf{S}}_\chi\, c_{13}^\tau + i\hat{\mathbf{v}}^\perp_T \frac{\hat{\mathbf{q}}}{m_N} \cdot \hat{\mathbf{S}}_\chi\, c_{14}^\tau + \frac{\hat{\mathbf{q}}}{m_N} \times \hat{\mathbf{v}}^\perp_T\, \frac{\hat{\mathbf{q}}}{m_N} \cdot \hat{\mathbf{S}}_\chi\, c_{15}^\tau \right] \,, \\
\hat{\boldsymbol{\ell}}^\tau_{\mathrm{C}} &= i\frac{\hat{\mathbf{q}}}{m_N} \times \hat{\mathbf{S}}_\chi\, c_5^\tau - \hat{\mathbf{S}}_\chi\, c_8^\tau \,,
\end{aligned}
$$

$$\begin{aligned}\hat{\boldsymbol{\ell}}^{\tau}_{\mathrm{SV}} &= \frac{1}{2}\left[\frac{\hat{\mathbf{q}}}{m_N}\, c^{\tau}_3 + i\hat{\mathbf{S}}_\chi\, c^{\tau}_{12} - \frac{\hat{\mathbf{q}}}{m_N}\times\hat{\mathbf{S}}_\chi\, c^{\tau}_{13} - i\frac{\hat{\mathbf{q}}}{m_N}\frac{\hat{\mathbf{q}}}{m_N}\cdot\hat{\mathbf{S}}_\chi\, c^{\tau}_{15}\right],\\ \hat{\ell}^{\tau}_{\mathrm{A}} &= 0\,. \end{aligned} \tag{7.4}$$

Here, $\hat{\mathbf{v}}^{\perp}_T \equiv \hat{\mathbf{v}}^{\perp} - \hat{\mathbf{v}}^{\perp}_N$, where $\hat{\mathbf{v}}^{\perp}_N$ is an operator acting on the space coordinates of a single nucleon [362]. For explicit coordinate space representations of the operators $\hat{\mathbf{q}}$, $\hat{\mathbf{v}}^{\perp}_N$, and $\hat{\mathbf{v}}^{\perp}_T$ we refer to [151]. We notice that the standard spin-independent and spin-dependent interactions, corresponding to the operators $\hat{\mathcal{O}}_1$ and $\hat{\mathcal{O}}_4$, respectively, only contribute to the vector and scalar operators $\hat{\ell}^{\tau}_{\mathrm{V}}$ and $\hat{\boldsymbol{\ell}}^{\tau}_{\mathrm{S}}$. On the other hand, the operator $\hat{\boldsymbol{\ell}}^{\tau}_{\mathrm{C}}$ multiplies the nuclear convection current which is also known from electroweak scattering off nuclei, while $\hat{\boldsymbol{\ell}}^{\tau}_{\mathrm{SV}}$ corresponds to the nuclear spin-velocity current and is specific to dark matter-nucleon interactions. Lastly, we remark that the vanishing of $\hat{\ell}^{\tau}_{\mathrm{A}}$ is based on the assumption that all nuclear ground states relevant for our purposes are eigenstates of P and CP.

These considerations allow us to calculate the differential cross section for the non-relativistic scattering of dark matter with a target nucleus of mass m_T and spin J [362]:

$$\begin{aligned}\frac{\mathrm{d}\sigma_T}{\mathrm{d}E_R} = \frac{2m_T}{(2J+1)\,v^2}\sum_{\tau,\tau'}\Bigg[&\sum_{k=M,\Sigma',\Sigma''} R^{\tau\tau'}_k\left(v^{\perp 2}_T, \frac{q^2}{m^2_N}\right) W^{\tau\tau'}_k(q^2)\\ &+ \frac{q^2}{m^2_N}\sum_{k=\Phi'',\Phi''M,\tilde{\Phi}',\Delta,\Delta\Sigma'} R^{\tau\tau'}_k\left(v^{\perp 2}_T, \frac{q^2}{m^2_N}\right) W^{\tau\tau'}_k(q^2)\Bigg]. \end{aligned} \tag{7.5}$$

This expression can be seen as the generalization of Eqs. (2.4) and (2.5) to the most general case within the non-relativistic effective theory of dark matter-nucleon interactions. Eq. (7.5) consists of eight terms, each one being the product of a nuclear response function $W^{\tau\tau'}_k$ and a dark matter response function $R^{\tau\tau'}_k$. The former have to be evaluated numerically, based on a nuclear shell model describing the various nuclear charges and currents defined in Eq. (7.3). In this work, we employ the results from [368] and [151] for the nuclei relevant for direct detection and capture in the Sun, respectively. On the other hand, $R^{\tau\tau'}_k$ are analytically known functions of q^2 and $v^{\perp 2}_T = v^2 - q^2/(4\mu^2_T)$ and are provided in Appendix D. In particular, from Eq. (D.1) one can infer that the pairs of operators $(\hat{\mathcal{O}}_1, \hat{\mathcal{O}}_3)$, $(\hat{\mathcal{O}}_4, \hat{\mathcal{O}}_5)$, $(\hat{\mathcal{O}}_4, \hat{\mathcal{O}}_6)$, $(\hat{\mathcal{O}}_8, \hat{\mathcal{O}}_9)$, $(\hat{\mathcal{O}}_{11}, \hat{\mathcal{O}}_{12})$, $(\hat{\mathcal{O}}_{11}, \hat{\mathcal{O}}_{15})$, and $(\hat{\mathcal{O}}_{12}, \hat{\mathcal{O}}_{15})$ interfere in the calculation of the scattering cross section due to terms proportional to $c^{\tau}_k c^{\tau'}_{k'}$, $k \neq k'$. In addition, also the isoscalar and isovector components of each operator $\hat{\mathcal{O}}_k$ interfere, due to the terms $c^{\tau}_k c^{\tau'}_k$, $\tau \neq \tau'$ present in Eq. (D.1). Other pairs of operators do not interfere, either due to the P and CP invariance of the underlying nuclear ground states, or due to the different dependence on the dark matter spin operator $\hat{\mathbf{S}}_\chi$. We refer to [377] for a more detailed discussion of the interference patterns in the calculation of direct detection exclusion limits.

Finally, we convert the scattering cross section given by Eq. (7.5) to a total number of events N expected at a direct detection experiment:

$$N = \mathcal{D}\int_0^\infty \mathrm{d}E_R \sum_T \epsilon_T(E_R)\,\frac{\mathrm{d}R_T}{\mathrm{d}E_R}\,. \tag{7.6}$$

Here, $\mathrm{d}R_T/\mathrm{d}E_R$ is the differential event rate which can be calculated from the scattering cross section by using the general expression given in Eq. (2.2). To this end, we assume that the velocity distribution of dark matter is given by a Maxwell-Boltzmann distribution (c.f. Eq. (1.5)), with parameters v_0 and v_{esc} as specified below. Furthermore, in Eq. (7.6), $\mathcal{D}$ is the exposure of the experiment, while $\epsilon_T(E_R)$ is the efficiency, i.e. the probability that a

nuclear recoil off the target nucleus T with energy E_R is actually detected. In Appendix A we provide these quantities for the direct detection experiments employed in this section.

The total number of expected events N is the relevant observable for all experiments reporting a null result; the DAMA collaboration, on the other hand, searches for the annual modulation of the event rate. Based on the general expression for the time dependence of $\mathrm{d}R_T/\mathrm{d}E_R$ provided in Eq. (2.9), the modulation amplitude in a given energy bin defined by the lower and upper boundaries E_- and E_+ is defined by

$$S_{\mathrm{DAMA}[E_-,E_+]} \equiv \frac{1}{E_+ - E_-} \cdot \frac{1}{2} \cdot \left(R_{\mathrm{DAMA}[E_-,E_+]}\Big|_{\text{June 1st}} - R_{\mathrm{DAMA}[E_-,E_+]}\Big|_{\text{Dec 1st}} \right) . \quad (7.7)$$

In this expression, $R_{\mathrm{DAMA}[E_-,E_+]}\big|_t$ is the event rate in the corresponding bin at time t, which can be calculated from Eq. (7.6), using $R = N/\mathcal{D}$ as well as the efficiency $\epsilon_T^{\mathrm{DAMA}[E_-,E_+]}(E_R) = \Phi\left(Q_T E_R, E_-, E_+\right)$. Here, Q_T denotes the quenching factor for the target isotope $T \in \{\mathrm{Na}, \mathrm{I}\}$, while $\Phi(Q_T E_R, E_-, E_+)$ is the probability that an event with nuclear recoil energy E_R, corresponding to a quenched energy of $Q_T E_R$, is reconstructed in the energy bin $[E_-, E_+]$. We calculate this quantity under the assumption of a Gaussian energy resolution as specified in [100].

Besides confronting the DAMA modulation signal to the null results from other direct detection experiments, we also consider the constraints arising from the non-observation of an excess of high-energy neutrinos from the direction of the Sun. As elaborated in Sec. 2.2, under the assumption of equilibrium between capture and annihilation of dark matter, neutrino telescopes such as IceCube [158] or Super-Kamiokande [170] set a constraint on the capture rate C of dark matter, separately for each dark matter mass and annihilation channel. Within the framework of non-relativistic dark matter-nucleon interactions, we compute C by inserting the expression for the scattering cross section, Eq. (7.5), in Eqs. (2.10)–(2.13).

To summarize, the formalism introduced in this section allows us to calculate the event rates in direct detection experiments as well as the capture rate of dark matter in the Sun for a given set of 28 coefficients c_k^τ appearing in Eq. (7.1), which fully specify the underlying particle physics model of dark matter. For our purposes, it is crucial to realize that the dependence of the rates on the 28-dimensional coefficient vector $\mathbf{c} = (c_1^{(0)}, c_1^{(1)}, c_3^{(0)}, c_3^{(1)}, ..., c_{15}^{(0)}, c_{15}^{(1)})^T$ can be written as a quadratic form,

$$\text{event rate} \propto \mathbf{c}^T \mathbb{X}\, \mathbf{c}\,, \quad (7.8)$$

with $\mathbb{X}$ being a real symmetric 28×28 matrix. For a given dark matter mass, this matrix encodes all information about nuclear responses, the dark matter velocity distribution as well as the specific details of the corresponding experiment such as exposure or efficiency, but it is independent of the particle physics model of dark matter, which only enters via the vector $\mathbf{c}$. We will show in the next section that the specific functional form of Eq. (7.8) allows for the development of a semi-analytical approach of comparing experimental results in the parameter space of the non-relativistic effective theory, without the need of manually scanning through all possible values of the coefficients c_k^τ.

7.2. Confronting the DAMA signal to null result experiments

In principle, the modulation signal observed by DAMA can be induced by any combination of the non-relativistic operators $\hat{\mathcal{O}}_k$. In order to provide a good fit to the data in the energy

Experiment	$N^{95\%\text{-u.l.}}$	$N^{99.9\%\text{-u.l.}}$
LUX	4.74 events	9.23 events
SuperCDMS	18.2 events	25.6 events
SIMPLE	5.26 events	11.9 events
PICO	4.74 events	9.23 events
COUPP ($E_T = 7.8$ keV)	6.30 events	11.2 events
COUPP ($E_T = 11$ keV)	7.75 events	13.0 events
COUPP ($E_T = 15.5$ keV)	14.4 events	21.1 events
PICASSO ($E_T = 1.73$ keV)	8.72 events/($\text{kg}_F \cdot \text{day}$)	18.0 events/($\text{kg}_F \cdot \text{day}$)
PICASSO ($E_T = 2.9$ keV)	3.21 events/($\text{kg}_F \cdot \text{day}$)	5.59 events/($\text{kg}_F \cdot \text{day}$)

Table 7.2.: 95% C.L. and 99.9% C.L. upper limits on the number of expected recoil events induced by dark matter scattering for the direct detection experiments considered in this section. These numbers follow from the implementation of the experimental set-ups described in Appendix A.

bin $[E_-, E_+]$, we require the coefficient vector $\mathbf{c} = (c_1^{(0)}, c_1^{(1)}, c_3^{(0)}, c_3^{(1)}, ..., c_{15}^{(0)}, c_{15}^{(1)})^T$ to fulfill the conditions

$$\mathbf{c}^T \, \mathbb{S}_{\text{DAMA}}(E_-, E_+; m_\chi) \, \mathbf{c} > S^{n_\sigma\text{-l.l.}}_{\text{DAMA}[E_-,E_+]} \tag{7.9}$$

$$\text{and} \quad \mathbf{c}^T \, \mathbb{S}_{\text{DAMA}}(E_-, E_+; m_\chi) \, \mathbf{c} < S^{n_\sigma\text{-u.l.}}_{\text{DAMA}[E_-,E_+]} \, . \tag{7.10}$$

Here, $S^{n_\sigma\text{-l.l.}}_{\text{DAMA}[E_-,E_+]}$ and $S^{n_\sigma\text{-u.l.}}_{\text{DAMA}[E_-,E_+]}$ is the n_σ-significance lower limit (l.l.) and upper limit (u.l.) on the modulation amplitude in the bin $[E_-, E_+]$, following from the observed amplitudes $(1.75\pm0.37)\times10^{-2}$, $(2.51\pm0.40)\times10^{-2}$ and $(2.16\pm0.40)\times10^{-2}$ $\text{day}^{-1}\,\text{kg}^{-1}\,\text{keV}^{-1}$ in the energy bins [2.0, 2.5], [2.5, 3.0] and [3.0, 3.5] keV, respectively. Furthermore, for a fixed dark matter mass m_χ, the 28×28 matrix $\mathbb{S}_{\text{DAMA}}(E_-, E_+; m_\chi)$ can be calculated by using the approach introduced in Sec. 7.1, in particular by employing Eq. (7.8).

Similarly, the results from the direct detection experiments reporting no excess of events over the known sources of background lead to the inequalities

$$\mathbf{c}^T \, \mathbb{N}_j(m_\chi) \, \mathbf{c} < N_j^{n_\sigma\text{-u.l.}} \, , \tag{7.11}$$

where the matrices $\mathbb{N}_j(m_\chi)$ again follow from the considerations in the previous section, separately for each experiment j. Furthermore, $N_j^{n_\sigma\text{-u.l.}}$ is the n_σ-significance upper limit on the total number of expected events N, which we provide in Table 7.2 for the direct detection experiments employed in this section, i.e. for LUX [102], SuperCDMS [109], SIMPLE [122], PICO [125], COUPP [120] (with nucleation thresholds $E_T = 7.8$, 11.0 and 15.5 keV) and PICASSO [123] (with nucleation thresholds $E_T = 1.73$ and 2.9 keV).

Also the null results from neutrino telescopes searching for a high-energy neutrino flux correlated with the direction of the Sun can be cast in a form equivalent to Eqs. (7.9)–(7.11):

$$\mathbf{c}^T \, \mathbb{C}_j(\chi\chi \to \text{final}; m_\chi) \, \mathbf{c} < C_j^{n_\sigma\text{-u.l.}}(\chi\chi \to \text{final}; m_\chi) \, . \tag{7.12}$$

Here, $C_j^{n_\sigma\text{-u.l.}}(\chi\chi \to \text{final}; m_\chi)$ is the n_σ-upper limit on the capture rate of dark matter with mass m_χ for the annihilation channel $\chi\chi \to$ final, following from a neutrino telescope labeled by j, and assuming equilibrium between captures and annihilations. Again, the

matrix $\mathbb{C}_j(\chi\chi \to \text{final}; m_\chi)$ can be calculated from the formalism defined in Sec. 7.1, using Eq. (7.8). In our numerical analysis, we employ the null results from Super-Kamiokande[1] for the annihilation channels $b\bar{b}$ and $\tau^+\tau^-/W^+W^-$, which are the commonly used examples for a soft and hard neutrino spectrum, respectively. We extract the corresponding 95% and 99.9% C.L. limits from the 90% C.L. limits on C provided in [170], by assuming that the relevant likelihood has a gaussian distribution centered at zero signal.

For the following discussion, we find it convenient to define the rescaled matrices

$$\mathbb{A}^{n_\sigma\text{-l.l}}_{\text{DAMA}[E_-,E_+]}(m_\chi) \equiv \frac{\mathbb{S}_{\text{DAMA}}(E_-,E_+;m_\chi)}{S^{n_\sigma\text{-l.l}}_{\text{DAMA}[E_-,E_+]}} \;, \quad \mathbb{A}^{n_\sigma\text{-u.l.}}_{\text{DAMA}[E_-,E_+]}(m_\chi) \equiv \frac{\mathbb{S}_{\text{DAMA}}(E_-,E_+;m_\chi)}{S^{n_\sigma\text{-u.l.}}_{\text{DAMA}[E_-,E_+]}} \;,$$
$$\mathbb{A}^{n_\sigma\text{-u.l.}}_{\text{DD},j}(m_\chi) \equiv \frac{\mathbb{N}_{\text{j}}(m_\chi)}{N^{n_\sigma\text{-u.l.}}_j} \;, \qquad \mathbb{A}^{n_\sigma\text{-u.l.}}_{\chi\chi\to\text{final}}(m_\chi) \equiv \frac{\mathbb{C}_{\text{j}}(\chi\chi \to \text{final}; m_\chi)}{C^{n_\sigma\text{-u.l.}}_j(\chi\chi \to \text{final}; m_\chi)} \;. \tag{7.13}$$

This allows us to rewrite Eq. (7.9) as

$$\mathbf{c}^T \; \mathbb{A}^{n_\sigma\text{-l.l.}}_{\text{DAMA}[E_-,E_+]}(m_\chi) \; \mathbf{c} > 1 \;, \tag{7.14}$$

while Eqs. (7.10), (7.11), (7.12) are transformed to the common form

$$\mathbf{c}^T \; \mathbb{A}^{n_\sigma\text{-u.l.}}_j(m_\chi) \; \mathbf{c} < 1 \;, \tag{7.15}$$

with j denoting either a DAMA upper limit, a null result from a direct detection experiment, or the constraint arising from Super-Kamiokande.

The last two inequalities have a simple geometrical interpretation: Eq. (7.14) corresponds to the exterior of an ellipsoid in the 28-dimensional parameter space of the theory, while, for fixed j, Eq. (7.15) describes the interior of an ellipsoid. Hence, for a given dark matter mass m_χ and a fixed energy bin $[E_-, E_+]$, the modulation signal observed by DAMA is incompatible with the null results if the region outside the ellipsoid defined by $\mathbb{A}^{n_\sigma\text{-l.l.}}_{\text{DAMA}[E_-,E_+]}(m_\chi)$ has no overlap with the intersection of all interiors of the ellipsoids defined by $\mathbb{A}^{n_\sigma\text{-u.l.}}_j(m_\chi)$, with j running over all null search experiments considered in the analysis. For the latter, we consider the set of the three upper limits on the modulation amplitude following from the DAMA data, as well as the nine constraints arising from the direct detection experiments listed in Table 7.2; these twelve upper limits are defined as the set $\mathcal{E}$. Furthermore, we consider the set $\mathcal{E}'$, which additionally includes the upper limit on the capture rate in the Sun following from the Super-Kamiokande data, either for the annihilation channel $b\bar{b}$ or $\tau^+\tau^-/W^+W^-$.

Operationally, for a fixed dark matter mass m_χ and a given energy bin $[E_-, E_+]$, we consider the 95% C.L. ellipsoids defined through the matrices $\mathbb{A}^{95\%\text{-u.l.}}_j$, and determine the maximal value of n_σ for which the intersection of the interior of all of these ellipsoids has no overlap with the exterior of the ellipsoid represented by $\mathbb{A}^{n_\sigma\text{-l.l.}}_{\text{DAMA}[E_-,E_+]}(m_\chi)$. This procedure is illustrated schematically (i.e. not based on actual data) in Fig. 7.1 for the case of only two operators. Finally, we quantify the tension between the dark matter interpretation of the DAMA modulation signal and the null results via $N^{\max}_\sigma = \max_{a\in\{1,2,3\}}\{n^{\max,\,(a)}_\sigma\}$, where $n^{\max,\,(a)}_\sigma$ is defined as the value of n_σ constructed as described above, for the DAMA energy bin labeled by $a \in \{1, 2, 3\}$. The precise statistical interpretation of $N^{\max}_\sigma$ is then as follows:

[1]The constraints from IceCube turn out to be irrelevant for the results of this section.

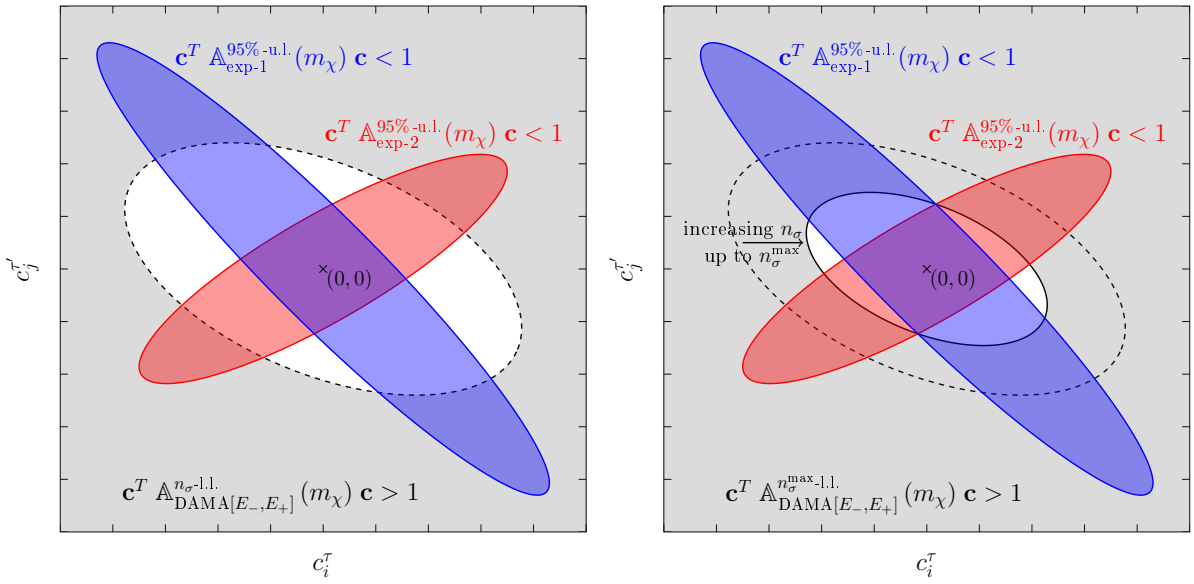

Figure 7.1.: Illustration of our method which quantifies the tension of the DAMA signal with the combination of null search experiments, for a simplified scenario involving only two operators with coefficients c_i^τ and $c_j^{\tau\prime}$. The regions allowed by the two null experiments "exp-1" and "exp-2" at 95% C.L. are shown as blue and red ellipses, respectively, and are calculated from Eq. (7.15). On the other hand, the n_σ-significance lower limit on the DAMA modulation amplitude following from Eq. (7.14) is shown as the gray region. If n_σ is small enough, the intersection between all of these regions is empty, as shown exemplary in the left panel. When increasing n_σ, the DAMA allowed gray region gets larger, and at some point there is a non-vanishing overlap with the intersection of the blue and red regions, which represent the null searches. The maximal value of n_σ for which the intersection is still empty is defined as $n_\sigma^{\max}$, corresponding to the situation shown in the right panel.

after imposing the 95% C.L. upper limits from the null results, the expected modulation amplitude in DAMA deviates from the measurement by $N_\sigma^{\max}$ standard deviations in at least one of the three energy bins in which DAMA observes a signal. We remark that for simplicity we fix the confidence level of the null results to 95% in this definition; however, our method can straightforwardly be applied to a different value of this confidence level. In order to study the dependence of our results on that point, we will in particular also derive results for $N_\sigma^{\max}$ by imposing instead a 99.9% C.L. for the upper limits following from the null search experiments.

While the considerations above define our method of quantifying the tension between DAMA and the null searches, we have not yet explained how we actually in practice determine whether the intersection of the ellipsoids defined by the matrices $\mathbb{A}_j^{95\%\text{-u.l.}}$, $j \in \mathcal{E}$, is fully contained in the ellipsoid represented by $\mathbb{A}^{n_\sigma\text{-l.l.}}_{\text{DAMA}[E_-,E_+]}$. For testing the validity of this statement, it is sufficient to find a set of real positive numbers $\zeta_j \geq 0$ satisfying [385]

$$
\begin{aligned}
&i)\ \sum_{j\,\in\,\mathcal{E}} \zeta_j < 1 \quad \text{and} \\
&ii)\ \left(\sum_{j\,\in\,\mathcal{E}} \zeta_j\, \mathbb{A}_j^{95\%\text{-u.l.}}\right) - \mathbb{A}^{n_\sigma\text{-l.l.}}_{\text{DAMA}[E_-,E_+]} \text{ is a positive definite matrix.}
\end{aligned}
\tag{7.16}
$$

If this is the case, the combination of Eqs. (7.14) and (7.15) has no solution[2], and hence the DAMA modulation in the bin $[E_-, E_+]$ is incompatible with the null searches $\mathcal{E}$. Numerically, we determine the existence of ζ_j satisfying the conditions *i*) and *ii*), which are a specific example of linear matrix inequalities [386], by means of the `feasp` solver implemented in MATLAB [387].

7.3. Discussion of the numerical results

Finally, we present in Fig. 7.2 the results for $N_\sigma^{\max}$, i.e. our measure of tension between DAMA and the null search experiments, as a function of the dark matter mass m_χ. The left and right panels correspond to dark matter with spin 1/2 and 0, respectively; in the language of the non-relativistic effective theory, in the latter case only the subset of operators $\{\mathcal{O}_1, \mathcal{O}_3, \mathcal{O}_7, \mathcal{O}_{10}\}$ contributes to the scattering cross section, as these operators do not involve the dark matter spin $\hat{\mathbf{S}}_\chi$, c.f. Table 7.1. Furthermore, the upper and lower panels of Fig. 7.2 correspond to two different choices of the quenching factors relevant for DAMA, namely $Q_{\text{Na}} = 0.3$ and $Q_{\text{I}} = 0.09$ [388], as well as $Q_{\text{Na}} = 0.4$ and $Q_{\text{I}} = 0.05$ [389], respectively. In all panels, the blue curves show our results when only taking into account direct detection experiments in the analysis, defined as the set $\mathcal{E}$ of experiments introduced in the previous section. On the other hand, the red curves correspond to the set $\mathcal{E}'$, i.e. they additionally include the Super-Kamiokande upper limits on the capture rate, assuming the annihilation channel $\tau^+\tau^-/W^+W^-$. We do not show separately the results for dark matter annihilations into $b\bar{b}$, as the resulting values for $N_\sigma^{\max}$ are identical to those obtained by only considering direct detection experiments, i.e. the set of experiments $\mathcal{E}$. Lastly, the solid curves correspond to our benchmark choice of astrophysical parameters, defined by $v_0 = 230\,\text{km/s}$ and $v_{\text{esc}} = 533\,\text{km/s}$ in the Maxwell-Boltzmann distribution, while the shaded bands were derived by varying these two parameters within the ranges $220 - 240$ km/s and $492 - 587$ km/s, respectively. It follows from Fig. 7.2 that our results are robust against reasonable changes of v_0 and v_{esc}; of course, a completely different velocity distribution of dark matter might potentially alter our conclusions in a more significant way. In this context, we remark that our results are fully independent of the local dark matter density ρ_0, as this quantity cancels out exactly when considering the tension between DAMA and the null searches.

As a general conclusion, in the framework of the non-relativistic effective theory we find a strong tension of the dark matter interpretation of the DAMA modulation signal with the null results of (in)direct detection experiments. Concretely, when considering only direct detection results, we find $N_\sigma^{\max} \gtrsim 5.1\sigma$ for the quenching factors $Q_{\text{Na}} = 0.3$ and $Q_{\text{I}} = 0.09$

[2] This statement follows from

$$
\mathbf{c}^T\, \mathbb{A}^{n_\sigma\text{-l.l.}}_{\text{DAMA}[E_-,E_+]} \mathbf{c} < \mathbf{c}^T \left(\sum_{j\,\in\,\mathcal{E}} \zeta_j \mathbb{A}_j^{95\%\text{-u.l.}}\right) \mathbf{c} < \sum_{j\,\in\,\mathcal{E}} \zeta_j < 1\,, \tag{7.17}
$$

where in the first step we use condition *ii*), in the second Eq. (7.15), and in the third condition *i*).

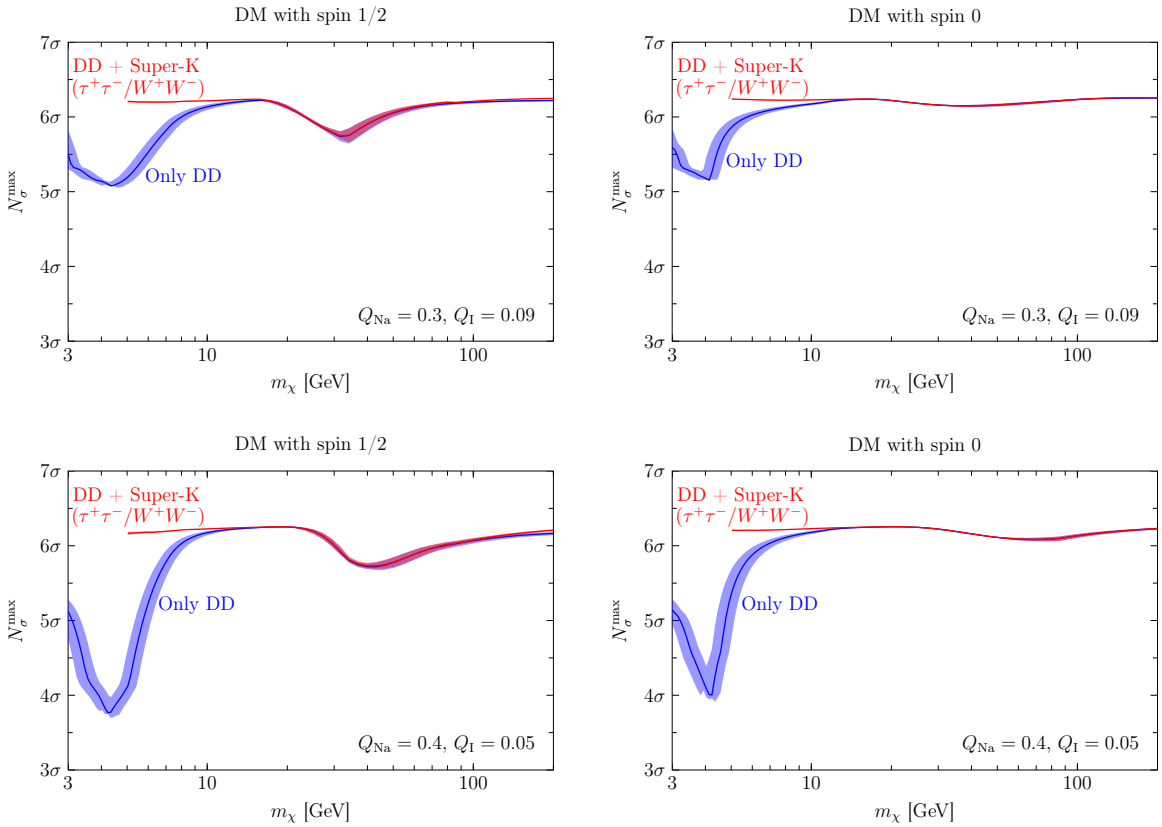

Figure 7.2.: Tension between DAMA and the null search experiments quantified by $N_\sigma^{\rm max}$, as a function of the dark matter mass m_χ, for dark matter with spin 1/2 (left panels) or spin 0 (right panels). In the upper and lower row, we assume different values for the quenching factors, as specified in each panel. The blue curves correspond to the upper limits derived solely from direct detection experiments, while the red curves additionally employ the Super-Kamiokande results, assuming annihilation into $\tau^+\tau^-/W^+W^-$. For each curve, the shaded band brackets the uncertainty on $N_\sigma^{\rm max}$ arising from varying the parameters v_0 and $v_{\rm esc}$ of the Maxwell-Boltzmann velocity distribution.

(upper panels), and $N_\sigma^{\rm max} \gtrsim 3.7\sigma$ for $Q_{\rm Na} = 0.4$ and $Q_{\rm I} = 0.05$ (lower panels). Also when increasing the confidence level of the null search experiments from 95% to 99.9%, the tension remains highly significant: $N_\sigma^{\rm max} \gtrsim 4.6\sigma$ (3.2σ) for $Q_{\rm Na} = 0.3$ and $Q_{\rm I} = 0.09$ ($Q_{\rm Na} = 0.4$ and $Q_{\rm I} = 0.05$). As expected, adding the results from Super-Kamiokande $(\tau^+\tau^-/W^+W^-)$ to our analysis leads to even more stringent results for $m_\chi \gtrsim 5\,\text{GeV}$, as it follows from the various panels of Fig. 7.2. We do not show the results for the set of experiments $\mathcal{E}'$ for $m_\chi \lesssim 5\,\text{GeV}$, as in this regime evaporation effects in the Sun start to become important.

By comparing the upper and lower panels of Fig. 7.2, it becomes clear that $N_\sigma^{\rm max}$ depends quite sensitively on the choice of the quenching factors, in particular on $Q_{\rm Na}$. A larger value of this quantity in general reduces the tension between DAMA and the null searches, as then already a smaller nuclear recoil energy is sufficient to produce a signal with a given quenched energy. Recent studies employing low-energy pulsed neutrons favor values of $Q_{\rm Na} \lesssim 0.2$ in the range from 3 to 52 keV [390], and hence strongly disfavor values of $Q_{\rm Na}$

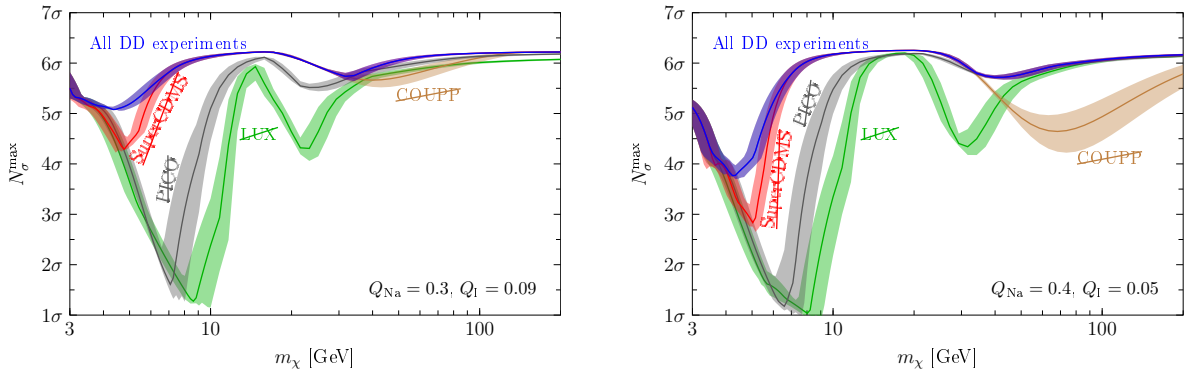

Figure 7.3.: The blue curve is the same as in Fig. 7.2 (spin 1/2 dark matter, direct detection experiments only), while the other lines show in addition the results derived when excluding LUX (green curve), Super-CDMS (red curve), PICO (gray curve) or COUPP (brown curve) from the set of experiments considered in the analysis.

larger than 0.4, assuming of course that the sodium quenching factor is universal across different experiments. Consequently, our results in the lower panel of Fig. 7.2 are very conservative with respect to this source of nuclear uncertainty.

Lastly, we investigate the importance of some of the individual direct detection experiments listed in Table 7.2 for our conclusions. To this end, we have repeated the calculation of $N_\sigma^{\rm max}$ as described above, but this time excluding one particular direct detection experiment from the set $\mathcal{E}$. The result is presented in Fig. 7.3, for the cases of taking out the LUX, Super-CDMS, PICO or COUPP experiment from the analysis. For comparison, we also show again the values of $N_\sigma^{\rm max}$ derived from the full set $\mathcal{E}$. It follows from this figure that in particular PICO and LUX are crucial for establishing the tension of DAMA with the null search experiments, and, to a lesser extent, also SuperCDMS and COUPP are relevant. This strong complementarity of different direct detection experiments can schematically be explained by Fig. 7.1: different target nuclei are (in)sensitive to different directions in the parameter space, corresponding to the orientation of the main axes of the various ellipsoids. This observation clearly asks for a continuation of the experimental program consisting in developing direct detection experiments with several different target nuclei.

We close this section by listing a few scenarios which are not covered by our analysis. First, for dark matter particles with spin 1 or larger, there exist (at least) two additional non-relativistic operators [379] beside the ones shown in Table 7.1. Secondly, we do not take into account scenarios in which the scattering of dark matter with nucleons proceeds via mediators with masses below the typical momentum transfer in direct detection experiments (or in the capture process in the Sun). Next, our analysis does not apply to models in which the truncation in the effective theory expansion at quadratic order in $\hat{\mathbf{q}}$ and at linear order in $\hat{\mathbf{v}}^\perp$ is not appropriate, although we are not aware of any specific scenario where this point is actually relevant. Moreover, dark matter could scatter inelastically with nuclei [391], interact with nucleons via two-body interactions [392], or scatter off electrons or atoms [324], not captured by our approach. Lastly, our results could be modified for dark matter velocity distributions strongly deviating from the Maxwell-Boltzmann one, c.f. also the discussion in

Sec. 1.2. Several of these points could actually be incorporated in the framework developed in this section, and are certainly worth further investigations. From the experimental side, the final word on the dark matter interpretation of the DAMA modulation signal is expected to come from future results of NaI-based detectors such as DM-Ice [116] or ANAIS [393].

8. A novel approach to derive halo-independent limits on dark matter properties

In the previous parts of this work, we have studied in various ways the upper limits on the dark matter scattering cross section with nuclei, which arise from null observations of direct detection experiments as well as from neutrino telescopes searching for a high-energy neutrino flux from the direction of the Sun. In the former case, the observable which is directly accessible to experiments is the recoil rate, while the latter is sensitive to the capture rate of dark matter, assuming equilibrium between capture and annihilation in the Sun (c.f. the general introduction in Sec. 2). In Sec. 3, 4, 5, 6 and 7, we then employed these observations in order to constrain relevant particle physics properties of the dark matter, by translating the upper limits on the observable rates into upper limits on the scattering cross section of dark matter with nucleons, considering various different types of interactions between dark matter and the Standard Model particles.

However, in this procedure we have always assumed so far that the velocity distribution of dark matter is in the form of a Maxwell-Boltzmann distribution, given by Eq. (2.7). As argued in Sec. 1.2, even though this is a well-motivated assumption, it is perfectly possible that the true velocity distribution deviates substantially from this simple expectation. In particular, the dark matter halo of our Galaxy might contain tidal streams or a dark disk component [394–397], which can have an substantial impact on the recoil and capture rates expected for a given particle physics model of dark matter.

In view of that situation, several *halo-independent methods* have been proposed [95–97, 398–409], which allow to analyze the data from direct detection experiments without specifying the velocity distribution. These approaches can be broadly divided into two categories. The first one is based on the observation that for scenarios in which the dark matter-nucleus scattering cross section is proportional to the inverse squared of the dark matter velocity, as it is the case for the spin-independent and spin-dependent interactions given in Eqs. (2.4) and (2.5), the recoil rate defined in Eq. (2.2) depends on the speed distribution in the rest frame of the Earth $f(v)$ as well as on the total dark matter-proton scattering cross section σ_p only via the function

$$\tilde{\eta}(v_{\min}) \equiv \frac{\rho_0 \sigma_p}{m_N} \int_{v_{\min}}^{\infty} \mathrm{d}v \, \frac{f(v)}{v} \,, \tag{8.1}$$

which is universally the same for all experiments. By comparing measurements and upper limits on $\tilde{\eta}(v_{\min})$ derived from different direct detection experiments, one can evaluate the compatibility of a positive claim of detection with other null results, without specifying the velocity distribution. The second category of existing halo-independent approaches focuses on the possibility of inferring fundamental particle physics properties of dark matter from positive signals in future direct detection experiments, by parametrizing either $f(v)$ or $\tilde{\eta}(v_{\min})$ in a sufficiently general way, and marginalizing or maximizing the likelihood

over the corresponding parameters. Along these lines, it already has been noticed [410,411] that neutrino telescopes can provide relevant information, due to the complementary dependence on the dark matter velocity distribution compared to direct detection experiments, as mentioned in Sec. 2.2.

In this section, we propose a novel halo-independent method based on combining null results from direct detection (DD) experiments and neutrino telescopes (NT). In contrast to the approaches introduced above, this method allows to use existing data for deriving an *upper limit* on the scattering cross section, which is independent of the velocity distribution. This upper limit can then be employed in order to robustly rule out particle physics models of dark matter, (virtually) free of astrophysical uncertainties. Furthermore, in the last part of this section we apply our method to derive a halo-independent *lower* limit on the scattering cross section, assuming a hypothetical signal in a future DD experiment.

8.1. Dark matter in the Solar System as a superposition of streams

For the following discussion, we assume that the dark matter halo is spatially homogeneous on the scale of the Solar System, and we denote its velocity distribution defined *in the rest frame of the Sun*[1] as $f(\vec{v})$. Our only assumption on this distribution is the existence of a maximal velocity $v_{\max}$, such that $f(\vec{v}) = 0$ for $v \equiv |\vec{v}| > v_{\max}$. Assuming that all dark matter particles in the halo are gravitationally bound to the Galaxy, $v_{\max}$ is given by the sum of the galactic escape velocity $v_{\rm esc} \simeq 533$ km/s [64] and the local velocity of the Sun with respect to the halo, $v_{\rm local} \simeq 244$ km/s [60–62], leading to $v_{\max} \simeq 777$ km/s. In Sec. 8.2, we will also comment on the implications of relaxing this assumption by considering larger values for $v_{\max}$. Furthermore, we normalize the unknown velocity distribution according to

$$\int_{v \leq v_{\max}} \mathrm{d}^3 v \, f(\vec{v}) = 1 \, . \tag{8.2}$$

Following Eq. (2.2) for the differential recoil rate at a direct detection experiment, as well as Eqs. (2.10)−(2.13) for the capture rate of dark matter in the Sun, the number of expected recoil events N at a DD experiment as well as the capture rate C are given by

$$N = \mathcal{E} \cdot \sum_T \int_0^\infty \mathrm{d}E_R \, \epsilon(E_R) \frac{\xi_T \rho_0}{m_T m_{\rm DM}} \int_{v \geq v_{\min}(E_R)} \mathrm{d}^3 v \, v f(\vec{v} + \vec{V}_\oplus(t)) \, \frac{\mathrm{d}\sigma_T}{\mathrm{d}E_R} \, , \tag{8.3}$$

$$C = \sum_T \int_0^R 4\pi r^2 \mathrm{d}r \, \eta_T(r) \frac{\rho_0}{m_{\rm DM}} \int_{v \leq u_{\max}(r)} \mathrm{d}^3 v \, \frac{f(\vec{v})}{v} \left(v^2 + [v_{\rm Sun,esc}(r)]^2 \right) \times \int_{m_{\rm DM} v^2/2}^{2\mu_T^2 \left(v^2 + \left[v_{\rm Sun,esc}(r) \right]^2 \right)/m_T} \mathrm{d}E_R \, \frac{\mathrm{d}\sigma_T}{\mathrm{d}E_R} \, . \tag{8.4}$$

In particular, the velocity distribution entering the number of recoil events is shifted with respect to the one relevant for the capture rate by $\vec{V}_\oplus(t)$, which is defined as the velocity of the Earth relative to the Sun (c.f. also Eq. (2.8)). Furthermore, ξ_T is the mass fraction of the nucleus T in the target material of the DD experiment, while $\epsilon(E_R)$ and $\mathcal{E}$ denote the detection efficiency and exposure, respectively, both depending on the experiment under

[1] In the notation of Sec. 2.1.1, our convention of defining $f(\vec{v})$ for the purpose of this section corresponds to $f(\vec{v}) \equiv f_{\rm 3D}^{\rm (Gal)}(\vec{v} + \vec{v}_{\rm LSR} + \vec{v}_{\odot,\rm pec})$.

consideration. In Appendix A, we specify these quantities for the experiments employed in this section. Lastly, in the following discussion we will assume that the scattering cross section $\mathrm{d}\sigma_T/\mathrm{d}E_R$ is either in the form of a spin-independent interaction with equal coupling to protons and neutrons, defined in Eq. (2.4), or in the form of a spin-dependent interaction with protons, given by Eq. (2.5).

Fixing furthermore the local dark matter density $\rho_0 \simeq 0.3\,\mathrm{GeV/cm^3}$, the only remaining ingredient for calculating the rates N and C in Eqs. (8.3) and (8.4) is the velocity distribution $f(\vec{v})$. Instead of assuming a fixed distribution such as the Maxwell-Boltzmann one, for the purpose of this section we decompose the dark matter population in the Solar System as

$$f(\vec{v}) = \int_{|\vec{v}_0|\leq v_{\max}} \mathrm{d}^3 v_0\, \delta^{(3)}(\vec{v}-\vec{v}_0) f(\vec{v}_0)\ . \tag{8.5}$$

Physically, this corresponds to a superposition of hypothetical streams with fixed velocities $\vec{v}_0$ with respect to the rest frame of the Sun, $f_{\vec{v}_0}(\vec{v}) = \delta^{(3)}(\vec{v}-\vec{v}_0)$. Inserting this expansion of $f(\vec{v})$ in Eqs. (8.3) and (8.4), and using the linearity of the recoil and capture rate in the velocity distribution, one obtains

$$\begin{aligned} N &= \int_{|\vec{v}_0|\leq v_{\max}} \mathrm{d}^3 v_0\, f(\vec{v}_0)\, N_{\vec{v}_0}\ , \\ C &= \int_{|\vec{v}_0|\leq v_{\max}} \mathrm{d}^3 v_0\, f(\vec{v}_0)\, C_{\vec{v}_0}\ , \end{aligned} \tag{8.6}$$

where $N_{\vec{v}_0}$ ($C_{\vec{v}_0}$) is the number of scattering events (the capture rate) corresponding to the velocity distribution $f_{\vec{v}_0}(\vec{v}) = \delta^{(3)}(\vec{v}-\vec{v}_0)$.

The null result of a given DD experiment can be formulated as an upper limit $N_{\max}$ on the expected number of dark matter induced scattering events[2]. In particular, in a hypothetical situation in which all dark matter particles have the same velocity $\vec{v}_0$ with respect to the solar frame, corresponding to a velocity $\vec{v}_0 - \vec{V}_\oplus(t)$ in the rest frame of the detector, the upper limit on the scattering cross section follows from $N_{\vec{v}_0} \leq N_{\max}$. For illustration, we show in Fig. 8.1 the resulting 90% C.L. upper limits on the spin-independent (upper panels) and spin-dependent cross section (lower panels) deduced from the null results of XENON100 [104] and COUPP [120], as a function of the stream velocity $v_0 = |\vec{v}_0|$, assuming for concreteness $m_{\mathrm{DM}} = 100\,\mathrm{GeV}$. In these plots, the various dashed red lines correspond to different angles $\measuredangle(\vec{v}_0, \vec{V}_\oplus)$, while the red solid line is defined to be the weakest among all these limits for a given speed v_0, which in the following we will denote as $\sigma^{\mathrm{DD}}_{\max}(v_0)$, either for the spin-independent or the spin-dependent cross section. This represents a conservative limit for a fixed value of v_0, as by construction one has $N_{\vec{v}_0}(\sigma) \geq N_{\max}$ for $\sigma \geq \sigma^{\mathrm{DD}}_{\max}(v_0)$.

Furthermore, the non-observation of an excess of a neutrino flux from the direction of the Sun leads to an upper limit on the annihilation rate Γ_A of dark matter (c.f. Sec. 2.2). Assuming equilibrium between captures and annihilations, this implies an upper limit $C_{\max}$ on the capture rate via Eq. (2.21), which depends on the dark matter mass and annihilation channel. For the scattering cross sections which are currently probed by neutrino telescopes, equilibration is achieved if the annihilation cross section in the Sun satisfies $(\sigma v)_{\mathrm{ann}} \gtrsim 10^{-28}\,\mathrm{cm^3/s}$, and hence in the following we will assume that this is the case[3]. Then, for

[2] We refer to Appendix A for details on the calculation of $N_{\max}$ for the different experiments considered in this section.

[3] Capture and annihilation in the Sun are in equilibrium if $\alpha_{\mathrm{eq}} \equiv \tanh^2\left(t_\odot \sqrt{C\cdot\Gamma_A}\right)$ is close to one, with $t_\odot$ and $\Gamma_A \propto (\sigma v)_{\mathrm{ann}}$ defined in Sec. 2.2. It is straightforward to check that for $(\sigma v)_{\mathrm{ann}} \gtrsim 10^{-28}\ \mathrm{cm^3/s}$ and for the capture rates C that are currently probed by IceCube or Super-Kamiokande, one has $\alpha_{\mathrm{eq}} \gtrsim 0.99$.

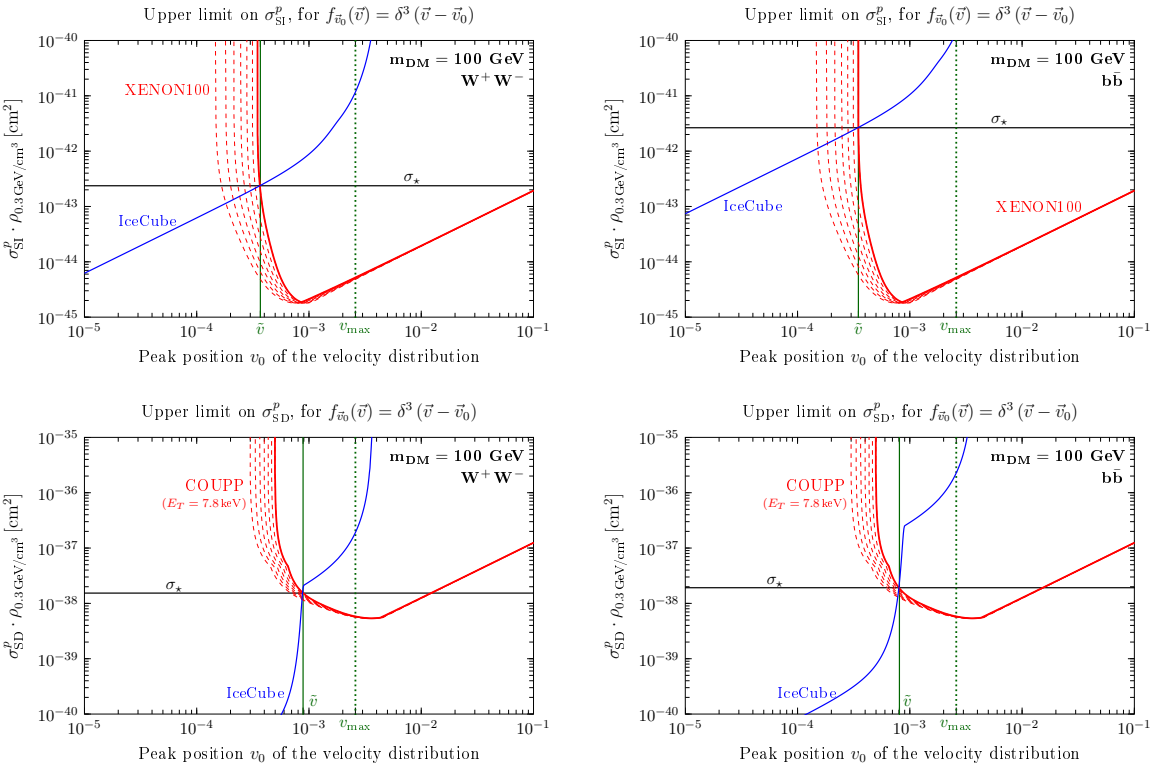

Figure 8.1.: Upper limits on the scattering cross section of dark matter with protons for $m_{\rm DM} = 100$ GeV, normalized to $\rho_0 = 0.3\,\rm GeV/cm^3$, and assuming velocity distributions of the form $f_{\vec{v}_0}(\vec{v}) = \delta^{(3)}(\vec{v} - \vec{v}_0)$. The upper (lower) panels correspond to spin-independent (spin-dependent) scattering, and the left (right) panels to annihilations into W^+W^- ($b\bar{b}$). Each dashed red line corresponds to a different angle between the stream velocity $\vec{v}_0$ and the Earth velocity $\vec{V}_\oplus$. In each panel, the minimal value of the cross section which is excluded for *all* values of v_0 by either the direct detection experiment or the neutrino telescope is denoted by $\sigma_\star$.

a velocity distribution given by a pure stream with velocity $\vec{v}_0$, the upper limit on the scattering cross section following from the corresponding NT can be calculated from the requirement that $C_{\vec{v}_0} \leq C_{\max}$. We show the 90% C.L. upper limit on σ following from the IceCube data [168] as a blue solid line in Fig. 8.1 for the case of spin-independent (upper panels) and spin-dependent interactions (lower panels), employing for concreteness $m_{\rm DM} = 100\,\text{GeV}$ as well as the annihilation final states W^+W^- (left panels) and $b\bar{b}$ (right panels)[4]. For each dark matter mass, interaction scenario and annihilation channel, this upper limit as a function of the stream speed v_0 is denoted as $\sigma^{\rm NT}_{\max}(v_0)$. By definition, one then has $C_{\vec{v}_0}(\sigma) \geq C_{\max}$ for $\sigma \geq \sigma^{\rm NT}_{\max}(v_0)$.

We now show that the information contained in the functions $\sigma^{\rm DD}_{\max}(v_0)$ and $\sigma^{\rm NT}_{\max}(v_0)$ is sufficient to calculate a conservative upper limit on the scattering cross section for a general velocity distribution $f(\vec{v})$, both for DD and NT experiments. First, by noting that the differential scattering cross section given by Eq. (2.4) or Eq. (2.5) is linear in $\sigma^p_{\rm SI}$ or $\sigma^p_{\rm SD}$, respectively, the number of expected scattering events in a DD experiment satisfies

$$N_{\vec{v}_0}(\sigma) = \frac{\sigma}{\sigma^{\rm DD}_{\max}(v_0)} N_{\vec{v}_0}[\sigma^{\rm DD}_{\max}(v_0)] \geq \frac{\sigma}{\sigma^{\rm DD}_{\max}(v_0)} N_{\max}\,, \tag{8.7}$$

where σ denotes either $\sigma^p_{\rm SI}$ or $\sigma^p_{\rm SD}$, and where we have used the defining property of the conservative upper limit $\sigma^{\rm DD}_{\max}(v_0)$, as introduced earlier on in this section. Inserting this inequality in Eq. (8.6), one obtains

$$N(\sigma) \geq \int_{|\vec{v}_0| \leq v_{\max}} \mathrm{d}^3 v_0 f(\vec{v}_0) \frac{\sigma}{\sigma^{\rm DD}_{\max}(v_0)} N_{\max}\,. \tag{8.8}$$

Finally, requiring that the expected number of scattering events $N(\sigma)$ satisfies the experimental upper limit, i.e. $N(\sigma) \leq N_{\max}$, the upper limit on the cross section following from the DD experiment can be written in the compact form

$$\sigma \leq \left[\int_{|\vec{v}_0| \leq v_{\max}} \mathrm{d}^3 v_0 \frac{f(\vec{v}_0)}{\sigma^{\rm DD}_{\max}(v_0)} \right]^{-1}\,. \tag{8.9}$$

Following similar steps, for a given dark matter mass and annihilation channel, the upper limit on the scattering cross section following from the null result of a NT is given by

$$\sigma \leq \left[\int_{|\vec{v}_0| \leq v_{\max}} \mathrm{d}^3 v_0 \frac{f(\vec{v}_0)}{\sigma^{\rm NT}_{\max}(v_0)} \right]^{-1}\,. \tag{8.10}$$

In particular, once the functions $\sigma^{\rm DD}_{\max}(v_0)$ and $\sigma^{\rm NT}_{\max}(v_0)$ have been calculated, this formalism allows for a fast evaluation of the upper limits on the scattering cross section for a fixed, but arbitrary velocity distribution $f(\vec{v})$.

8.2. A halo-independent upper limit on the scattering cross section

As mentioned initially in Sec. 2.2, direct detection experiments and neutrino telescopes are sensitive to different parts of the dark matter velocity space. Quantitatively, this can be

[4]The kink in the upper limit following from the IceCube data in the case of spin-dependent interactions is due to the fact that for low velocities the capture process is dominated by scatterings off H, while for larger velocities scattering off ^{14}N becomes important.

directly inferred from Fig. 8.1, which shows the upper limits on the scattering cross section as a function of the stream velocity v_0: direct detection experiments are insensitive to WIMPs with very small velocities, corresponding to the upturn of the red curves at small v_0, as in this case the recoil of the nucleus is below the threshold of the corresponding experiment. However, in this region of the velocity space, the upper limits from neutrino telescopes are strongest, which can be traced back to the fact that slow-moving WIMPs are captured more efficiently in the Sun. On the other hand, it follows from the figure that direct detection experiments retain sensitivity for large v_0, while the capture process gets more and more inefficient in this part of the velocity space.

In particular, at least for the dark matter mass used in Fig. 8.1, this complementarity of direct detection experiments and neutrino telescopes leads to a finite upper limit on the scattering cross section which is valid for *every* stream speed v_0. In other words, the combination of both types of experiments allows for probing the complete range of dark matter velocities. Based on this observation, we will show in this section that it is possible to derive an upper limit on the scattering cross section which is independent of the velocity distribution, by using the formalism of decomposing the velocity distribution in terms of infinitely many streams, as introduced in Sec. 8.1.

To this end, we first define

$$\sigma_* \equiv \max\left\{\sigma_{\rm max}^{\rm DD}(\tilde{v}), \sigma_{\rm max}^{\rm DD}(v_{\rm max})\right\} \ , \tag{8.11}$$

where $\tilde{v}$ is the speed for which $\sigma_{\rm max}^{\rm DD}(\tilde{v}) = \sigma_{\rm max}^{\rm NT}(\tilde{v})$. With this definition, for a given dark matter mass and annihilation channel, σ_* is the largest value of the scattering cross section which is allowed by both a concrete direct detection experiment *and* by a concrete neutrino telescope, assuming that the true velocity distribution of dark matter is in the form of a pure stream with speed between 0 and $v_{\rm max}$. The construction of $\tilde{v}$ and σ_* is illustrated in Fig. 8.1 for a dark matter mass $m_{\rm DM} = 100$ GeV, assuming annihilations into W^+W^- (left panels) and $b\bar{b}$ (right panels), employing XENON100 and IceCube in the case of spin-independent interactions (upper panels), and COUPP as well as IceCube for spin-dependent interactions (lower panels). By construction, the functions $\sigma_{\rm max}(v_0)$ are then bounded from above by

$$\sigma_{\rm max}^{\rm DD}(v_0) \leq \sigma_* \quad \text{for } \tilde{v} \leq v_0 \leq v_{\rm max} \ , \tag{8.12}$$

$$\sigma_{\rm max}^{\rm NT}(v_0) \leq \sigma_* \quad \text{for } 0 \leq v_0 \leq \tilde{v} \ . \tag{8.13}$$

We now combine the upper limits arising from a given direct detection experiment and a neutrino telescope. To this end, we first note that Eq. (8.9) implies

$$\begin{aligned} \sigma &\leq \left[\int_{0\leq v_0\leq v_{\rm max}} {\rm d}^3 v_0 \frac{f(\vec{v}_0)}{\sigma_{\rm max}^{\rm DD}(v_0)}\right]^{-1} \\ &\leq \left[\int_{\tilde{v}\leq v_0\leq v_{\rm max}} {\rm d}^3 v_0 \frac{f(\vec{v}_0)}{\sigma_{\rm max}^{\rm DD}(v_0)}\right]^{-1} \ . \end{aligned} \tag{8.14}$$

Inserting Eq. (8.12), and defining

$$\delta_f \equiv \int_{\tilde{v}\leq v_0\leq v_{\rm max}} {\rm d}^3 v_0 \, f(\vec{v}_0) \ , \tag{8.15}$$

one obtains

$$\sigma \leq \frac{\sigma_*}{\delta_f} \ . \tag{8.16}$$

A similar rationale can be applied to the upper limit on the cross section following from a neutrino telescope, given by Eq. (8.10). Using in this case Eq. (8.13), we arrive at

$$\sigma \leq \frac{\sigma_*}{1-\delta_f} \,, \tag{8.17}$$

with the factor $1-\delta_f$ following from the definition of δ_f in Eq. (8.15) and the normalization of the velocity distribution, Eq. (8.2).

Finally, by combining the upper limit from the direct detection experiment, Eq. (8.16), with the upper limit from the neutrino telescope given by Eq. (8.17), we obtain

$$\sigma \leq 2\sigma_* \,, \tag{8.18}$$

independently of the value of δ_f, and hence independently of the velocity distribution $f(\vec{v})$. This equation is the main result of this section: for a fixed dark matter mass and annihilation channel, the combination of a direct detection experiment and a neutrino telescope leads to the upper limit $2\sigma_*$ on the scattering cross section, which is valid for all possible velocity distributions $f(\vec{v})$. Here, σ_* is defined via Eq. (8.11), which is based on considering upper limits for stream-like velocity distributions. We also notice that the upper limit given by Eq. (8.18) can only be saturated for velocity distributions satisfying $\delta_f = 1/2$.

The resulting halo-independent upper limits are shown in Fig. 8.2 as a function of the dark matter mass, with the upper panels (lower panels) corresponding to spin-independent (spin-dependent) interactions. Furthermore, the left panels assume that dark matter annihilates into $W^+W^-/\tau^+\tau^-$, while the right panels correspond to annihilation into $b\bar{b}$. For obtaining these results, we apply the method described above for each dark matter mass and for each combination of one direct detection experiment with one neutrino telescope. For the former, we consider XENON100 [104] and SuperCDMS [109] for spin-independent scattering, as well as COUPP [120] and SIMPLE [122] for the spin-dependent case, while for the latter we use the results from IceCube [168] and Super-Kamiokande [170]. Finally, for a fixed dark matter mass, we take the smallest value of $2\sigma_\star$ arising from each possible combination of experiments as our final halo-independent upper limit. Furthermore, let us remark that, while being independent of the velocity distribution, these upper limits still depend on the value of the local dark matter density ρ_0. The results in Fig. 8.2 correspond to $\rho_0 = 0.3\,\mathrm{GeV/cm^3}$, and can be rescaled linearly for any other choice of ρ_0.

For comparison, we also show in Fig. 8.2 the upper limits on the scattering cross section assuming the Standard Halo Model (SHM), i.e. employing a Maxwell-Boltzmann distribution with a velocity dispersion $\sigma = 282$ km/s and galactic escape velocity $v_{\rm esc} = 533$ km/s. The upper limits from Super-CDMS and XENON100 for that specific choice of the velocity distribution are shown as solid black lines in the upper panels (corresponding to spin-independent scattering), while in the lower panels (corresponding to spin-dependent scattering) they are presented for SIMPLE and COUPP. Furthermore, the black dashed lines show the corresponding upper limits from IceCube and Super-Kamiokande. By construction, for a fixed dark matter mass the halo-independent limit is always weaker than the SHM upper limit derived from one of the direct detection experiments or neutrino telescopes. Nevertheless, for some scenarios our limits are remarkably strong, reaching $\sigma^p_{\rm SI} \lesssim 10^{-43}\,(10^{-42})$ cm^2 and $\sigma^p_{\rm SD} \lesssim 10^{-37}\,(3\times10^{-37})$ cm^2, for annihilations into W^+W^- ($b\bar{b}$) at $m_{\rm DM} = 1\,\mathrm{TeV}$, assuming $\rho_0 = 0.3\,\mathrm{GeV/cm^3}$. Moreover, for the case of spin-independent scattering the halo-independent limits are stronger than those obtained by IceCube or Super-Kamiokande for the SHM, while they are only a factor of a few worse than the SHM limits from SIMPLE or COUPP for the spin-dependent scenario.

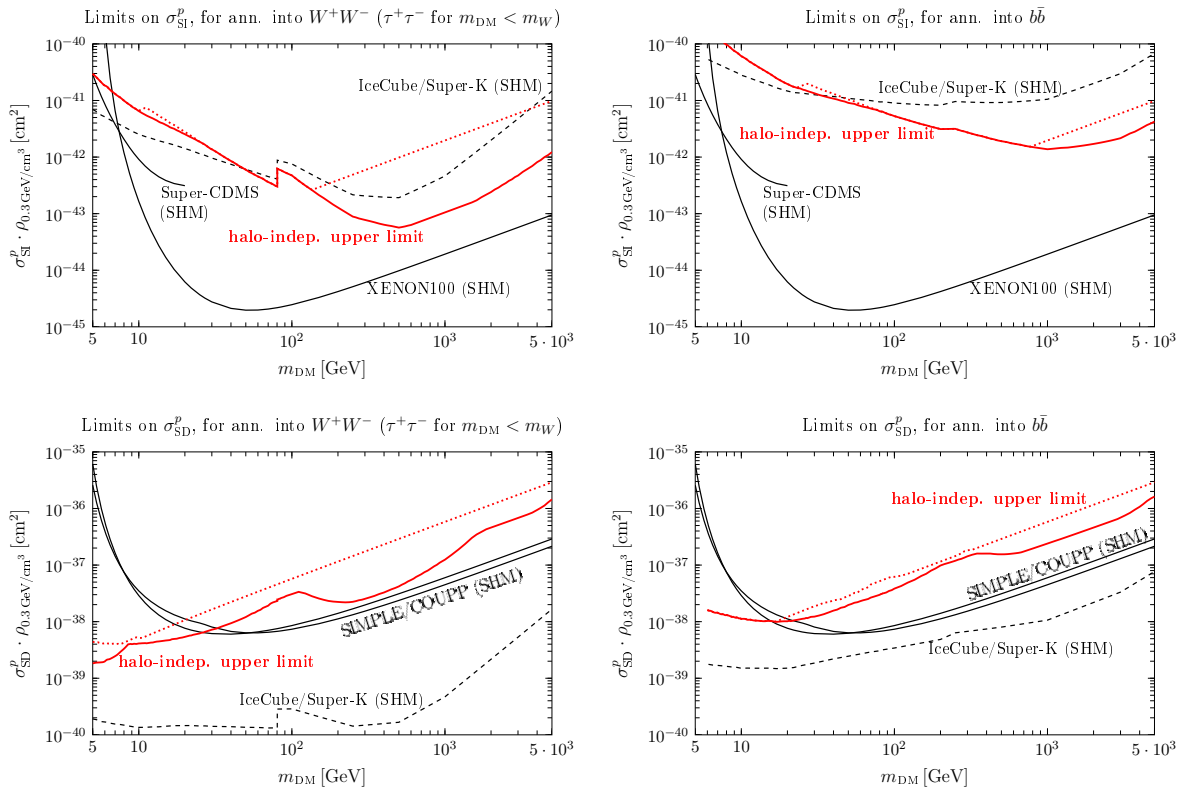

Figure 8.2.: Halo-independent upper limits on $\sigma^p_{\rm SI}$ (upper panels) and $\sigma^p_{\rm SD}$ (lower panels), normalized to $\rho_0 = 0.3\,\text{GeV/cm}^3$. The left panels correspond to dark matter annihilating into $W^+W^-/\tau^+\tau^-$, while the right panels show the results for the annihilation channel $b\bar{b}$. Our main result is the red solid line, corresponding to $v_{\rm max} = 777\,\text{km/s}$, while the red dotted curves assume $v_{\rm max} = 0.05c$. For comparison, the black solid and dashed curves show the upper limits derived under the assumption of the Standard Halo Model (SHM), as defined in the text.

It is important to stress that the limits derived in this section rely only on rather weak assumptions, in contrast to the limits corresponding to a Maxwell-Boltzmann distribution. One implicit assumption behind the formalism developed in this section is that the local dark matter density and velocity distribution have been constant over the equilibration time of captures and annihilations, which typically is of the order of 10-100 million years, corresponding to $0.2 - 2\%$ of the age of the Sun. Furthermore, the red solid curves in Fig. 8.2 are derived under the assumption that the velocity distribution $f(\vec{v})$ is zero for $v > v_{\rm max} = 777$ km/s, which is automatically fulfilled if all dark matter particles of the halo are gravitationally bound to the Galaxy (c.f. the discussion in Sec. 1.2). We have checked that even if the value of $v_{\rm max}$ is doubled, our limits only change for a small range of dark matter masses, since for reasonable values of $v_{\rm max}$ the largest value of the scattering cross section $\sigma_\star$ is typically attained at the velocity $\tilde{v}$, as can be seen from Fig. 8.1. In order to test the ultimate impact of the assumption regarding the maximal velocity of dark matter particles, we have calculated the limits for the extreme case of $v_{\rm max} = 0.05c$, which roughly corresponds to the largest value of velocities for which the non-relativistic description of dark matter-nucleus scattering is valid. These limits are shown in Fig. 8.2 as red dotted lines and

are at most one order of magnitude less stringent than our standard results assuming the much more realistic value $v_{\max} = 777$ km/s.

We conclude this section by commenting on the expected improvement of the halo-independent upper limits with upcoming data from direct detection experiments and neutrino telescopes. For the case of spin-independent interactions, it follows from Fig. 8.1 that a substantial improvement of the limits could be obtained by lowering the threshold of the direct detection experiments, corresponding to a shift of the location of the upturn of the red curves to smaller values of v_0. This development could be achievable with e.g. the SuperCDMS-Snolab experiment [133], which plans to have a threshold well below 1 keV. Also, the halo-independent upper limit on the spin-independent cross section could be significantly improved by increasing the exposure of the neutrino telescopes, using e.g. several years of data with the full 86-string configuration of IceCube [412]. On the other hand, for spin-dependent scattering, the lower panels of Fig. 8.1 imply that currently the exposures of the relevant direct detection experiments are the main limiting factors. Hence, future upgrades of the PICO experiment [413] featuring a much larger target mass would help in improving the halo-independent upper limits on $\sigma^p_{\rm SD}$.

8.3. Lower limit on the cross section from signal events

In the previous section, we have shown that the formalism of decomposing the velocity distribution in infinitely many streams via Eq. (8.5) can be used in order to set an halo-independent upper limit on the scattering cross section, using the complementary information from direct detection experiments and neutrino telescopes. In the following, we discuss the possibility of using the same formalism for determining the dark matter parameters in the case of a positive signal in a future xenon based direct detection experiment, again without specifying the velocity distribution $f(\vec{v})$. In contrast to the previous section, we focus on the implications of direct detection experiments alone, and do not consider the complementary information from neutrino telescopes.

For the future direct detection experiment, we employ a setup close to the expectations for XENON1T [129], assuming a detector with an exposure of 1 ton $\cdot$ yr, which is sensitive with 100% detection efficiency to recoil energies between 3 and 45 keV, with an energy resolution $\sigma(E_R) = 0.6\,\text{keV}\sqrt{E_R/\text{keV}}$ [414]. We furthermore consider a benchmark scenario where the true dark matter parameters are given by $m_{\rm DM}^{(\rm true)} = 100\,\text{GeV}$ and $\sigma_{\rm SI}^{p(\rm true)} = 10^{-46}\,\text{cm}^2$, and where the actual velocity distribution is given by the SHM. This scenario is compatible with all existing constraints, and in particular lies approximately one order of magnitude below the current LUX limit. In the future XENON1T-like experiment, this would lead to $\simeq 19$ events (neglecting Poisson fluctuations in the actually observed number of events), resulting in a 90% C.L. lower limit on the number of recoil events $N_{\min} = 14.0$.

Based on this lower limit, we now show that it is possible to derive a halo-independent *lower* limit on the scattering cross section, using the formalism developed earlier in this section. To this end, similar as in Sec. 8.1, we start by considering a hypothetical situation in which all dark matter particles have a velocity $\vec{v}_0$ in the rest frame of the Sun. Then, for a given dark matter mass $m_{\rm DM}$, a lower limit on the spin-independent scattering cross section follows from requiring $N_{\vec{v}_0} \geq N_{\min}$, and, for fixed v_0, we define $\sigma^{\rm DD}_{\min}(v_0)$ to be the minimum of all lower limits corresponding to different angles between the stream velocity $\vec{v}_0$ and the velocity of the Earth $\vec{V}_\oplus$. Then, by definition, one has $N_{\vec{v}_0}(\sigma) \leq N_{\min}$ for $\sigma \leq \sigma^{\rm DD}_{\min}(v_0)$. This construction is illustrated in Fig. 8.3, using for concreteness $m_{\rm DM} = 300\,\text{GeV}$. Similar as in

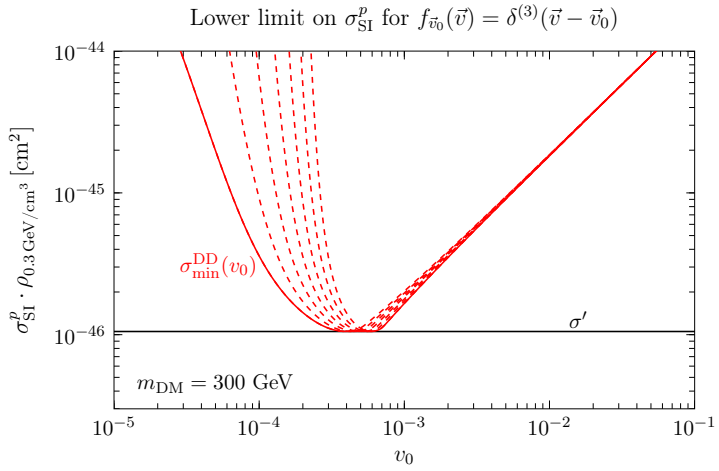

Figure 8.3.: Lower limit on the spin-independent scattering cross section of dark matter with protons, normalized to $\rho_0 = 0.3\,\mathrm{GeV/cm^3}$, based on the hypothetical detection of 19 recoil events in a XENON1T-like future experiment, for $m_{\rm DM} = 300\,\mathrm{GeV}$, and assuming velocity distributions of the form $f_{\vec{v}_0}(\vec{v}) = \delta^{(3)}(\vec{v} - \vec{v}_0)$. The black solid line shows σ', which is defined to be the minimum of the function $\sigma^{\rm DD}_{\rm min}(v_0)$.

Fig. 8.1, the various dashed red lines correspond to different angles $\measuredangle(\vec{v}_0, \vec{V}_\oplus)$, while the red solid line shows $\sigma^{\rm DD}_{\rm min}(v_0)$. Completely analogously to the rationale behind Eqs. (8.7), (8.8) and (8.9), we then deduce a lower limit on the scattering cross section for a given velocity distribution $f(\vec{v})$ (still for a fixed dark matter mass $m_{\rm DM}$):

$$\sigma \geq \left[\int_{|\vec{v}_0| \leq v_{\rm max}} \mathrm{d}^3 v_0 \frac{f(\vec{v}_0)}{\sigma^{\rm DD}_{\rm min}(v_0)} \right]^{-1} . \tag{8.19}$$

For each value of $m_{\rm DM}$, the function $\sigma^{\rm DD}_{\rm min}(v_0)$ has a minimum, which we denote as σ', and which is shown in Fig. 8.3 for $m_{\rm DM} = 300\,\mathrm{GeV}$. Physically, the value of v_0 at which the minimum of $\sigma^{\rm DD}_{\rm min}(v_0)$ is attained corresponds to the velocity of dark matter particles to which the direct detection experiment is most sensitive. Finally, from Eqs. (8.2) and (8.19) we obtain a halo-independent lower limit on the scattering cross section, i.e. a lower limit which is independent of the choice of $f(\vec{v})$:

$$\sigma \geq \sigma' . \tag{8.20}$$

We then repeat this construction of σ' for all possible values of $m_{\rm DM}$, and show in Fig. 8.4 as a red solid line the resulting halo-independent lower limit on the spin-independent scattering cross section with protons as a function of the dark matter mass. Furthermore, in this plot the black dot represents the true dark matter parameters, while the gray shaded band is the reconstructed 90% C.L. region assuming the SHM. Moreover, for comparison the blue dotted curve shows a halo-independent lower limit on $\sigma^p_{\rm SI}$ based on the general inequality

$$\int_{v > v_{\rm min}} \mathrm{d}^3 v \, \frac{f(\vec{v})}{v} \leq \frac{1}{v_{\rm min}} , \tag{8.21}$$

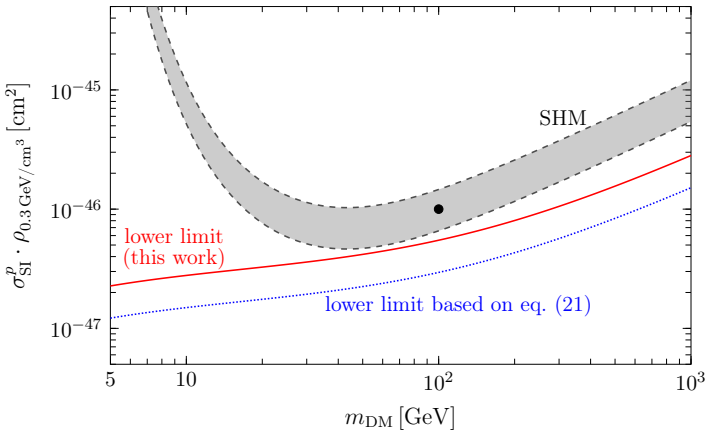

Figure 8.4.: Halo-independent lower limit on $\sigma^p_{\rm SI} \cdot \rho_{0.3\,{\rm GeV/cm^3}}$, following from the hypothetical observation of 19 recoil events in a XENON1T-like experiment (red line), and using the novel approach derived in this section. Moreover, the gray band shows the reconstructed 90% C.L. region assuming the SHM, while the blue dotted line corresponds to the halo-independent lower limit derived from Eq. (8.21). Furthermore, the black dot represents the true dark matter mass and scattering cross section.

as recently proposed in [415]. Remarkably, the lower limit on the scattering cross section obtained using the approach introduced in this section is only a factor of $\simeq 2$ below the true value of the cross section. We have checked that this conclusion is robust against a change of the true dark matter mass as long as $m^{\rm (true)}_{\rm DM} \gtrsim 30\,{\rm GeV}$, and also does not change significantly with the number of observed events, as long as it is larger than $\simeq 5$.

Finally, we note that our method is based solely on the total number of observed events, while in a realistic situation of a positive detection also some information about the distribution of recoil energies will be available. Hence, the approach discussed in this section is particularly well-suited in an early stage of dark matter discovery, when only a few events are detected, not allowing for a precise reconstruction of the recoil spectrum. Eventually, with the presence of more data a determination of the latter will be possible, which allows for breaking the degeneracy between the dark matter mass and scattering cross section by means of other halo-independent methods [403, 406].

Part IV

CONCLUSIONS

Conclusions

More than 100 years have passed since the initial suggestions for the presence of dark matter in our Universe. While its existence is nowadays a widely accepted fact, the lack of an unambiguous positive signal in an experiment searching for a non-gravitational interaction of dark matter leaves the determination of its particle physics properties to be a still open task. In this thesis, we have approached this puzzle by employing data from direct detection, indirect detection and collider experiments in order to constrain the properties of the dark matter particle. Specifically, we have focused on the phenomenology of WIMPs, which in principle are expected to produce a signal in all of these three search strategies. Hence, throughout this thesis we have put a strong emphasis on the complementarity of the various detection methods for WIMPs, and we have shown that depending on the details of the particle- and astrophysics of dark matter, different search strategies can provide the most stringent constraint on the properties of the dark matter particle.

After giving a general introduction to dark matter and in particular to searches for WIMPs in part I, we have studied in part II the phenomenology of t-channel simplified models, in which the dark matter particle is a singlet under the Standard Model gauge group and couples via a Yukawa interaction to a Standard Model fermion f and a charged heavy mediator. The various scenarios within this class of models differ by the spin assignment of the dark matter and mediator particle: in Sec. 3 we considered Dirac dark matter coupling to a scalar mediator, while in Sec. 4 we studied a scenario in which the dark matter particle is a real scalar interacting with a vector-like fermionic mediator. Lastly, in Sec. 5 we investigated the case of Majorana dark matter coupling to a Standard Model fermion via a scalar mediator.

While similar in their basic structure, we have shown that the phenomenologies of these scenarios differ significantly from case to case. This is largely due to the fact that for real scalar and Majorana dark matter the lowest-order $2 \to 2$ annihilation process $\mathrm{DM}\,\mathrm{DM} \to f\bar{f}$ is helicity- and velocity-suppressed: the s-wave component of the annihilation cross section vanishes in the limit $m_f \to 0$; in the case of real scalar dark matter also the p-wave contribution is zero for massless fermions f. This suppression naturally asks for the inclusion of higher-order annihilation processes, which we have shown to be highly relevant both during the freeze-out of dark matter, as well as for the indirect detection phenomenology of the corresponding scenario. In particular, we have demonstrated in Sec. 4.3 that in the model of real scalar dark matter coupling to a Standard Model lepton one expects strong gamma-ray spectral features arising from the virtual internal bremsstrahlung of a photon or from the one-loop annihilation into photons, and confronted these predictions to experimental data. Moreover, in Sec. 4.4 we have shown that for real scalar dark matter coupling to a Standard Model quark, there are strong constraints arising both from direct detection experiments as well as from searches for the production of the colored mediator at the LHC. Also these results are directly related to the higher-order annihilation channels, as in this scenario the $2 \to 3$ and one-loop processes dominate the total annihilation cross section of dark matter during freeze-out, and thus set the value of the Yukawa coupling entering the rates in direct detection and collider experiments. Lastly, in Sec. 5 we have investigated the impact of the higher-order processes on the physics of dark matter annihilation in the Sun in the context

of a simplified model of Majorana dark matter, and we have shown that the inclusion of the $2 \to 3$ channels greatly improves the prospects to observe a high-energy neutrino flux from the direction of the Sun in such a scenario.

On the other hand, in Sec. 3 we have seen that the annihilation of the Dirac dark matter candidate into a fermion-antifermion pair proceeds without any suppression, rendering the higher-order annihilation processes irrelevant for the computation of the total annihilation cross section today or during freeze-out. In that scenario, we then focused on the constraints on the parameter space of the model arising from direct searches. In contrast to real scalar or Majorana dark matter, Dirac dark matter allows for a vector interaction with quarks which leads to a significantly enhanced scattering rate. We have shown that both in the case of coupling to a quark as well as for coupling to a lepton, the results from the LUX experiment strongly constrain this simplified model; this is quite remarkable in particular for the latter case, as in that scenario all scattering processes are induced only at the one-loop level. Furthermore, our results imply that future direct detection experiments such as XENON1T or DARWIN have excellent prospects to probe all of the remaining parameter space of the model compatible with the observed relic abundance of dark matter.

In part III of this thesis, we then left the path of simplified models, and discussed various model-independent methods of analyzing data from direct and indirect detection experiments. Concretely, in Sec. 6 we investigated generic higher-order corrections to the annihilation process of dark matter in the Sun, in scenarios in which the annihilation proceeds dominantly via the coupling to a light Standard Model fermion. We have demonstrated that these corrections can be crucial in the calculation of the high-energy neutrino flux which is potentially detectable by neutrino telescopes such as IceCube, and we were able to derive for the first time upper limits on the scattering cross section of dark matter with nucleons for the case of annihilation into e^+e^-, $u\bar{u}$ or $d\bar{d}$. Subsequently, in Sec. 7 we turned to an investigation of the DAMA modulation signal, which in principle can be interpreted as being induced by scattering events of dark matter with the target nuclei. However, it is well known that this signal is subject to severe constraints from other direct detection experiments which observe a rate consistent with the corresponding background expectations. We quantified this tension in the framework of the non-relativistic effective theory for dark matter-nucleon interactions, fully taking into account all relevant scattering operators including their possible interferences. By developing a novel semi-analytical method for comparing experimental results in the high-dimensional parameter space of the effective theory, we were able to show that even with this large freedom regarding the possible particle physics properties of dark matter, a significant tension between DAMA and the null searches is inevitable. Lastly, in Sec. 8 we performed an analysis of data from direct detection experiments and neutrino telescopes which is model-independent from the point of view of astrophysics, i.e. it does not depend on a specific choice of the galactic velocity distribution of dark matter. In that section we derived for the first time a halo-independent upper limit on the scattering cross section of dark matter with nucleons from direct detection and neutrino telescope data, which hence constitutes a bound that is fully robust with respect to the astrophysical uncertainty arising from the unknown velocity distribution of dark matter in the Milky Way. We also demonstrated that our method allows for the construction of a halo-independent lower limit on the dark matter scattering cross section in case of a positive detection in a future direct detection experiment.

All in all, it is fair to say that in view of the currently operating as well as the near-future experiments, the WIMP paradigm is under siege. In several well-motivated scenarios of WIMP dark matter, a significant part of the parameter space has already been excluded, but there is still a variety of interesting models which are consistent with all current constraints. In the next decade, we expect more sensitive data for all search strategies of dark matter: ton-scale direct detection experiments such as XENON1T, LZ or DARWIN will further push the sensitivity to the scattering cross section of dark matter with nucleons, and indirect detection experiments such as CTA or AMS-02 will probe smaller and smaller values of the annihilation cross section of dark matter. Last but not least, there is the hope that a signal associated to dark matter emerges from run two of the LHC. In view of this tremendous experimental progress expected in the future, it is more important than ever to further develop strategies of interpreting the combination of the various data sets, having in mind the large set of possibilities both regarding the particle physics as well as the astrophysics of dark matter.

APPENDICES

A. Derivation of direct detection limits

In this appendix, we present the details of our implementation of direct detection experiments, relevant for the calculation of the corresponding upper limits in Sec. 3, 7 and 8. For each experiment, we follow the prescriptions suggested by the respective collaboration as closely as possible. Furthermore, in each case we validate our approach by comparing the published upper limit on the standard spin-independent and/or spin-dependent scattering cross section with the upper limits derived using our implementation of the data. We confirmed that for all experiments considered in this work, our upper limit either matches the corresponding result from the experimental collaboration, or is slightly more conservative.

LUX (results from 2013, employed in Sec. 3)

We calculate the number of dark matter-induced recoil events following [369, 416] by extracting the number of expected photoelectrons (PE) as a function of the recoil energy from Fig. 4 of [101], using the intersections of the red solid line with the contours of constant E_R. Following the LUX collaboration, we do not model recoils below 3 keV. Furthermore, we assume $\sigma_{\rm PMT} = 0.37$ in the calculation of the single-photoelectron resolution of the photomultipliers. The acceptance as a function of the S_1 signal is given by the red dashed line in Fig. 1 of [101], which we additionally multiply by a factor 1/2 corresponding (approximately) to the fraction of events falling into the region below the mean nuclear recoil band shown as the red solid line in Fig. 4 of [101]. This approximation is well-justified for large dark matter masses, while it underestimates the number of signal events for dark matter masses below $\simeq 20\,\text{GeV}$, leading to conservative upper limits. After running with an exposure of $85.3 \times 118.3\,\text{kg} \cdot \text{days}$, LUX observed one event in the S_1 range between 2 PE and 30 PE. Setting conservatively the number of expected background events to zero, the 90% C.L. upper limit on the number of signal events is given by $N_{\rm max} = 3.89$.

LUX (results from 2015, employed in Sec. 7)

The most recent data release of the LUX collaboration is based on an exposure of $1.4 \cdot 10^4\,\text{kg} \cdot \text{days}$ [102]. The detection efficiency as a function of the nuclear recoil energy is given in Fig. 1 of [102], which we employ only for $E_R \geq 1.1\,\text{keV}$. Everything below the red solid curve of Fig. 2 in [102] is considered as a signal event, which we take into account by an additional factor 1/2 in the efficiency (see the comment in the previous paragraph regarding the validity of this approximation). Lastly, we multiply the total efficiency by a constant factor $(18/20)^2$, corresponding to a cut $r < 18\,\text{cm}$ on the fiducial radius. With one observed event in the signal region, and assuming conservatively zero background events, we obtain the 95% and 99.9% C.L. upper limits $N_{\rm max} = 4.74$ and 9.23 on the number of expected recoil events, respectively.

XENON100

We calculate the detection efficiency for XENON100 following [416], using the scintillation efficiency $\mathcal{L}_{\text{eff}}(E_R)$ from [417], which we set to zero below 3 keV. The efficiency of detecting a S_1 signal in the range [3 PE, 30 PE], as well as the efficiency related to the cut on S_2 is taken from [104]. The collaboration observed two events after running with an exposure of 7636.4 kg · days; setting the number of background events conservatively to zero, we derive a 90% C.L. upper limit $N_{\text{max}} = 5.32$ on the number of expected recoil events.

SuperCDMS

Here, we use the latest data release [109], based on an exposure of 577 kg·days. The efficiency as a function of $E_R \in [1.6\,\text{keV}, 10\,\text{keV}]$ is given in Fig. 1 of [109]. After unblinding, 11 events have been observed, with a level of background that is not fully understood. Hence, we again are conservative and set the number of background events to zero, leading to 90%, 95% and 99.9% C.L. upper limits $N_{\text{max}} = 16.6$, 18.2 and 25.6, respectively.

SIMPLE

The SIMPLE experiment is based on a $C_2Cl\,F_5$ target. For the calculation within the non-relativistic effective theory discussed in Sec. 7, we conservatively only take into account scattering of F, as there are no results available for the nuclear response functions of C and Cl. We employ the combined Stage I and II data [122], with a total exposure of 20.18 kg·days. We assume a detection efficiency $\epsilon(E_R) = 1 - \exp(-3.6(E_R/E_T - 1))$ with $E_T = 8\,\text{keV}$, as suggested by the collaboration, and consider recoils up to 500 keV. In total, 11 events have been observed, which has to be compared to the conservative background expectation of 14.5 events [122]. The 90%, 95% and 99.9% C.L. upper limits using the Feldman-Cousins method are then given by $N_{\text{max}} = 4.02$, 5.26 and 11.9, respectively.

COUPP

COUPP is based on a $C\,F_3I$ target; for the non-relativistic effective theory employed in Sec. 7 we only consider scattering of F and I, again due to the absence of detailed nuclear form factor calculations of carbon. In the data release [120], the results have been presented for three nucleation thresholds $E_T = 7.8\,\text{keV}$, 11.0 keV and 15.5 keV, which can be treated as independent experiments. For scattering off fluor, the bubble efficiency is taken to be $\epsilon(E_R) = 1 - \exp\left(0.15\,(1 - E_R/E_T)\right)$, while for iodine we assume $\epsilon(E_R) = \theta\,(E_R - E_T)$. The effective exposures (number of observed events) in the three data sets are given by 55.8 kg · days (2), 70.0 kg · days (3), and 311.7 kg · days (8), respectively. Setting in each case the number of expected background events to zero, the 90%, 95% and 99.9% C.L. limits are given by $N_{\text{max}} = 5.32$, 6.30 and 11.2 for $E_T = 7.8\,\text{keV}$, by $N_{\text{max}} = 6.68$, 7.75 and 13.0 for $E_T = 11.0\,\text{keV}$, and by $N_{\text{max}} = 12.99$, 14.4 and 21.1 for $E_T = 15.5\,\text{keV}$, respectively.

PICASSO

For the implementation of the PICASSO experiment, which employs a C_4F_{10} target, we again only take into account scattering off F in Sec. 7. We consider the data obtained with the energy thresholds $E_T = 1.73$ keV and 2.9 keV, presented in [123]. The detection efficiency is modeled via $\epsilon(E_R) = 1 - \exp\left(2.5\,(1 - E_R/E_T)\right)$. Following the collaboration, we assume a Gaussian distribution of the error in each energy bin, leading to the 95% (99.9%)

C.L. Feldman-Cousin upper limit $N_{\max} = 8.72$ (18.0) per kg of fluor per day for bin number 1, and 3.21 (5.59) for bin number 2.

PICO

Also for PICO, based on a C_3F_8 target, we only consider scattering off fluor for the calculation of the rates in the non-relativistic effective theory. The detection efficiency is given by the dashed line in Fig. 3 of [124]. After running with an exposure of $129\,\mathrm{kg}\cdot\mathrm{days}$ [125], one event has been observed; setting conservatively the number of background events to zero, we obtain a 95% (99.9%) C.L. upper limit $N_{\max} = 4.74$ (9.23).

B. Annihilation cross sections for real scalar and Majorana dark matter

B.1. Real scalar dark matter

In this appendix, we provide the results for the VIB and one-loop annihilation cross sections of a real scalar dark matter particle S coupling via a Yukawa coupling to a Dirac fermion ψ and a Standard Model fermion f_R, as defined in Eq. (4.3). All cross sections have been calculated in the limit $v \to 0$, and were obtained with the help of FeynCalc [277] and LoopTools [418]. For convenience, in this appendix we use $\mu \equiv r^2 \equiv m_\psi^2/m_S^2$.

Virtual internal bremsstrahlung

The differential and total cross sections for the internal bremsstrahlung of a photon, $SS \to f\bar{f}\gamma$, are given by

$$\frac{\mathrm{d}(\sigma v)_{f\bar{f}\gamma}}{\mathrm{d}x} = \frac{y^4 \alpha_{\mathrm{em}} N_c Q_f^2}{4\pi^2 m_S^2} (1-x) \left[\frac{2x}{(\mu+1)(\mu+1-2x)} - \frac{x}{(\mu+1-x)^2} - \frac{(\mu+1)(\mu+1-2x)}{2(\mu+1-x)^3} \log\left(\frac{\mu+1}{\mu+1-2x}\right) \right], \quad \text{(B.1)}$$

$$(\sigma v)_{f\bar{f}\gamma} = \frac{y^4 \alpha_{\mathrm{em}} N_c Q_f^2}{8\pi^2 m_S^2} \left[(\mu+1) \left\{ \frac{\pi^2}{6} - \log^2\left(\frac{\mu+1}{2\mu}\right) - 2\mathrm{Li}_2\left(\frac{\mu+1}{2\mu}\right) \right\} + \frac{4\mu+3}{\mu+1} + \frac{(4\mu+1)(\mu-1)}{2\mu} \log\left(\frac{\mu-1}{\mu+1}\right) \right], \quad \text{(B.2)}$$

where $\alpha_{\mathrm{em}} \equiv e^2/(4\pi)$ is the electromagnetic fine structure constant, $x \equiv E_\gamma/m_S$, Q_f is the electric charge of the fermion f in units of $|e|$, and $N_c = 3\,(1)$ if f is a quark (lepton). For the case of S coupling to a Standard Model quark, the cross sections for VIB of a gluon, $SS \to f\bar{f}g$, are obtained by replacing $\alpha_{\mathrm{em}} \to 4\alpha_S$, $N_c \to 1$, $Q_f \to 1$ in these expressions. On the other hand, for the internal bremsstrahlung of a Z boson we find the following double-differential annihilation cross section:

$$\frac{\mathrm{d}(\sigma v)_{f\bar{f}Z}}{\mathrm{d}x\,\mathrm{d}z} = \frac{y^4 \alpha_{\mathrm{em}} \tan^2\theta_W N_c Q_f^2}{\pi^2 m_S^2 (1-\mu-2z)^2 (3+\mu-2x-2z)^2} \times \left\{ (1-x)\left[x^2 - 2x(1-z) + 2(1-z)^2\right] + \frac{\xi}{4}(x^2-2x+2) \right\}, \quad \text{(B.3)}$$

with $x = E_Z/m_S$, $z = E_f/m_S$ and $\xi = m_Z^2/m_S^2$. In that case, the total cross section $(\sigma v)_{f\bar{f}Z}$ can only be obtained numerically. Also notice that the expression for $\mathrm{d}(\sigma v)_{f\bar{f}Z}/(\mathrm{d}x\,\mathrm{d}z)$ has a different functional dependence on x and z compared to the corresponding process involving Majorana dark matter; this is contrast to the annihilation into $f\bar{f}\gamma$, which for real scalar dark matter is simply a factor of 8 larger than for Majorana dark matter [88].

One-loop annihilation into gauge bosons

The annihilation $SS \to \gamma\gamma$ is generated at the one-loop level, with one representative diagram shown in the right panel of Fig. 4.2. For vanishing dark matter velocity, gauge invariance in form of the Ward identity implies the following structure of the matrix element:

$$i\mathcal{M}_{\gamma\gamma} = -\frac{i\alpha_{\rm em} Q_f^2\, y^2}{\pi} \epsilon_\mu^*(k_1)\epsilon_\nu^*(k_2) g^{\mu\nu} \mathcal{A}_{\gamma\gamma}. \tag{B.4}$$

Here, $\epsilon_\mu(k)$ is the polarization vector of the photon, and $\mathcal{A}_{\gamma\gamma}$ is the one-loop form factor for the annihilation process, for which we obtain the expression

$$\begin{aligned}\mathcal{A}_{\gamma\gamma} &= 2 + m_S^2 \left\{ \frac{1-\mu-\epsilon}{1+\mu-\epsilon}\frac{2\epsilon}{\mu-\epsilon} C_0\left(-m_S^2, m_S^2, 0; m_f^2, m_\psi^2, m_f^2\right)\right. \\ &+ \frac{1-\epsilon-\mu}{1+\epsilon-\mu}\frac{2\mu}{\epsilon-\mu} C_0\left(-m_S^2, m_S^2, 0; m_\psi^2, m_f^2, m_\psi^2\right) + \frac{4\epsilon\,(1-\epsilon)}{1+\mu-\epsilon} C_0\left(4m_S^2, 0, 0; m_f^2, m_f^2, m_f^2\right) \\ &+ \left.\frac{4\mu\,(1-\mu)}{1+\epsilon-\mu} C_0\left(4m_S^2, 0, 0; m_\psi^2, m_\psi^2, m_\psi^2\right)\right\}. \end{aligned} \tag{B.5}$$

where $\epsilon = m_f^2/m_S^2$, and where C_0 is the scalar three-point Passarino-Veltman integral [419] defined by

$$C_0\left(p_1^2, (p_1-p_2)^2, p_2^2; m_1^2, m_2^2, m_3^2\right) = \int \frac{d^d\ell}{i\pi^2} \frac{1}{\ell^2 - m_1^2} \frac{1}{(\ell+p_1)^2 - m_2^2} \frac{1}{(\ell+p_2)^2 - m_3^2}. \tag{B.6}$$

The form factor $\mathcal{A}_{\gamma\gamma}$ greatly simplifies in the limit $m_f \to 0$, which is applicable for all cases discussed in this work:

$$\mathcal{A}_{\gamma\gamma}\Big|_{m_f=0} = 2 + \mathrm{Li}_2\left(\frac{1}{\mu}\right) - \mathrm{Li}_2\left(-\frac{1}{\mu}\right) - 2\mu \arcsin^2\left(\frac{1}{\sqrt{\mu}}\right). \tag{B.7}$$

Our result for $\mathcal{A}_{\gamma\gamma}$ differs from the one reported in [420], while we agree with the recent result in [312]. We have checked that our full expression of $i\mathcal{M}_{\gamma\gamma}$ satisfies the Ward identity, and furthermore we have cross-checked $\mathrm{Im}(\mathcal{A}_{\gamma\gamma})$ against the result deduced from the optical theorem [421]. Finally, the annihilation cross section for the one-loop annihilation into photons is given by

$$(\sigma v)_{\gamma\gamma} = \frac{y^4 \alpha_{\rm em}^2 N_c^2 Q_f^4}{32\pi^3 m_S^2} \left|\mathcal{A}_{\gamma\gamma}\right|^2. \tag{B.8}$$

If S couples to a Standard Model quark, it can also annihilate into a pair of gluons, $SS \to gg$, with a cross section given by Eq. (B.8), after replacing $\alpha_{\rm em}^2 \to 2\alpha_S^2$, $N_c \to 1$, $Q_f \to 1$.

Finally[1], the matrix element for $SS \to \gamma Z$ can be cast as

$$i\mathcal{M}_{\gamma Z} = \frac{i\alpha_{\rm em} Q_f^2 y^2 \tan\theta_W}{\pi} \epsilon_\mu^*(k_1)\epsilon_\nu^*(k_2) g^{\mu\nu} \mathcal{A}_{\gamma Z}\,, \tag{B.9}$$

with $\epsilon_\mu(k_1)$ and $\epsilon_\mu(k_2)$ being the polarization vectors of the Z boson and the photon, respectively. The form factor $\mathcal{A}_{\gamma Z}$ is given by

[1] We neglect the contribution of $SS \to ZZ$ to the relic density.

$$
\begin{aligned}
\mathcal{A}_{\gamma Z} \;=\; & 2-\frac{\xi}{4-\xi}B_0\left(m_Z^2;m_f^2,m_f^2\right)-\frac{\xi}{4-\xi}B_0\left(m_Z^2;m_\psi^2,m_\psi^2\right)\\
&+\frac{2\xi\left(1+\mu+\epsilon\right)}{\left(4-\xi\right)\left(1+\mu-\epsilon\right)\left(1+\epsilon-\mu\right)}\left[1-\frac{1-\mu+\epsilon}{1+\mu+\epsilon}\frac{\epsilon}{2}\right]B_0\left(m_S^2;m_f^2,m_\psi^2\right)\\
&-\frac{\epsilon}{1+\mu-\epsilon}\frac{\xi}{4-\xi}B_0\left(4m_S^2;m_f^2,m_f^2\right)-\frac{2\mu}{1+\epsilon-\mu}\frac{\xi}{4-\xi}B_0\left(4m_S^2;m_\psi^2,m_\psi^2\right)\\
&+m_S^2\left\{\frac{\epsilon}{2}\frac{4-4\epsilon-\xi}{1+\mu-\epsilon}C_0\left(m_Z^2,4m_S^2,0;m_f^2,m_f^2,m_f^2\right)\right.\\
&+\mu\frac{4-4\mu-\xi}{1+\epsilon-\mu}C_0\left(m_Z^2,4m_S^2,0;m_\psi^2,m_\psi^2,m_\psi^2\right)\\
&+\frac{\epsilon}{2}\left[\frac{\left(4+\xi\right)\left(-2+2\mu+2\epsilon+\xi\right)}{\left(1+\mu-\epsilon\right)\left(4\epsilon-4\mu+\xi\right)}+\frac{1}{2}\frac{4-4\epsilon-\xi}{1+\mu-\epsilon}\right]\times\\
&\qquad C_0\left(-m_S^2+\frac{m_Z^2}{2},m_S^2,0;m_f^2,m_\psi^2,m_f^2\right)\\
&+\frac{\mu}{2}\left[\frac{\left(4+\xi\right)\left(-2+2\epsilon+2\mu+\xi\right)}{\left(1+\epsilon-\mu\right)\left(4\mu-4\epsilon+\xi\right)}-\frac{8\epsilon}{4\mu-4\epsilon+\xi}\right]\times\\
&\qquad C_0\left(-m_S^2+\frac{m_Z^2}{2},m_S^2,0;m_\psi^2,m_f^2,m_\psi^2\right)\\
&+\left[\frac{2\xi\left(1+\mu\right)+\epsilon\left(4\mu-\xi\right)}{4\left(1+\mu-\epsilon\right)}-\frac{4\left(1+\mu\right)}{4-\xi}+\frac{4\mu\left(1+\mu-2\epsilon\right)}{4\mu-4\epsilon+\xi}\right]\times\\
&\qquad C_0\left(-m_S^2+\frac{m_Z^2}{2},m_S^2,m_Z^2;m_f^2,m_\psi^2,m_f^2\right)\\
&+\left[\frac{2\mu\left(1-\mu+3\epsilon\right)+\xi\left(1+\epsilon\right)}{2\left(1+\epsilon-\mu\right)}-\frac{4\left(1+\mu+\epsilon\right)}{4-\xi}+\frac{4\epsilon\left(1+3\mu+\epsilon\right)}{4\epsilon-4\mu+\xi}\right]\times\\
&\qquad \left.C_0\left(-m_S^2+\frac{m_Z^2}{2},m_S^2,m_Z^2;m_\psi^2,m_f^2,m_\psi^2\right)\right\},
\end{aligned}
\tag{B.10}
$$

with B_0 defined by

$$
B_0\left(p_1^2;m_1^2,m_2^2\right)=\int\frac{d^d\ell}{i\pi^2}\frac{1}{\ell^2-m_1^2}\frac{1}{\left(\ell+p_1\right)^2-m_2^2}. \tag{B.11}
$$

The cross section in this case is given by

$$
(\sigma v)_{\gamma Z}=\frac{y^4\alpha_{\rm em}^2N_c^2Q_f^4\tan^2\theta_W}{16\pi^3m_S^2}\left(1-\frac{m_Z^2}{4m_S^2}\right)\left|\mathcal{A}_{\gamma Z}\right|^2. \tag{B.12}
$$

B.2. Majorana dark matter

Here we present the expressions for the annihilation cross sections relevant for the simplified model of Majorana dark matter discussed in Sec. 5 and 6.2, in the limit $m_f \to 0$ and $v \to 0$, employing FeynCalc [277] for parts of the computations. The results for annihilations into $\gamma\gamma$ and gg have also been presented in [422,423], for γZ in [424], for $f_R\bar{f}_R\gamma$ in [204–206], for $f_R\bar{f}_RZ$ in [329] and for $f_R\bar{f}_Rg$ in [205]; on the other hand, the cross-section for the one-loop annihilation into ZZ is derived for the first time in this work.

Virtual internal bremsstrahlung

Defining $x = E_V/m_\chi$, with $V = \gamma, Z, g$, $z = E_f/m_\chi$, $\xi = m_Z^2/m_\chi^2$, as well as $\mu = m_\eta^2/m_\chi^2$, we find

$$\frac{\mathrm{d}(\sigma v)_{f_R\bar{f}_R\gamma}}{\mathrm{d}E_\gamma\,\mathrm{d}E_f} = \frac{q_f^2 N_C \alpha_{\mathrm{em}} y^4 (1-x)\left[x^2 - 2x(1-z) + 2(1-z)^2\right]}{8\pi^2 m_\chi^4 (1-2z-\mu)^2 (3-2x-2z+\mu)^2}\,, \tag{B.13}$$

$$\begin{aligned}\frac{\mathrm{d}(\sigma v)_{f_R\bar{f}_R Z}}{\mathrm{d}E_Z\,\mathrm{d}E_f} &= \frac{q_f^2 N_c \tan^2(\theta_W)\alpha_{\mathrm{em}} y^4}{8\pi^2 m_\chi^4 (1-2z-\mu)^2 (3-2x-2z+\mu)^2} \\ &\quad\times\Big\{(1-x)\left[x^2 - 2x(1-z) + 2(1-z)^2\right] \\ &\quad + \xi\left[x^2 + 2z^2 + 2xz - 4z\right]/4 - \xi^2/8\Big\}\,,\end{aligned} \tag{B.14}$$

$$\begin{aligned}\frac{\mathrm{d}(\sigma v)_{f_R\bar{f}_R g}}{\mathrm{d}E_\gamma\,\mathrm{d}E_f} &= \frac{\left(N_c^2-1\right)\alpha_{\mathrm{s}}(m_\chi) y^4}{16\pi^2 m_\chi^4 (1-2z-\mu)^2 (3-2x-2z+\mu)^2} \\ &\quad\times (1-x)\left[x^2 - 2x(1-z) + 2(1-z)^2\right]\,.\end{aligned} \tag{B.15}$$

For a given annihilation channel, the spectrum of gauge bosons is obtained by integrating the double-differential cross section over the dimensionless fermion energy z, with limits given by $z^{\mathrm{min/max}} = 1 - (x \pm \sqrt{x^2 - M_V^2/m_\chi^2})/2$. Moreover, the total cross-section follows from integrating over x from $x^{\mathrm{min}} = M_V/m_\chi$ to $x^{\mathrm{max}} = 1 + M_V^2/(4m_\chi^2)$.

One-loop annihilation into gauge bosons

Defining $\mathrm{Li}_2(x)$ as the dilogarithm function, the total cross sections for the one-loop annihilations into gauge bosons read

$$(\sigma v)_{\gamma\gamma} = \frac{N_C^2\, q_f^4\, \alpha_{\mathrm{em}}^2\, y^4}{256\pi^3\, m_\chi^2}\left[\mathrm{Li}_2\left(-\frac{m_\chi^2}{m_\eta^2}\right) - \mathrm{Li}_2\left(\frac{m_\chi^2}{m_\eta^2}\right)\right]^2\,, \tag{B.16}$$

$$(\sigma v)_{gg} = \frac{2\,\alpha_{\mathrm{s}}^2\, y^4}{256\pi^3\, m_\chi^2}\left[\mathrm{Li}_2\left(-\frac{m_\chi^2}{m_\eta^2}\right) - \mathrm{Li}_2\left(\frac{m_\chi^2}{m_\eta^2}\right)\right]^2\,, \tag{B.17}$$

$$(\sigma v)_{\gamma\mathrm{Z}} = \frac{|\mathcal{A}_{\gamma\mathrm{Z}}|^2}{512\,\pi^3\, m_\chi^6\, m_\eta^4 \left(1 - \frac{m_{\mathrm{Z}}^2}{4\,m_\chi^2}\right)\left(1 - \frac{m_{\mathrm{Z}}^4}{16\,m_\eta^4}\right)^2}\,, \tag{B.18}$$

$$(\sigma v)_{\mathrm{ZZ}} = \frac{|\mathcal{A}_{\mathrm{ZZ}}|^2}{1024\,\pi^3\, m_\chi^6\, m_\eta^4 \sqrt{1 - \frac{m_{\mathrm{Z}}^2}{m_\chi^2}}}\,. \tag{B.19}$$

Here, $\mathcal{A}_{\gamma\mathrm{Z}}$ and $\mathcal{A}_{\mathrm{ZZ}}$ are given by

$$\begin{aligned}\mathcal{A}_{\gamma\mathrm{Z}} = N_C\, q_f^2\, \alpha_{\mathrm{em}}\, y^2\, \tan(\theta_{\mathrm{W}})\left(1 - \frac{m_{\mathrm{Z}}^2}{4\,m_\eta^2}\right)\Bigg\{ \\ m_{\mathrm{Z}}^2\left(\frac{m_\chi^4 + m_\eta^4}{2} + \frac{m_{\mathrm{Z}}^2\left(m_\eta^2 - m_\chi^2\right)}{4} + \frac{m_{\mathrm{Z}}^4}{16}\right)\, \mathrm{C}_0\left(m_\chi^2, m_{\mathrm{Z}}^2, \frac{m_{\mathrm{Z}}^2}{2} - m_\chi^2, m_\eta^2, 0, 0\right)\end{aligned}$$

$$
\begin{aligned}
&+ 2\, m_\eta^2 \left(m_\chi^2 - \frac{m_{\rm Z}^2}{4}\right)^2 \mathrm{C}_0\left(m_\chi^2, 0, \frac{m_{\rm Z}^2}{2} - m_\chi^2, 0, m_\eta^2, m_\eta^2\right) \\
&+ \left(m_\eta^2 + \frac{m_{\rm Z}^2}{4}\right)\left(2m_\chi^4 - m_\chi^2 m_{\rm Z}^2 + \frac{m_\eta^2 m_{\rm Z}^2}{2}\right) \mathrm{C}_0\left(m_\chi^2, m_{\rm Z}^2, \frac{m_{\rm Z}^2}{2} - m_\chi^2, 0, m_\eta^2, m_\eta^2\right) \\
&+ \frac{m_{\rm Z}^2}{2}\left(m_\eta^2 + \frac{m_{\rm Z}^2}{4}\right)\left[2\sqrt{\frac{4m_\eta^2}{m_{\rm Z}^2} - 1}\ \mathrm{arccot}\left(\sqrt{\frac{4m_\eta^2}{m_{\rm Z}^2} - 1}\right) - \log\frac{m_{\rm Z}^2}{m_\eta^2} + i\pi\right]\Bigg\}, \qquad \text{(B.20)}
\end{aligned}
$$

$$
\begin{aligned}
\mathcal{A}_{\rm ZZ} = N_C\, q_f^2\, \alpha_{\rm em}\, y^2\, \tan^2(\theta_{\rm W}) \Bigg\{ & m_{\rm Z}^2\left(m_\chi^4 + m_\eta^4 - m_\chi^2 m_{\rm Z}^2\right) \mathrm{C}_0\left(m_\chi^2, m_{\rm Z}^2, -m_\chi^2 + m_{\rm Z}^2, m_\eta^2, 0, 0\right) \\
&+ \left[4m_\chi^4 m_\eta^2 + \left(-m_\chi^4 - 4m_\chi^2 m_\eta^2 + m_\eta^4\right) m_{\rm Z}^2 + m_\chi^2 m_{\rm Z}^4\right] \mathrm{C}_0\left(m_\chi^2, m_{\rm Z}^2, -m_\chi^2 + m_{\rm Z}^2, 0, m_\eta^2, m_\eta^2\right) \\
&+ m_\eta^2\, m_{\rm Z}^2 \left[2\sqrt{\frac{4m_\eta^2}{m_{\rm Z}^2} - 1}\ \mathrm{arccot}\left(\sqrt{\frac{4m_\eta^2}{m_{\rm Z}^2} - 1}\right) - \log\frac{m_{\rm Z}^2}{m_\eta^2} + i\pi\right]\Bigg\}, \qquad \text{(B.21)}
\end{aligned}
$$

with C_0 being a Passarino-Veltman function. We verified that these expressions satisfy

$$
(\sigma v)_{\rm ZZ}\big|_{\tan(\theta_{\rm W})\equiv 1} \overset{m_{\rm Z}\to 0}{\longrightarrow} (\sigma v)_{\gamma\gamma}\,, \qquad (\sigma v)_{\gamma{\rm Z}}\big|_{\tan(\theta_{\rm W})\equiv 1} \overset{m_{\rm Z}\to 0}{\longrightarrow} 2\,(\sigma v)_{\gamma\gamma}\,. \qquad \text{(B.22)}
$$

C. Derivation of limits from the IceCube data

Description of the approach

In this appendix, we describe our method of calculating upper limits on the annihilation rate of dark matter in the Sun, employing the IceCube 79-string data; here, we follow largely the approach presented in [349].

Starting from a given muon (anti-)neutrino flux $\mathrm{d}\Phi_{\nu/\bar{\nu}}/\mathrm{d}E$, the number of expected muon and antimuon signal events is given by [349]

$$\theta_{\mathrm{S}} = t_{\mathrm{exp}} \int_0^\infty L\left(E, \phi_{\mathrm{cut}}\right) \left(A_\nu\left(E\right) \frac{\mathrm{d}\Phi_\nu}{\mathrm{d}E} + A_{\bar{\nu}}\left(E\right) \frac{\mathrm{d}\Phi_{\bar{\nu}}}{\mathrm{d}E} \right) \mathrm{d}E \,. \tag{C.1}$$

Here, t_{exp} denotes the live-time of the IceCube analysis [167], and $A_{\nu/\bar{\nu}}\left(E\right)$ is the effective area for detecting muon neutrinos/antineutrinos. We take the total effective area $A_\nu\left(E\right) + A_{\bar{\nu}}\left(E\right)$ of the IceCube 79-string analysis from [167], and decompose it into separate effective areas for neutrinos and antineutrinos following [425]. Moreover, the angular loss factor $L\left(E, \phi_{\mathrm{cut}}\right)$ is defined as the probability that a muon track originating from a neutrino with energy E is reconstructed with an angle $\phi \leq \phi_{\mathrm{cut}}$ with respect to the position of the Sun:

$$L\left(E, \phi_{\mathrm{cut}}\right) = 1 - \exp\left[-\frac{1}{2} \left(\frac{\phi_{\mathrm{cut}}}{\sigma_\theta\left(E\right)} \right)^2 \right] . \tag{C.2}$$

This definition of $L\left(E, \phi_{\mathrm{cut}}\right)$ is based on the assumption that the muon track directions are Gaussian distributed around the median angle $\sigma_\theta\left(E\right)$, which we take from [167].

We then obtain 95% C.L. limits on θ_S (and hence on the annihilation rate of dark matter in the Sun) by means of the CL_s method, which is based on an hypothesis test using the likelihood ratio

$$X = \frac{\mathcal{L}\left(n_{\mathrm{obs}} \mid \theta_{\mathrm{S}} + \theta_{\mathrm{BG}}\right)}{\mathcal{L}\left(n_{\mathrm{obs}} \mid \theta_{\mathrm{BG}}\right)} \,. \tag{C.3}$$

The definition of the likelihood functions and the corresponding p-values are given in [349], while we take the number of observed (background) events $n_{\mathrm{obs}}\left(\theta_{\mathrm{BG}}\right)$ as a function of the cut angle ϕ_{cut} from [168].

In our analysis, we choose ϕ_{cut} such that the upper limit on the annihilation rate is optimized. To this end, we first calculate the upper limit expected in the absence of a signal, i.e. the hypothetical limit under the assumption $n_{\mathrm{obs}} = \theta_{\mathrm{BG}}$, for the eight different cut angles ϕ_{cut} between 3° and 8.5° defined in [168]. We then determine the cut angle leading to the most stringent upper limit within this background-only hypothesis, and employ it for calculating our final upper limit based on the actually observed number of events n_{obs}. In this way, the choice of the optimal cut angle is not influenced by the actual data, guaranteeing that our procedure is unbiased. We show the optimal cut angle as a function of the dark matter mass in Fig. C.1 for the simplified model of Majorana dark matter coupling to u_R

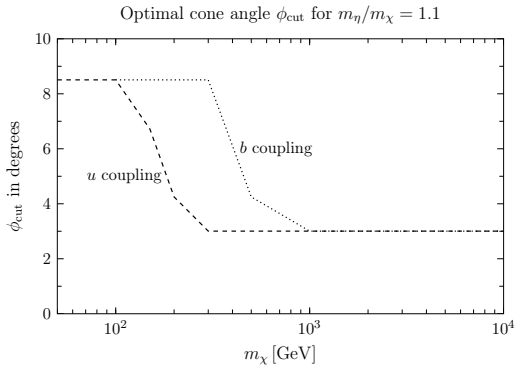

Figure C.1.: Optimal cut angle $\phi_{\rm cut}$ as a function of the mass of the Majorana dark matter candidate discussed in Sec. 5, for $m_\eta/m_\chi = 1.1$, and both for coupling to up- and to bottom-quarks. See text for details.

or b_R discussed in Sec. 5, employing for concreteness the mass splitting $m_\eta/m_\chi = 1.1$. A neutrino spectrum peaking at large energies, such as the one arising from the $u\bar{u}Z$ final state (c.f. Fig. 5.3) favors a smaller cut angle, as the mean angle between the muon track and the incoming neutrino decreases with neutrino energy. Hence, the optimal cut angle is typically smaller for dark matter coupling to u_R than to b_R, as in the latter case the neutrino spectrum has a larger contribution from the $b\bar{b}g$ final state, which is dominated by low-energetic neutrinos, as it follows from Fig. 5.3.

Finally, we remark that the data of the IceCube 79-string analysis is split into three distinct sets, denoted as "Winter high", "Winter low" and "Summer low" [168]. Each of them is optimized to a different type of muon events; in particular, the "Summer low" data set consists of downward going muons detected in DeepCore, using the remaining IceCube detector as a veto for the huge atmospheric muon background. For a given neutrino flux, we apply the procedure outlined in the previous paragraphs separately for each of these three data sets, and use the most stringent upper limit as our final result. In most of the parameter space of the Majorana dark matter model, the "Winter high" event category leads to the optimal limit, except for $m_\chi \lesssim 200\,\text{GeV}$, where the other two data sets can be relevant.

Upper limits from IceCube for annihilations into ZZ or gg

In Table C.1 and Fig. C.2, we present the 90% C.L. upper limits on the spin-dependent and spin-independent scattering cross section of dark matter with protons following from the IceCube data for annihilations into ZZ and gg, calculated using the approach introduced in the previous section. These results are necessary for obtaining the upper limits on the scattering cross section in scenarios in which the dark matter particle interacts via a contact interaction with light fermions, and where the annihilation proceeds dominantly into gauge boson pairs at the one-loop level, c.f. Sec. 6.1.2 and in particular Eq. (6.8).

m_{DM}[GeV]	$\sigma_{\mathrm{SD}}^{\mathrm{max},ZZ}$[cm^2]	$\sigma_{\mathrm{SI}}^{\mathrm{max},ZZ}$[cm^2]	$\sigma_{\mathrm{SD}}^{\mathrm{max},gg}$[cm^2]	$\sigma_{\mathrm{SI}}^{\mathrm{max},gg}$[cm^2]
100	$3.51 \cdot 10^{-40}$	$7.88 \cdot 10^{-43}$	$9.77 \cdot 10^{-37}$	$2.19 \cdot 10^{-39}$
120	$2.87 \cdot 10^{-40}$	$5.65 \cdot 10^{-43}$	$6.07 \cdot 10^{-37}$	$1.19 \cdot 10^{-39}$
150	$3.01 \cdot 10^{-40}$	$5.10 \cdot 10^{-43}$	$3.93 \cdot 10^{-37}$	$6.65 \cdot 10^{-40}$
200	$1.50 \cdot 10^{-40}$	$2.12 \cdot 10^{-43}$	$2.72 \cdot 10^{-37}$	$3.85 \cdot 10^{-40}$
300	$2.36 \cdot 10^{-40}$	$2.69 \cdot 10^{-43}$	$2.10 \cdot 10^{-37}$	$2.39 \cdot 10^{-40}$
500	$2.96 \cdot 10^{-40}$	$2.73 \cdot 10^{-43}$	$2.20 \cdot 10^{-37}$	$2.03 \cdot 10^{-40}$
700	$4.28 \cdot 10^{-40}$	$3.57 \cdot 10^{-43}$	$2.08 \cdot 10^{-37}$	$1.73 \cdot 10^{-40}$
1000	$7.10 \cdot 10^{-40}$	$5.49 \cdot 10^{-43}$	$3.56 \cdot 10^{-37}$	$2.75 \cdot 10^{-40}$
2000	$2.57 \cdot 10^{-39}$	$1.81 \cdot 10^{-42}$	$5.06 \cdot 10^{-37}$	$3.57 \cdot 10^{-40}$
3000	$6.17 \cdot 10^{-39}$	$4.22 \cdot 10^{-42}$	$6.84 \cdot 10^{-37}$	$4.68 \cdot 10^{-40}$
5000	$1.85 \cdot 10^{-38}$	$1.24 \cdot 10^{-41}$	$1.16 \cdot 10^{-36}$	$7.76 \cdot 10^{-40}$
7000	$3.80 \cdot 10^{-38}$	$2.52 \cdot 10^{-41}$	$1.65 \cdot 10^{-36}$	$1.09 \cdot 10^{-39}$
10000	$7.92 \cdot 10^{-38}$	$5.21 \cdot 10^{-41}$	$2.56 \cdot 10^{-36}$	$1.68 \cdot 10^{-39}$

Table C.1.: 90% C.L. upper limits on the spin-dependent and spin-independent scattering cross section of dark matter with protons, for annihilations with 100% branching ratio into ZZ or into gg, and for various values of the dark matter mass m_{DM}.

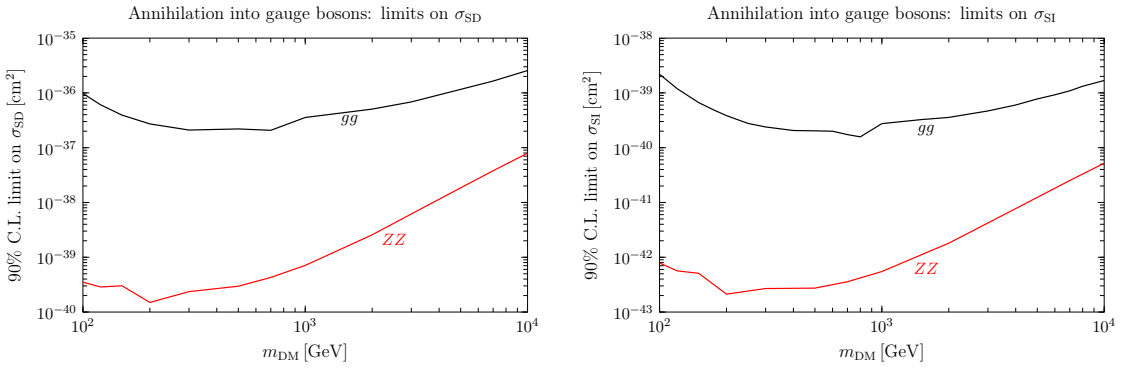

Figure C.2.: 90% C.L. upper limits on the spin-dependent (left plot) and spin-independent scattering cross section (right plot) of dark matter with protons, for annihilations with 100% branching ratio into ZZ (red curves) or into gg (black curves).

D. Non-relativistic dark matter response functions

In the following, we list the dark matter response functions $R_k^{\tau\tau'}$ entering Eq. (7.5), which is the basis for the computation of the scattering cross section in the framework of the non-relativistic effective theory of dark matter-nucleon interactions. Here, $v_T^{\perp 2} \equiv v^2 - q^2/(4\mu_T^2)$, with μ_T being the dark matter-nucleus reduced mass, while j_χ denotes the dark matter spin.

$$
\begin{aligned}
R_M^{\tau\tau'}\left(v_T^{\perp 2}, \frac{q^2}{m_N^2}\right) &= c_1^\tau c_1^{\tau'} + \frac{j_\chi(j_\chi+1)}{3}\left[\frac{q^2}{m_N^2} v_T^{\perp 2} c_5^\tau c_5^{\tau'} + v_T^{\perp 2} c_8^\tau c_8^{\tau'} + \frac{q^2}{m_N^2} c_{11}^\tau c_{11}^{\tau'}\right] \\
R_{\Phi''}^{\tau\tau'}\left(v_T^{\perp 2}, \frac{q^2}{m_N^2}\right) &= \frac{q^2}{4m_N^2} c_3^\tau c_3^{\tau'} + \frac{j_\chi(j_\chi+1)}{12}\left(c_{12}^\tau - \frac{q^2}{m_N^2} c_{15}^\tau\right)\left(c_{12}^{\tau'} - \frac{q^2}{m_N^2} c_{15}^{\tau'}\right) \\
R_{\Phi'' M}^{\tau\tau'}\left(v_T^{\perp 2}, \frac{q^2}{m_N^2}\right) &= c_3^\tau c_1^{\tau'} + \frac{j_\chi(j_\chi+1)}{3}\left(c_{12}^\tau - \frac{q^2}{m_N^2} c_{15}^\tau\right) c_{11}^{\tau'} \\
R_{\tilde{\Phi}'}^{\tau\tau'}\left(v_T^{\perp 2}, \frac{q^2}{m_N^2}\right) &= \frac{j_\chi(j_\chi+1)}{12}\left[c_{12}^\tau c_{12}^{\tau'} + \frac{q^2}{m_N^2} c_{13}^\tau c_{13}^{\tau'}\right] \\
R_{\Sigma''}^{\tau\tau'}\left(v_T^{\perp 2}, \frac{q^2}{m_N^2}\right) &= \frac{q^2}{4m_N^2} c_{10}^\tau c_{10}^{\tau'} + \frac{j_\chi(j_\chi+1)}{12}\Big[c_4^\tau c_4^{\tau'} + \\
&\quad \frac{q^2}{m_N^2}(c_4^\tau c_6^{\tau'} + c_6^\tau c_4^{\tau'}) + \frac{q^4}{m_N^4} c_6^\tau c_6^{\tau'} + v_T^{\perp 2} c_{12}^\tau c_{12}^{\tau'} + \frac{q^2}{m_N^2} v_T^{\perp 2} c_{13}^\tau c_{13}^{\tau'}\Big] \\
R_{\Sigma'}^{\tau\tau'}\left(v_T^{\perp 2}, \frac{q^2}{m_N^2}\right) &= \frac{1}{8}\left[\frac{q^2}{m_N^2} v_T^{\perp 2} c_3^\tau c_3^{\tau'} + v_T^{\perp 2} c_7^\tau c_7^{\tau'}\right] + \frac{j_\chi(j_\chi+1)}{12}\Big[c_4^\tau c_4^{\tau'} + \\
&\quad \frac{q^2}{m_N^2} c_9^\tau c_9^{\tau'} + \frac{v_T^{\perp 2}}{2}\left(c_{12}^\tau - \frac{q^2}{m_N^2} c_{15}^\tau\right)\left(c_{12}^{\tau'} - \frac{q^2}{m_N^2} c_{15}^{\tau\prime}\right) + \frac{q^2}{2m_N^2} v_T^{\perp 2} c_{14}^\tau c_{14}^{\tau'}\Big] \\
R_\Delta^{\tau\tau'}\left(v_T^{\perp 2}, \frac{q^2}{m_N^2}\right) &= \frac{j_\chi(j_\chi+1)}{3}\left[\frac{q^2}{m_N^2} c_5^\tau c_5^{\tau'} + c_8^\tau c_8^{\tau'}\right] \\
R_{\Delta\Sigma'}^{\tau\tau'}\left(v_T^{\perp 2}, \frac{q^2}{m_N^2}\right) &= \frac{j_\chi(j_\chi+1)}{3}\left[c_5^\tau c_4^{\tau'} - c_8^\tau c_9^{\tau'}\right].
\end{aligned}
\tag{D.1}
$$

Acknowledgements

First, I would like to thank my thesis advisor Alejandro Ibarra for his support and advice, for suggesting so many interesting topics to work on, but also for giving me the necessary freedom to pursue my own ideas. Also, I am particularly thankful for his support allowing me to attend a large number of conferences and summer schools all around the world, leading to valuable experiences both at the professional and personal level. I also acknowledge the financial support by the Universität Bayern e.V., the Studienstiftung des Deutschen Volkes, and the TUM Graduate School.

I am grateful that I had the opportunity to conduct my research in collaboration with a large number of excellent scientists, and I definitely profited a lot from all of them. Also, I was lucky to work in the very pleasant atmosphere of the T30d and T30e groups here at TUM; thanks to all of you for making the last years such an enjoyable time! In particular, this includes Karin, who always supported me when it came to bureaucratic complications. Furthermore, I thank my good friend and office mate for more than four years, Sergio "Paco" López Gehler. I really enjoyed our time in four different offices, and I honestly thank you for providing the right amount of distraction from work, which made daily working life much more fun.

I am indebted to all of my family for their strong support over the last years, for being always there for me, and for encouraging me to pursue my way in science. Lastly, I thank Kathi for enriching my life in so many ways by her unconditional love and support.

Bibliography

[1] B. Kelvin (1904), Baltimore lectures on molecular dynamics and the wave theory of light, https://archive.org/details/baltimorelecture00kelviala. Accessed: 2016-06-10.

[2] E. Öpik, Bull. de la Soc. Astr. de Russie, 21, 150, 1915.

[3] J. C. Kapteyn, *First Attempt at a Theory of the Arrangement and Motion of the Sidereal System*, *Astrophys. J.* **55** (1922) 302–328.

[4] J. H. Oort, *The force exerted by the stellar system in the direction perpendicular to the galactic plane and some related problems*, *Bulletin of the Astronomical Institutes of the Netherlands* **6** (Aug., 1932) 249.

[5] G. Bertone and D. Hooper, *A History of Dark Matter*, `arXiv:1605.04909`.

[6] A. Ibarra, M. Totzauer, and S. Wild, *High-energy neutrino signals from the Sun in dark matter scenarios with internal bremsstrahlung*, *JCAP* **1312** (2013) 043, [`arXiv:1311.1418`].

[7] A. Ibarra, M. Totzauer, and S. Wild, *Higher order dark matter annihilations in the Sun and implications for IceCube*, *JCAP* **1404** (2014) 012, [`arXiv:1402.4375`].

[8] A. Ibarra, T. Toma, M. Totzauer, and S. Wild, *Sharp Gamma-ray Spectral Features from Scalar Dark Matter Annihilations*, *Phys. Rev.* **D90** (2014), no. 4 043526, [`arXiv:1405.6917`].

[9] A. Ibarra and S. Wild, *Dirac dark matter with a charged mediator: a comprehensive one-loop analysis of the direct detection phenomenology*, *JCAP* **1505** (2015), no. 05 047, [`arXiv:1503.03382`].

[10] F. Ferrer, A. Ibarra, and S. Wild, *A novel approach to derive halo-independent limits on dark matter properties*, *JCAP* **1509** (2015), no. 09 052, [`arXiv:1506.03386`].

[11] F. Giacchino, A. Ibarra, L. L. Honorez, M. H. G. Tytgat, and S. Wild, *Signatures from Scalar Dark Matter with a Vector-like Quark Mediator*, *JCAP* **1602** (2016), no. 02 002, [`arXiv:1511.04452`].

[12] R. Catena, A. Ibarra, and S. Wild, *DAMA confronts null searches in the effective theory of dark matter-nucleon interactions*, *JCAP* **1605** (2016), no. 05 039, [`arXiv:1602.04074`].

[13] L. Bergstrom, *Nonbaryonic dark matter: Observational evidence and detection methods*, *Rept. Prog. Phys.* **63** (2000) 793, [`hep-ph/0002126`].

[14] G. Bertone, D. Hooper, and J. Silk, *Particle dark matter: Evidence, candidates and constraints*, *Phys. Rept.* **405** (2005) 279–390, [`hep-ph/0404175`].

[15] P. Gorenstein and W. Tucker, *Astronomical Signatures of Dark Matter*, *Adv. High Energy Phys.* **2014** (2014) 878203.

[16] K. G. Begeman, A. H. Broeils, and R. H. Sanders, *Extended rotation curves of spiral galaxies: Dark haloes and modified dynamics*, *Mon. Not. Roy. Astron. Soc.* **249** (1991) 523.

[17] V. C. Rubin and W. K. Ford, Jr., *Rotation of the Andromeda Nebula from a Spectroscopic Survey of Emission Regions*, *Astrophys. J.* **159** (1970) 379–403.

[18] V. C. Rubin, N. Thonnard, and W. K. Ford, Jr., *Rotational properties of 21 SC galaxies with a large range of luminosities and radii, from NGC 4605 /R = 4kpc/ to UGC 2885 /R = 122 kpc/*, *Astrophys. J.* **238** (1980) 471.

[19] F. Zwicky, *Die Rotverschiebung von extragalaktischen Nebeln*, *Helv. Phys. Acta* **6** (1933) 110–127.

[20] K. R. Lang, *Astrophysical formulae: Vol. 1: Radiation, gas processes and high-energy astrophysics. Vol. 2: Space, time, matter and cosmology*. 1999.

[21] F. Zwicky, *On the Masses of Nebulae and of Clusters of Nebulae*, *Astrophys. J.* **86** (1937) 217–246.

[22] A. B. Newman, T. Treu, R. S. Ellis, D. J. Sand, C. Nipoti, J. Richard, and E. Jullo, *The Density Profiles of Massive, Relaxed Galaxy Clusters: I. The Total Density Over 3 Decades in Radius*, *Astrophys. J.* **765** (2013) 24, [arXiv:1209.1391].

[23] D. Clowe, M. Bradac, A. H. Gonzalez, M. Markevitch, S. W. Randall, C. Jones, and D. Zaritsky, *A direct empirical proof of the existence of dark matter*, *Astrophys. J.* **648** (2006) L109–L113, [astro-ph/0608407].

[24] M. Bartelmann and P. Schneider, *Weak gravitational lensing*, *Phys. Rept.* **340** (2001) 291–472, [astro-ph/9912508].

[25] M. Milgrom, *A Modification of the Newtonian dynamics as a possible alternative to the hidden mass hypothesis*, *Astrophys. J.* **270** (1983) 365–370.

[26] B. Famaey and S. McGaugh, *Modified Newtonian Dynamics (MOND): Observational Phenomenology and Relativistic Extensions*, *Living Rev. Rel.* **15** (2012) 10, [arXiv:1112.3960].

[27] G. W. Angus, H. Shan, H. Zhao, and B. Famaey, *On the Law of Gravity, the Mass of Neutrinos and the Proof of Dark Matter*, *Astrophys. J.* **654** (2007) L13–L16, [astro-ph/0609125].

[28] A. N. Taylor, S. Dye, T. J. Broadhurst, N. Benitez, and E. van Kampen, *Gravitational lens magnification and the mass of abell 1689*, *Astrophys. J.* **501** (1998) 539, [astro-ph/9801158].

[29] S. Weinberg, *Cosmology*. Cosmology. OUP Oxford, 2008.

[30] J. L. Cervantes-Cota and G. Smoot, *Cosmology today-A brief review*, *AIP Conf. Proc.* **1396** (2011) 28–52, [arXiv:1107.1789].

[31] W. Hu and S. Dodelson, *Cosmic microwave background anisotropies*, *Ann. Rev. Astron. Astrophys.* **40** (2002) 171–216, [astro-ph/0110414].

[32] **Planck**, P. A. R. Ade *et. al.*, *Planck 2015 results. XIII. Cosmological parameters*, arXiv:1502.01589.

[33] R. H. Cyburt, B. D. Fields, K. A. Olive, and T.-H. Yeh, *Big Bang Nucleosynthesis: 2015*, *Rev. Mod. Phys.* **88** (2016) 015004, [arXiv:1505.01076].

[34] **Particle Data Group**, K. A. Olive *et. al.*, *Review of Particle Physics*, *Chin. Phys.* **C38** (2014) 090001.

[35] **SDSS**, K. N. Abazajian *et. al.*, *The Seventh Data Release of the Sloan Digital Sky Survey*, *Astrophys. J. Suppl.* **182** (2009) 543–558, [arXiv:0812.0649].

[36] E. Bertschinger, *Simulations of structure formation in the universe*, *Ann. Rev. Astron. Astrophys.* **36** (1998) 599–654.

[37] A. Del Popolo, *Dark matter and structure formation a review*, *Astron. Rep.* **51** (2007) 169–196, [arXiv:0801.1091].

[38] B. Moore, S. Ghigna, F. Governato, G. Lake, T. R. Quinn, J. Stadel, and P. Tozzi, *Dark matter substructure within galactic halos*, *Astrophys. J.* **524** (1999) L19–L22, [astro-ph/9907411].

[39] A. V. Maccio', G. Stinson, C. B. Brook, J. Wadsley, H. M. P. Couchman, S. Shen, B. K. Gibson, and T. Quinn, *Halo expansion in cosmological hydro simulations: towards a baryonic solution of the cusp/core problem in massive spirals*, *Astrophys. J.* **744** (2012) L9, [arXiv:1111.5620].

[40] T. K. Chan, D. Keres, J. Onorbe, P. F. Hopkins, A. L. Muratov, C. A. Faucher-GiguÃ¨re, and E. Quataert, *The impact of baryonic physics on the structure of dark matter haloes: the view from the FIRE cosmological simulations*, *Mon. Not. Roy. Astron. Soc.* **454** (2015), no. 3 2981–3001, [arXiv:1507.02282].

[41] F. Iocco, M. Pato, and G. Bertone, *Evidence for dark matter in the inner Milky Way*, *Nature Phys.* **11** (2015) 245–248, [arXiv:1502.03821].

[42] M. Pato and F. Iocco, *The Dark Matter Profile of the Milky Way: a Non-parametric Reconstruction*, *Astrophys. J.* **803** (2015), no. 1 L3, [arXiv:1504.03317].

[43] M. Pato, F. Iocco, and G. Bertone, *Dynamical constraints on the dark matter distribution in the Milky Way*, *JCAP* **1512** (2015), no. 12 001, [arXiv:1504.06324].

[44] J. Diemand, M. Kuhlen, P. Madau, M. Zemp, B. Moore, D. Potter, and J. Stadel, *Clumps and streams in the local dark matter distribution*, *Nature* **454** (2008) 735–738, [arXiv:0805.1244].

[45] V. Springel, J. Wang, M. Vogelsberger, A. Ludlow, A. Jenkins, A. Helmi, J. F. Navarro, C. S. Frenk, and S. D. M. White, *The Aquarius Project: the subhalos of galactic halos*, *Mon. Not. Roy. Astron. Soc.* **391** (2008) 1685–1711, [arXiv:0809.0898].

[46] J. F. Navarro, C. S. Frenk, and S. D. M. White, *The Structure of cold dark matter halos*, *Astrophys. J.* **462** (1996) 563–575, [astro-ph/9508025].

[47] M. Gustafsson, M. Fairbairn, and J. Sommer-Larsen, *Baryonic Pinching of Galactic Dark Matter Haloes*, *Phys. Rev.* **D74** (2006) 123522, [astro-ph/0608634].

[48] O. Y. Gnedin, D. Ceverino, N. Y. Gnedin, A. A. Klypin, A. V. Kravtsov, R. Levine, D. Nagai, and G. Yepes, *Halo Contraction Effect in Hydrodynamic Simulations of Galaxy Formation*, arXiv:1108.5736.

[49] F. Iocco, M. Pato, G. Bertone, and P. Jetzer, *Dark Matter distribution in the Milky Way: microlensing and dynamical constraints*, *JCAP* **1111** (2011) 029, [arXiv:1107.5810].

[50] J. Einasto, *On the Construction of a Composite Model for the Galaxy and on the Determination of the System of Galactic Parameters*, *Trudy Astrofizicheskogo Instituta Alma-Ata* **5** (1965) 87–100.

[51] A. W. Graham, D. Merritt, B. Moore, J. Diemand, and B. Terzic, *Empirical models for Dark Matter Halos. I. Nonparametric Construction of Density Profiles and Comparison with Parametric Models*, *Astron. J.* **132** (2006) 2685–2700, [astro-ph/0509417].

[52] W. J. G. de Blok, *The Core-Cusp Problem*, *Adv. Astron.* **2010** (2010) 789293, [arXiv:0910.3538].

[53] P. Mollitor, E. Nezri, and R. Teyssier, *Baryonic and dark matter distribution in cosmological simulations of spiral galaxies*, *Mon. Not. Roy. Astron. Soc.* **447** (2015), no. 2 1353–1369, [arXiv:1405.4318].

[54] D. N. Spergel and P. J. Steinhardt, *Observational evidence for selfinteracting cold dark matter*, *Phys. Rev. Lett.* **84** (2000) 3760–3763, [astro-ph/9909386].

[55] F. J. Kerr and D. Lynden-Bell, *Review of galactic constants*, *Mon. Not. Roy. Astron. Soc.* **221** (1986) 1023.

[56] R. Catena and P. Ullio, *A novel determination of the local dark matter density*, *JCAP* **1008** (2010) 004, [arXiv:0907.0018].

[57] J. Bovy and S. Tremaine, *On the local dark matter density*, *Astrophys. J.* **756** (2012) 89, [arXiv:1205.4033].

[58] A. K. Drukier, K. Freese, and D. N. Spergel, *Detecting Cold Dark Matter Candidates*, *Phys. Rev.* **D33** (1986) 3495–3508.

[59] J. Bovy *et. al.*, *The Milky Way's circular velocity curve between 4 and 14 kpc from APOGEE data*, *Astrophys. J.* **759** (2012) 131, [arXiv:1209.0759].

[60] **SDSS**, X. X. Xue *et. al.*, *The Milky Way's Circular Velocity Curve to 60 kpc and an Estimate of the Dark Matter Halo Mass from Kinematics of 2400 SDSS Blue Horizontal Branch Stars*, *Astrophys. J.* **684** (2008) 1143–1158, [arXiv:0801.1232].

[61] P. J. McMillan and J. J. Binney, *The uncertainty in Galactic parameters*, *Mon. Not. Roy. Astron. Soc.* **402** (2010) 934, [arXiv:0907.4685].

[62] J. Bovy, D. W. Hogg, and H.-W. Rix, *Galactic masers and the Milky Way circular velocity*, *Astrophys. J.* **704** (2009) 1704–1709, [arXiv:0907.5423].

[63] M. J. Reid *et. al.*, *Trigonometric Parallaxes of High Mass Star Forming Regions: the Structure and Kinematics of the Milky Way*, *Astrophys. J.* **783** (2014) 130, [arXiv:1401.5377].

[64] T. Piffl *et. al.*, *The RAVE survey: the Galactic escape speed and the mass of the Milky Way*, *Astron. Astrophys.* **562** (2014) A91, [arXiv:1309.4293].

[65] J. Binney and S. Tremaine, *Galactic Dynamics: Second Edition*. Princeton University Press, 2008.

[66] M. Vogelsberger, A. Helmi, V. Springel, S. D. M. White, J. Wang, C. S. Frenk, A. Jenkins, A. D. Ludlow, and J. F. Navarro, *Phase-space structure in the local dark matter distribution and its signature in direct detection experiments*, *Mon. Not. Roy. Astron. Soc.* **395** (2009) 797–811, [arXiv:0812.0362].

[67] M. Lisanti, *Lectures on Dark Matter Physics*, in *Theoretical Advanced Study Institute in Elementary Particle Physics: New Frontiers in Fields and Strings (TASI 2015) Boulder, CO, USA, June 1-26, 2015*, 2016. arXiv:1603.03797.

[68] C. Kelso, C. Savage, M. Valluri, K. Freese, G. S. Stinson, and J. Bailin, *The impact of baryons on the direct detection of dark matter*, arXiv:1601.04725.

[69] N. Bozorgnia, F. Calore, M. Schaller, M. Lovell, G. Bertone, C. S. Frenk, R. A. Crain, J. F. Navarro, J. Schaye, and T. Theuns, *Simulated Milky Way analogues: implications for dark matter direct searches*, arXiv:1601.04707.

[70] K. Kadota, T. Sekiguchi, and H. Tashiro, *A new constraint on millicharged dark matter from galaxy clusters*, arXiv:1602.04009.

[71] K. Griest, *Galactic Microlensing as a Method of Detecting Massive Compact Halo Objects*, *Astrophys. J.* **366** (1991) 412–421.

[72] **MACHO**, C. Alcock *et. al.*, *The MACHO project LMC microlensing results from the first two years and the nature of the galactic dark halo*, *Astrophys. J.* **486** (1997) 697–726, [astro-ph/9606165].

[73] S. W. Randall, M. Markevitch, D. Clowe, A. H. Gonzalez, and M. Bradac, *Constraints on the Self-Interaction Cross-Section of Dark Matter from Numerical Simulations of the Merging Galaxy Cluster 1E 0657-56*, *Astrophys. J.* **679** (2008) 1173–1180, [arXiv:0704.0261].

[74] A. H. G. Peter, M. Rocha, J. S. Bullock, and M. Kaplinghat, *Cosmological Simulations with Self-Interacting Dark Matter II: Halo Shapes vs. Observations*, *Mon. Not. Roy. Astron. Soc.* **430** (2013) 105, [arXiv:1208.3026].

[75] A. S. Szalay and G. Marx, *Neutrino rest mass from cosmology*, *Astronomy and Astrophysics* **49** (June, 1976) 437–441.

[76] R. Cowsik and J. McClelland, *An Upper Limit on the Neutrino Rest Mass*, *Phys. Rev. Lett.* **29** (1972) 669–670.

[77] J. Bonn *et. al.*, *The Mainz neutrino mass experiment*, *Nucl. Phys. Proc. Suppl.* **91** (2001) 273–279. [PoShep2001,192(2001)].

[78] J. Ellis and K. A. Olive, *Supersymmetric Dark Matter Candidates*, arXiv:1001.3651.

[79] E. W. Kolb and R. Slansky, *Dimensional Reduction in the Early Universe: Where Have the Massive Particles Gone?*, *Phys. Lett.* **B135** (1984) 378.

[80] H.-C. Cheng, K. T. Matchev, and M. Schmaltz, *Radiative corrections to Kaluza-Klein masses*, *Phys. Rev.* **D66** (2002) 036005, [hep-ph/0204342].

[81] P. Sikivie, *Axion Cosmology*, *Lect. Notes Phys.* **741** (2008) 19–50, [astro-ph/0610440]. [,19(2006)].

[82] S. Dodelson and L. M. Widrow, *Sterile-neutrinos as dark matter*, *Phys. Rev. Lett.* **72** (1994) 17–20, [hep-ph/9303287].

[83] R. Adhikari *et. al.*, *A White Paper on keV Sterile Neutrino Dark Matter*, *Submitted to: White paper* (2016) [arXiv:1602.04816].

[84] E. W. Kolb and M. S. Turner, *The Early Universe*, *Front. Phys.* **69** (1990) 1–547.

[85] P. Gondolo and G. Gelmini, *Cosmic abundances of stable particles: Improved analysis*, *Nucl. Phys.* **B360** (1991) 145–179.

[86] K. Griest and D. Seckel, *Three exceptions in the calculation of relic abundances*, *Phys. Rev.* **D43** (1991) 3191–3203.

[87] G. Belanger, F. Boudjema, A. Pukhov, and A. Semenov, *micrOMEGAs3: A program for calculating dark matter observables*, *Comput. Phys. Commun.* **185** (2014) 960–985, [arXiv:1305.0237].

[88] F. Giacchino, L. Lopez-Honorez, and M. H. Tytgat, *Scalar Dark Matter Models with Significant Internal Bremsstrahlung*, *JCAP* **1310** (2013) 025, [arXiv:1307.6480].

[89] G. Steigman, B. Dasgupta, and J. F. Beacom, *Precise Relic WIMP Abundance and its Impact on Searches for Dark Matter Annihilation*, *Phys. Rev.* **D86** (2012) 023506, [arXiv:1204.3622].

[90] M. W. Goodman and E. Witten, *Detectability of Certain Dark Matter Candidates*, *Phys. Rev.* **D31** (1985) 3059.

[91] D. G. Cerdeno and A. M. Green, *Direct detection of WIMPs*, arXiv:1002.1912.

[92] G. Jungman, M. Kamionkowski, and K. Griest, *Supersymmetric dark matter*, *Phys. Rept.* **267** (1996) 195–373, [hep-ph/9506380].

[93] J. D. Lewin and P. F. Smith, *Review of mathematics, numerical factors, and corrections for dark matter experiments based on elastic nuclear recoil*, *Astropart. Phys.* **6** (1996) 87–112.

[94] V. A. Bednyakov and F. Simkovic, *Nuclear spin structure in dark matter search: The Finite momentum transfer limit*, *Phys. Part. Nucl.* **37** (2006) S106–S128, [hep-ph/0608097].

[95] P. J. Fox, J. Liu, and N. Weiner, *Integrating Out Astrophysical Uncertainties*, *Phys. Rev.* **D83** (2011) 103514, [arXiv:1011.1915].

[96] M. T. Frandsen, F. Kahlhoefer, C. McCabe, S. Sarkar, and K. Schmidt-Hoberg, *Resolving astrophysical uncertainties in dark matter direct detection*, *JCAP* **1201** (2012) 024, [arXiv:1111.0292].

[97] P. Gondolo and G. B. Gelmini, *Halo independent comparison of direct dark matter detection data*, *JCAP* **1212** (2012) 015, [arXiv:1202.6359].

[98] K. Freese, M. Lisanti, and C. Savage, *Colloquium: Annual modulation of dark matter*, *Rev. Mod. Phys.* **85** (2013) 1561–1581, [arXiv:1209.3339].

[99] R. Schoenrich, J. Binney, and W. Dehnen, *Local Kinematics and the Local Standard of Rest*, *Mon. Not. Roy. Astron. Soc.* **403** (2010) 1829, [arXiv:0912.3693].

[100] C. Savage, G. Gelmini, P. Gondolo, and K. Freese, *Compatibility of DAMA/LIBRA dark matter detection with other searches*, *JCAP* **0904** (2009) 010, [arXiv:0808.3607].

[101] **LUX**, D. S. Akerib *et. al.*, *First results from the LUX dark matter experiment at the Sanford Underground Research Facility*, *Phys. Rev. Lett.* **112** (2014) 091303, [arXiv:1310.8214].

[102] **LUX**, D. S. Akerib *et. al.*, *Improved WIMP scattering limits from the LUX experiment*, arXiv:1512.03506.

[103] **LUX**, D. S. Akerib *et. al.*, *First spin-dependent WIMP-nucleon cross section limits from the LUX experiment*, arXiv:1602.03489.

[104] **XENON100**, E. Aprile *et. al.*, *Dark Matter Results from 225 Live Days of XENON100 Data*, *Phys. Rev. Lett.* **109** (2012) 181301, [arXiv:1207.5988].

[105] **XENON100**, E. Aprile *et. al.*, *Limits on spin-dependent WIMP-nucleon cross sections from 225 live days of XENON100 data*, *Phys. Rev. Lett.* **111** (2013), no. 2 021301, [arXiv:1301.6620].

[106] **XENON10**, J. Angle *et. al.*, *A search for light dark matter in XENON10 data*, *Phys. Rev. Lett.* **107** (2011) 051301, [arXiv:1104.3088]. [Erratum: Phys. Rev. Lett.110,249901(2013)].

[107] **XMASS**, K. Abe *et. al.*, *Direct dark matter search by annual modulation in XMASS-I*, arXiv:1511.04807.

[108] **PANDA-X**, A. Tan *et. al.*, *Dark Matter Search Results from the Commissioning Run of PandaX-II*, arXiv:1602.06563.

[109] **SuperCDMS**, R. Agnese *et. al.*, *Search for Low-Mass Weakly Interacting Massive Particles with SuperCDMS*, *Phys. Rev. Lett.* **112** (2014), no. 24 241302, [arXiv:1402.7137].

[110] **CDMS-II**, Z. Ahmed *et. al.*, *Results from a Low-Energy Analysis of the CDMS II Germanium Data*, *Phys. Rev. Lett.* **106** (2011) 131302, [arXiv:1011.2482].

[111] **SuperCDMS**, R. Agnese *et. al.*, *WIMP-Search Results from the Second CDMSlite Run*, *Phys. Rev. Lett.* (2015) [arXiv:1509.02448]. [Phys. Rev. Lett.116,071301(2016)].

[112] **CoGeNT**, C. E. Aalseth *et. al.*, *Search for An Annual Modulation in Three Years of CoGeNT Dark Matter Detector Data*, arXiv:1401.3295.

[113] **EDELWEISS**, E. Armengaud *et. al.*, *A search for low-mass WIMPs with EDELWEISS-II heat-and-ionization detectors*, *Phys. Rev.* **D86** (2012) 051701, [arXiv:1207.1815].

[114] **DAMIC**, J. Barreto *et. al.*, *Direct Search for Low Mass Dark Matter Particles with CCDs*, *Phys. Lett.* **B711** (2012) 264–269, [arXiv:1105.5191].

[115] R. Bernabei *et. al.*, *Final model independent result of DAMA/LIBRA-phase1*, *Eur. Phys. J.* **C73** (2013) 2648, [arXiv:1308.5109].

[116] **DM-Ice**, E. Barbosa de Souza *et. al.*, *First Search for a Dark Matter Annual Modulation Signal with NaI(Tl) in the Southern Hemisphere by DM-Ice17*, *Submitted to: Phys. Rev. Lett.* (2016) [arXiv:1602.05939].

[117] S. C. Kim *et. al.*, *New Limits on Interactions between Weakly Interacting Massive Particles and Nucleons Obtained with CsI(Tl) Crystal Detectors*, *Phys. Rev. Lett.* **108** (2012) 181301, [arXiv:1204.2646].

[118] **CRESST-II**, G. Angloher *et. al.*, *Results on low mass WIMPs using an upgraded CRESST-II detector*, *Eur. Phys. J.* **C74** (2014), no. 12 3184, [arXiv:1407.3146].

[119] **CRESST**, G. Angloher *et. al.*, *Results on light dark matter particles with a low-threshold CRESST-II detector*, *Eur. Phys. J.* **C76** (2016), no. 1 25, [arXiv:1509.01515].

[120] **COUPP**, E. Behnke *et. al.*, *First Dark Matter Search Results from a 4-kg CF_3I Bubble Chamber Operated in a Deep Underground Site*, *Phys. Rev.* **D86** (2012), no. 5 052001, [arXiv:1204.3094]. [Erratum: Phys. Rev.D90,no.7,079902(2014)].

[121] **PICO**, C. Amole *et. al.*, *Dark Matter Search Results from the PICO-60 CF_3I Bubble Chamber*, *Submitted to: Phys. Rev. D* (2015) [arXiv:1510.07754].

[122] M. Felizardo *et. al.*, *Final Analysis and Results of the Phase II SIMPLE Dark Matter Search*, *Phys. Rev. Lett.* **108** (2012) 201302, [arXiv:1106.3014].

[123] **PICASSO**, S. Archambault *et. al.*, *Constraints on Low-Mass WIMP Interactions on ^{19}F from PICASSO*, *Phys. Lett.* **B711** (2012) 153–161, [arXiv:1202.1240].

[124] **PICO**, C. Amole *et. al.*, *Dark Matter Search Results from the PICO-2L C_3F_8 Bubble Chamber*, *Phys. Rev. Lett.* **114** (2015), no. 23 231302, [arXiv:1503.00008].

[125] **PICO**, C. Amole *et. al.*, *Improved Dark Matter Search Results from PICO-2L Run-2*, arXiv:1601.03729.

[126] **CDMS**, R. Agnese *et. al.*, *Silicon Detector Dark Matter Results from the Final Exposure of CDMS II*, *Phys. Rev. Lett.* **111** (2013), no. 25 251301, [arXiv:1304.4279].

[127] C. E. Aalseth *et. al.*, *Maximum Likelihood Signal Extraction Method Applied to 3.4 years of CoGeNT Data*, arXiv:1401.6234.

[128] G. Angloher *et. al.*, *Results from 730 kg days of the CRESST-II Dark Matter Search*, *Eur. Phys. J.* **C72** (2012) 1971, [arXiv:1109.0702].

[129] **XENON**, E. Aprile *et. al.*, *Physics reach of the XENON1T dark matter experiment*, *Submitted to: JCAP* (2015) [arXiv:1512.07501].

[130] **LZ**, D. S. Akerib *et. al.*, *LUX-ZEPLIN (LZ) Conceptual Design Report*, arXiv:1509.02910.

[131] **DARWIN Consortium**, L. Baudis, *DARWIN: dark matter WIMP search with noble liquids*, *J. Phys. Conf. Ser.* **375** (2012) 012028, [arXiv:1201.2402].

[132] **CRESST**, G. Angloher *et. al.*, *Probing low WIMP masses with the next generation of CRESST detector*, arXiv:1503.08065.

[133] http://cdms.berkeley.edu/scdmssnolab.html. Accessed: 2016-03-03.

[134] B. Cabrera, L. M. Krauss, and F. Wilczek, *Bolometric Detection of Neutrinos*, *Phys. Rev. Lett.* **55** (1985) 25.

[135] J. Billard, L. Strigari, and E. Figueroa-Feliciano, *Implication of neutrino backgrounds on the reach of next generation dark matter direct detection experiments*, *Phys. Rev.* **D89** (2014), no. 2 023524, [arXiv:1307.5458].

[136] P. Cushman *et. al.*, *Working Group Report: WIMP Dark Matter Direct Detection*, in *Community Summer Study 2013: Snowmass on the Mississippi (CSS2013) Minneapolis, MN, USA, July 29-August 6, 2013*, 2013. arXiv:1310.8327.

[137] D. N. Spergel, *The Motion of the Earth and the Detection of Wimps*, *Phys. Rev.* **D37** (1988) 1353.

[138] F. Mayet *et. al.*, *A review of the discovery reach of directional Dark Matter detection*, arXiv:1602.03781.

[139] W. H. Press and D. N. Spergel, *Capture by the sun of a galactic population of weakly interacting massive particles*, *Astrophys. J.* **296** (1985) 679–684.

[140] J. Silk, K. A. Olive, and M. Srednicki, *The Photino, the Sun and High-Energy Neutrinos*, *Phys. Rev. Lett.* **55** (1985) 257–259.

[141] A. Gould, *Resonant Enhancements in WIMP Capture by the Earth*, *Astrophys. J.* **321** (1987) 571.

[142] J. N. Bahcall, A. M. Serenelli, and S. Basu, *New solar opacities, abundances, helioseismology, and neutrino fluxes*, *Astrophys. J.* **621** (2005) L85–L88, [astro-ph/0412440].

[143] G. Ingelman and M. Thunman, *High-energy neutrino production by cosmic ray interactions in the sun*, *Phys. Rev.* **D54** (1996) 4385–4392, [hep-ph/9604288].

[144] **ANTARES**, S. Adrian-Martinez *et. al.*, *First results on dark matter annihilation in the Sun using the ANTARES neutrino telescope*, *JCAP* **1311** (2013) 032, [arXiv:1302.6516].

[145] Figure by Joakim Edsjo, taken from http://www.amanda.uci.edu/results.html. Accessed: 2016-03-17.

[146] J. Kumar, J. G. Learned, S. Smith, and K. Richardson, *Tools for Studying Low-Mass Dark Matter at Neutrino Detectors*, *Phys. Rev.* **D86** (2012) 073002, [arXiv:1204.5120].

[147] N. Bernal, J. Martin-Albo, and S. Palomares-Ruiz, *A novel way of constraining WIMPs annihilations in the Sun: MeV neutrinos*, *JCAP* **1308** (2013) 011, [arXiv:1208.0834].

[148] J. Lundberg and J. Edsjo, *WIMP diffusion in the solar system including solar depletion and its effect on earth capture rates*, *Phys. Rev.* **D69** (2004) 123505, [astro-ph/0401113].

[149] P. Gondolo, J. Edsjo, P. Ullio, L. Bergstrom, M. Schelke, and E. A. Baltz, *DarkSUSY: Computing supersymmetric dark matter properties numerically*, *JCAP* **0407** (2004) 008, [astro-ph/0406204].

[150] A. Serenelli, S. Basu, J. W. Ferguson, and M. Asplund, *New Solar Composition: The Problem With Solar Models Revisited*, *Astrophys. J.* **705** (2009) L123–L127, [arXiv:0909.2668].

[151] R. Catena and B. Schwabe, *Form factors for dark matter capture by the Sun in effective theories*, *JCAP* **1504** (2015), no. 04 042, [arXiv:1501.03729].

[152] K. Griest and D. Seckel, *Cosmic Asymmetry, Neutrinos and the Sun*, *Nucl. Phys.* **B283** (1987) 681. [Erratum: Nucl. Phys.B296,1034(1988)].

[153] M. Cirelli, N. Fornengo, T. Montaruli, I. A. Sokalski, A. Strumia, and F. Vissani, *Spectra of neutrinos from dark matter annihilations*, *Nucl. Phys.* **B727** (2005) 99–138, [hep-ph/0506298]. [Erratum: Nucl. Phys.B790,338(2008)].

[154] G. Busoni, A. De Simone, and W.-C. Huang, *On the Minimum Dark Matter Mass Testable by Neutrinos from the Sun*, *JCAP* **1307** (2013) 010, [arXiv:1305.1817].

[155] T. Sjostrand, S. Mrenna, and P. Z. Skands, *PYTHIA 6.4 Physics and Manual*, *JHEP* **05** (2006) 026, [hep-ph/0603175].

[156] T. Sjostrand, S. Mrenna, and P. Z. Skands, *A Brief Introduction to PYTHIA 8.1*, *Comput. Phys. Commun.* **178** (2008) 852–867, [arXiv:0710.3820].

[157] S. Ritz and D. Seckel, *Detailed Neutrino Spectra From Cold Dark Matter Annihilations in the Sun*, *Nucl. Phys.* **B304** (1988) 877.

[158] **IceCube**, M. G. Aartsen *et. al.*, *Improved limits on dark matter annihilation in the Sun with the 79-string IceCube detector and implications for supersymmetry*, arXiv:1601.00653.

[159] **ANTARES**, S. Adrian-Martinez *et. al.*, *Limits on Dark Matter Annihilation in the Sun using the ANTARES Neutrino Telescope*, arXiv:1603.02228.

[160] **Super-Kamiokande**, K. Bays *et. al.*, *Supernova Relic Neutrino Search at Super-Kamiokande*, *Phys. Rev.* **D85** (2012) 052007, [arXiv:1111.5031].

[161] C. Rott, J. Siegal-Gaskins, and J. F. Beacom, *New Sensitivity to Solar WIMP Annihilation using Low-Energy Neutrinos*, *Phys. Rev.* **D88** (2013) 055005, [arXiv:1208.0827].

[162] M. Blennow, J. Edsjo, and T. Ohlsson, *Neutrinos from WIMP annihilations using a full three-flavor Monte Carlo*, *JCAP* **0801** (2008) 021, [arXiv:0709.3898].

[163] P. Baratella, M. Cirelli, A. Hektor, J. Pata, M. Piibeleht, and A. Strumia, *PPPC 4 DMν: a Poor Particle Physicist Cookbook for Neutrinos from Dark Matter annihilations in the Sun*, *JCAP* **1403** (2014) 053, [arXiv:1312.6408].

[164] M. C. Gonzalez-Garcia, M. Maltoni, and T. Schwetz, *Global Analyses of Neutrino Oscillation Experiments*, arXiv:1512.06856.

[165] L. Wolfenstein, *Neutrino Oscillations in Matter*, *Phys. Rev.* **D17** (1978) 2369–2374.

[166] A. Strumia and F. Vissani, *Neutrino masses and mixings and...*, hep-ph/0606054.

[167] M. Danninger, PhD thesis, Stockholm University.

[168] **IceCube**, M. G. Aartsen *et. al.*, *Search for dark matter annihilations in the Sun with the 79-string IceCube detector*, *Phys. Rev. Lett.* **110** (2013), no. 13 131302, [arXiv:1212.4097].

[169] **IceCube**, M. G. Aartsen *et. al.*, *The IceCube Neutrino Observatory - Contributions to ICRC 2015 Part IV: Searches for Dark Matter and Exotic Particles*, arXiv:1510.05226.

[170] **Super-Kamiokande**, K. Choi *et. al.*, *Search for neutrinos from annihilation of captured low-mass dark matter particles in the Sun by Super-Kamiokande*, *Phys. Rev. Lett.* **114** (2015), no. 14 141301, [arXiv:1503.04858].

[171] **Baikal**, A. D. Avrorin *et. al.*, *Search for neutrino emission from relic dark matter in the Sun with the Baikal NT200 detector*, *Astropart. Phys.* **62** (2014) 12–20, [arXiv:1405.3551].

[172] M. M. Boliev, S. V. Demidov, S. P. Mikheyev, and O. V. Suvorova, *Search for muon signal from dark matter annihilations inthe Sun with the Baksan Underground Scintillator Telescope for 24.12 years*, *JCAP* **1309** (2013) 019, [arXiv:1301.1138].

[173] A. Ibarra, D. Tran, and C. Weniger, *Indirect Searches for Decaying Dark Matter*, *Int. J. Mod. Phys.* **A28** (2013) 1330040, [arXiv:1307.6434].

[174] http://dpnc.unige.ch/dampe/. Accessed: 2016-04-12.

[175] W. Atwood *et. al.*, *The large area telescope on the fermi gamma-ray space telescope mission*, *The Astrophysical Journal* **697** (2009), no. 2 1071.

[176] https://www.mpi-hd.mpg.de/hfm/HESS/HESS.shtml. Accessed: 2016-04-03.

[177] https://magic.mpp.mpg.de/. Accessed: 2016-04-03.

[178] T. Bringmann and C. Weniger, *Gamma Ray Signals from Dark Matter: Concepts, Status and Prospects*, *Phys. Dark Univ.* **1** (2012) 194–217, [arXiv:1208.5481].

[179] H. Bloemen, *Diffuse galactic gamma-ray emission*, *Ann. Rev. Astron. Astrophys.* **27** (1989) 469–516.

[180] **Fermi-LAT**, M. Ackermann *et. al.*, *Searching for Dark Matter Annihilation from Milky Way Dwarf Spheroidal Galaxies with Six Years of Fermi Large Area Telescope Data*, *Phys. Rev. Lett.* **115** (2015), no. 23 231301, [arXiv:1503.02641].

[181] M. G. Walker, *Dark Matter in the Milky Way's Dwarf Spheroidal Satellites*, arXiv:1205.0311.

[182] G. Battaglia, A. Helmi, and M. Breddels, *Internal kinematics and dynamical models of dwarf spheroidal galaxies around the Milky Way*, *New Astron. Rev.* **57** (2013) 52–79, [arXiv:1305.5965].

[183] L. E. Strigari, *Galactic Searches for Dark Matter*, *Phys. Rept.* **531** (2013) 1–88, [arXiv:1211.7090].

[184] **HESS**, A. Abramowski *et. al.*, *Search for Dark Matter Annihilation Signals from the Fornax Galaxy Cluster with H.E.S.S*, *Astrophys. J.* **750** (2012) 123, [arXiv:1202.5494]. [Erratum: Astrophys. J.783,63(2014)].

[185] M. Ajello *et. al.*, *The Origin of the Extragalactic Gamma-Ray Background and Implications for Dark-Matter Annihilation*, *Astrophys. J.* **800** (2015), no. 2 L27, [arXiv:1501.05301].

[186] **Fermi-LAT**, S. Zimmer, *Galaxy Clusters with the Fermi-LAT: Status and Implications for Cosmic Rays and Dark Matter Physics*, in *Fifth International Fermi Symposium Nagoya, Japan, October 20-24, 2014*, vol. C141020.1, 2015. arXiv:1502.02653.

[187] L. Goodenough and D. Hooper, *Possible Evidence For Dark Matter Annihilation In The Inner Milky Way From The Fermi Gamma Ray Space Telescope*, arXiv:0910.2998.

[188] D. Hooper and L. Goodenough, *Dark Matter Annihilation in The Galactic Center As Seen by the Fermi Gamma Ray Space Telescope*, *Phys. Lett.* **B697** (2011) 412–428, [arXiv:1010.2752].

[189] D. Hooper and T. Linden, *On The Origin Of The Gamma Rays From The Galactic Center*, *Phys. Rev.* **D84** (2011) 123005, [arXiv:1110.0006].

[190] K. N. Abazajian and M. Kaplinghat, *Detection of a Gamma-Ray Source in the Galactic Center Consistent with Extended Emission from Dark Matter Annihilation and Concentrated Astrophysical Emission*, *Phys. Rev.* **D86** (2012) 083511, [arXiv:1207.6047]. [Erratum: Phys. Rev.D87,129902(2013)].

[191] T. Daylan, D. P. Finkbeiner, D. Hooper, T. Linden, S. K. N. Portillo, N. L. Rodd, and T. R. Slatyer, *The characterization of the gamma-ray signal from the central Milky Way: A case for annihilating dark matter*, *Phys. Dark Univ.* **12** (2016) 1–23, [arXiv:1402.6703].

[192] F. Calore, I. Cholis, and C. Weniger, *Background model systematics for the Fermi GeV excess*, *JCAP* **1503** (2015) 038, [arXiv:1409.0042].

[193] F. Calore, I. Cholis, C. McCabe, and C. Weniger, *A Tale of Tails: Dark Matter Interpretations of the Fermi GeV Excess in Light of Background Model Systematics*, *Phys. Rev.* **D91** (2015), no. 6 063003, [arXiv:1411.4647].

[194] E. Carlson and S. Profumo, *Cosmic Ray Protons in the Inner Galaxy and the Galactic Center Gamma-Ray Excess*, *Phys. Rev.* **D90** (2014), no. 2 023015, [arXiv:1405.7685].

[195] J. Petrovic, P. D. Serpico, and G. Zaharijas, *Galactic Center gamma-ray "excess" from an active past of the Galactic Centre?*, *JCAP* **1410** (2014), no. 10 052, [arXiv:1405.7928].

[196] I. Cholis, C. Evoli, F. Calore, T. Linden, C. Weniger, and D. Hooper, *The Galactic Center GeV Excess from a Series of Leptonic Cosmic-Ray Outbursts*, *JCAP* **1512** (2015), no. 12 005, [arXiv:1506.05119].

[197] C. Gordon and O. Macias, *Dark Matter and Pulsar Model Constraints from Galactic Center Fermi-LAT Gamma Ray Observations*, *Phys. Rev.* **D88** (2013), no. 8 083521, [arXiv:1306.5725]. [Erratum: Phys. Rev.D89,no.4,049901(2014)].

[198] K. N. Abazajian, N. Canac, S. Horiuchi, and M. Kaplinghat, *Astrophysical and Dark Matter Interpretations of Extended Gamma-Ray Emission from the Galactic Center*, *Phys. Rev.* **D90** (2014), no. 2 023526, [arXiv:1402.4090].

[199] R. Bartels, S. Krishnamurthy, and C. Weniger, *Strong support for the millisecond pulsar origin of the Galactic center GeV excess*, *Phys. Rev. Lett.* **116** (2016), no. 5 051102, [arXiv:1506.05104].

[200] S. K. Lee, M. Lisanti, B. R. Safdi, T. R. Slatyer, and W. Xue, *Evidence for Unresolved γ-Ray Point Sources in the Inner Galaxy*, *Phys. Rev. Lett.* **116** (2016), no. 5 051103, [arXiv:1506.05124].

[201] M. Srednicki, S. Theisen, and J. Silk, *Cosmic Quarkonium: A Probe of Dark Matter*, *Phys. Rev. Lett.* **56** (1986) 263. [Erratum: Phys. Rev. Lett.56,1883(1986)].

[202] S. Rudaz, *Cosmic Production of Quarkonium?*, *Phys. Rev. Lett.* **56** (1986) 2128.

[203] L. Bergstrom and H. Snellman, *Observable Monochromatic Photons From Cosmic Photino Annihilation*, *Phys. Rev.* **D37** (1988) 3737–3741.

[204] L. Bergstrom, *Radiative Processes in Dark Matter Photino Annihilation*, *Phys. Lett.* **B225** (1989) 372.

[205] R. Flores, K. A. Olive, and S. Rudaz, *Radiative Processes in Lsp Annihilation*, *Phys. Lett.* **B232** (1989) 377–382.

[206] T. Bringmann, L. Bergstrom, and J. Edsjo, *New Gamma-Ray Contributions to Supersymmetric Dark Matter Annihilation*, *JHEP* **01** (2008) 049, [arXiv:0710.3169].

[207] A. Ibarra, S. Lopez Gehler, and M. Pato, *Dark matter constraints from box-shaped gamma-ray features*, *JCAP* **1207** (2012) 043, [arXiv:1205.0007].

[208] A. Ibarra, S. Lopez-Gehler, E. Molinaro, and M. Pato, *Gamma-ray triangles: a possible signature of asymmetric dark matter in indirect searches*, arXiv:1604.01899.

[209] C. Garcia-Cely and J. Heeck, *Polynomial spectral features from dark matter and connection to the diphoton resonance*, arXiv:1605.08049.

[210] **Fermi-LAT**, M. Ackermann *et. al.*, *Updated search for spectral lines from Galactic dark matter interactions with pass 8 data from the Fermi Large Area Telescope*, *Phys. Rev.* **D91** (2015), no. 12 122002, [arXiv:1506.00013].

[211] **HESS**, A. Abramowski *et. al.*, *Search for Photon-Linelike Signatures from Dark Matter Annihilations with H.E.S.S.*, *Phys. Rev. Lett.* **110** (2013) 041301, [arXiv:1301.1173].

[212] B. Anderson, S. Zimmer, J. Conrad, M. Gustafsson, M. SÃ¡nchez-Conde, and R. Caputo, *Search for Gamma-Ray Lines towards Galaxy Clusters with the Fermi-LAT*, *JCAP* **1602** (2016), no. 02 026, [arXiv:1511.00014].

[213] J. Aleksic *et. al.*, *Optimized dark matter searches in deep observations of Segue 1 with MAGIC*, *JCAP* **1402** (2014) 008, [arXiv:1312.1535].

[214] A. Geringer-Sameth and S. M. Koushiappas, *Dark matter line search using a joint analysis of dwarf galaxies with the Fermi Gamma-ray Space Telescope*, *Phys. Rev.* **D86** (2012) 021302, [arXiv:1206.0796].

[215] T. Bringmann, X. Huang, A. Ibarra, S. Vogl, and C. Weniger, *Fermi LAT Search for Internal Bremsstrahlung Signatures from Dark Matter Annihilation*, *JCAP* **1207** (2012) 054, [arXiv:1203.1312].

[216] C. Weniger, *A Tentative Gamma-Ray Line from Dark Matter Annihilation at the Fermi Large Area Telescope*, *JCAP* **1208** (2012) 007, [arXiv:1204.2797].

[217] U. Giaccari *et. al.*, *Anisotropy studies in the cosmic ray proton flux with the PAMELA experiment*, *Nucl. Phys. Proc. Suppl.* **239-240** (2013) 123–128.

[218] **AMS**, M. Aguilar *et. al.*, *First Result from the Alpha Magnetic Spectrometer on the International Space Station: Precision Measurement of the Positron Fraction in Primary Cosmic Rays of 0.5-350 GeV*, *Phys. Rev. Lett.* **110** (2013) 141102.

[219] **PAMELA**, O. Adriani *et. al.*, *PAMELA results on the cosmic-ray antiproton flux from 60 MeV to 180 GeV in kinetic energy*, *Phys. Rev. Lett.* **105** (2010) 121101, [arXiv:1007.0821].

[220] O. Adriani *et. al.*, *Measurement of the flux of primary cosmic ray antiprotons with energies of 60-MeV to 350-GeV in the PAMELA experiment*, *JETP Lett.* **96** (2013) 621–627. [Pisma Zh. Eksp. Teor. Fiz.96,693(2012)].

[221] **PAMELA**, O. Adriani *et. al.*, *An anomalous positron abundance in cosmic rays with energies 1.5-100 GeV*, *Nature* **458** (2009) 607–609, [arXiv:0810.4995].

[222] **PAMELA**, O. Adriani *et. al.*, *Cosmic-Ray Positron Energy Spectrum Measured by PAMELA*, *Phys. Rev. Lett.* **111** (2013) 081102, [arXiv:1308.0133].

[223] A. Kounine, Talk at the "AMS Days at CERN", 2015. http://indico.cern.ch/event/381134. Accessed: 2016-04-08.

[224] **AMS**, L. Accardo *et. al.*, *High Statistics Measurement of the Positron Fraction in Primary Cosmic Rays of 0.5-500 GeV with the Alpha Magnetic Spectrometer on the International Space Station*, *Phys. Rev. Lett.* **113** (2014) 121101.

[225] **AMS**, M. Aguilar *et. al.*, *Electron and Positron Fluxes in Primary Cosmic Rays Measured with the Alpha Magnetic Spectrometer on the International Space Station*, *Phys. Rev. Lett.* **113** (2014) 121102.

[226] R. Kappl, A. Reinert, and M. W. Winkler, *AMS-02 Antiprotons Reloaded*, *JCAP* **1510** (2015), no. 10 034, [arXiv:1506.04145].

[227] http://physics.aps.org/articles/v6/40. Accessed: 2016-04-06.

[228] T. Delahaye, J. Lavalle, R. Lineros, F. Donato, and N. Fornengo, *Galactic electrons and positrons at the Earth:new estimate of the primary and secondary fluxes*, *Astron. Astrophys.* **524** (2010) A51, [arXiv:1002.1910].

[229] V. S. Berezinskii, S. V. Bulanov, V. A. Dogiel, and V. S. Ptuskin, *Astrophysics of cosmic rays*. 1990.

[230] D. Maurin, F. Donato, R. Taillet, and P. Salati, *Cosmic rays below z=30 in a diffusion model: new constraints on propagation parameters*, *Astrophys. J.* **555** (2001) 585–596, [astro-ph/0101231].

[231] A. Oliva, Talk at the "AMS Days at CERN", 2015. http://indico.cern.ch/event/381134. Accessed: 2016-04-08.

[232] N. Fornengo, L. Maccione, and A. Vittino, *Constraints on particle dark matter from cosmic-ray antiprotons*, *JCAP* **1404** (2014), no. 04 003, [arXiv:1312.3579].

[233] G. Giesen, M. Boudaud, Y. Genolini, V. Poulin, M. Cirelli, P. Salati, and P. D. Serpico, *AMS-02 antiprotons, at last! Secondary astrophysical component and immediate implications for Dark Matter*, *JCAP* **1509** (2015), no. 09 023, [arXiv:1504.04276].

[234] F. Donato, N. Fornengo, D. Maurin, and P. Salati, *Antiprotons in cosmic rays from neutralino annihilation*, *Phys. Rev.* **D69** (2004) 063501, [astro-ph/0306207].

[235] T. Bringmann, F. Donato, and R. A. Lineros, *Radio data and synchrotron emission in consistent cosmic ray models*, *JCAP* **1201** (2012) 049, [arXiv:1106.4821].

[236] J. Lavalle, D. Maurin, and A. Putze, *Direct constraints on diffusion models from cosmic-ray positron data: Excluding the minimal model for dark matter searches*, *Phys. Rev.* **D90** (2014) 081301, [arXiv:1407.2540].

[237] **Fermi-LAT**, M. Ackermann *et. al.*, *Measurement of separate cosmic-ray electron and positron spectra with the Fermi Large Area Telescope*, *Phys. Rev. Lett.* **108** (2012) 011103, [arXiv:1109.0521].

[238] M. Cirelli, M. Kadastik, M. Raidal, and A. Strumia, *Model-independent implications of the e+-, anti-proton cosmic ray spectra on properties of Dark Matter*, *Nucl. Phys.* **B813** (2009) 1–21, [arXiv:0809.2409]. [Addendum: Nucl. Phys.B873,530(2013)].

[239] A. Ibarra, D. Tran, and C. Weniger, *Decaying Dark Matter in Light of the PAMELA and Fermi LAT Data*, *JCAP* **1001** (2010) 009, [arXiv:0906.1571].

[240] M. Cirelli, *Status of Indirect (and Direct) Dark Matter searches*, arXiv:1511.02031.

[241] T. R. Slatyer, *Indirect dark matter signatures in the cosmic dark ages. I. Generalizing the bound on s-wave dark matter annihilation from Planck results*, *Phys. Rev.* **D93** (2016), no. 2 023527, [arXiv:1506.03811].

[242] M. Di Mauro, F. Donato, N. Fornengo, R. Lineros, and A. Vittino, *Interpretation of AMS-02 electrons and positrons data*, *JCAP* **1404** (2014) 006, [arXiv:1402.0321].

[243] L. Bergstrom, T. Bringmann, I. Cholis, D. Hooper, and C. Weniger, *New limits on dark matter annihilation from AMS cosmic ray positron data*, *Phys. Rev. Lett.* **111** (2013) 171101, [arXiv:1306.3983].

[244] A. Ibarra, A. S. Lamperstorfer, and J. Silk, *Dark matter annihilations and decays after the AMS-02 positron measurements*, *Phys. Rev.* **D89** (2014), no. 6 063539, [arXiv:1309.2570].

[245] F. Donato, N. Fornengo, and P. Salati, *Anti-deuterons as a signature of supersymmetric dark matter*, *Phys. Rev.* **D62** (2000) 043003, [hep-ph/9904481].

[246] E. Carlson, A. Coogan, T. Linden, S. Profumo, A. Ibarra, and S. Wild, *Antihelium from Dark Matter*, *Phys. Rev.* **D89** (2014), no. 7 076005, [arXiv:1401.2461].

[247] M. Cirelli, N. Fornengo, M. Taoso, and A. Vittino, *Anti-helium from Dark Matter annihilations*, *JHEP* **08** (2014) 009, [arXiv:1401.4017].

[248] A. Ibarra and S. Wild, *Prospects of antideuteron detection from dark matter annihilations or decays at AMS-02 and GAPS*, *JCAP* **1302** (2013) 021, [arXiv:1209.5539].

[249] N. Fornengo, L. Maccione, and A. Vittino, *Dark matter searches with cosmic antideuterons: status and perspectives*, *JCAP* **1309** (2013) 031, [arXiv:1306.4171].

[250] T. Aramaki, C. J. Hailey, S. E. Boggs, P. von Doetinchem, H. Fuke, S. I. Mognet, R. A. Ong, K. Perez, and J. Zweerink, *Antideuteron Sensitivity for the GAPS Experiment*, *Astropart. Phys.* **74** (2016) 6–13, [arXiv:1506.02513].

[251] T. Aramaki *et. al.*, *Review of the theoretical and experimental status of dark matter identification with cosmic-ray antideuterons*, *Phys. Rept.* **618** (2016) 1–37, [arXiv:1505.07785].

[252] A. Birkedal, K. Matchev, and M. Perelstein, *Dark matter at colliders: A Model independent approach*, *Phys. Rev.* **D70** (2004) 077701, [hep-ph/0403004].

[253] E. A. Bagnaschi *et. al.*, *Supersymmetric Dark Matter after LHC Run 1*, *Eur. Phys. J.* **C75** (2015) 500, [arXiv:1508.01173].

[254] J. Goodman, M. Ibe, A. Rajaraman, W. Shepherd, T. M. P. Tait, and H.-B. Yu, *Constraints on Light Majorana dark Matter from Colliders*, *Phys. Lett.* **B695** (2011) 185–188, [arXiv:1005.1286].

[255] **CMS**, V. Khachatryan *et. al.*, *Search for dark matter, extra dimensions, and unparticles in monojet events in proton-proton collisions at sqrt(s) = 8 TeV*, *Eur. Phys. J.* **C75** (2015), no. 5 235, [arXiv:1408.3583].

[256] **ATLAS**, G. Aad *et. al.*, *Search for new phenomena in final states with an energetic jet and large missing transverse momentum in pp collisions at $\sqrt{s}$ =8 TeV with the ATLAS detector*, *Eur. Phys. J.* **C75** (2015), no. 7 299, [arXiv:1502.01518]. [Erratum: Eur. Phys. J.C75,no.9,408(2015)].

[257] G. Busoni, A. De Simone, E. Morgante, and A. Riotto, *On the Validity of the Effective Field Theory for Dark Matter Searches at the LHC*, *Phys. Lett.* **B728** (2014) 412–421, [arXiv:1307.2253].

[258] O. Buchmueller, M. J. Dolan, and C. McCabe, *Beyond Effective Field Theory for Dark Matter Searches at the LHC*, *JHEP* **01** (2014) 025, [arXiv:1308.6799].

[259] J. Abdallah *et. al.*, *Simplified Models for Dark Matter and Missing Energy Searches at the LHC*, arXiv:1409.2893.

[260] D. Abercrombie *et. al.*, *Dark Matter Benchmark Models for Early LHC Run-2 Searches: Report of the ATLAS/CMS Dark Matter Forum*, arXiv:1507.00966.

[261] J. Abdallah *et. al.*, *Simplified Models for Dark Matter Searches at the LHC*, *Phys. Dark Univ.* **9-10** (2015) 8–23, [arXiv:1506.03116].

[262] P. Agrawal, S. Blanchet, Z. Chacko, and C. Kilic, *Flavored Dark Matter, and Its Implications for Direct Detection and Colliders*, *Phys. Rev.* **D86** (2012) 055002, [arXiv:1109.3516].

[263] Y. Bai and J. Berger, *Fermion Portal Dark Matter*, *JHEP* **11** (2013) 171, [arXiv:1308.0612].

[264] Y. Bai and J. Berger, *Lepton Portal Dark Matter*, *JHEP* **08** (2014) 153, [arXiv:1402.6696].

[265] S. Chang, R. Edezhath, J. Hutchinson, and M. Luty, *Leptophilic Effective WIMPs*, *Phys. Rev.* **D90** (2014), no. 1 015011, [arXiv:1402.7358].

[266] P. Agrawal, Z. Chacko, and C. B. Verhaaren, *Leptophilic Dark Matter and the Anomalous Magnetic Moment of the Muon*, *JHEP* **08** (2014) 147, [arXiv:1402.7369].

[267] P. Agrawal, B. Batell, D. Hooper, and T. Lin, *Flavored Dark Matter and the Galactic Center Gamma-Ray Excess*, *Phys. Rev.* **D90** (2014), no. 6 063512, [arXiv:1404.1373].

[268] J. Kopp, L. Michaels, and J. Smirnov, *Loopy Constraints on Leptophilic Dark Matter and Internal Bremsstrahlung*, *JCAP* **1404** (2014) 022, [arXiv:1401.6457].

[269] Z.-H. Yu, X.-J. Bi, Q.-S. Yan, and P.-F. Yin, *Tau Portal Dark Matter models at the LHC*, *Phys. Rev.* **D91** (2015), no. 3 035008, [arXiv:1410.3347].

[270] A. DiFranzo, K. I. Nagao, A. Rajaraman, and T. M. P. Tait, *Simplified Models for Dark Matter Interacting with Quarks*, *JHEP* **11** (2013) 014, [arXiv:1308.2679]. [Erratum: JHEP01,162(2014)].

[271] M. Drees and M. Nojiri, *Neutralino - nucleon scattering revisited*, *Phys. Rev.* **D48** (1993) 3483–3501, [hep-ph/9307208].

[272] J. Hisano, K. Ishiwata, and N. Nagata, *Gluon contribution to the dark matter direct detection*, *Phys. Rev.* **D82** (2010) 115007, [arXiv:1007.2601].

[273] P. Gondolo and S. Scopel, *On the sbottom resonance in dark matter scattering*, *JCAP* **1310** (2013) 032, [arXiv:1307.4481].

[274] A. Alloul, N. D. Christensen, C. Degrande, C. Duhr, and B. Fuks, *FeynRules 2.0 - A complete toolbox for tree-level phenomenology*, *Comput. Phys. Commun.* **185** (2014) 2250–2300, [arXiv:1310.1921].

[275] A. Belyaev, N. D. Christensen, and A. Pukhov, *CalcHEP 3.4 for collider physics within and beyond the Standard Model*, *Comput. Phys. Commun.* **184** (2013) 1729–1769, [arXiv:1207.6082].

[276] J. R. Ellis, K. A. Olive, and C. Savage, *Hadronic Uncertainties in the Elastic Scattering of Supersymmetric Dark Matter*, *Phys. Rev.* **D77** (2008) 065026, [arXiv:0801.3656].

[277] R. Mertig, M. Bohm, and A. Denner, *FEYN CALC: Computer algebraic calculation of Feynman amplitudes*, *Comput. Phys. Commun.* **64** (1991) 345–359.

[278] J. M. Alarcon, L. S. Geng, J. Martin Camalich, and J. A. Oller, *The strangeness content of the nucleon from effective field theory and phenomenology*, *Phys. Lett.* **B730** (2014) 342–346, [arXiv:1209.2870].

[279] M. M. Pavan, I. I. Strakovsky, R. L. Workman, and R. A. Arndt, *The Pion nucleon Sigma term is definitely large: Results from a G.W.U. analysis of pi nucleon scattering data*, *PiN Newslett.* **16** (2002) 110–115, [hep-ph/0111066].

[280] L. Alvarez-Ruso, T. Ledwig, J. Martin Camalich, and M. J. Vicente-Vacas, *Nucleon mass and pion-nucleon sigma term from a chiral analysis of lattice QCD data*, *Phys. Rev.* **D88** (2013), no. 5 054507, [arXiv:1304.0483].

[281] M. A. Shifman, A. I. Vainshtein, and V. I. Zakharov, *Remarks on Higgs Boson Interactions with Nucleons*, *Phys. Lett.* **B78** (1978) 443.

[282] J. M. Cline, K. Kainulainen, P. Scott, and C. Weniger, *Update on scalar singlet dark matter*, *Phys. Rev.* **D88** (2013) 055025, [arXiv:1306.4710]. [Erratum: Phys. Rev.D92,no.3,039906(2015)].

[283] M. E. Peskin and D. V. Schroeder, *An Introduction to quantum field theory*. 1995.

[284] T. Banks, J.-F. Fortin, and S. Thomas, *Direct Detection of Dark Matter Electromagnetic Dipole Moments*, arXiv:1007.5515.

[285] A. Beniwal, F. Rajec, C. Savage, P. Scott, C. Weniger, M. White, and A. G. Williams, *Combined analysis of effective Higgs portal dark matter models*, arXiv:1512.06458.

[286] A. Kumar and S. Tulin, *Top-flavored dark matter and the forward-backward asymmetry*, *Phys. Rev.* **D87** (2013), no. 9 095006, [arXiv:1303.0332].

[287] **CMS**, S. Chatrchyan *et. al.*, *Search for new physics in the multijet and missing transverse momentum final state in proton-proton collisions at $\sqrt{s}$= 8 TeV*, *JHEP* **06** (2014) 055, [arXiv:1402.4770].

[288] **ATLAS**, G. Aad *et. al.*, *Search for squarks and gluinos with the ATLAS detector in final states with jets and missing transverse momentum using $\sqrt{s} = 8$ TeV proton–proton collision data*, *JHEP* **09** (2014) 176, [arXiv:1405.7875].

[289] **ATLAS**, G. Aad *et. al.*, *Search for direct production of charginos, neutralinos and sleptons in final states with two leptons and missing transverse momentum in pp collisions at $\sqrt{s} = 8$ TeV with the ATLAS detector*, *JHEP* **05** (2014) 071, [arXiv:1403.5294].

[290] **CMS**, V. Khachatryan *et. al.*, *Searches for electroweak production of charginos, neutralinos, and sleptons decaying to leptons and W, Z, and Higgs bosons in pp collisions at 8 TeV*, *Eur. Phys. J.* **C74** (2014), no. 9 3036, [arXiv:1405.7570].

[291] **ATLAS**, G. Aad *et. al.*, *Search for new phenomena in events with a photon and missing transverse momentum in pp collisions at $\sqrt{s} = 8$ TeV with the ATLAS detector*, *Phys. Rev.* **D91** (2015), no. 1 012008, [arXiv:1411.1559]. [Erratum: Phys. Rev.D92,no.5,059903(2015)].

[292] **ATLAS**, G. Aad *et. al.*, *Search for pair-produced third-generation squarks decaying via charm quarks or in compressed supersymmetric scenarios in pp collisions at $\sqrt{s} = 8$ TeV with the ATLAS detector*, *Phys. Rev.* **D90** (2014), no. 5 052008, [arXiv:1407.0608].

[293] **ATLAS**, *Search for New Phenomena in Monojet plus Missing Transverse Momentum Final States using 10fb-1 of pp Collisions at sqrts=8 TeV with the ATLAS detector at the LHC*, .

[294] **SLD Electroweak Group, DELPHI, ALEPH, SLD, SLD Heavy Flavour Group, OPAL, LEP Electroweak Working Group, L3**, S. Schael *et. al.*, *Precision electroweak measurements on the Z resonance*, *Phys. Rept.* **427** (2006) 257–454, [hep-ex/0509008].

[295] http://lepsusy.web.cern.ch/lepsusy/www/sleptons_summer04/slep_final.html.

[296] M. Garny, A. Ibarra, and S. Vogl, *Signatures of Majorana dark matter with t-channel mediators*, arXiv:1503.01500.

[297] G. Bertone, C. Jackson, G. Shaughnessy, T. M. Tait, and A. Vallinotto, *The WIMP Forest: Indirect Detection of a Chiral Square*, *Phys.Rev.* **D80** (2009) 023512, [arXiv:0904.1442].

[298] V. Silveira and A. Zee, *Scalar Phantoms*, *Phys.Lett.* **B161** (1985) 136.

[299] J. McDonald, *Gauge singlet scalars as cold dark matter*, *Phys.Rev.* **D50** (1994) 3637–3649, [hep-ph/0702143].

[300] C. Burgess, M. Pospelov, and T. ter Veldhuis, *The Minimal model of nonbaryonic dark matter: A Singlet scalar*, *Nucl.Phys.* **B619** (2001) 709–728, [hep-ph/0011335].

[301] B. Patt and F. Wilczek, *Higgs-field portal into hidden sectors*, hep-ph/0605188.

[302] A. Goudelis, Y. Mambrini, and C. Yaguna, *Antimatter signals of singlet scalar dark matter*, *JCAP* **0912** (2009) 008, [arXiv:0909.2799].

[303] C. E. Yaguna, *Gamma rays from the annihilation of singlet scalar dark matter*, *JCAP* **0903** (2009) 003, [arXiv:0810.4267].

[304] M. Gonderinger, Y. Li, H. Patel, and M. J. Ramsey-Musolf, *Vacuum Stability, Perturbativity, and Scalar Singlet Dark Matter*, *JHEP* **01** (2010) 053, [arXiv:0910.3167].

[305] S. Profumo, L. Ubaldi, and C. Wainwright, *Singlet Scalar Dark Matter: monochromatic gamma rays and metastable vacua*, *Phys. Rev.* **D82** (2010) 123514, [arXiv:1009.5377].

[306] A. Djouadi, O. Lebedev, Y. Mambrini, and J. Quevillon, *Implications of LHC searches for Higgs–portal dark matter*, *Phys. Lett.* **B709** (2012) 65–69, [arXiv:1112.3299].

[307] M. Duerr, P. Fileviez Perez, and J. Smirnov, *Scalar Dark Matter: Direct vs. Indirect Detection*, arXiv:1509.04282.

[308] C. Boehm and P. Fayet, *Scalar dark matter candidates*, *Nucl. Phys.* **B683** (2004) 219–263, [hep-ph/0305261].

[309] D. A. Vasquez, C. Boehm, and J. Idarraga, *Signature of Sub GeV Dark Matter particles at LHC and TEVATRON*, *Phys. Rev.* **D83** (2011) 115017, [arXiv:0912.5373].

[310] P. Fileviez Perez and M. B. Wise, *Baryon Asymmetry and Dark Matter Through the Vector-Like Portal*, *JHEP* **1305** (2013) 094, [arXiv:1303.1452].

[311] T. Toma, *Internal Bremsstrahlung Signature of Real Scalar Dark Matter and Consistency with Thermal Relic Density*, *Phys.Rev.Lett.* **111** (2013) 091301, [arXiv:1307.6181].

[312] F. Giacchino, L. Lopez-Honorez, and M. H. G. Tytgat, *Bremsstrahlung and Gamma Ray Lines in 3 Scenarios of Dark Matter Annihilation*, *JCAP* **1408** (2014) 046, [arXiv:1405.6921].

[313] J. Kumar and D. Marfatia, *Matrix element analyses of dark matter scattering and annihilation*, *Phys. Rev.* **D88** (2013), no. 1 014035, [arXiv:1305.1611].

[314] F. Luo and T. You, *Enhancement of Majorana Dark Matter Annihilation Through Higgs Bremsstrahlung*, *JCAP* **1312** (2013) 024, [arXiv:1310.5129].

[315] Sommerfeld, A. (1931). Über die Beugung und Bremsung der Elektronen. Ann. Phys., 403: 257-330. doi: 10.1002/andp.19314030302.

[316] A. De Simone, G. F. Giudice, and A. Strumia, *Benchmarks for Dark Matter Searches at the LHC*, *JHEP* **06** (2014) 081, [arXiv:1402.6287].

[317] S. Cassel, *Sommerfeld factor for arbitrary partial wave processes*, *J. Phys.* **G37** (2010) 105009, [arXiv:0903.5307].

[318] R. Iengo, *Sommerfeld enhancement: General results from field theory diagrams*, *JHEP* **05** (2009) 024, [arXiv:0902.0688].

[319] X. Chu, T. Hambye, T. Scarna, and M. H. G. Tytgat, *What if Dark Matter Gamma-Ray Lines come with Gluon Lines?*, *Phys. Rev.* **D86** (2012) 083521, [arXiv:1206.2279].

[320] A. M. Galper *et. al.*, *Status of the GAMMA-400 Project*, *Adv. Space Res.* **51** (2013) 297–300, [arXiv:1201.2490].

[321] M. Garny, A. Ibarra, M. Pato, and S. Vogl, *Internal bremsstrahlung signatures in light of direct dark matter searches*, *JCAP* **1312** (2013) 046, [arXiv:1306.6342].

[322] **Fermi-LAT**, M. Ackermann *et. al.*, *Search for gamma-ray spectral lines with the Fermi large area telescope and dark matter implications*, *Phys. Rev.* **D88** (2013) 082002, [arXiv:1305.5597].

[323] K. Bernlohr *et. al.*, *Monte Carlo design studies for the Cherenkov Telescope Array*, *Astropart. Phys.* **43** (2013) 171–188, [arXiv:1210.3503].

[324] J. Kopp, V. Niro, T. Schwetz, and J. Zupan, *DAMA/LIBRA and leptonically interacting Dark Matter*, *Phys. Rev.* **D80** (2009) 083502, [arXiv:0907.3159].

[325] **XENON1T**, E. Aprile, *The XENON1T Dark Matter Search Experiment*, *Springer Proc. Phys.* **148** (2013) 93–96, [arXiv:1206.6288].

[326] M. Kachelriess, P. D. Serpico, and M. A. Solberg, *On the role of electroweak bremsstrahlung for indirect dark matter signatures*, *Phys. Rev.* **D80** (2009) 123533, [arXiv:0911.0001].

[327] P. Ciafaloni, M. Cirelli, D. Comelli, A. De Simone, A. Riotto, and A. Urbano, *On the Importance of Electroweak Corrections for Majorana Dark Matter Indirect Detection*, *JCAP* **1106** (2011) 018, [arXiv:1104.2996].

[328] M. Garny, A. Ibarra, and S. Vogl, *Antiproton constraints on dark matter annihilations from internal electroweak bremsstrahlung*, *JCAP* **1107** (2011) 028, [arXiv:1105.5367].

[329] M. Garny, A. Ibarra, and S. Vogl, *Dark matter annihilations into two light fermions and one gauge boson: General analysis and antiproton constraints*, *JCAP* **1204** (2012) 033, [arXiv:1112.5155].

[330] A. Pukhov, E. Boos, M. Dubinin, V. Edneral, V. Ilyin, D. Kovalenko, A. Kryukov, V. Savrin, S. Shichanin, and A. Semenov, *CompHEP: A Package for evaluation of Feynman diagrams and integration over multiparticle phase space*, hep-ph/9908288.

[331] A. Pukhov, *CalcHEP 2.3: MSSM, structure functions, event generation, batchs, and generation of matrix elements for other packages*, hep-ph/0412191.

[332] L. J. Gleeson and W. I. Axford, *Solar Modulation of Galactic Cosmic Rays*, *Astrophys. J.* **154** (1968) 1011.

[333] T. Bringmann and P. Salati, *The galactic antiproton spectrum at high energies: Background expectation vs. exotic contributions*, *Phys. Rev.* **D75** (2007) 083006, [astro-ph/0612514].

[334] **Fermi-LAT**, M. Ackermann *et. al.*, *Dark matter constraints from observations of 25 Milky Way satellite galaxies with the Fermi Large Area Telescope*, *Phys. Rev.* **D89** (2014) 042001, [arXiv:1310.0828].

[335] **ATLAS**, T. A. collaboration, *Search for direct-slepton and direct-chargino production in final states with two opposite-sign leptons, missing transverse momentum and no jets in 20/fb of pp collisions at sqrt(s) = 8 TeV with the ATLAS detector*, .

[336] LEPSUSYWG, ALEPH, DELPHI, L3 and OPAL experiments, note LEPSUSYWG/04-01.1, http://lepsusy.web.cern.ch/lepsusy/Welcome.html. Accessed: 2016-04-19.

[337] J. Hisano, R. Nagai, and N. Nagata, *Effective Theories for Dark Matter Nucleon Scattering*, *JHEP* **05** (2015) 037, [arXiv:1502.02244].

[338] N. Kidonakis, *Next-to-next-to-leading soft-gluon corrections for the top quark cross section and transverse momentum distribution*, *Phys. Rev.* **D82** (2010) 114030, [arXiv:1009.4935].

[339] S. Chang, R. Edezhath, J. Hutchinson, and M. Luty, *Effective WIMPs*, *Phys. Rev.* **D89** (2014), no. 1 015011, [arXiv:1307.8120].

[340] **ATLAS**, T. A. collaboration, *Search for squarks and gluinos with the ATLAS detector in final states with jets and missing transverse momentum and 20.3 fb^{-1} of $\sqrt{s} = 8$ TeV proton-proton collision data*, .

[341] J. Alwall, R. Frederix, S. Frixione, V. Hirschi, F. Maltoni, O. Mattelaer, H. S. Shao, T. Stelzer, P. Torrielli, and M. Zaro, *The automated computation of tree-level and next-to-leading order differential cross sections, and their matching to parton shower simulations*, *JHEP* **07** (2014) 079, [arXiv:1405.0301].

[342] M. Drees, H. Dreiner, D. Schmeier, J. Tattersall, and J. S. Kim, *CheckMATE: Confronting your Favourite New Physics Model with LHC Data*, *Comput. Phys. Commun.* **187** (2014) 227–265, [arXiv:1312.2591].

[343] M. Asano, T. Bringmann, and C. Weniger, *Indirect dark matter searches as a probe of degenerate particle spectra*, *Phys. Lett.* **B709** (2012) 128–132, [arXiv:1112.5158].

[344] **OPAL**, G. Abbiendi *et. al.*, *Search for scalar top and scalar bottom quarks at LEP*, *Phys. Lett.* **B545** (2002) 272–284, [hep-ex/0209026]. [Erratum: Phys. Lett.B548,258(2002)].

[345] N. F. Bell, J. B. Dent, A. J. Galea, T. D. Jacques, L. M. Krauss, and T. J. Weiler, *W/Z Bremsstrahlung as the Dominant Annihilation Channel for Dark Matter, Revisited*, *Phys. Lett.* **B706** (2011) 6–12, [arXiv:1104.3823].

[346] N. F. Bell, J. B. Dent, T. D. Jacques, and T. J. Weiler, *Dark Matter Annihilation Signatures from Electroweak Bremsstrahlung*, *Phys. Rev.* **D84** (2011) 103517, [arXiv:1101.3357].

[347] M. Garny, A. Ibarra, M. Pato, and S. Vogl, *Closing in on mass-degenerate dark matter scenarios with antiprotons and direct detection*, *JCAP* **1211** (2012) 017, [arXiv:1207.1431].

[348] M. Garny, A. Ibarra, S. Rydbeck, and S. Vogl, *Majorana Dark Matter with a Coloured Mediator: Collider vs Direct and Indirect Searches*, *JHEP* **06** (2014) 169, [arXiv:1403.4634].

[349] **IceCube**, P. Scott *et. al.*, *Use of event-level neutrino telescope data in global fits for theories of new physics*, *JCAP* **1211** (2012) 057, [arXiv:1207.0810].

[350] M. Garny, A. Ibarra, M. Pato, and S. Vogl, *On the spin-dependent sensitivity of XENON100*, *Phys. Rev.* **D87** (2013), no. 5 056002, [arXiv:1211.4573].

[351] **CMS**, S. Chatrchyan *et. al.*, *Search for supersymmetry in hadronic final states with missing transverse energy using the variables α_T and b-quark multiplicity in pp collisions at $\sqrt{s} = 8$ TeV*, *Eur. Phys. J.* **C73** (2013), no. 9 2568, [arXiv:1303.2985].

[352] P. Ciafaloni, D. Comelli, A. Riotto, F. Sala, A. Strumia, and A. Urbano, *Weak Corrections are Relevant for Dark Matter Indirect Detection*, *JCAP* **1103** (2011) 019, [arXiv:1009.0224].

[353] M. Ciafaloni, P. Ciafaloni, and D. Comelli, *Towards collinear evolution equations in electroweak theory*, *Phys. Rev. Lett.* **88** (2002) 102001, [hep-ph/0111109].

[354] P. Ciafaloni and D. Comelli, *Electroweak evolution equations*, *JHEP* **11** (2005) 022, [hep-ph/0505047].

[355] G. Altarelli and G. Parisi, *Asymptotic Freedom in Parton Language*, *Nucl. Phys.* **B126** (1977) 298–318.

[356] J. R. Christiansen and T. Sjostrand, *Weak Gauge Boson Radiation in Parton Showers*, *JHEP* **04** (2014) 115, [arXiv:1401.5238].

[357] J.-Y. Chen, E. W. Kolb, and L.-T. Wang, *Dark matter coupling to electroweak gauge and Higgs bosons: an effective field theory approach*, *Phys. Dark Univ.* **2** (2013) 200–218, [arXiv:1305.0021].

[358] E. Fernandez-Martinez and R. Mahbubani, *The Gran Sasso muon puzzle*, *JCAP* **1207** (2012) 029, [arXiv:1204.5180].

[359] J. H. Davis, *Fitting the annual modulation in DAMA with neutrons from muons and neutrinos*, *Phys. Rev. Lett.* **113** (2014) 081302, [arXiv:1407.1052].

[360] R. Bernabei *et. al.*, *No role for neutrons, muons and solar neutrinos in the DAMA annual modulation results*, *Eur. Phys. J.* **C74** (2014), no. 12 3196, [arXiv:1409.3516].

[361] J. Klinger and V. A. Kudryavtsev, *Muon-induced neutrons do not explain the DAMA data*, *Phys. Rev. Lett.* **114** (2015), no. 15 151301, [arXiv:1503.07225].

[362] A. L. Fitzpatrick, W. Haxton, E. Katz, N. Lubbers, and Y. Xu, *The Effective Field Theory of Dark Matter Direct Detection*, *JCAP* **1302** (2013) 004, [arXiv:1203.3542].

[363] E. Del Nobile, G. B. Gelmini, A. Georgescu, and J.-H. Huh, *Reevaluation of spin-dependent WIMP-proton interactions as an explanation of the DAMA data*, *JCAP* **1508** (2015), no. 08 046, [arXiv:1502.07682].

[364] S. Scopel, K.-H. Yoon, and J.-H. Yoon, *Generalized spin-dependent WIMP-nucleus interactions and the DAMA modulation effect*, *JCAP* **1507** (2015), no. 07 041, [arXiv:1505.01926].

[365] C. Arina, E. Del Nobile, and P. Panci, *Dark Matter with Pseudoscalar-Mediated Interactions Explains the DAMA Signal and the Galactic Center Excess*, *Phys. Rev. Lett.* **114** (2015) 011301, [arXiv:1406.5542].

[366] M. J. Dolan, F. Kahlhoefer, C. McCabe, and K. Schmidt-Hoberg, *A taste of dark matter: Flavour constraints on pseudoscalar mediators*, *JHEP* **03** (2015) 171, [arXiv:1412.5174]. [Erratum: JHEP07,103(2015)].

[367] A. L. Fitzpatrick and K. M. Zurek, *Dark Moments and the DAMA-CoGeNT Puzzle*, *Phys. Rev.* **D82** (2010) 075004, [arXiv:1007.5325].

[368] N. Anand, A. L. Fitzpatrick, and W. C. Haxton, *Weakly interacting massive particle-nucleus elastic scattering response*, *Phys. Rev.* **C89** (2014), no. 6 065501, [arXiv:1308.6288].

[369] M. Cirelli, E. Del Nobile, and P. Panci, *Tools for model-independent bounds in direct dark matter searches*, *JCAP* **1310** (2013) 019, [arXiv:1307.5955].

[370] R. J. Hill and M. P. Solon, *WIMP-nucleon scattering with heavy WIMP effective theory*, *Phys.Rev.Lett.* **112** (2014) 211602, [arXiv:1309.4092].

[371] R. Catena and P. Gondolo, *Global fits of the dark matter-nucleon effective interactions*, *JCAP* **1409** (2014), no. 09 045, [arXiv:1405.2637].

[372] M. I. Gresham and K. M. Zurek, *Effect of nuclear response functions in dark matter direct detection*, *Phys. Rev.* **D89** (2014), no. 12 123521, [arXiv:1401.3739].

[373] R. Catena, *Analysis of the theoretical bias in dark matter direct detection*, *JCAP* **1409** (2014), no. 09 049, [arXiv:1407.0127].

[374] R. Catena, *Prospects for direct detection of dark matter in an effective theory approach*, *JCAP* **1407** (2014) 055, [arXiv:1406.0524].

[375] V. Gluscevic and A. H. G. Peter, *Understanding WIMP-baryon interactions with direct detection: A Roadmap*, *JCAP* **1409** (2014), no. 09 040, [arXiv:1406.7008].

[376] P. Panci, *New Directions in Direct Dark Matter Searches*, *Adv.High Energy Phys.* **2014** (2014) 681312, [arXiv:1402.1507].

[377] R. Catena and P. Gondolo, *Global limits and interference patterns in dark matter direct detection*, *JCAP* **1508** (2015), no. 08 022, [arXiv:1504.06554].

[378] V. Gluscevic, M. I. Gresham, S. D. McDermott, A. H. G. Peter, and K. M. Zurek, *Identifying the Theory of Dark Matter with Direct Detection*, arXiv:1506.04454.

[379] J. B. Dent, L. M. Krauss, J. L. Newstead, and S. Sabharwal, *General analysis of direct dark matter detection: From microphysics to observational signatures*, *Phys. Rev.* **D92** (2015), no. 6 063515, [arXiv:1505.03117].

[380] Z.-L. Liang and Y.-L. Wu, *Direct detection and solar capture of spin-dependent dark matter*, *Phys.Rev.* **D89** (2014), no. 1 013010, [arXiv:1308.5897].

[381] J. Blumenthal, P. Gretskov, M. Krämer, and C. Wiebusch, *Effective field theory interpretation of searches for dark matter annihilation in the Sun with the IceCube Neutrino Observatory*, *Phys.Rev.* **D91** (2015), no. 3 035002, [arXiv:1411.5917].

[382] R. Catena, *Dark matter signals at neutrino telescopes in effective theories*, *JCAP* **1504** (2015), no. 04 052, [arXiv:1503.04109].

[383] R. Catena, *Dark matter directional detection in non-relativistic effective theories*, *JCAP* **1507** (2015), no. 07 026, [arXiv:1505.06441].

[384] B. J. Kavanagh, *New directional signatures from the nonrelativistic effective field theory of dark matter*, *Phys. Rev.* **D92** (2015), no. 2 023513, [arXiv:1505.07406].

[385] I. Pólik and T. Terlaky, *A survey of the s-lemma*, *SIAM Rev.* **49** (July, 2007) 371–418.

[386] S. Boyd, L. El Ghaoui, E. Feron, and V. Balakrishnan, *Linear Matrix Inequalities in System and Control Theory*, vol. 15 of *Studies in Applied Mathematics*. SIAM, Philadelphia, PA, June, 1994.

[387] MATLAB, *version 8.3.0.532 (R2014a)*. The MathWorks Inc., Natick, Massachusetts, 2014.

[388] R. Bernabei *et. al.*, *New limits on WIMP search with large-mass low-radioactivity NaI(Tl) set-up at Gran Sasso*, *Phys. Lett.* **B389** (1996) 757–766.

[389] K. Fushimi, H. Ejiri, H. Kinoshita, N. Kudomi, K. Kume, K. Nagata, H. Ohsumi, K. Okada, H. Sano, and J. Tanaka, *Application of a large volume NaI scintillator to search for dark matter*, *Phys. Rev.* **C47** (1993) 425–428.

[390] J. Xu *et. al.*, *Scintillation Efficiency Measurement of Na Recoils in NaI(Tl) Below the DAMA/LIBRA Energy Threshold*, *Phys. Rev.* **C92** (2015), no. 1 015807, [arXiv:1503.07212].

[391] G. Barello, S. Chang, and C. A. Newby, *A Model Independent Approach to Inelastic Dark Matter Scattering*, *Phys. Rev.* **D90** (2014), no. 9 094027, [arXiv:1409.0536].

[392] M. Hoferichter, P. Klos, and A. Schwenk, *Chiral power counting of one- and two-body currents in direct detection of dark matter*, *Phys. Lett.* **B746** (2015) 410–416, [arXiv:1503.04811].

[393] J. AmarÃ© *et. al.*, *The ANAIS Dark Matter Project: Status and Prospects*, in *14th Marcel Grossmann Meeting on Recent Developments in Theoretical and Experimental General Relativity, Astrophysics, and Relativistic Field Theories (MG14) Rome, Italy, July 12-18, 2015*, 2016. arXiv:1601.01184.

[394] J. I. Read, G. Lake, O. Agertz, and V. P. Debattista, *Thin, thick and dark discs in LCDM*, *Mon. Not. Roy. Astron. Soc.* **389** (2008) 1041–1057, [arXiv:0803.2714].

[395] J. I. Read, L. Mayer, A. M. Brooks, F. Governato, and G. Lake, *A dark matter disc in three cosmological simulations of Milky Way mass galaxies*, *Mon. Not. Roy. Astron. Soc.* **397** (2009) 44, [arXiv:0902.0009].

[396] C. W. Purcell, J. S. Bullock, and M. Kaplinghat, *The Dark Disk of the Milky Way*, *Astrophys. J.* **703** (2009) 2275–2284, [arXiv:0906.5348].

[397] F. S. Ling, E. Nezri, E. Athanassoula, and R. Teyssier, *Dark Matter Direct Detection Signals inferred from a Cosmological N-body Simulation with Baryons*, *JCAP* **1002** (2010) 012, [arXiv:0909.2028].

[398] P. J. Fox, G. D. Kribs, and T. M. P. Tait, *Interpreting Dark Matter Direct Detection Independently of the Local Velocity and Density Distribution*, *Phys. Rev.* **D83** (2011) 034007, [arXiv:1011.1910].

[399] C. McCabe, *The Astrophysical Uncertainties Of Dark Matter Direct Detection Experiments*, *Phys. Rev.* **D82** (2010) 023530, [arXiv:1005.0579].

[400] C. McCabe, *DAMA and CoGeNT without astrophysical uncertainties*, *Phys. Rev.* **D84** (2011) 043525, [arXiv:1107.0741].

[401] J. Herrero-Garcia, T. Schwetz, and J. Zupan, *Astrophysics independent bounds on the annual modulation of dark matter signals*, *Phys. Rev. Lett.* **109** (2012) 141301, [arXiv:1205.0134].

[402] E. Del Nobile, G. Gelmini, P. Gondolo, and J.-H. Huh, *Generalized Halo Independent Comparison of Direct Dark Matter Detection Data*, *JCAP* **1310** (2013) 048, [arXiv:1306.5273].

[403] B. J. Kavanagh and A. M. Green, *Model independent determination of the dark matter mass from direct detection experiments*, *Phys. Rev. Lett.* **111** (2013), no. 3 031302, [arXiv:1303.6868].

[404] B. J. Kavanagh, *Parametrizing the local dark matter speed distribution: a detailed analysis*, *Phys. Rev.* **D89** (2014), no. 8 085026, [arXiv:1312.1852].

[405] P. J. Fox, Y. Kahn, and M. McCullough, *Taking Halo-Independent Dark Matter Methods Out of the Bin*, *JCAP* **1410** (2014), no. 10 076, [arXiv:1403.6830].

[406] B. Feldstein and F. Kahlhoefer, *A new halo-independent approach to dark matter direct detection analysis*, *JCAP* **1408** (2014) 065, [arXiv:1403.4606].

[407] B. Feldstein and F. Kahlhoefer, *Quantifying (dis)agreement between direct detection experiments in a halo-independent way*, *JCAP* **1412** (2014), no. 12 052, [arXiv:1409.5446].

[408] A. J. Anderson, P. J. Fox, Y. Kahn, and M. McCullough, *Halo-Independent Direct Detection Analyses Without Mass Assumptions*, *JCAP* **1510** (2015), no. 10 012, [arXiv:1504.03333].

[409] N. Bozorgnia and T. Schwetz, *What is the probability that direct detection experiments have observed Dark Matter?*, *JCAP* **1412** (2014), no. 12 015, [arXiv:1410.6160].

[410] B. J. Kavanagh, M. Fornasa, and A. M. Green, *Probing WIMP particle physics and astrophysics with direct detection and neutrino telescope data*, *Phys. Rev.* **D91** (2015), no. 10 103533, [arXiv:1410.8051].

[411] M. Blennow, J. Herrero-Garcia, and T. Schwetz, *A halo-independent lower bound on the dark matter capture rate in the Sun from a direct detection signal*, *JCAP* **1505** (2015), no. 05 036, [arXiv:1502.03342].

[412] WIMP Annihilations in the Sun : A search using first year of operation of the completed IceCube neutrino telescope. Talk by M. Rameez at Moriond 2015.

[413] http://www.picoexperiment.com/. Accessed: 2015-08-18.

[414] M. Pato, L. Baudis, G. Bertone, R. Ruiz de Austri, L. E. Strigari, and R. Trotta, *Complementarity of Dark Matter Direct Detection Targets*, *Phys. Rev.* **D83** (2011) 083505, [arXiv:1012.3458].

[415] M. Blennow, J. Herrero-Garcia, T. Schwetz, and S. Vogl, *Halo-independent tests of dark matter direct detection signals: local DM density, LHC, and thermal freeze-out*, *JCAP* **1508** (2015), no. 08 039, [arXiv:1505.05710].

[416] **XENON100**, E. Aprile *et. al.*, *Likelihood Approach to the First Dark Matter Results from XENON100*, *Phys. Rev.* **D84** (2011) 052003, [arXiv:1103.0303].

[417] **XENON100**, E. Aprile *et. al.*, *Dark Matter Results from 100 Live Days of XENON100 Data*, *Phys. Rev. Lett.* **107** (2011) 131302, [arXiv:1104.2549].

[418] T. Hahn and M. Perez-Victoria, *Automatized one loop calculations in four-dimensions and D-dimensions*, *Comput. Phys. Commun.* **118** (1999) 153–165, [hep-ph/9807565].

[419] G. Passarino and M. J. G. Veltman, *One Loop Corrections for e+ e- Annihilation Into mu+ mu- in the Weinberg Model*, *Nucl. Phys.* **B160** (1979) 151.

[420] S. Tulin, H.-B. Yu, and K. M. Zurek, *Three Exceptions for Thermal Dark Matter with Enhanced Annihilation to $\gamma\gamma$*, *Phys. Rev.* **D87** (2013), no. 3 036011, [arXiv:1208.0009].

[421] M. Asano, T. Bringmann, G. Sigl, and M. Vollmann, *130 GeV gamma-ray line and generic dark matter model building constraints from continuum gamma rays, radio, and antiproton data*, *Phys. Rev.* **D87** (2013), no. 10 103509, [arXiv:1211.6739].

[422] L. Bergstrom and P. Ullio, *Full one loop calculation of neutralino annihilation into two photons*, *Nucl. Phys.* **B504** (1997) 27–44, [hep-ph/9706232].

[423] Z. Bern, P. Gondolo, and M. Perelstein, *Neutralino annihilation into two photons*, *Phys. Lett.* **B411** (1997) 86–96, [hep-ph/9706538].

[424] P. Ullio and L. Bergstrom, *Neutralino annihilation into a photon and a Z boson*, *Phys. Rev.* **D57** (1998) 1962–1971, [hep-ph/9707333].

[425] C. A. Arguelles and J. Kopp, *Sterile neutrinos and indirect dark matter searches in IceCube*, *JCAP* **1207** (2012) 016, [arXiv:1202.3431].